CLAS12 analysis note: Measurement of the cross-section of the photoproduction of the J/ψ meson near the production threshold with the CLAS12 detector.

Pierre Chatagnon[1]*,
Stepan Stepanyan[2],
Mariana Tenorio-Pita[3],
Richard Tyson[2]

[1]Irfu/DPhN, CEA, F91191 Gif-sur-Yvette, France
[2]Thomas Jefferson National Accelerator Facility, Newport News, Virginia 23606
[3]Old Dominion University, Norfolk, Virginia

February 13, 2025

Abstract

This analysis note details the steps performed to extract the total and differential cross section of the photoproduction of J/ψ near the production threshold. The data used for this analysis were taken in 2018 and 2019, with a 10.6 and 10.2 GeV electron beam scattering on a liquid hydrogen target. The aim of this analysis is to publish both the integrated and t-differential cross section, as well as the interpretation of these data in terms of gluonic content of the proton.

*Contact person (pierrec@jlab.org)

Contents

1 Motivations and previous results

The photoproduction of the J/Ψ meson off a nucleon (in the case of this analysis, a proton) has long been identified as an important process to probe the gluon distribution inside the nucleon [1]. Figure 1 shows the diagram of the reaction assuming the produced J/ψ interacts with the nucleon only by the exchange of gluons. Recent theoretical developments [2, 3, 4, 5, 6] have suggested that the gluon Gravitational Form Factors (GFFs) of the proton [7, 8] can be access via the measurement of the t-dependence of the cross section. Lattice QCD calculation have also provided good estimates for the gluon GFFs recently [9, 10, 11]. Comprehensive reviews on the theoretical and experimental results on GFFs can be found in [12, 13, 14].

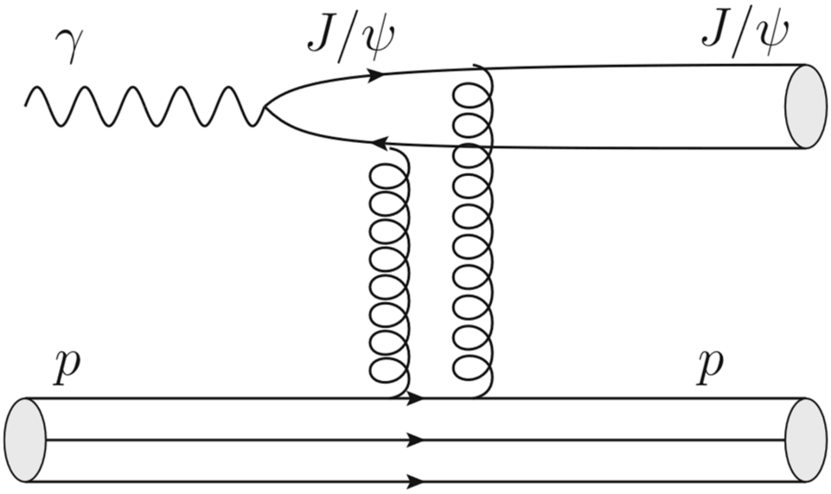

Figure 1: Diagram representing the photoproduction of the meson J/ψ on the proton.

1.1 Experimental results

While photoproduction of J/ψ off a proton has already been measured both at HERA [15, 16] and at LHC experiments in ultra-peripheral collisions, this measurement near its energy threshold is only possible when the initial photon has an energy about 8.2 GeV in the lab frame. Measuring this reaction in this kinematic with large statistics has only been been made possible by the 12-GeV upgrade of the CEBAF accelerator at JLab [17]. Two recent measurements have been performed at Jefferson Lab: first by the GlueX collaboration [18], and by the E12-16-007 experiment in Hall C [19].

In the case of the GlueX measurement, a tagged-photon beam is shined on a di-hydrogen target and the J/ψ is reconstructed in its electron-positron final state. Both the total cross section as a function of the incoming real photon energy and the differential cross section as a function of t have been extracted. The GlueX results are reported in Fig. 2.

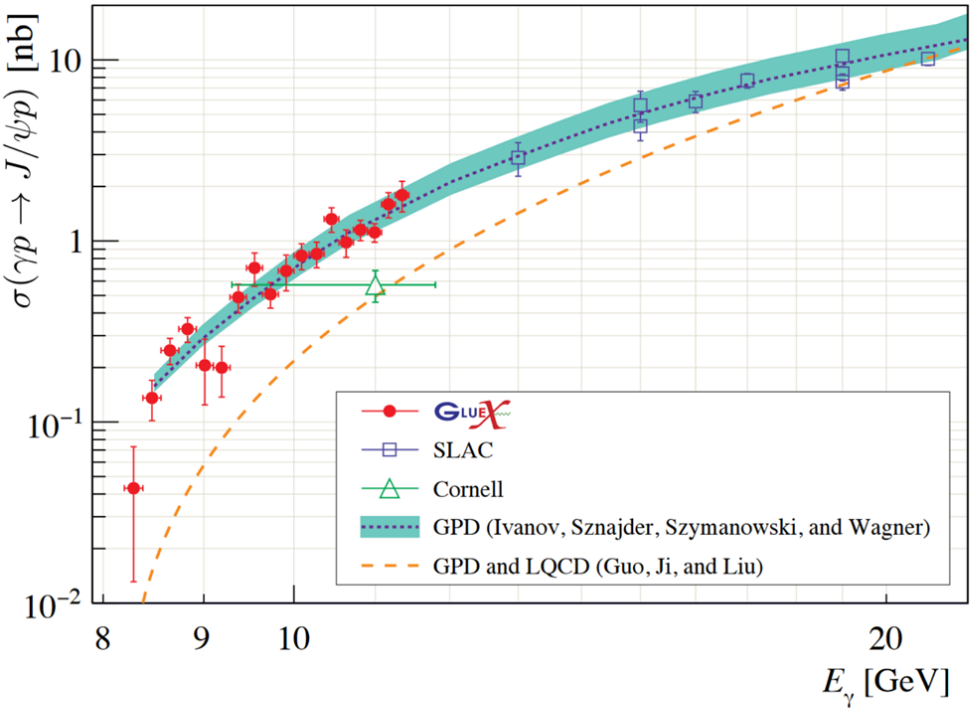

(a) Total cross section for the photoproduction of J/ψ measured by the GlueX collaboration.

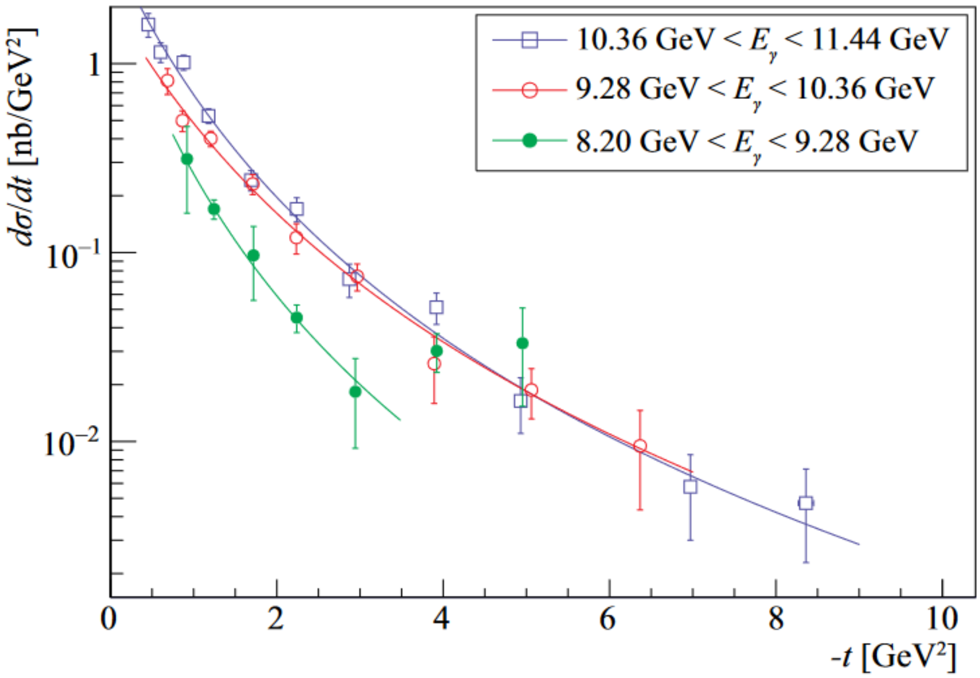

(b) Differential cross section for the photoproduction of J/ψ measured by the GlueX collaboration.

Figure 2: J/ψ photoproduction results from the GlueX collaboration. [18]

The Hall C measurement have used an untagged photon beam scattering of a proton target. The electron-positron pair from the decay of the J/ψ is then detected in the HMS and SHMS spectrometers respectively. The results reported for this experiment only include the differential cross-section as a function of the squared momentum transferred to the proton, $-t$. Figure 3 shows the differential cross-section measured by the JPsi-007 in Hall C.

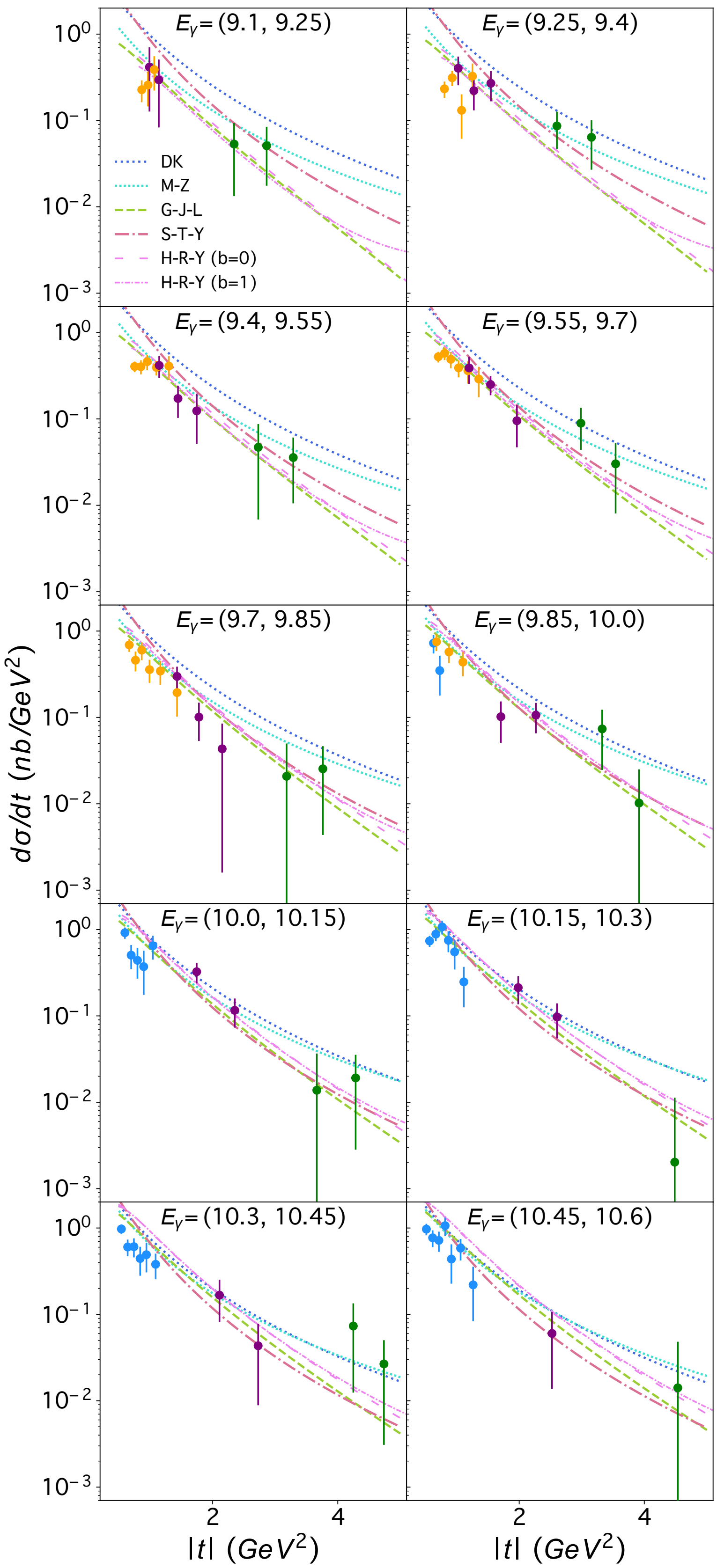

Figure 3: Differential cross-section of the near-threshold photoproduction of J/ψ as a function of the Mandelstam variable $-t$, obtained by the E12-16-007 experiment in Hall C.

1.2 Theoretical models and interpretation in terms of gluons distribution in the proton

The Gravitational Form Factors (GFFs) of the proton have been an active topic of research recently. They appear in the matrix element of the QCD energy-momentum tensor which reads:

$$\langle p_f, s_f | T^{\mu,\nu}_{q,g}(0) | p_i, s_i \rangle = \\ \bar{u}(p_f, s_f)\Big(A_{q,g}(t)\gamma^{\{\mu}P^{\nu\}} + B_{q,g}\frac{iP^{\{\mu}\sigma^{\nu\}\rho}\Delta_\rho}{2M_N} + C_{g,q}\frac{\Delta^\mu\Delta^\nu - g^{\mu\nu}\Delta^2}{M_N} + \bar{C}_{q,g}(t)M_N g^{\mu,\nu}\Big)u(p_i, s_i), \tag{1}$$

where the GFFs are the functions $A_{q,g}(t)$, $B_{q,g}(t)$, $C_{g,q}$, and $\bar{C}_{q,g}(t)$ for gluons and quarks respectively. The gluon GFFs can be related to the gluon GPDs, via their integration of the momentum fraction x as:

$$\int_0^1 dx H_g(x,\xi,t) = A^g_{2,0}(t) + (2\xi)^2 C^g_2 \tag{2}$$

$$\int_0^1 dx E_g(x,\xi,t) = B^g_{2,0}(t) - (2\xi)^2 C^g_2 \tag{3}$$

Assuming Vector-Meson-Dominance, i.e. the exchange of a pair of gluons between the proton and the J/ψ (as depicted in Figure 1, various models have been develop to relate the differential cross-section of the near theshold J/ψ photoproduction to the gluon GFFs of the proton. Note that in all models so far, the $B_{q,g}(t)$ forms factors are assumed to be small according to LQCD findings [10, 11] and thus ignored. Because it is mostly unkow from lattice calculation, the $\bar{C}_g(t)$ form factors is ignored, while its true effect might be large [20, 21] as $\bar{C}(0)$ is related to the trace anomaly of the QCD EMT.

A model based on holographic QCD has been developped in [5, 22, 23, 24]. The differential cross-section is then parametrized as:

$$\frac{d\sigma}{dt} = \mathcal{N}^2 \times \frac{e^2}{64\pi(s-M^2)^2} \times \frac{[A_g(t) + \eta^2 D_g(t)]^2}{A_g^2(0)} \times \tilde{F}(s) \times 8, \tag{4}$$

where $A_g(t)$ and $D_g(t) = 4 \cdot C_g(t)$ are the GFFs defined above, and η and $\mathcal{N} \times e$ are given respectively by:

$$\eta = \frac{M_{J/\psi}}{2(s - m_p^2) - M^2_{J/\psi} + t}, \tag{5}$$

, and

$$\mathcal{N} \times e = 2.032 \text{ nb GeV}^{-2}. \tag{6}$$

Another model based GPDs has been developed in [3, 6]. The GFFs appear in an integral of GPDs and the differential cross section reads:

$$\frac{d\sigma}{dt} = \frac{\alpha_{EM} e_Q^2}{4(s-M^2)^2}\frac{(16\pi\alpha_s)^2}{3M_{J/\psi}}|\psi_{NR}|^2|G(t,\xi)|^2, \tag{7}$$

where

$$|G(t,\xi)|^2 = \frac{4}{\xi^4}\{(1 - \frac{t}{4M_N^2})E_2^2 - 2E_2(H_2+E_2) + (1-\xi^2)(H_2+E_2)^2\}, \tag{8}$$

with H_2 and E_2 defined as:

$$H_2(t,\xi) = A^g_{2,0}(t) + (2\xi)^2 C^g_2, \tag{9}$$

and

$$E_2(t,\xi) = B^g_{2,0}(t) - (2\xi)^2 C^g_2. \tag{10}$$

Finally, the other quantities involved in this model are the non-relativistic wave function of the J/ψ ,

$$|\psi_{NR}|^2 = 1.0952/(4\pi) \text{ GeV}^3, \tag{11}$$

the momentum skewness ξ,

$$\xi = \frac{(-M_{J\psi}^2 + t)}{(2s + t - 2m_p^2 - M_{J\psi}^2)}, \tag{12}$$

and the charge of the charm quark in units of the proton charge, e_Q.

In both models, the functional form of the GFFs is not given. Previous works have been using a tripole dependence for both the A and C form factors:

$$A_g(t) = \frac{A(0)}{\left(1 - \frac{t}{m_A^2}\right)^3} \tag{13}$$

$$C_g(t) = \frac{C(0)}{\left(1 - \frac{t}{m_C^2}\right)^3} \tag{14}$$

From the differential cross-section data obtained by the Hall C measurement, an extraction of the proton gluonic GFFs has been performed using both the GPD-based model and the holographic QCD model. Figure 4 show the extracted GFFs obtained from these results.

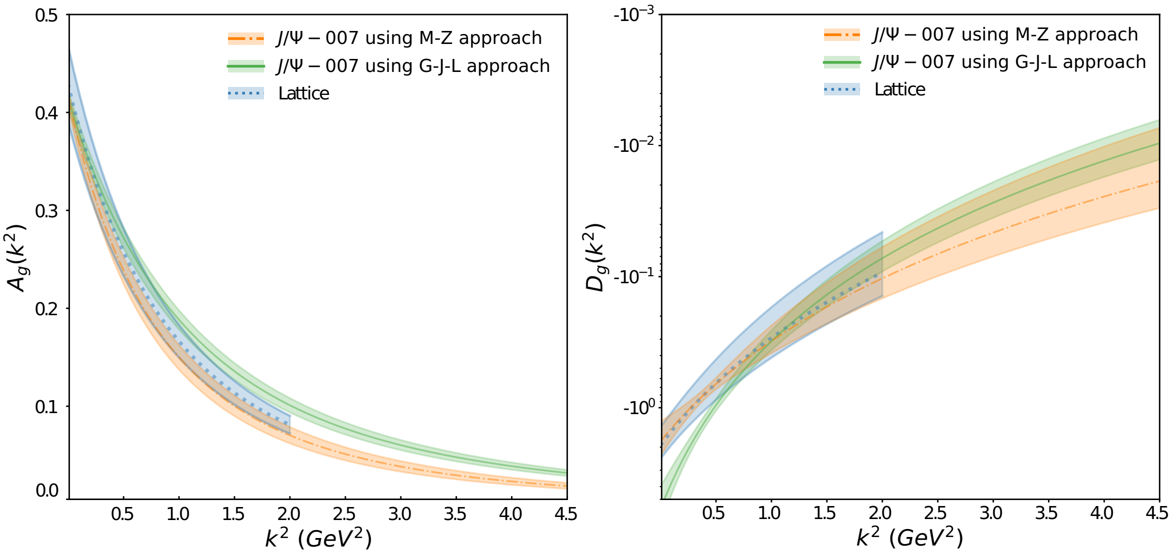

Figure 4: Extraction of gluonic Gravitational Form Factors, performed using the differential cross-section extracted by the E12-16-007 experiment in Hall C. Figure from [19], corrected in [25]

From the $D_g(t) = 4C_g(t)$ form factors, it is possible to extract a pressure distribution produced by the gluons in the proton. From the Fourier transform of $D_g(t)$ and assuming a tripole dependence, one gets:

$$\tilde{D}(r) = \int \frac{d^3\Delta}{(2\pi)^3} e^{-i\Delta \cdot r} D(\Delta, m_C) = \int \frac{d^3\Delta}{(2\pi)^3} e^{-i\Delta \cdot r} \frac{D(0)}{(1 + \frac{\Delta^2}{m_C^2})^3} = D(0) \frac{m_C^3}{32\pi}(1 + m_C r) e^{-m_C r}, \tag{15}$$

which can then be used to derive a transverse and shear pressure profile as:

$$r^2 p(r) = \frac{1}{6m_N} \frac{d}{dr} \left(r^2 \frac{d}{dr} \tilde{D}(r) \right) = \frac{1}{6m_p} \frac{4C(0) \times m_C^5}{32\pi} \times r^2 \times (m_C \times r - 3) e^{-m_D \times r}, \tag{16}$$

and

$$r^2 s(r) = -\frac{1}{4m_N} r^3 \frac{d}{dr} \left(\frac{1}{r} \frac{d}{dr} \tilde{D}(r) \right) = \frac{-1}{4m_p} \frac{4C(0) \times m_C^6}{32\pi} \times r^3 e^{-m_C \times r}, \tag{17}$$

where we assumed the tripole dependence and used Equation 15 to compute the derivative.

Finally, one can also define the mass and scalar radius of the proton as:

$$\langle r_m^2 \rangle_g = 6 \frac{1}{A_g(0)} \frac{dA_g(t)}{dt}\bigg|_{t=0} - 6 \frac{1}{A_g(0)} \frac{C_g(0)}{M_N^2} = \frac{18}{m_A^2} - 6 \frac{1}{A_g(0)} \frac{C_g(0)}{M_N^2}, \tag{18}$$

$$\langle r_s^2 \rangle_g = 6 \frac{1}{A_g(0)} \frac{dA_g(t)}{dt}\bigg|_{t=0} - 18 \frac{1}{A_g(0)} \frac{C_g(0)}{M_N^2} = \frac{18}{m_A^2} - 18 \frac{1}{A_g(0)} \frac{C_g(0)}{M_N^2}. \tag{19}$$

1.3 Open-charm and pentaquark contributions

The interpretation of the differential cross-section in term of gluon GFFs is valid if the process can indeed be described by the exchange of two gluons. However, one could should also included open-charm loop (as in Figure 5a) and potential pentaquark contributions (as in Figure 5b) to properly describe the process near threshold. A lot of work has been done to estimate the impact of both of these contributions and their potential signal in the data (see for example [26, 27] for open-charm results, and [28, 29, 30, 31, 32] for discussions on potential pentaquark contributions).

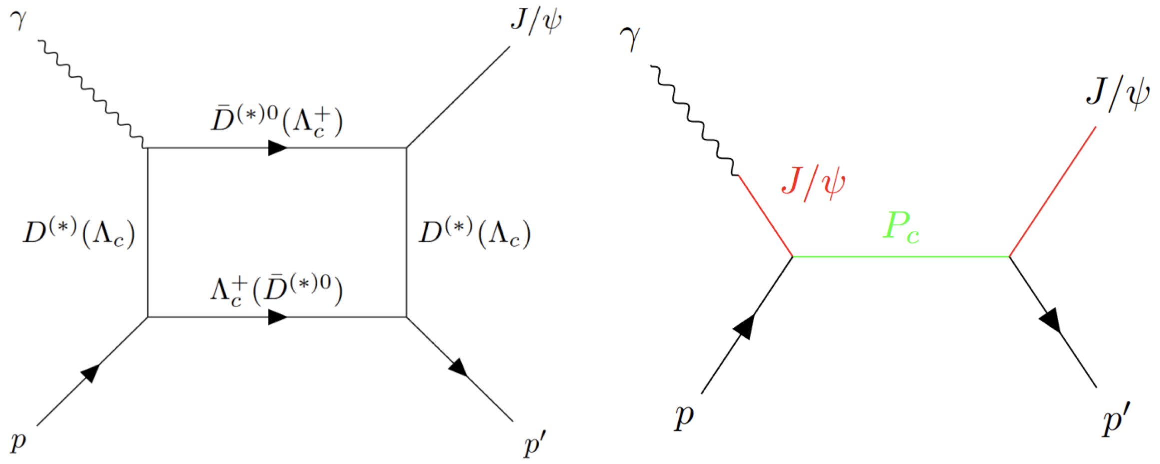

(a) Open-charm loop (b) Pentaquark production

Figure 5: Additional diagrams which have to be considered when describing the photoproduction of J/ψ near threshold.

Particularly, the cusp seen in GlueX data just above photon energies of 9 GeV has been thoroughly analyzed by the JPAC collaboration in [27]. The results suggests that VMD might not be applicable and calls for more data, especially as a function of the incoming photon energy.

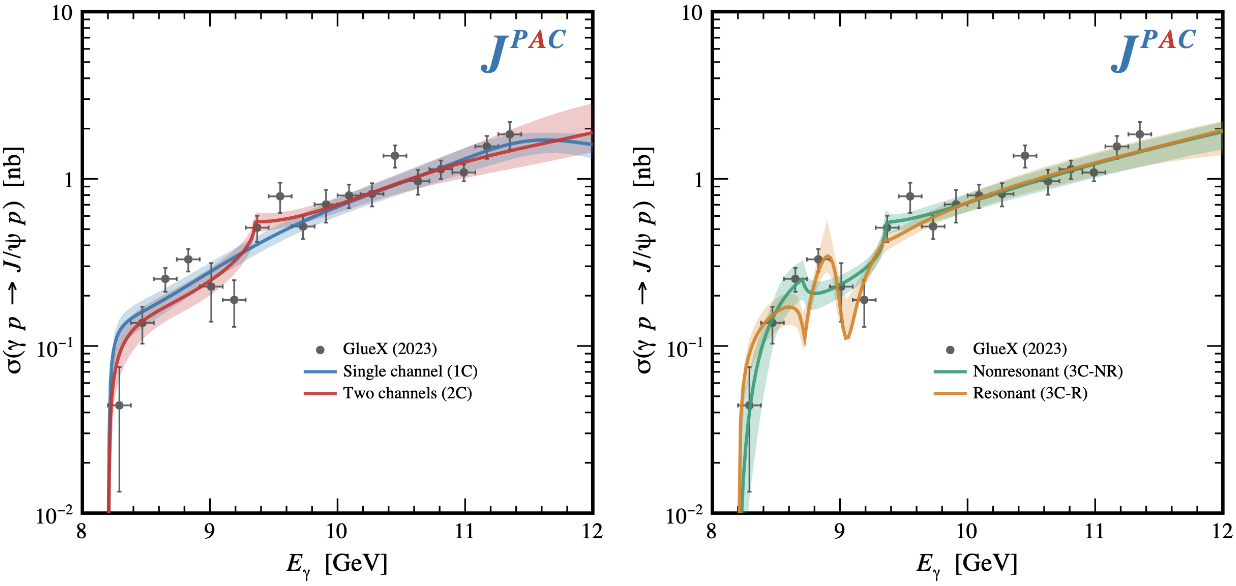

Figure 6: Analysis of the GlueX results by the JPAC collaboration [27]. Three models have been derived in this work: 1-C only including interaction between the proton and the J/ψ , 2-C including intermediate $\bar{D}^* - \Lambda_C$ and 3-C where both $\bar{D}^{(*)} - \Lambda_C$ channels are considered.

2 Analysis code, data and Monte Carlo Samples

2.1 Analysis code repositories

The generators used in this analysis can be found publicly at the following addresses:

- Grape website (see Ref. [33] for details),
- TCSGen github page,
- JPsiGen github page.

The analysis code used to apply the event selection and produce the TTrees used in the rest of the analysis can be found here. Complete documentation for this code will be added soon.

2.2 Data sample and initial selection

For this analysis, the pass 2 RGA dataset is skimmed using the *jpsitcs* train. At the time this note is written the files can be found at the following location:

- Fall 2018 inbending:

  `/cache/clas12/rg-a/production/recon/fall2018/torus-1/pass2/main/train/jpsitcs/*`

- Fall 2018 outbending:

  `/cache/clas12/rg-a/production/recon/fall2018/torus+1/pass2/train/jpsitcs/*`

- Spring 2019 inbending:

  `/cache/clas12/rg-a/production/recon/spring2019/torus-1/pass2/dst/train/jpsitcs/*`

First, a pre-selection of the events using the CLAS12 QADB is done. The QADB tool (see the QADB github page) is used to perform this step by requiring each event to satisfy the *OkForAsymmetry* criteria. The accumulated charge for the events passing this criteria is retrieved for each analysed run (see Table 1 for a detailed summary of the accumulated charges per run period and Appendix E for a detailed run-by-run summary).

2.3 Monte-Carlo samples and processing

For this analysis, three event generators are used (see section 2.1 for code availability):

- Grape, to generate the virtual photon contribution of the Bethe-Heitler continuum, starting at invariant mass of 2 GeV,
- TCSGen, to generate the real photon contribution of the Bethe-Heitler continuum, starting at invariant mass of 2 GeV,
- JPsiGen (with and without radiative effects), to generate the J/ψ signal.

The OSG portal is used to generate the MC samples and pass them to GEMC [34], the Geant4 [35] based Monte-Carlo simulation of CLAS12.

The MC samples have been produced with the following version of the simulation and reconstruction:

- GEMC: 5.10
- CoatJava: 10.0.7

In total, 24 Monte Carlo samples are produced: one per experimental configuration, per beam current and per generator. Three additional samples are produced using JPsiGen without radiative effects to compute the radiative correction factors. Table 1 summarizes all the Monte Carlo and data samples used in this analysis.

<table>
<tr><th rowspan="2">Sample type</th><th colspan="6">Configuration/Beam current/Charge</th></tr>
<tr><th colspan="3">Fall 18 in.</th><th colspan="2">Fall 18 out.</th><th>Spring 19</th></tr>
<tr><td>Data</td><td>45 nA
26.312 mC</td><td>50 nA
4.00 mC</td><td>55 nA
5.355 mC</td><td>40 nA
11.831 mC</td><td>50 nA
20.620 mC</td><td>50 nA
45.994 mC</td></tr>
<tr><td>Grape</td><td colspan="5">8.2M each</td><td>6.7M each</td></tr>
<tr><td>TCSGen</td><td colspan="5">2M each</td><td>1.5M each</td></tr>
<tr><td>JPsiGen</td><td colspan="6">2M each</td></tr>
<tr><td>JPsiGen (no rad.)</td><td colspan="6">3M each</td></tr>
<tr><td colspan="7">Total of 24 MC samples and 3 Data samples</td></tr>
</table>

Table 1: Summary of the MC and Data samples used for this analysis.

2.4 Radiative effect in Monte Carlo

A comprehensive description of the method used to take into account the radiative effect is done in Appendix P for Bethe-Heitler events and Q for J/ψ events.

2.5 MC/data normalization

For this analysis, we have normalized all MC histograms to their expected yields, i.e. using the estimated cross-sections provided by the generator and the accumulated charge of the corresponding run period. The following section describes the procedure used to normalized MC and data histograms throughout this analysis. This material is adapted from an internal note available here.

2.5.1 Integrated luminosity factor for RG-A

For fixed-target experiments such as CLAS12, the integrated luminosity depends on the total beam charge on target and the target parameters (length and density). It can be written as:

$$\mathcal{L}_{\mathcal{INT}} = N_{beam} \times n_{Target} = \frac{Q}{e} \times \frac{l \cdot \rho \cdot N_t \cdot N_A \cdot C}{M_t}, \tag{20}$$

where N_{beam} is the total number of electron that crossed the target and n_{Target} is the number of "target" particle per area in the target of CLAS12. Each of these two quantities can be expressed in terms of the following values for the RGA dataset:

- l [in cm]: 5 cm
- ρ [in $g.cm^{-3}$]: 0.0708 $g.cm^{-3}$ (Density of liquid di-hydrogen)
- N_t [No units]: 2, the number of "target" proton in dihydrogen
- N_A [in mol^{-1}]: the Avogadro number ($6.02 \times 10^{23} mol^{-1}$)
- C [No units]: Conversion factor from cm^{-2} to pb^{-1} (10^{-36})
- e [in C] : the electron charge ($1.602 \times 10^{-19} C$)
- M_t [in $g.mol^{-1}$]: 2.016 $g.mol^{-1}$ Molar mass of dihydrogen

Replacing the numerical values in the general formula, the integrated luminosity for RG-A reads:

$$\mathcal{L}_{\mathcal{INT}} = 1316.875 \times 10^3 \times Q[\text{in C}]\ pb^{-1} \tag{21}$$

or

$$\mathcal{L}_{\mathcal{INT}} = 1316.875 \times Q[\text{in mC}]\ pb^{-1} \tag{22}$$

2.5.2 Monte-Carlo re-weighting

There are two types of Monte-Carlo generators: unweighted and weighted MC. In the first case, each event produced by the Monte-Carlo can be treated as a data-event. In the second case, each MC event is assigned a weight used to weight the event when filling histograms. The normalization data/MC is slightly different in these two cases.

2.5.2.1 Monte-Carlo with un-weighted events

In the majority of Monte-Carlo event generators, each generated event do not carry any weight and can be treated exactly as a data event. This is the case of GRAPE. In this case, when using the generator, users are provided with the total cross-section of the process over the phase-space where events have been produced. This cross-section is referred as σ_{GEN_TOT} [in pb]. The total number of generated events for this given phase-space is denoted N_{GEN}.

To normalize an un-weighted MC sample to a given dataset with integrated luminosity $\mathcal{L}_{\mathcal{INT}}$ [in $pb^{-}1$], one should assign to each MC event a weight equal to:

$$\omega = \frac{\mathcal{L}_{\mathcal{INT}} \cdot \sigma_{GEN\_TOT}}{N_{GEN}}. \tag{23}$$

The weight factor ω is constant. Hence, one can scale all MC histograms by this same factor instead of re-weighting each event.

2.5.2.2 Monte-Carlo with weighted events

Some generators provide weights for each event. Usually these weights correspond to the cross-section at the given kinematics of the events multiplied by a phase-space factor accounting for the fact that the events are randomly generated over a certain limited phase-space. This is the case for TCSGen and JPsiGen.

To normalize a weighted MC sample to a given dataset with integrated luminosity $\mathcal{L}_{\mathcal{INT}}$ [in $pb^{-}1$], one should assign to each MC event a weight equal to:

$$\omega = \frac{\mathcal{L}_{\mathcal{INT}} \cdot \omega_{GEN}}{N_{GEN}}, \tag{24}$$

where ω_{GEN} is the weight provided by the generator.

3 General analysis strategy and tools

The analysis aims at measuring the cross section of the photoproduction of the J/ψ meson. As CLAS12 does not have a photon beam, we aim at selecting this reaction in the quasi-photoproduction regime, where an electron from the beam emits a real photon. In this case, the reaction of interest is:

$$ep \to (e')\gamma p \to (e')J/\psi\; p' \to (X)e^+e^-p', \tag{25}$$

where the kinematics of the missing particle X can be fully reconstructed if all final state particles e^-, e^+ and p are detected. The missing particle 4-vector can be expressed as:

$$p^\mu_X = p^\mu_{beam} + p^\mu_p - p^\mu_{e+} - p^\mu_{e+} - p^\mu_{p'}. \tag{26}$$

3.1 Particle identification

The measurement of exclusive J/ψ photoproduction requires the identification of the scattered proton, and the two leptons from the decay of the J/ψ meson. The following sections details the procedure used to identify these particles.

3.1.1 Proton identification

The standard event builder of CLAS12 (see [36] for more details) is used to identify the scattered proton. No other cut is applied. In section 7.1.5, a systematic error on this identification is estimated by varying the proton χ^2 cut.

3.1.2 Lepton identification

The electron and the positron are first identified using the standard CLAS12 event builder (see Ref.[36] for more details). However, it has been shown that at large momentum (above 4.5 GeV), there is a large contamination from positive and negative pions in the positron and electron samples respectively (see for example the approved TCS analysis note). Thus an additional Boosted-Decision-Tree-based algorithm is used to reduce this background for particle above 4.5 GeV. We developed an identification algorithm using information obtained from the CLAS12 calorimeter to distinguished between positrons and pions above the HTCC threshold. This algorithm is largely based on the approved algorithm used in the published TCS measurement. More details on this new version of the algorithm can be found in a dedicated note here. Thus, in the following, we only show the material justifying the approach. A Boosted-Decision-Tree is trained on single lepton (pion) Monte Carlo events (including a trigger electron in the opposite sector as the other particle). Signal events are defined as lepton being identified as leptons. Background events are defined as pions being identified as leptons. The 9 input variables of the BDT are the angles and momentum in the lab frame of the particle, its sampling fractions in each of the calorimeters subsystems, defined as:

$$SF = \frac{E_{PCAL/ECIN/ECOUT}}{P}, \tag{27}$$

and the second moment of the shower, in each of the calorimeter subsystem defined as:

$$M_2 = \frac{m_{2u} + m_{2v} + m_{2w}}{3}, \tag{28}$$

where m_{2u}, m_{2v}, and m_{2w} are the 2^{nd} moments of the shower on each readout side of the calorimeter (u, v, and w), defined as:

$$m_2 = \frac{\sum_{strip}(x-D)^2\ln(E)}{\sum_{strip}\ln(E)}, \tag{29}$$

where x is the position of the hit in u, v or w, E is the associated energy of the hit in the calorimeter and D is the log-weighted mean position of the shower defined as:

$$D = \frac{\sum_{strip} x\ln(E)}{\sum_{strip}\ln(E)}. \tag{30}$$

.

Figures 7 and 8 show the momenta and angles of the generated true events and true positive, and the generated true negative and the false positive, in the Fall 2018 inbending case. The ratio of the respective spectra are also shown. One can see that the BDT is able to preserve almost 98% of the true signal event while reducing the false positive background to 6%. More importantly, one can verify that there is little correlation of the efficiency with the particle kinematic. This ensure that these estimation for signal efficiency and background rejection can be applied throughout the entire phase space of the analysis.

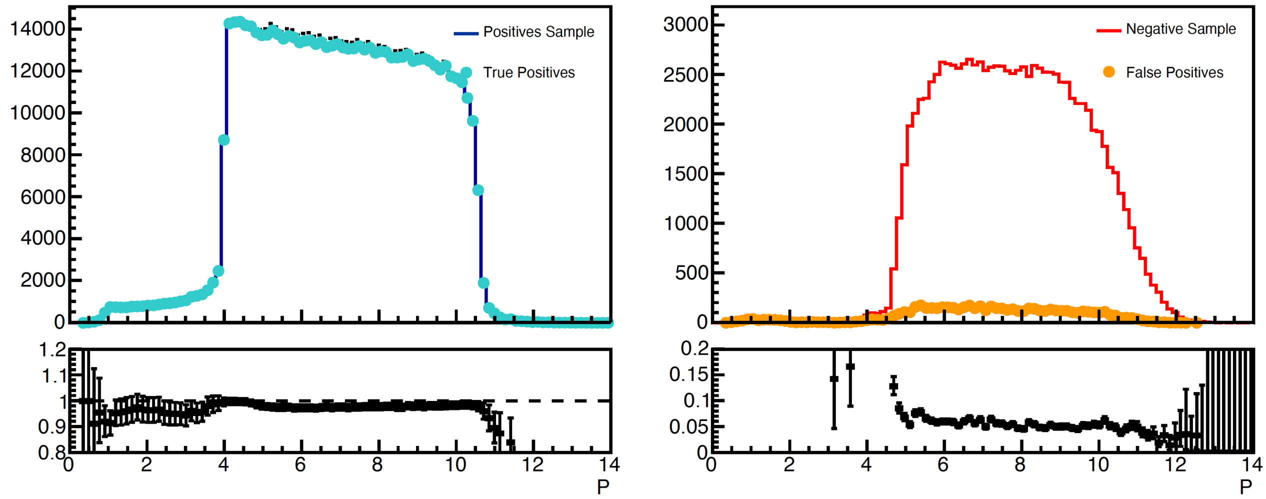

Figure 7: Momentum spectra for the generated signal events and the true positive events (left), and the generated background events and the false positive events (right).

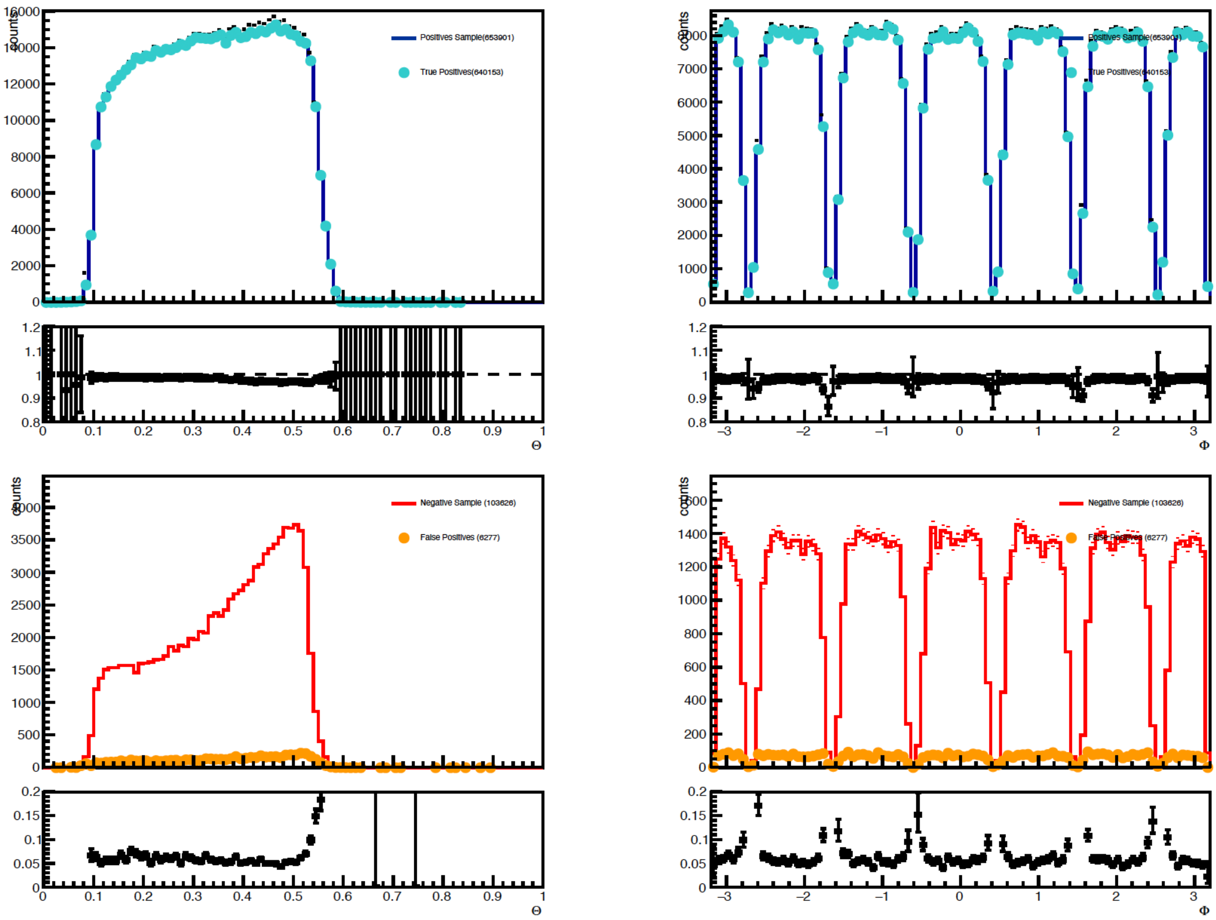

Figure 8: Polar (left) and azimuthal (right) angles spectra for the generated signal events and the true positive events (top), and the generated background events and the false positive events (bottom).

Six BDTs have been used in this analysis: two per era (one for electrons and one for positrons).

As the training of the BDTs is done on simulation only, a validation is done on data. This consists in using two sets of real-data events for signal and background estimation. The signal is estimated using radiated eleastic events:

$$e^- p \to e^{-(+)}\gamma X \tag{31}$$

while the background is estimated using positive pion electro-production:

$$ep \to e' e^+_{m_\pi} X, \tag{32}$$

where a positron is detected and for which the pion mass is assigned. More details on the treatment, including the missing neutron fit for the background sample in data, of these events can be found in the note. Assuming the efficiency is constant over the whole analysis phase space, as justified above, one can look at the ROC curve of the BDT. This is done using MC and data samples. Figure 9 shows the ROC curves for simulation and data for positrons and for each era. It can be seen that in the inbending case, the two curves are very close to each other, while in the outbending case, the discrepancy is larger. To qualitatively estimate this discrepancy, the ratio of the signal efficiency is computed as a function of the cut applied on the BDT output. This is done for both magnetic field configuration of the Fall 2018 era and for both leptons (in Figure 10 and 11 for Fall 2018 inbending, and in Appendix O.1 for all other eras) . At the standard cut value of 0.0, the ratio for both leptons in the inbending case deviates by 5% from the unity. We will use these numbers to estimate the normalization using the single particle efficiency in section 4.4.

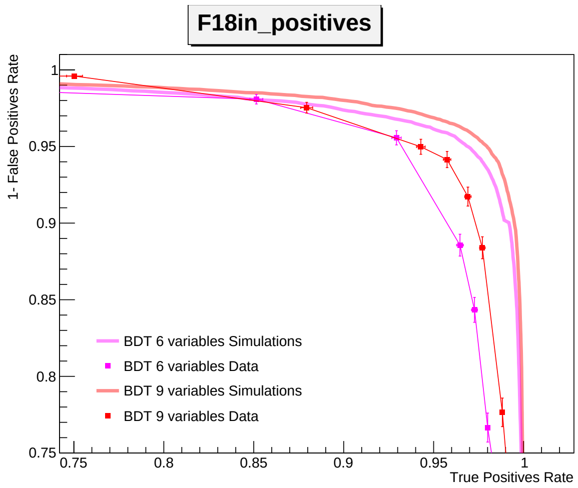

(a) Fall 2018 Inbending positrons

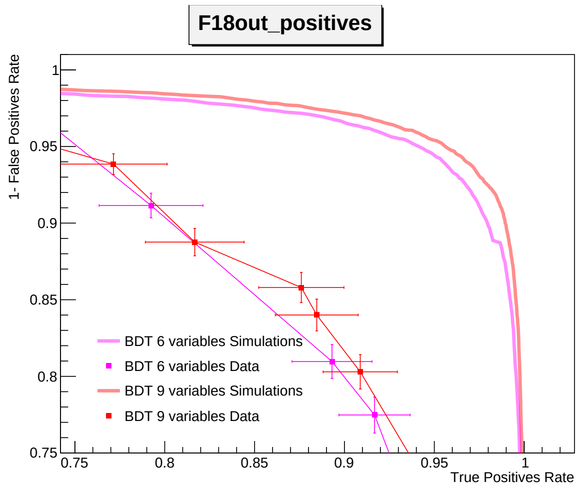

(b) Fall 2018 Outbending positrons

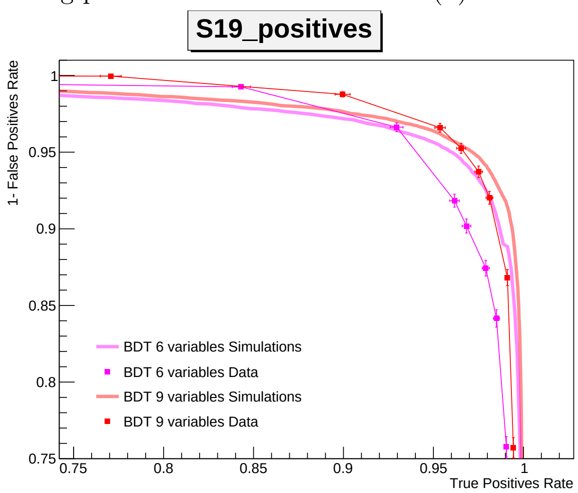

(c) Spring 2019 positrons

Figure 9: ROC curve comparing the results of the validation on Data (square points) and simulation (solid line) for BDT-6 (not used in this analysis) and BDT-9 variable models for (a) Fall 2018 inbending, (b) Fall 2018 outbending positrons, and (c) Spring 2019. In both cases, the results from the data are lower than those in MC, but the trend is consistent with simulation results.

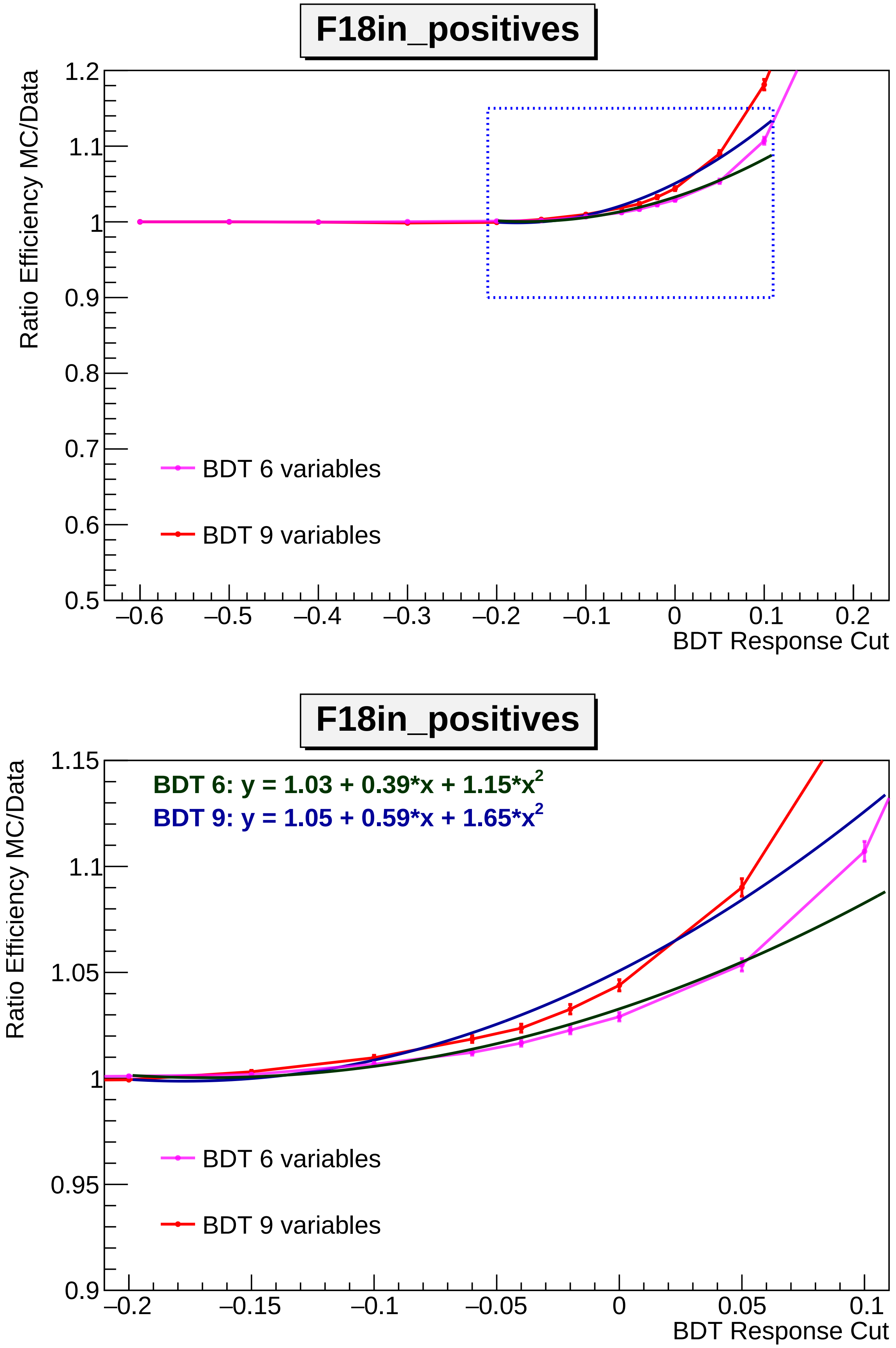

Figure 10: Ratios of efficiencies MC to data for positron identification classifiers for the Fall 2018 inbending data sets as a function of the cut in the response. The lower plot is a zoom in the region of the cut value at 0.0. The BDT used in this analysis is referenced as 'BDT 9 variables'.

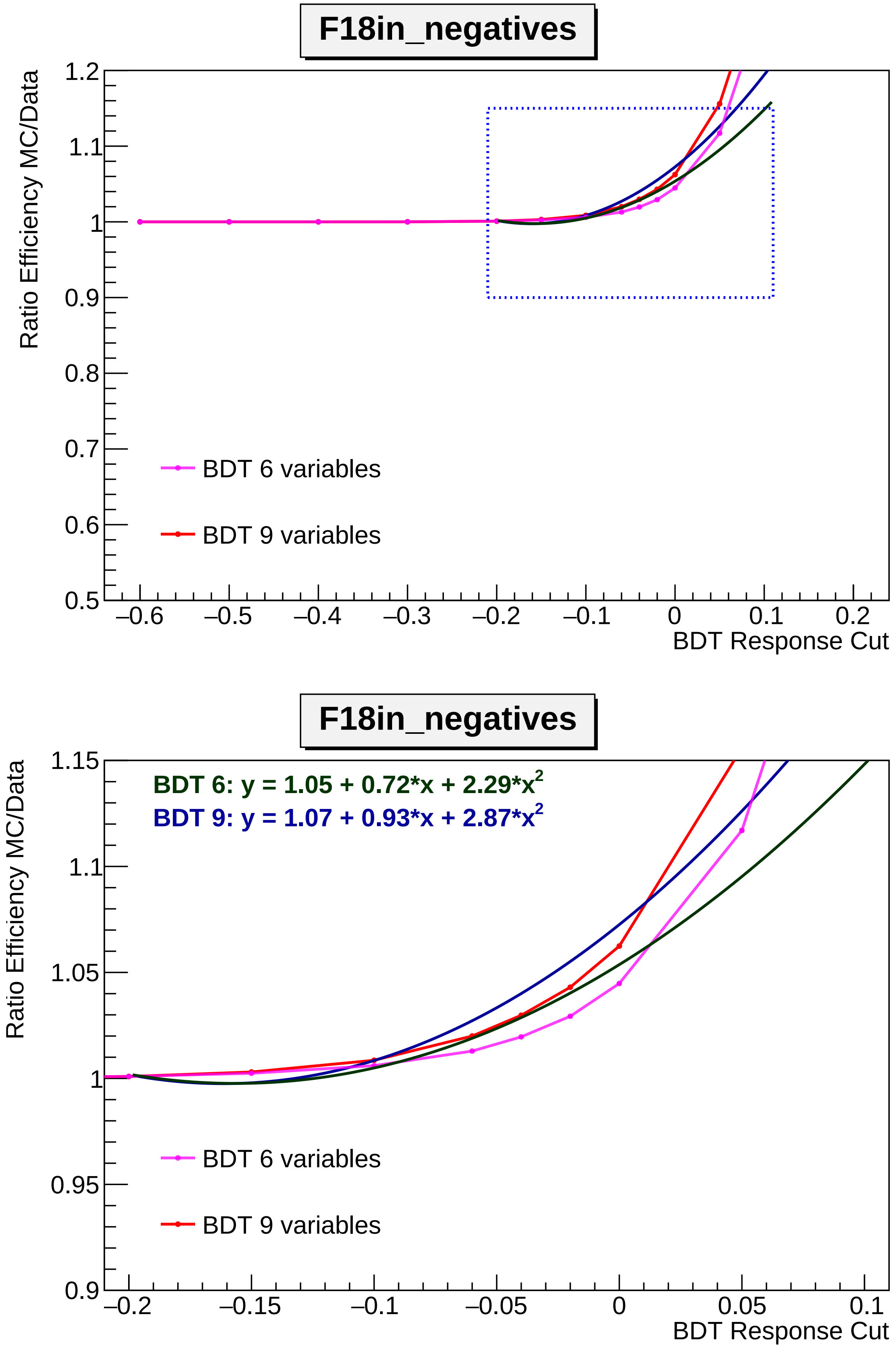

Figure 11: Ratios of efficiencies MC to data for electron identification classifiers for the Fall 2018 inbending data sets as a function of the cut in the response. The lower plot is a zoom in the region of the cut value at 0.0.

3.1.3 Radiated photons correction

It has been shown for the TCS measurement, that some leptons may radiated photons in the target material. This leads to the detection of energetic photons in the azimuthal vicinity of the lepton which emitted the photon. In Figure 12, the angular distances of electron and positrons with photons detected in the same event is shown. A strong enhancement is visible when the azimuthal angle difference between the lepton and photon is small. In this case, the photons have been radiated by the corresponding lepton, and the lepton momenta must be corrected for this effect.

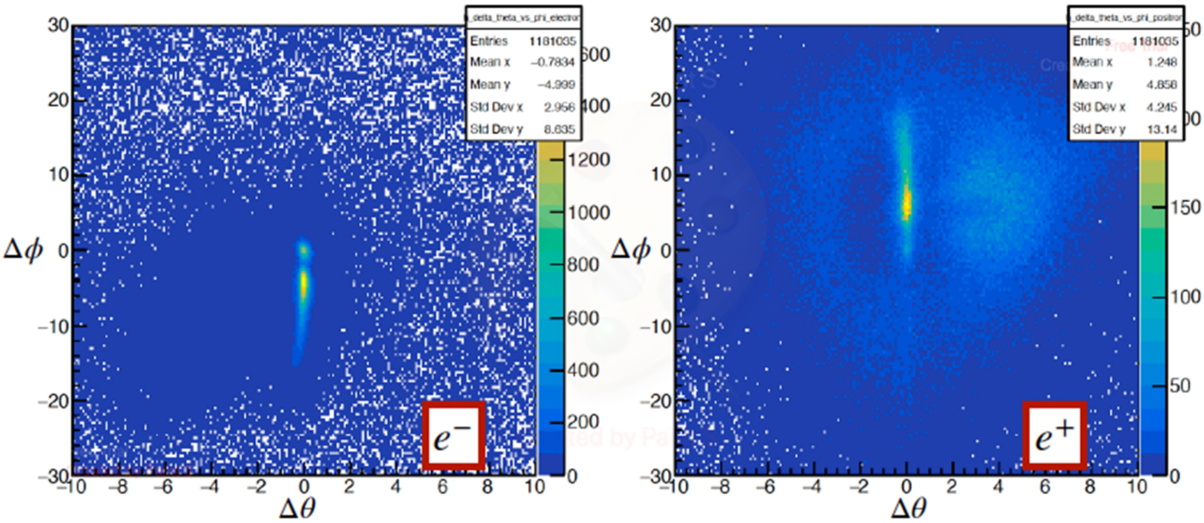

Figure 12: Difference of polar and azimuthal angles of leptons (electron on the left and positron on the right) and photons in the data samples used in this analysis. A clear azimuthal correlation is visible.

To account for this radiation, the lepton momenta are corrected by the detected photon momenta as:

$$\vec{p}_{lep.\ corr.} = \vec{p}_{lep.\ uncorr.} + \sum_{\gamma} \vec{p}_{\gamma} \tag{33}$$

when their azimuthal difference is smaller than 1.5°.

3.1.4 Lepton momentum correction

The J/ψ peak mean in fits to the electron positron mass is lower than the J/ψ mass of 3.097 GeV by about 15 MeV. This is indicative of a need for corrections to the lepton momentum. Data derived momentum corrections are established from elastic scattering (ie $e_{beam}p \to e_f p$) and radiative elastic scattering (ie $e_{beam} \to e_i \gamma_r p \to e_f p X$) in RG-A fall2018 data. For radiative electron scattering the initial and final state electron momentum (p_i and p_f respectively) can be calculated as:

$$\begin{aligned} p_i &= \frac{M_p}{1 - \cos\theta_{e^-}} \left(\cos\theta_{e^-} + \sin\theta_{e^-} \frac{\cos\theta_p}{\sin\theta_p} - 1 \right) \\ p_f &= \frac{p_i}{1 + \frac{p_i}{M_p}(1 - \cos\theta_{e^-})} \end{aligned} \tag{34}$$

for $\theta_{e,p}$ the polar angle of the final state electron or proton and M_p the mass of the (target) proton. The momentum correction is then obtained by taking the relative difference between the calculated and reconstructed momentum, $\frac{\Delta P}{P}$. A first assumption made here is that the resolution on the polar angle is much better than the resolution of the momentum, which is demonstrated in simulation, and so the dominant contribution to $\frac{\Delta P}{P}$ comes from the resolution on the momentum. The second assumption is that the electron and proton polar angles are measured along the same axis. This is not necessarily the case as the proton will be detected in the central detector whereas the electron will be detected in the forward detector. To correct any misalignment between the two detectors, the electron beam momentum (p_{beam}) and final state electron polar angle θ_{e^-} can be calculated in elastic scattering as:

$$p_{beam} = \frac{M_p}{1-\cos\theta_{e^-}}\left(\cos\theta_{e^-} + \sin\theta_{e^-}\frac{\cos\theta_p}{\sin\theta_p} - 1\right) \tag{35}$$
$$\theta_{e^-} = 2\arctan\left(\left(\frac{p_{beam}}{M_p}+1\right)\frac{\sin\theta_p}{\cos\theta_p}\right)^{-1}$$

The strategy for the corrections goes as follows: first any misalignment between the CD and FD is corrected using elastic scattering. Next, the electron final state momentum is corrected from radiative elastic scattering. A final assumption is made that electrons in inbending data are equivalent to positrons in outbending data (and vice versa) with regards to momentum corrections. The corrections are therefore established in inbending data and applied to inbending electrons and outbending positrons and established in outbending data and applied to outbending electrons and inbending positrons.

Elastic scattering and radiative elastic scattering can be identified first by looking at the azimuthal angle difference between the electron and proton, which should be 180^o. Figure 13 shows this angle difference for inbending and outbending data. A clear peak is observed, and cuts are placed to select the range from 178-182^o.

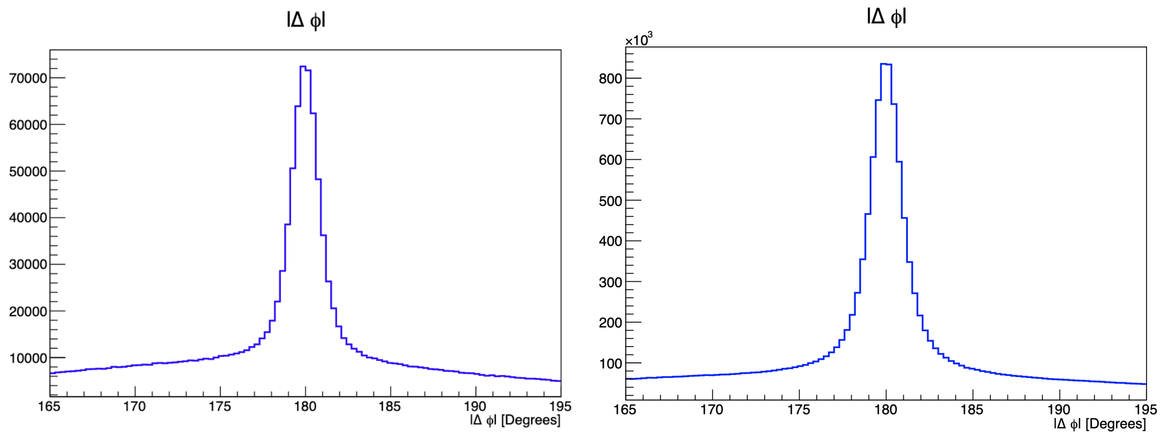

Figure 13: The azimuthal angle difference between the proton and e- in elastic scattering and radiative elastic scattering in inbending (left) and outbending (right) RG-A data.

Radiative elastic scattering can then be separated from elastic scattering by looking at the missing mass of $ep \to e'X$ and the transverse missing momentum fraction in $ep \to e'pX$. The first should peak at the proton mass for elastics scattering, whereas the second should peak at zero for radiative elastic scattering. Figure 14 shows these two quantities produced on the proton in inbending and outbending data. The proton peak can be clearly identified in the missing mass of $ep \to e'X$ and a range of 0.6 to 1.3 GeV is selected for elastic scattering. The missing transverse momentum fraction peaks at zero for $ep \to e'pX$ and the range below 0.015 is selected for radiative elastic scattering.

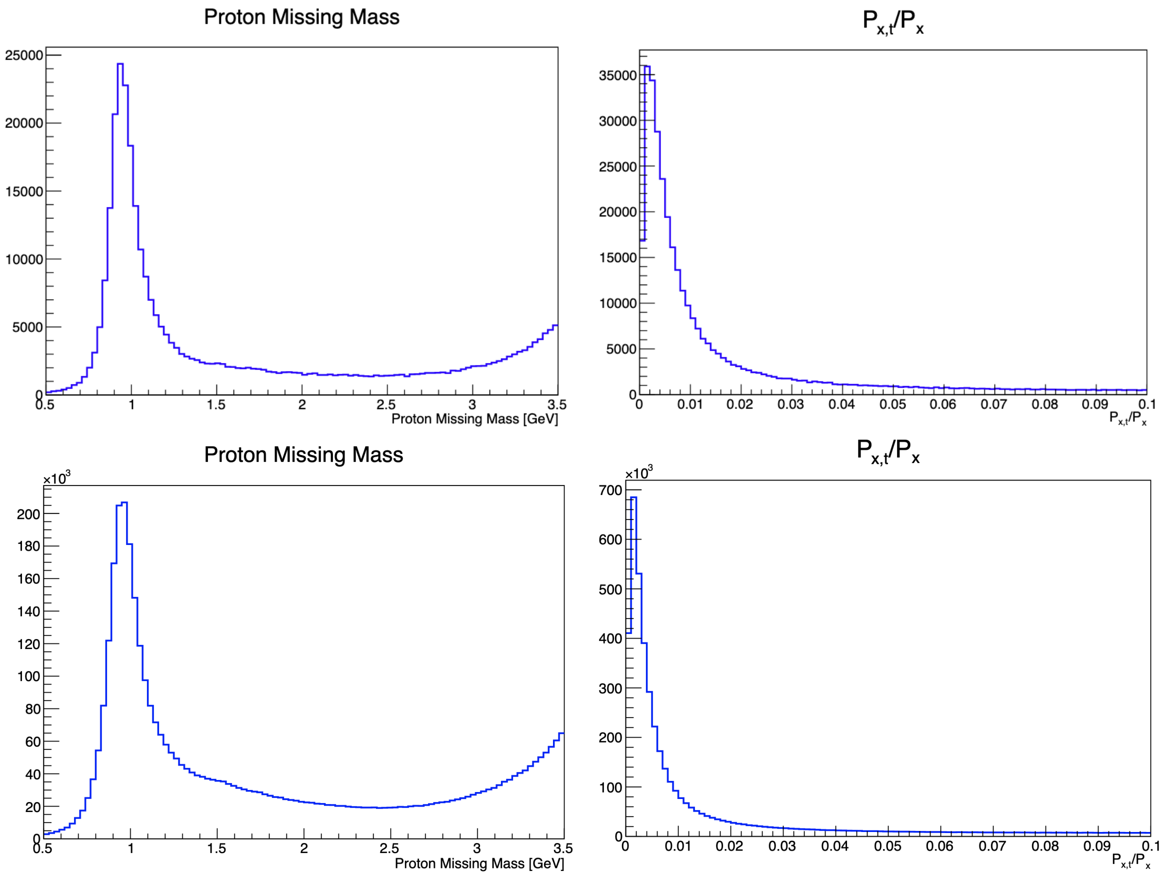

Figure 14: The missing mass $ep \to e'X$ (left) and the missing transverse momentum fraction of $ep \to e'pX$ (right) in inbending (top) and outbending (bottom) data.

The difference between the reconstructed electron polar angle θ_{e^-} as a function of azimuthal angle and the one calculated using equation 35 is shown in Figure 15 for the inbending and outbending elastic scattering on the proton datasets. The difference in θ_{e^-} is fitted for each sector, and this oscillation as a function of ϕ_{e-} is then fitted with

$$\Delta\theta_{e^-} = q_0 * \sin\left((q_1 + \phi_{e^-})\frac{\pi}{180}\right) + q_2 \tag{36}$$

which accounts for a misalignment between two axes.

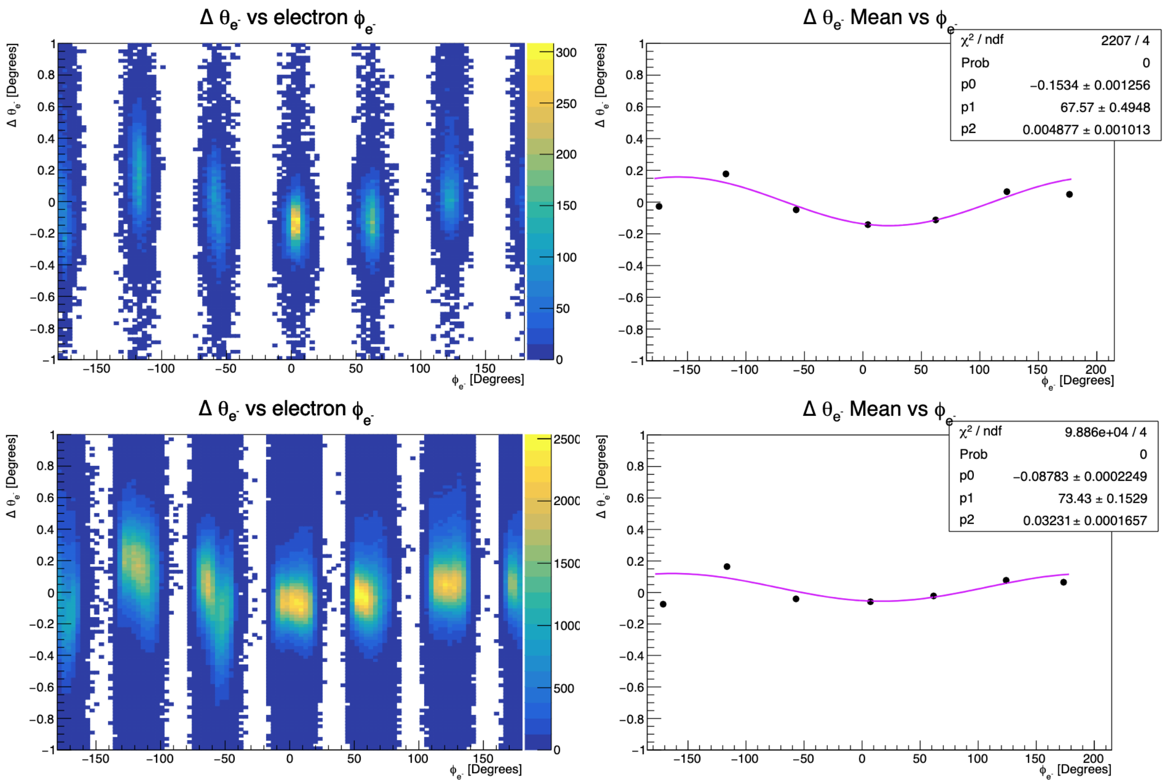

Figure 15: The difference between calculated and reconstructed electron polar angle (θ_{e^-}) as a function of azimuthal angle (ϕ_{e^-}) in the RG-A inbending dataset (top) and in the RG-A outbending dataset (bottom).

The parametrisation as a function of ϕ_{e^-} is then used to correct the misalignment between the CD and FD by correcting θ_{e^-} in Equation 34. The relative difference between the reconstructed and calculated electron momentum is shown as function of momentum in Figure 16 for the RG-A inbending and outbending radiative elastic scattering on the proton datasets. The relative difference is fitted with

$$\frac{\Delta P}{P} = p_0 + p_1 * P + p_2 * P^2 + \frac{p_3}{P} + \frac{p_4}{P^2}. \tag{37}$$

Table 2 summarizes the fitted paramaters.

Parameters	p_1	p_2	p_3	p_4	p_5
Inbending	9.376e-03	-7.808e-04	1.063e-04	-2.029e-02	4.121e-02
Outbending	-6.520e-02	7.099e-03	-5.929e-05	2.145e-01	-1.153e-01

Table 2: Parameters for the lepton momentum correction.

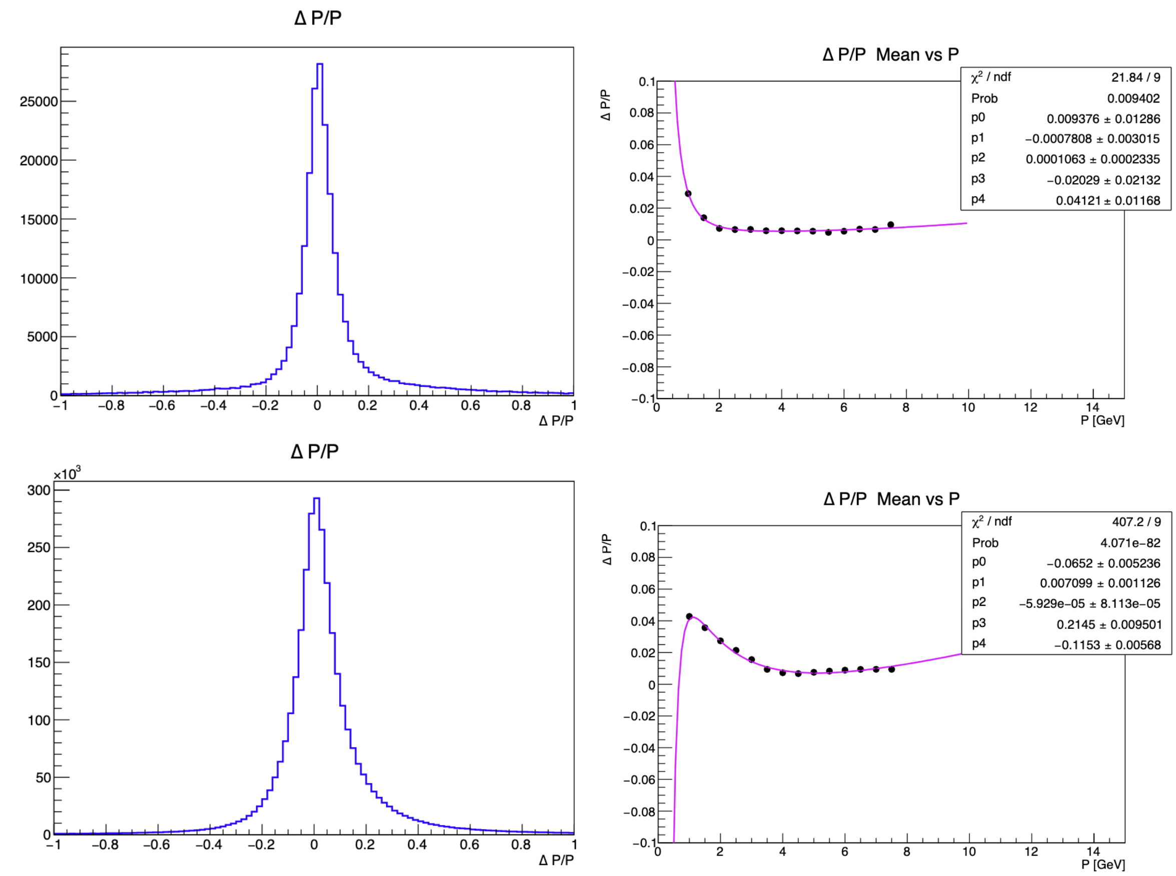

Figure 16: The difference between calculated and reconstructed electron momentum as a function of momentum in the inbending dataset (top) and in the outbending dataset (bottom).

The lepton momentum correction is applied to the both leptons of the J/ψ photoproduction events. For the inbending dataset, the electron is corrected by its own correction function, while the positron is corrected by the outbending electron function. The reverse logic is applied for the outbending dataset. The Spring 2019 dataset is corrected using the function derived for the Fall 2018 dataset.

Figure 17 shows the effect of the momentum correction for the leptons in the mass region of the J/ψ . Except a shift of the J/ψ peak toward larger mass in the inbending case, no qualitative change in the data is seen.

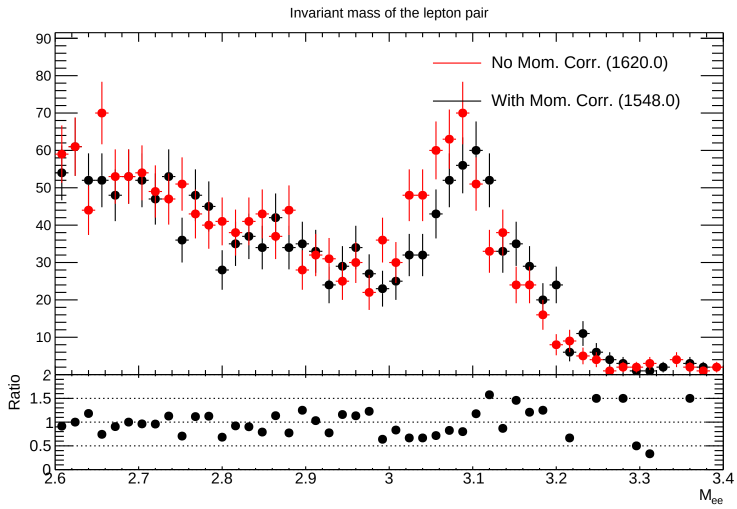

(a) Fall 2018 Inbending

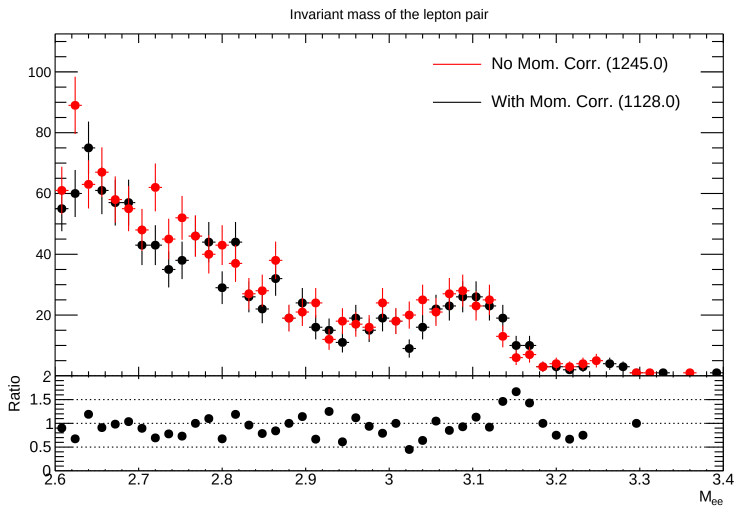

(b) Fall 2018 Outbending

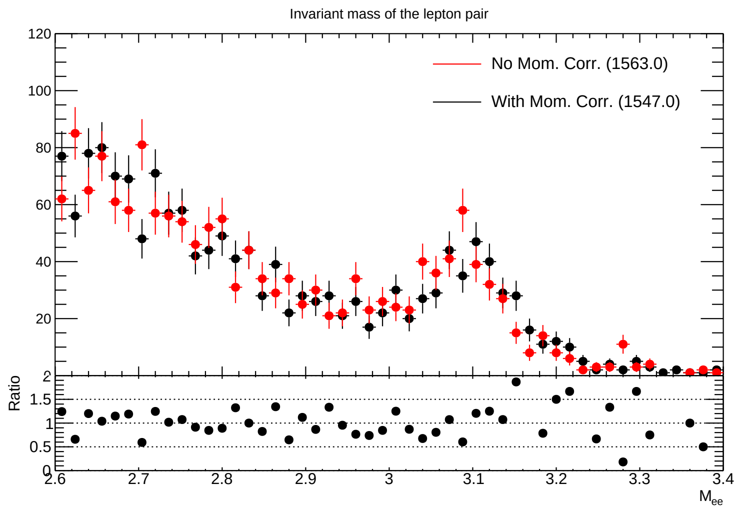

(c) Spring 2019

Figure 17: Invariant mass of the lepton pair in the J/ψ region, before and after momentum corrections of the leptons.

3.1.5 Proton energy loss in the forward detector

Finally, a correction of the proton momentum due to energy loss is derived from Monte Carlo and applied on both data and MC samples. The correction is derived here only for the FD protons, which are the only one considered in this analysis. The relative difference of the reconstructed momentum with respect to the generated one, i.e.:

$$\frac{\Delta_P}{p_{REC}} = \frac{p_{REC} - p_{GEN}}{p_{REC}}, \tag{38}$$

is shown in Figure 18 as a function of the reconstructed polar angle of the proton. Because the behavior of the relative difference is changing at round 27°, the correction is derived in two distinct polar angle region: for $\theta_{pREC} < 27°$ and $\theta_{pREC} > 27°$.

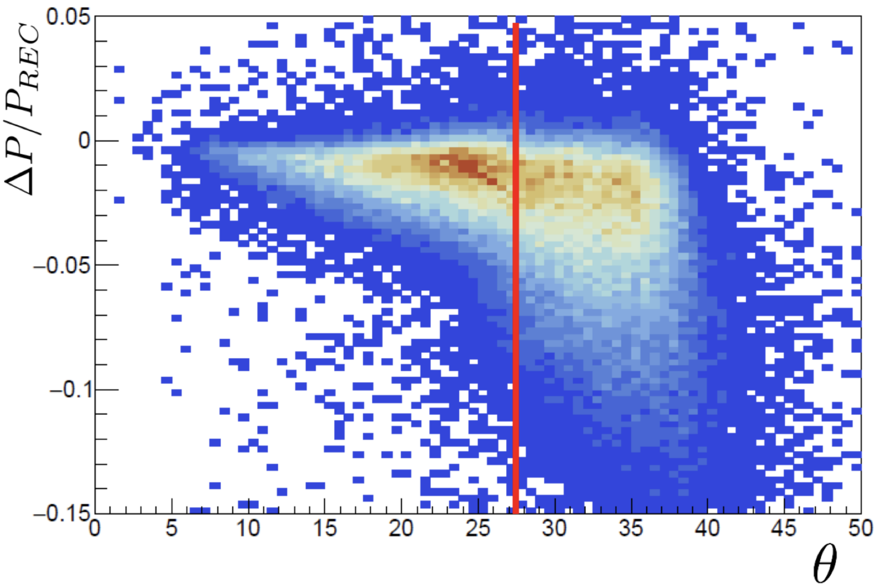

Figure 18: Relative difference between the reconstructed and the generated momenta of FD protons, for Fall 2018 inbending BH MC events and as a function of their reconstructed polar angle. This plot is done before any correction is applied.

The relative momentum difference is fitted, as a function of reconstructed momentum, with the following function:

$$Corr_{proton}(p) = (a \cdot e^{b+c\cdot p}) \times (d + e \cdot p + f \cdot p^2). \tag{39}$$

Figure 19 shows the fitted function for both polar angle regions, for a Fall 2018 inbending Monte-Carlo sample.

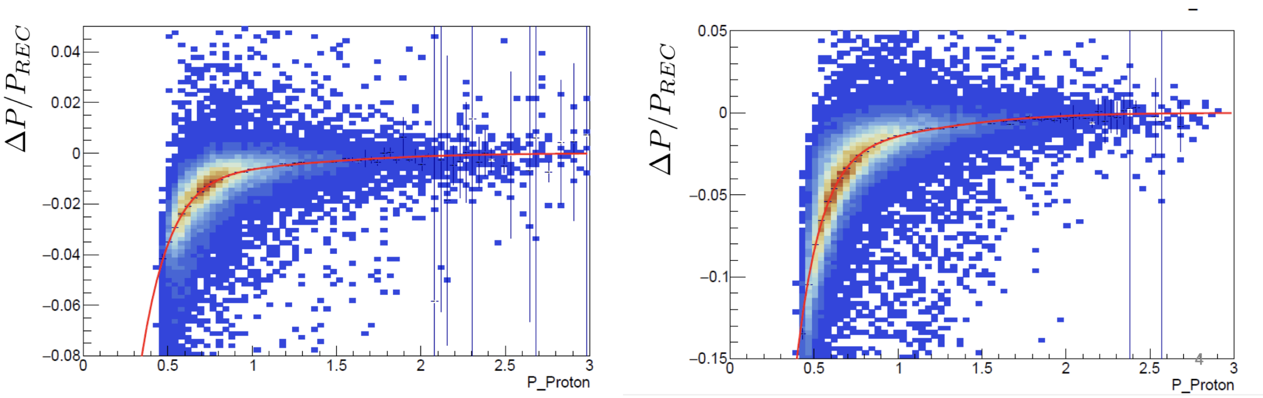

(a) $\theta_{pREC} < 27°$

(b) $\theta_{pREC} > 27°$

Figure 19: Proton correction function

The fit parameters obtained for both polar angle regions are summarized in Table 3.

Parameters	a	b	c	d	e	f
$\theta_{pREC} < 27°$	44.2175	4.33855	-3.35995	-0.000146557	0.000265887	-0.000174179
$\theta_{pREC} > 27°$	53.038	5.36114	-3.85085	-0.000139053	0.000272721	-0.000193624

Table 3: Parameters for the proton energy loss correction.

These parameters are obtained using a BH Fall 2018 inbending Monte-Carlo sample. We then test if the parameters can be applied to the two other data-taking era. In Figure 20, the relative difference of proton momenta in the FD for all three era used in this analysis are shown after correction, validating the corrections derived in this section. After correction, the relative momentum difference is under 5% for all three era.

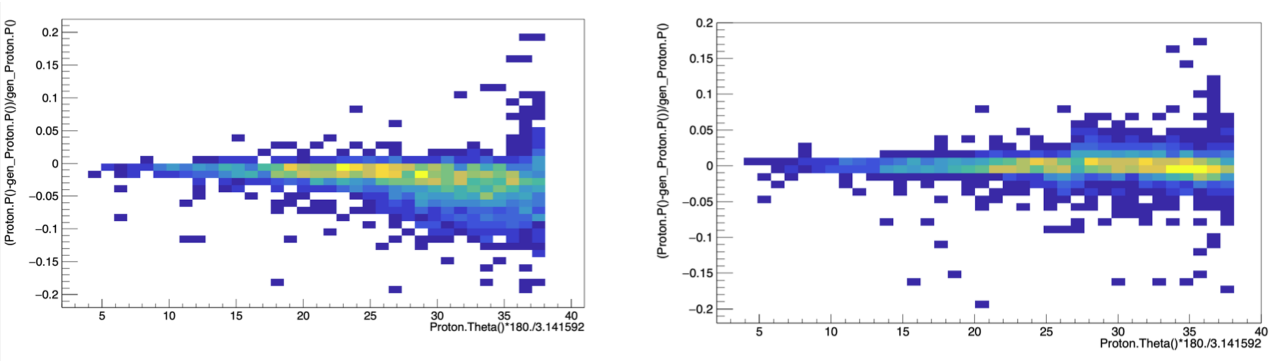

(a) Fall 2018 inbending

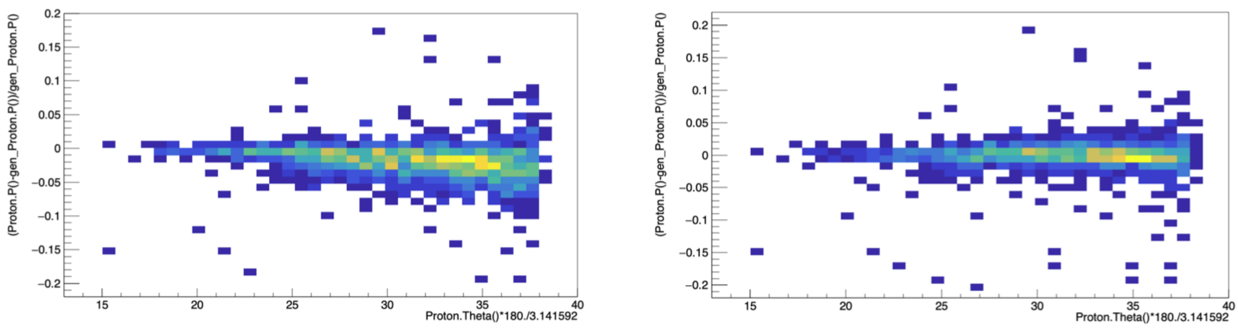

(b) Fall 2018 outbending

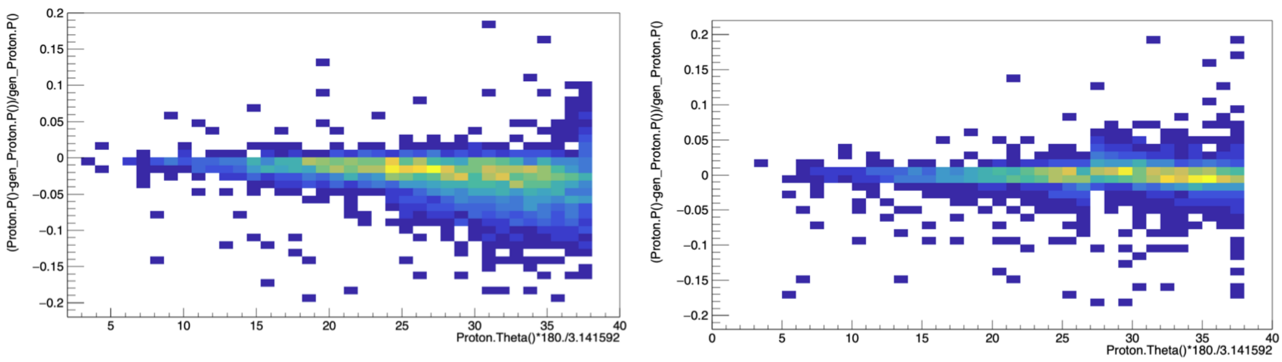

(c) Spring 2019 inbending

Figure 20: Relative difference of the proton momentum as a function of its reconstructed angle, before and after applying the correction derived in this section.

3.2 Event selection

For this analysis, we use quasi-real photoproduction events. The final state particles of interest are e^+e^-p and events with the following topology are selected:

- exactly one proton in the FD,
- exactly one positron in the FD with momentum larger than 1.7 GeV,
- exactly one electron in the FD with momentum larger than 1.7 GeV,
- any other particle which is not e^-, e^+ or p.

The selection cuts listed below are applied:

- Sampling Fraction of both leptons larger than 0.15,
- Same sectors for the ECAL and HTCC hits for both leptons,
- HTCC time of both leptons within a 4ns window.

Finally, to ensure the selection of photoproduction events, two exclusivity cuts are applied:

- on the reconstructed virtuality of the incoming real photon: $0.0\ \mathrm{GeV}^2 < \tilde{Q}^2 < 0.5\ \mathrm{GeV}^2$,
- and on the reconstructed missing mass squared of the undetected particle: $|M_X^2| < 0.4\ \mathrm{GeV}^2$,

where $\tilde{Q}^2$ and M_X^2 are obtained from the final state 4-vectors as:

$$\tilde{Q}^2 = 2 \cdot E_{beam} \cdot E_X(1 - \cos\theta_X) \tag{40}$$

and

$$M_X^2 = (p^\mu_{beam} - (p^\mu_p + p^\mu_{e+} + p^\mu_{e-} - p^\mu_{target}))^2 \tag{41}$$

Figure 21 shows the $\tilde{Q}^2$ versus M_X^2 plane for Fall 2018 inbending with all selection cuts applied except for the exclusivity cuts. An enhancement can be seen in the region where $\tilde{Q}^2$ and M_X^2 are small.

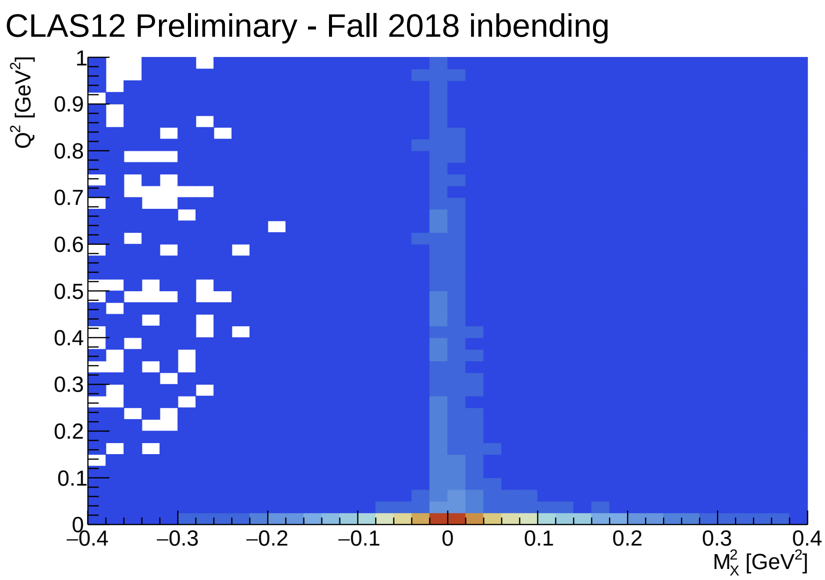

Figure 21: Exclusivity variables $\tilde{Q}^2$ versus M_X^2 plane for the Fall 2018 inbending dataset with all cuts mentioned above applied except for the exclusivity cuts.

Figure 22 a) shows the invariant mass of the lepton pair as a function of the reconstructed $\tilde{Q}^2$ for Fall 2018 inbending data. Figure 22 b) shows the invariant mass as a function of the square of the missing mass. In both cases the J/ψ events are clearly visible close to the J/ψ mass of 3.097 GeV.

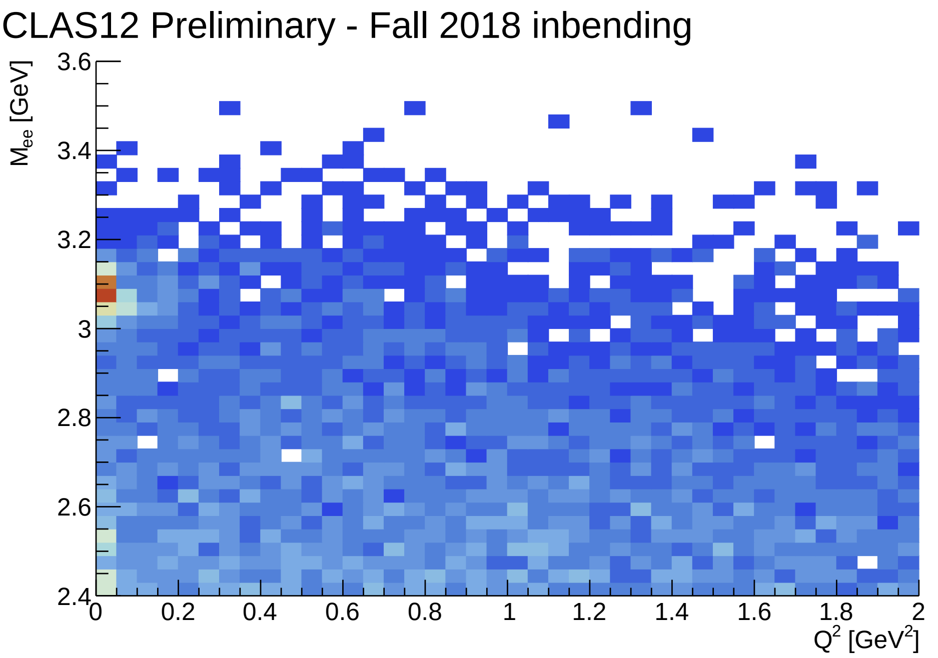

(a) Invariant mass as a function of the reconstructed photon virtuality

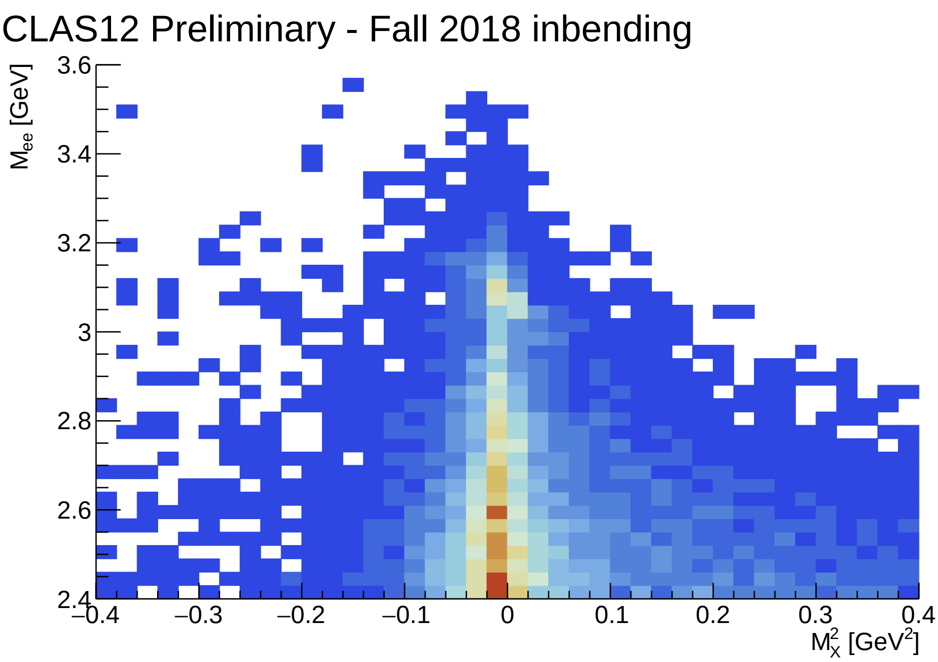

(b) Invariant mass as a function of the missing mass squared

Figure 22: Invariant mass of the lepton pair as a function of the exclusivity variables, for the Fall 2018 dataset.

3.3 Fiducial cuts

Fiducial cuts on the PCAL are applied. The U and V shower position of both leptons in the PCAL is required to be more than 9 cm away from the edge of the PCAL (corresponding to the RG-A Pass 1 PCAL cut, see RG-A analysis note). Furthermore, a dead paddle cut is applied to remove section of the PCAL which were not functioning optimally during the data taking. The cuts are equivalent to the one used in the approved analysis for inclusive cross-section measurement available here. Table 4 summarizes the cuts used to remove these faulty PCAL regions. These cuts are applied on both data and MC samples throughout the whole analysis.

Sector	U	V	W
1	-	-	$72 < W < 93$ $210 < W < 231$
2	-	$100 < V < 115$	-
3	-	-	-
4	-	$228 < V < 242$	-
5	-	-	-
6	-	-	$170 < W < 194$

Table 4: Summary of the cuts used to remove the dead paddles of the PCAL for the RG-A dataset. For each sector and each view (U,V and W) the regions (in cm) which are removed are specified.

4 Background modelization and Normalization factor

The MC simulation of CLAS12 might not reproduce exactly all the feature of the true experiment and the detection efficiency obtained from the CLAS12 simulation and the real efficiency might not be the same. In order to correct for this difference, the Bethe-Heitler yield below the J/ψ peak can be compared in data and Monte Carlo. To be able to perform such a comparison, one has to have a good description of all the physics contributions seen in the data sample.

In this section, two methods to evaluate the ratio of efficiency in data and Monte-Carlo (called normalization factor in the following) are presented.

The first method relies on fully describing all the data spectra with normalized Monte-Carlo samples. In section 4.1, data is compared with the J/ψ and Bethe-Heitler MC samples, to clearly highlight the presence of a large background which needs to be modeled. A method to model this background, and thus extracted a normalization factor is detailed in sections and 4.2 4.3. Finally, an alternative method to extract the normalization factor based on signle particle efficiencies is presented in section 4.4.

4.1 Early MC/Data comparison

The data and MC samples used in this analysis are processed according to the methods and tools presented before. MC samples are normalized according to the method presented in section 2.5. Figures 23 and 24 show the comparison between data and MC for various variables. It can be seen in Figure 23 that the region of high virtuality $\tilde{Q}^2$ is not reproduced by the MC samples described so far. This is due to the existence of a large background which has not been taken into account yet in this analysis. This background mostly consists of events with a misidentified positron or a positron from photon conversion detected in correlation with a scattered electron. In the following, a method is described to model this background.

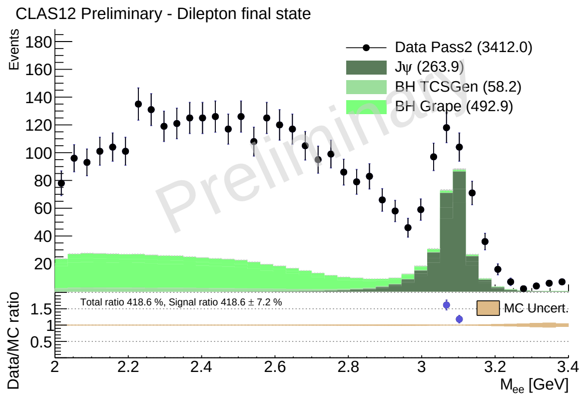

(a) Dilepton invariant mass

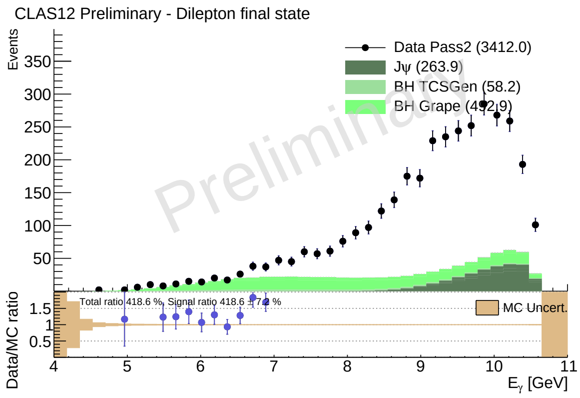

(b) Reconstructed photon energy

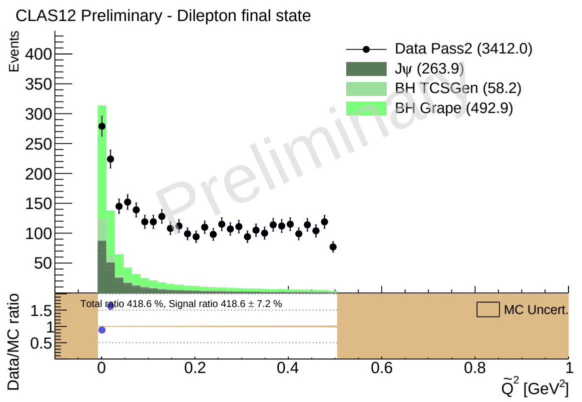

(c) Reconstructed photon virtuality

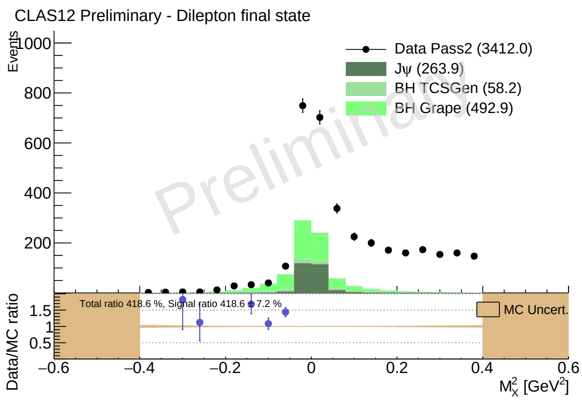

(d) Missing mass

Figure 23: Invariant mass, photon energy spectra and exclusivity variables for quasi-photoproduction event, and for the Fall 2018 inbending dataset.

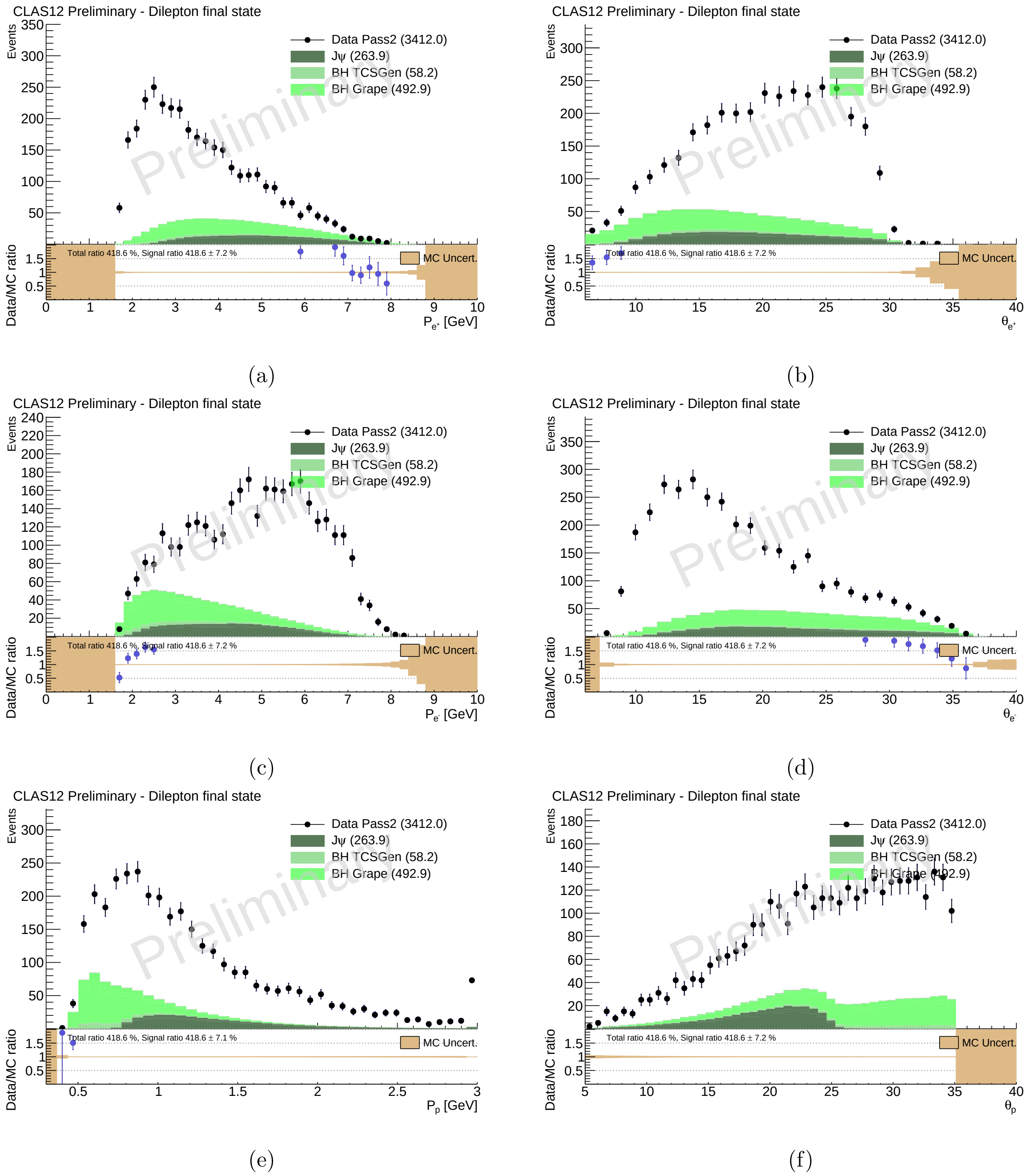

Figure 24: Final state particle momenta and polar angle for selected quasi-photoproduction events, and for the Fall 2018 inbending dataset.

4.2 Background model

In order to model the high-$\tilde{Q}^2$ background, an event mixing approach was developed (see section 4.2.1). To better match the obtained spectra, a weight is applied event-by-event to match the probability distribution function of the mixed event sample and the data in a region where background is expected to be dominant (see section 4.2.2).

4.2.1 Event mixing

Quasi-photoproduction events (selected using the following cuts: 0.0 GeV^2 $< \tilde{Q}^2 <$ 2.0 GeV^2, $|M_X^2| <$ 0.4 GeV^2) are mixed together to provide an initial sample to model the high-$\tilde{Q}^2$ background. One electron, one positron and one proton from 3 distinct events are randomly selected from the sample, the corresponding missing mass M_X^2 and photon virtuality $\tilde{Q}^2$ are computed and required to be within the quasi-photoproduction region ($0.0\ \mathrm{GeV}^2 < \tilde{Q}^2 < 2.0\ \mathrm{GeV}^2$, $|M_X^2| < 0.4\ \mathrm{GeV}^2$). Note that we allow $\tilde{Q}^2$ to be larger than $0.5\ \mathrm{GeV}^2$ for validation purposes that will be described later.

This mixed event sample does not reproduce well the data spectra, and we thus need to re-weight each events to do so as described in the next section.

4.2.2 Definition of the training, validation and signal regions

The mixed event sample cover the range of reconstructed photon virtuality from 0 to 2 GeV^2. We divide the reconstructed photon virtuality range of both data and mixed events sample in 3 distinct region used to define, validate and apply the re-weighting technique:

- The training region is defined as $0.5\ \mathrm{GeV}^2 < \tilde{Q}^2 < 1.5\ \mathrm{GeV}^2$. In this region, most of the events are background. We will reweight the mixed-event sample so that all spectra in data and re-weight-mixed-event sample match.
- The validation region is defined as $1.5\ \mathrm{GeV}^2 < \tilde{Q}^2 < 2.0\ \mathrm{GeV}^2$. In this region, we also expect mostly background. We will use this region to validate the re-weighting.
- Finally, the signal region is defined as $0.0\ \mathrm{GeV}^2 < \tilde{Q}^2 < 0.5\ \mathrm{GeV}^2$. In this region, we do have our signal of interest. Once the re-weighting procedure has been validated, we can use the same weights to model our background in this region of interest.

The 3 regions described above are illustrated in Figure 25.

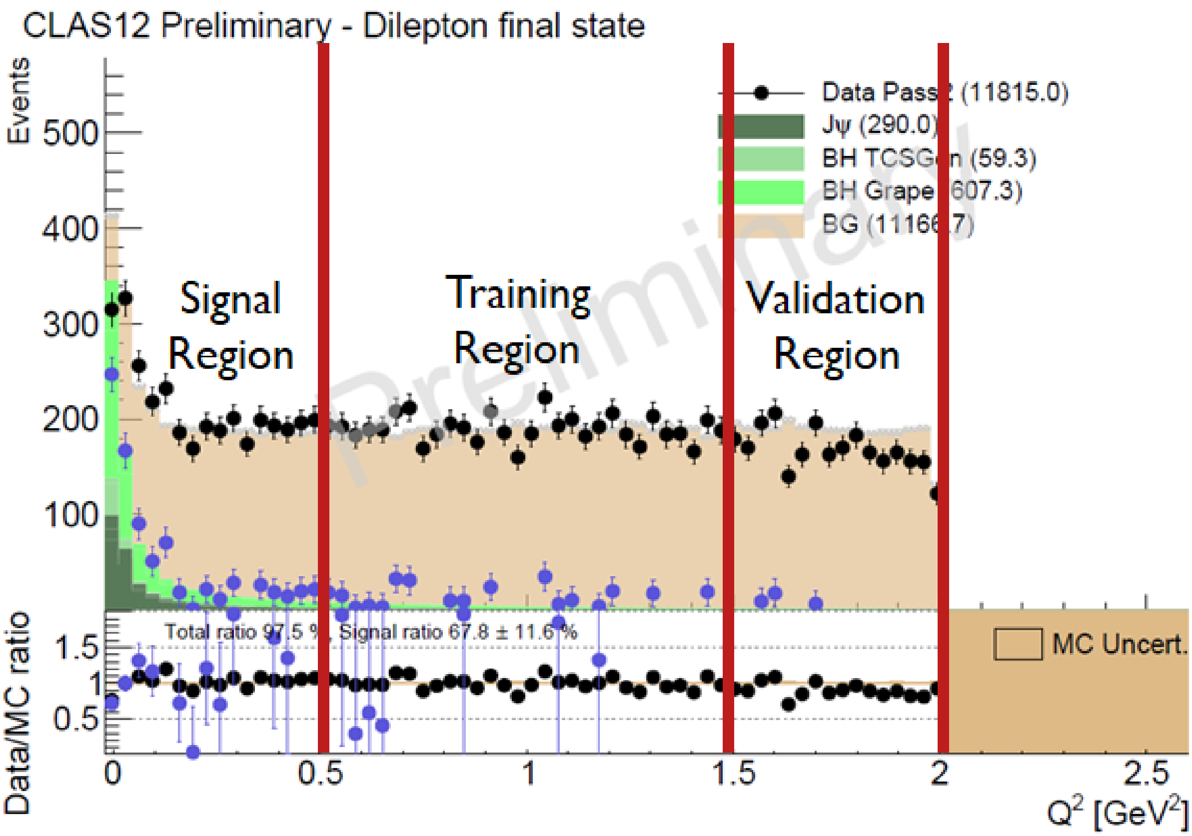

Figure 25: Reconstructed virtuality of the initial photon. The data, MC samples and re-weighted background are shown. The figure also displays the limit of the 3 distinct regions used to train and validate the re-weighting approach.

4.2.3 Event re-weighting procedure

As mentioned earlier in this section, the mixed event samples do not reproduce the background in the data sample. This can be seen in the training region, mostly populated by background events. In Figure 26, the spectra of the invariant mass, the missing mass, the reconstructed photon energy and the momenta and polar angle of each final state particle is shown for both data and mixed events in the validation region. Most of the shape of the spectra do not match.

To reweight our mixed event background, we use the method described in [37]. The code is available on the github page of the project. This re-weighting procedure consists in training a Boosted-Decision-Tree on a source sample (our mixed event samples) and a target sample (our data sample). The BDT is trained on a certain subset of the variables of the source and target samples. The trained BDT provides a weight for each source event will ensure that the multi-variate probability distribution, defined by the training variables, of the source matches the pdf of the target sample. Thus this method allows to match not only the integrated spectra, as shown in Figure 27, but also all the spectra in which a cut on the input variable is applied.

For this analysis, we trained the BDT on 9 variables, shown in Figure 26: invariant mass of the lepton pair, missing mass, photon energy, momenta and polar angles of the 3 final state particles. Note that because, we use $\tilde{Q}^2$ as our variable to define the signal and training region we cannot use it in the training. However, it can be seen in the following that the $\tilde{Q}^2$ spectra of the background are well reproduced. Ineed, it can bee seen that many variables which were not included in the list of training variables are also very well reproduced after training (see Figure 123 (e) and (f) for example). For each dataset, the mixing and re-weighting steps are repeated. Three re-weighted-mixed-event samples are thus used in this analysis.

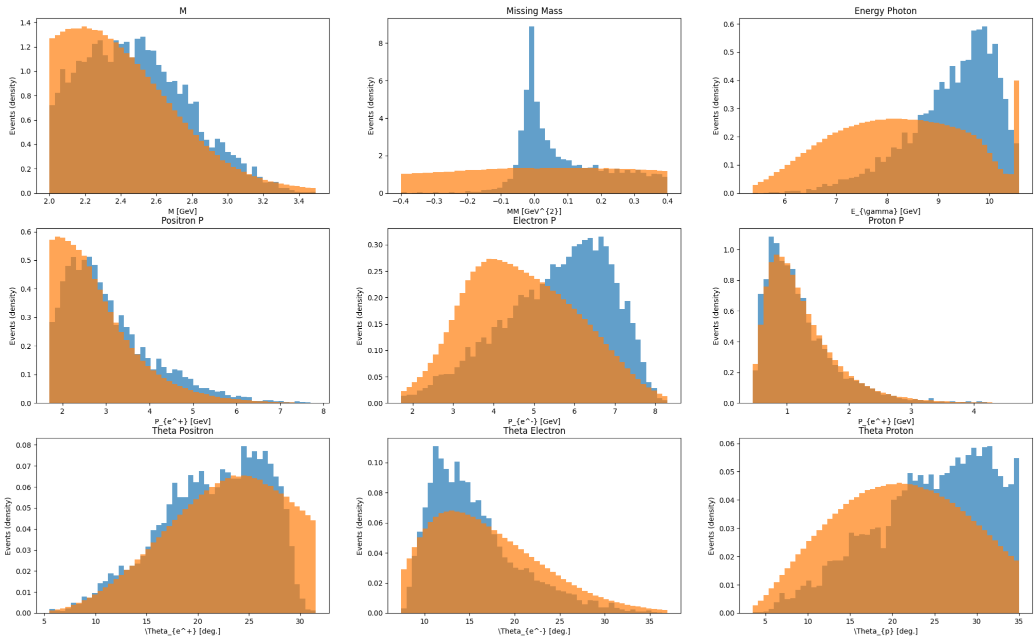

Figure 26: Training variables spectra for data in blue, and mixed events in orange, in the training region $\tilde{Q}^2 \in [0.5, 1.5]$ GeV^2, for the Fall 2018 inbending dataset, and before re-weighting.

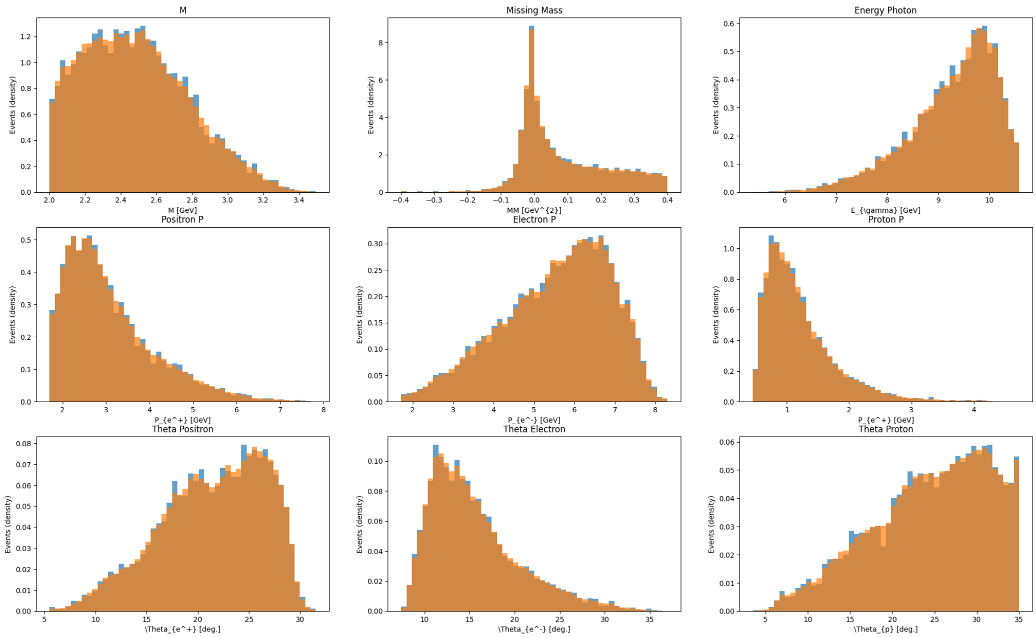

Figure 27: Training variable spectra after reweighting for the Fall 2018 inbending dataset, in the training region $\tilde{Q}^2 \in [0.5, 1.5]$ GeV^2.

4.2.4 Overall background normalization factor

The re-weighting procedure presented in the previous section, only allows to match the multivariate pdf of the data and mixed-event sample in the training region. One needs to normalize the re-weighted mixed events by a single factor in order to match the data. This factor is a single number and is completely arbitrary and depends in particular on the number of mixed events. The background normalization factor is determined so that the sum of MC J/ψ , MC Bethe-Heitler, and background events in the training region is exactly equal to the number of data event in the same region. Figure 28 illustrate the determination of the background normalization factor the Fall 2018 inbending dataset.

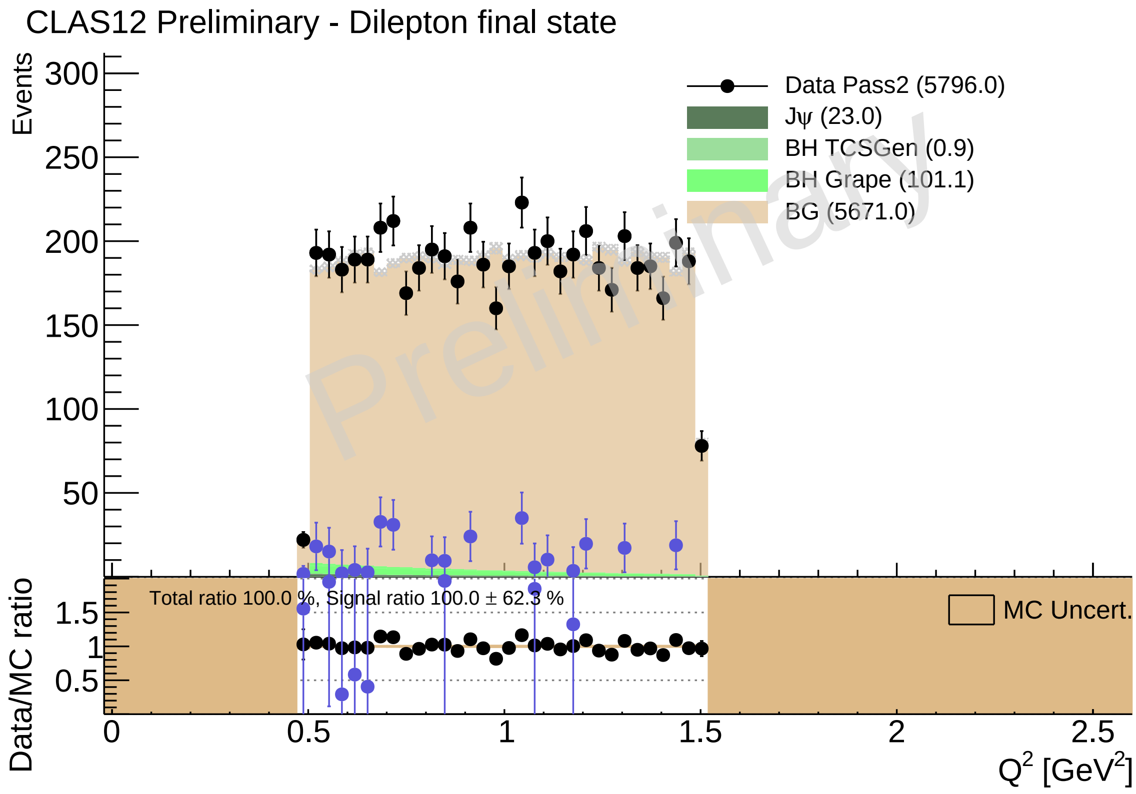

Figure 28: $\tilde{Q}^2$ spectrum in the training region for the Fall 18 inbending dataset. The overall background normalization factor for the background is determined so that the estimated number of BH, J/ψ and background events add up to the number of data event in the training region.

Appendix J shows some variables spectra in the training region $\tilde{Q}^2 \in [0.5, 1.5]$ GeV^2 for the Fall 2018 inbending dataset after the overall background normalization factor is applied. In this analysis, only 3 such background normalization factor are used, one per re-weighted-mixed-event sample.

4.2.5 Validation of the re-weighting approach

Appendix L shows some variables spectra in the validation region $\tilde{Q}^2 \in [1.5, 2.0]$ GeV^2 for the Fall 2018 inbending dataset. Overall, in this region where we expect that the background will largely dominates, we reproduce the data spectra up to a 10% error. This can be shown in Figure 29 showing the invariant mass spectrum for events in the validation region. The normalization of the background is done using the same factor as for the training and signal region. We do not use this difference in the following of the analysis. However, we shown in section 4.4 that we can estimate the normalization factor with an estimated error of 15% which is consistent with the 10% discrepancy found here. The same behavior is found for the Fall 2018 outbending and Spring 2019 samples.

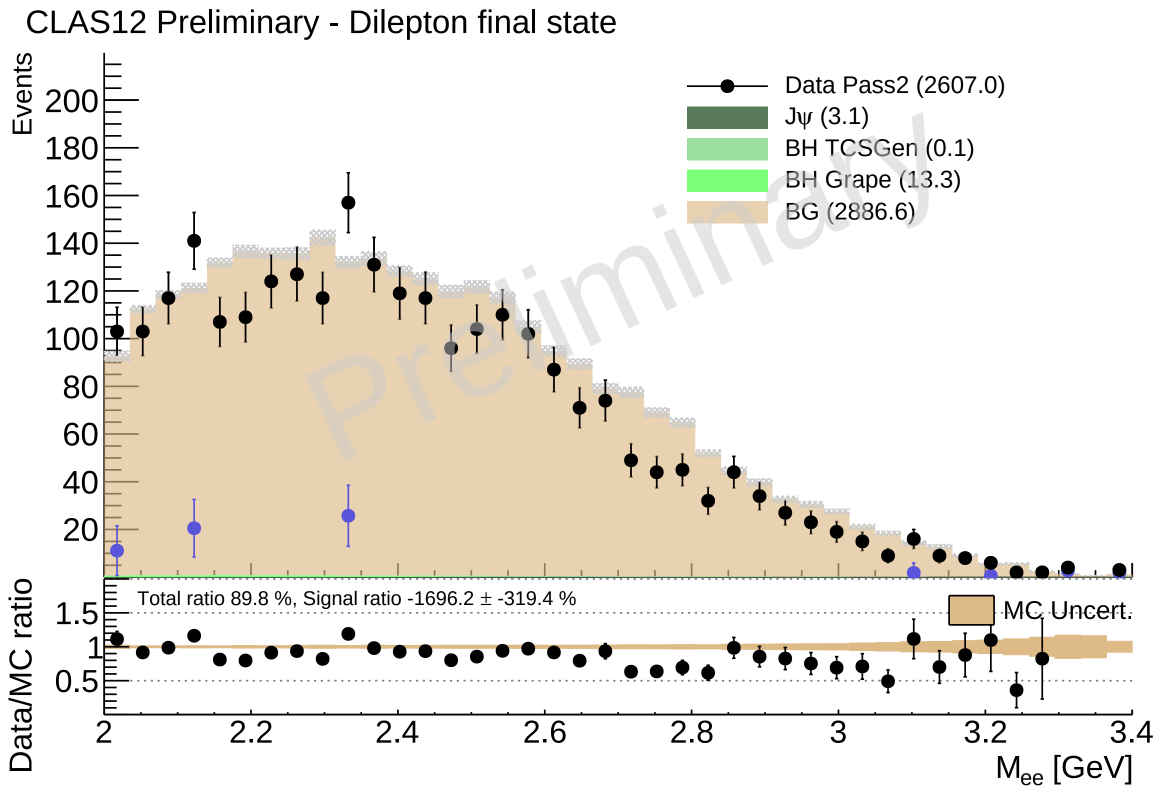

Figure 29: Invariant mass spectrum of the data and the MC and BG samples in the validation region. The number of events in the data is reproduced by the MC and BG samples with a 10% difference.

4.2.6 MC/Data comparison in the signal region

A MC/data comparison in the signal region for the Fall 2018 inbending and outbending periods, including the background model, is available in Appendix K and Appendix M respectively. The MC/data comparison for the Spring 2019 period is in Appendix N.

Here, we present only a subset of relevant plots to justify the approach in the region of interest for this analysis. Each plot shows the spectra for the considered dataset (Fall 2018 inbending and outbending, and Spring 2019), superimposed on the sum of all the contributions to the expected spectrum obtained by stacking normalized MC spectra as well as the background sample described in the previous section. The blue data points corresponds to the data histograms where the background spectra has been subtracted bin per bin.

4.2.6.1 Fall 2018 inbending

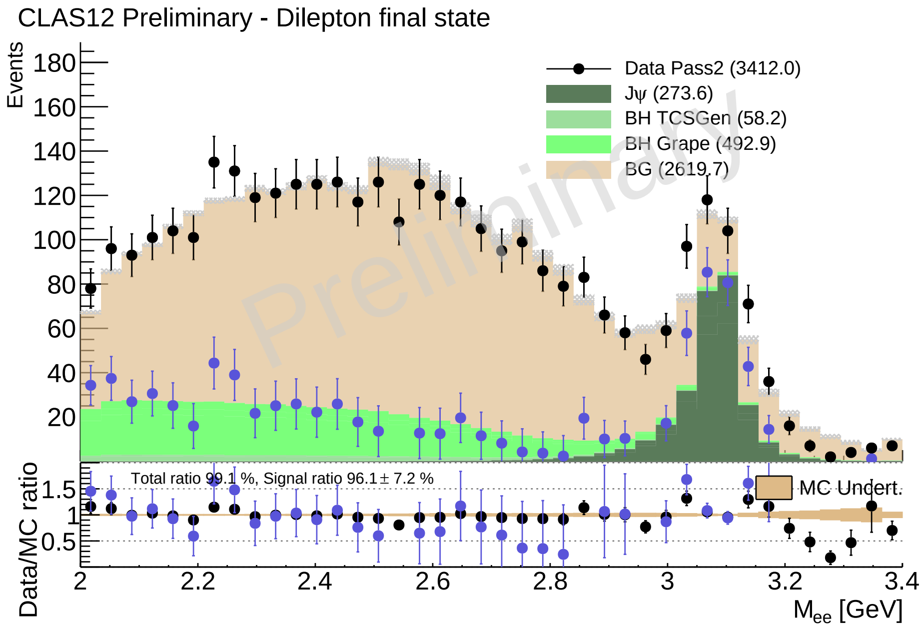

(a) Lepton invariant mass

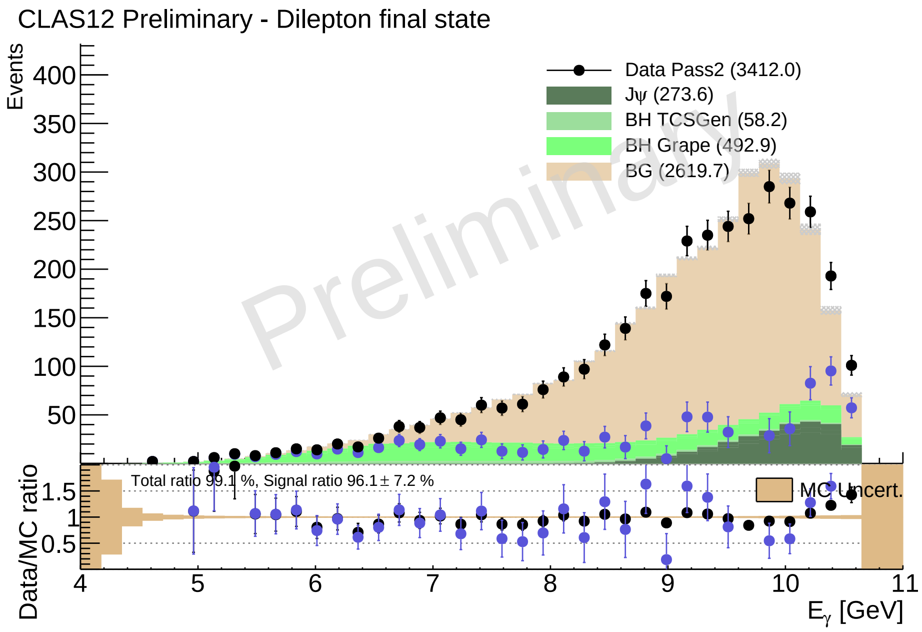

(b) Photon energy

Figure 30: Complete description of the Fall 2018 inbending spectra, including properly normalized signal MC samples (J/ψ and Bethe-Heitler) and background.

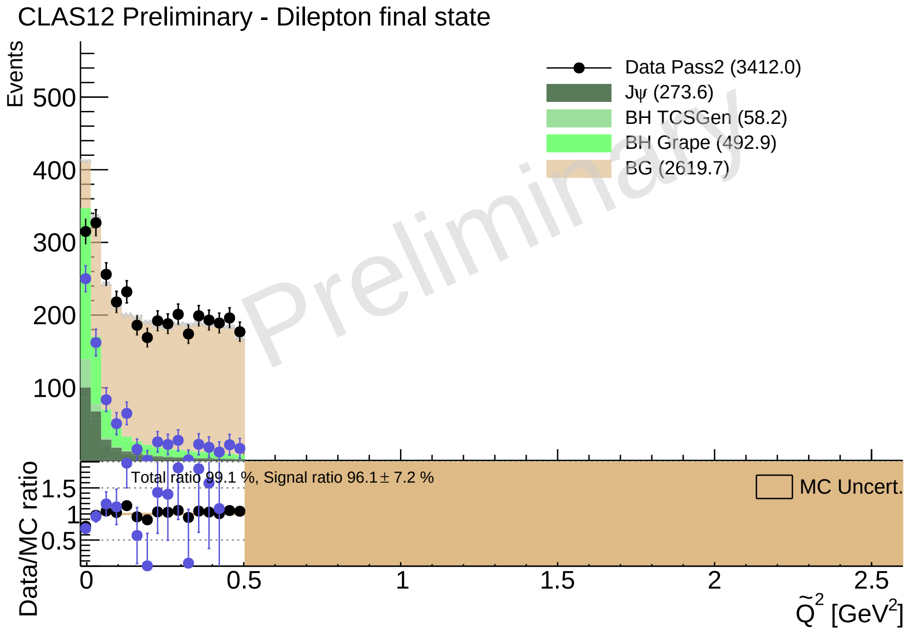

(a) Reconstructed virtuality of the photon

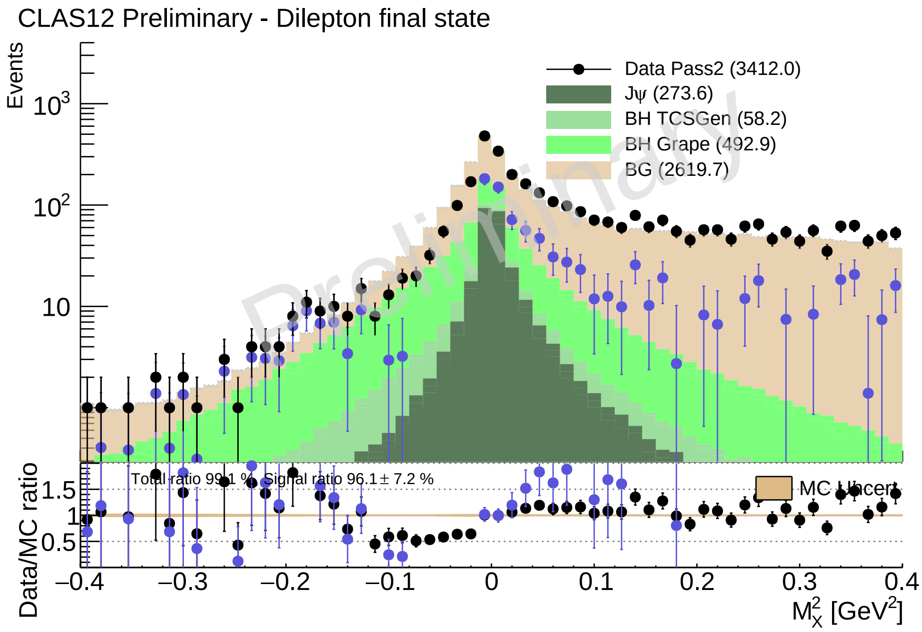

(b) Missing mass squared

Figure 31: Complete description of the Fall 2018 inbending spectra, including properly normalized signal MC samples (J/ψ and Bethe-Heitler) and background.

570 #### 4.2.6.2 Fall 2018 outbending

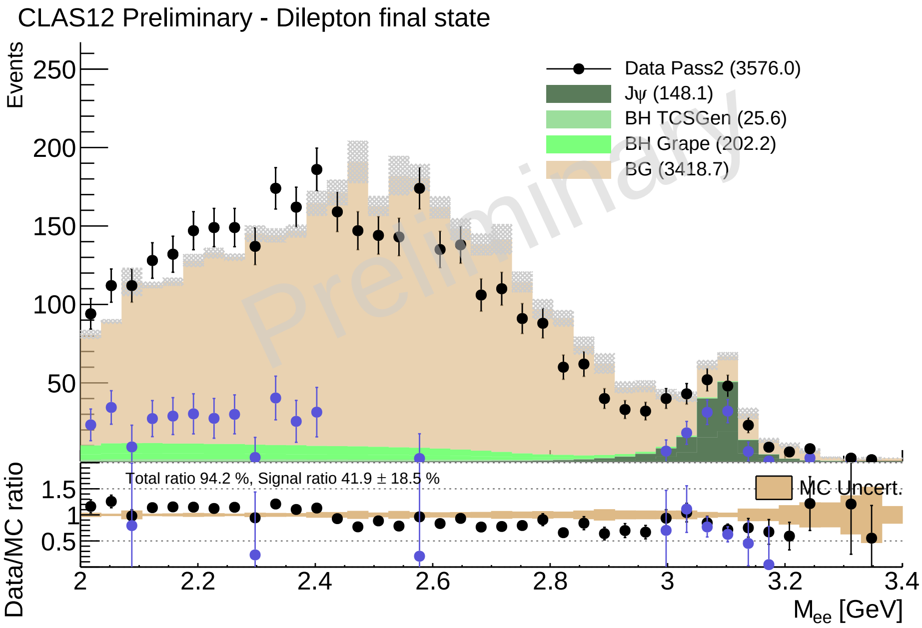

(a) Lepton invariant mass

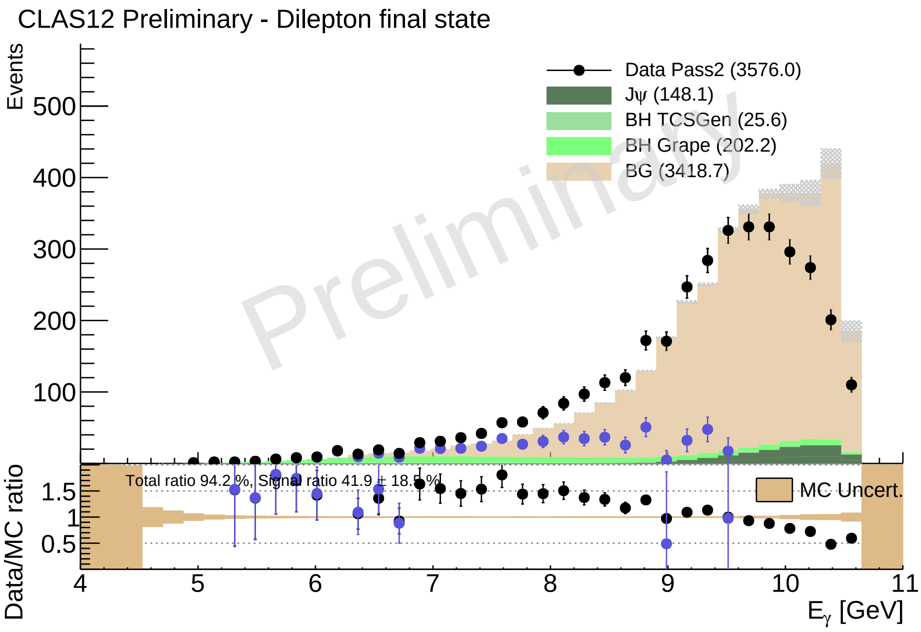

(b) Photon energy

Figure 32: Complete description of the Fall 2018 outbending spectra, including properly normalized signal MC samples (J/ψ and Bethe-Heitler) and background.

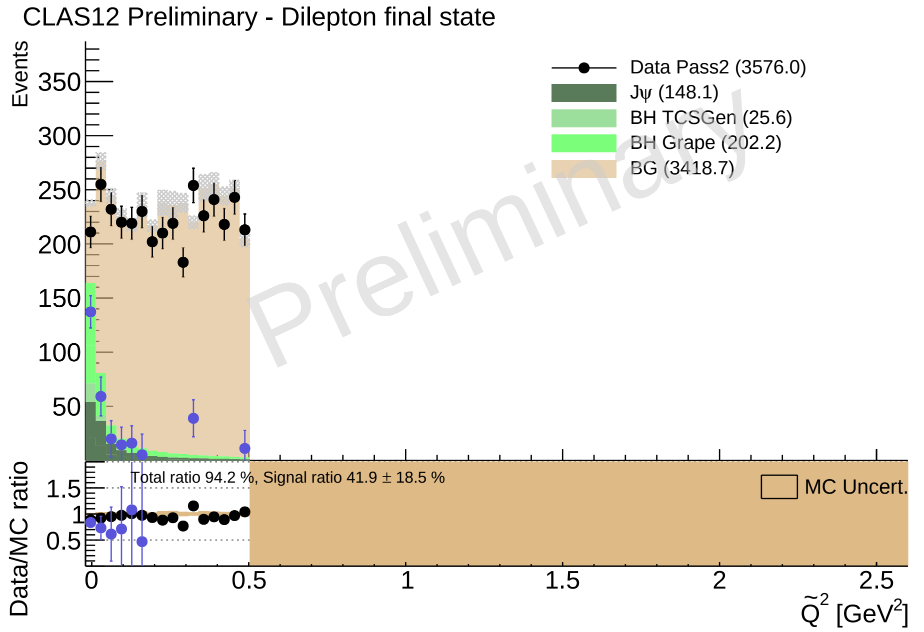

(a) Reconstructed virtuality of the photon

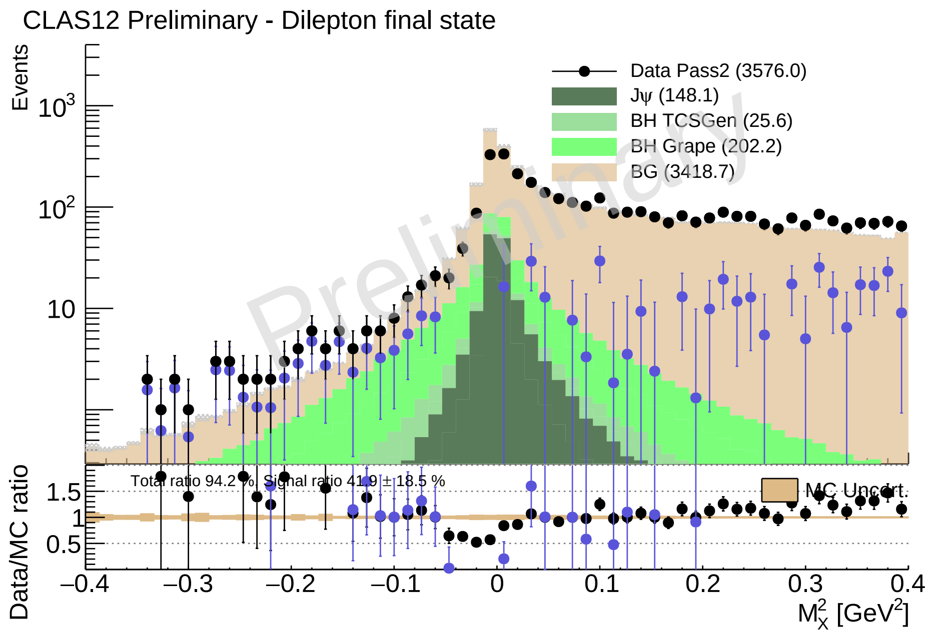

(b) Missing mass squared

Figure 33: Complete description of the Fall 2018 outbending spectra, including properly normalized signal MC samples (J/ψ and Bethe-Heitler) and background.

4.2.6.3 Spring 2019

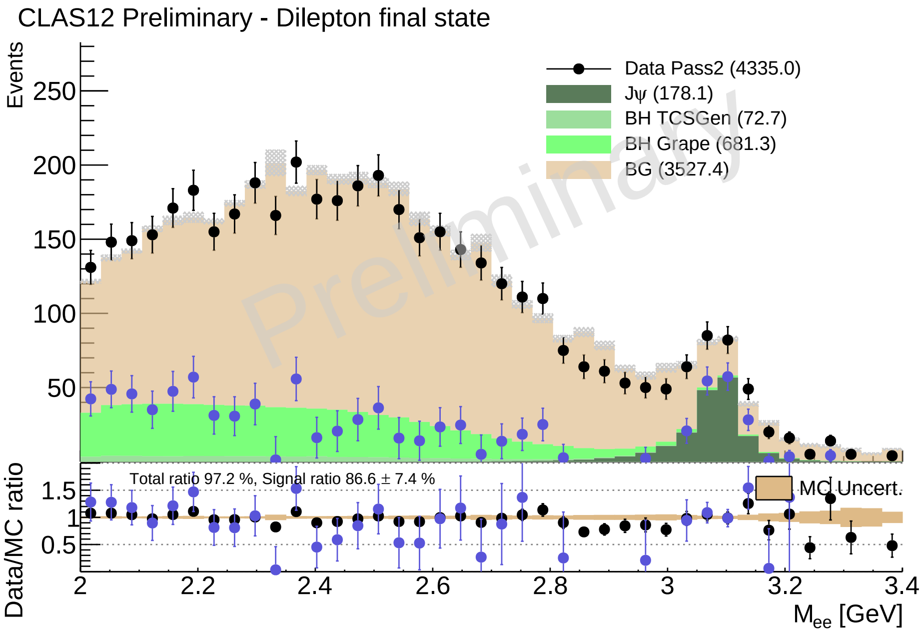

(a) Lepton invariant mass

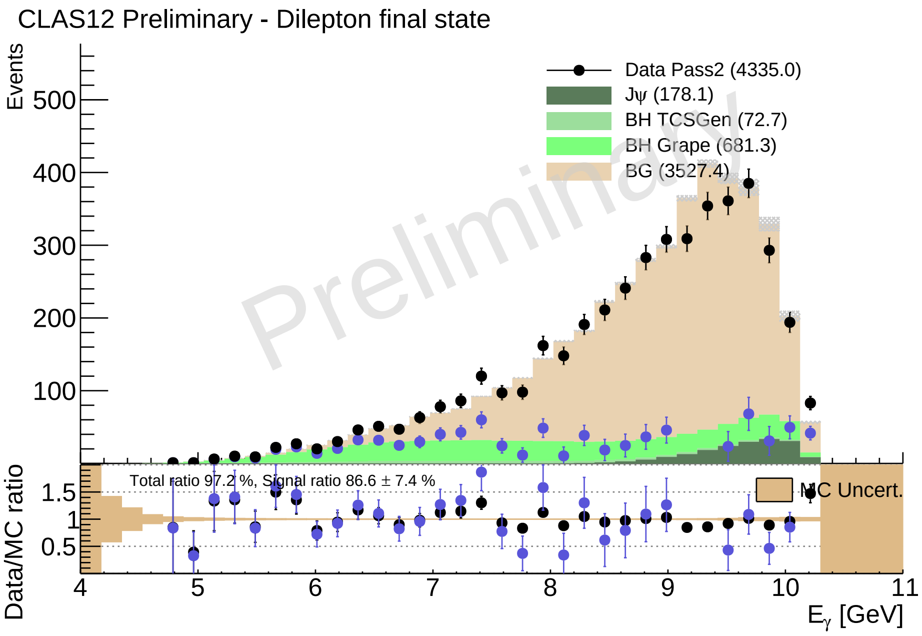

(b) Photon energy

Figure 34: Complete description of the Spring 2019 2018 spectra, including properly normalized signal MC samples (J/ψ and Bethe-Heitler) and background.

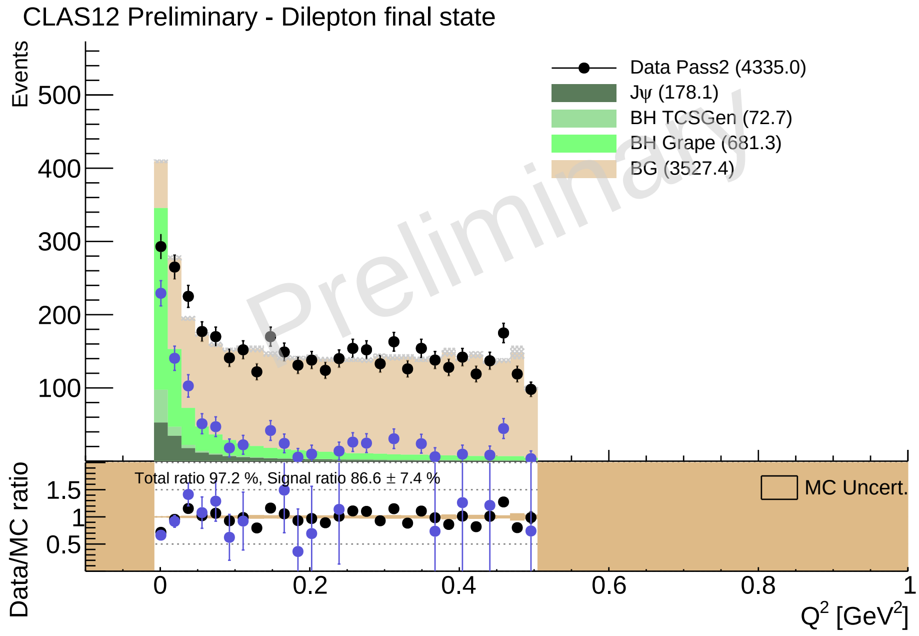

(a) Reconstructed virtuality of the photon

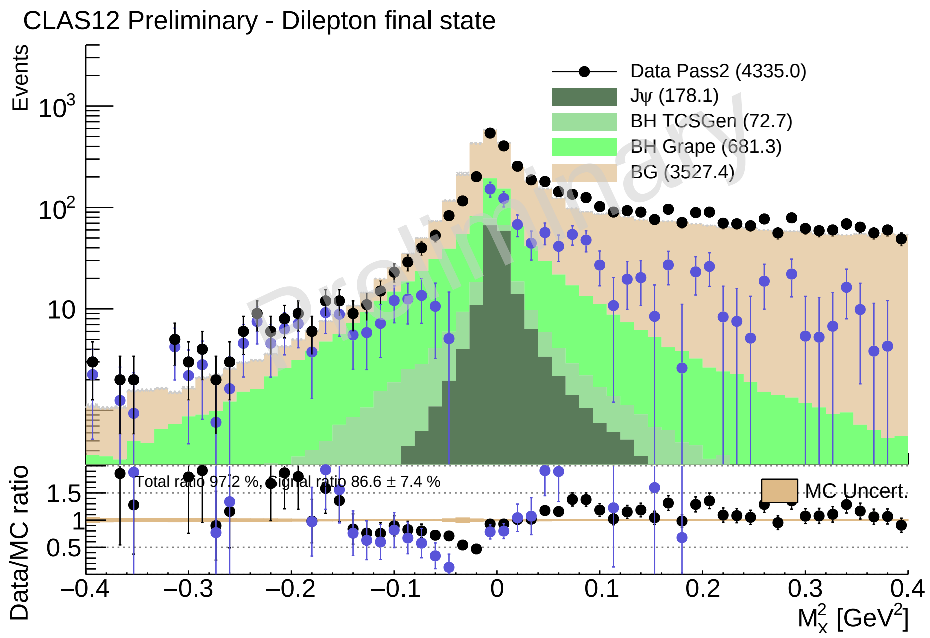

(b) Missing mass squared

Figure 35: Complete description of the Spring 2019 2018 spectra, including properly normalized signal MC samples (J/ψ and Bethe-Heitler) and background.

4.3 Estimation of the normalization factor using the re-weighted-mixed-events samples

In the invariant mass range [2.4, 2.9] GeV, the background yield, described in the previous section, is subtracted from the data yield and the ratio of background-free yield to MC yield provides an estimate of data to MC efficiency ratio ω_c as:

$$\omega_c = \frac{N_{Data} - N_{BG}}{N_{SIM\ BH}}. \tag{42}$$

This procedure is done for the Fall 2018 inbending and Spring 2019 dataset. For the Fall 2018 dataset, the ratio of background to Bethe-Heitler events in the [2.4, 2.9] GeV is too large to extract any meaningful figure (See Figure 121 in appendix). We thus use the factor obtained for the Fall 2018 inbending period.

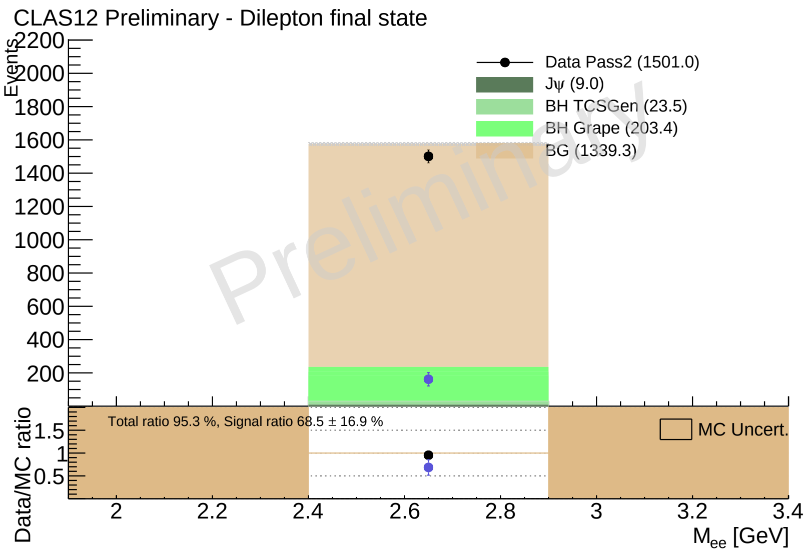

Figure 36: Normalization factor extraction for the Fall 2018 inbending dataset. The Bethe-Heitler event yield in data and MC is compared in the $M \in [2.4, 2.9]$ GeV region. The MC/Data ratio after background subtraction is 68.5%.

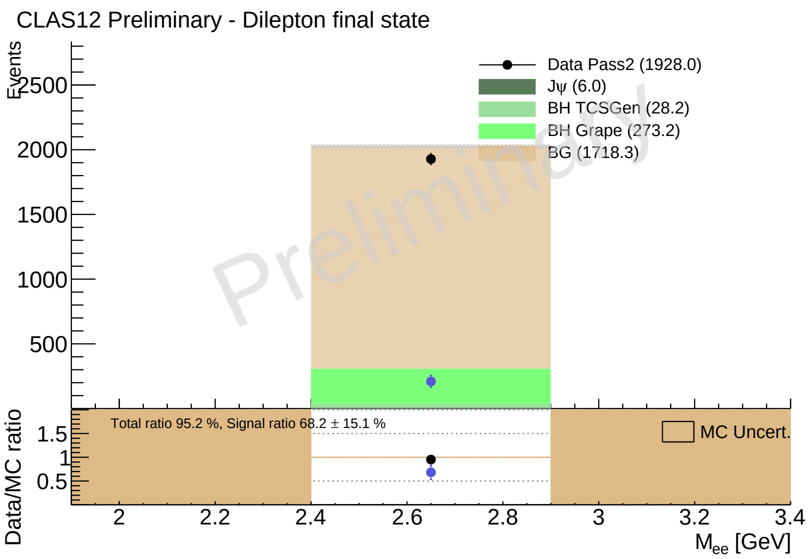

Figure 37: Normalization factor extraction for the Spring 2019 inbending dataset. The Bethe-Heitler event yield in data and MC is compared in the $M \in [2.4, 2.9]$ GeV region. The MC/Data ratio after background subtraction is 68.2%.

For the following, unless explicitly written otherwise, the normalization factor ω_c is set to 0.69 irrespective of the run period.

4.4 Estimation of the normalization factor from single particle efficiencies

An overall normalization factor is derived in section 4.3 to account for the efficiencies mismatch between real data and MC. In order to assess the reweighed-mixed-events method presented in the previous section, we recomputed the normalization factor using an independent method described here.

The BH MC samples used in this analysis were used to compute the single particle efficiency for electron and positron as a function of beam current. All the cuts used in this analysis are used when applicable to each particle, except the exclusivity cuts. Three methods were used to derive these efficiencies:

1) a reconstructed/generated ratio

$$\epsilon_1 = \frac{N_{REC}}{N_{GEN}} \tag{43}$$

2) a 3-to-2 reconstructed particle ratio

$$\epsilon_2 = \frac{N_{e^-e^+p}}{N_{e^+p}}, \tag{44}$$

3) and a 2-to-1 reconstructed particle ratio

$$\epsilon_3 = \frac{N_{e^-e^+}}{N_{e^+}}. \tag{45}$$

These equation are given in the case of the computation of the electron efficiency, in the positron case the indexes e^-/e^+ have to be swapped. For each of the beam current used in the analysis, the three efficiencies are computed, for electron and positrons. A straight line fit is done assuming full efficiency at zero current. Finally, the average of the three method presented above is computed. The final fit and their average can be seen in Figures 38 and 39 for electrons and positrons respectively, in the inbending case.

Additionally, the efficiency of CLAS12 for electron and positron can be estimated from data using charged hadrons efficiency. Here the number of charged hadrons of a given charge detected in correlation with an electron in a different sector is normalized to the total number of detected electron. It is displayed in Figures 38 and 39. The ratio of the average of the three MC methods and of the data efficiency is computed for each beam current of RG-A.

We can then estimate the ratio of efficiency between MC and data for the final state of interest of this analysis. We assume that all protons in the FD are well identified in the fiducial region of the FD. This is supported by Figure 40 where the efficiency of detection of protons in the FD is estimated for MC and data. For the proton, the ratio of efficiency is found to be different from the unity with 1.5% deviation, which is ignored.

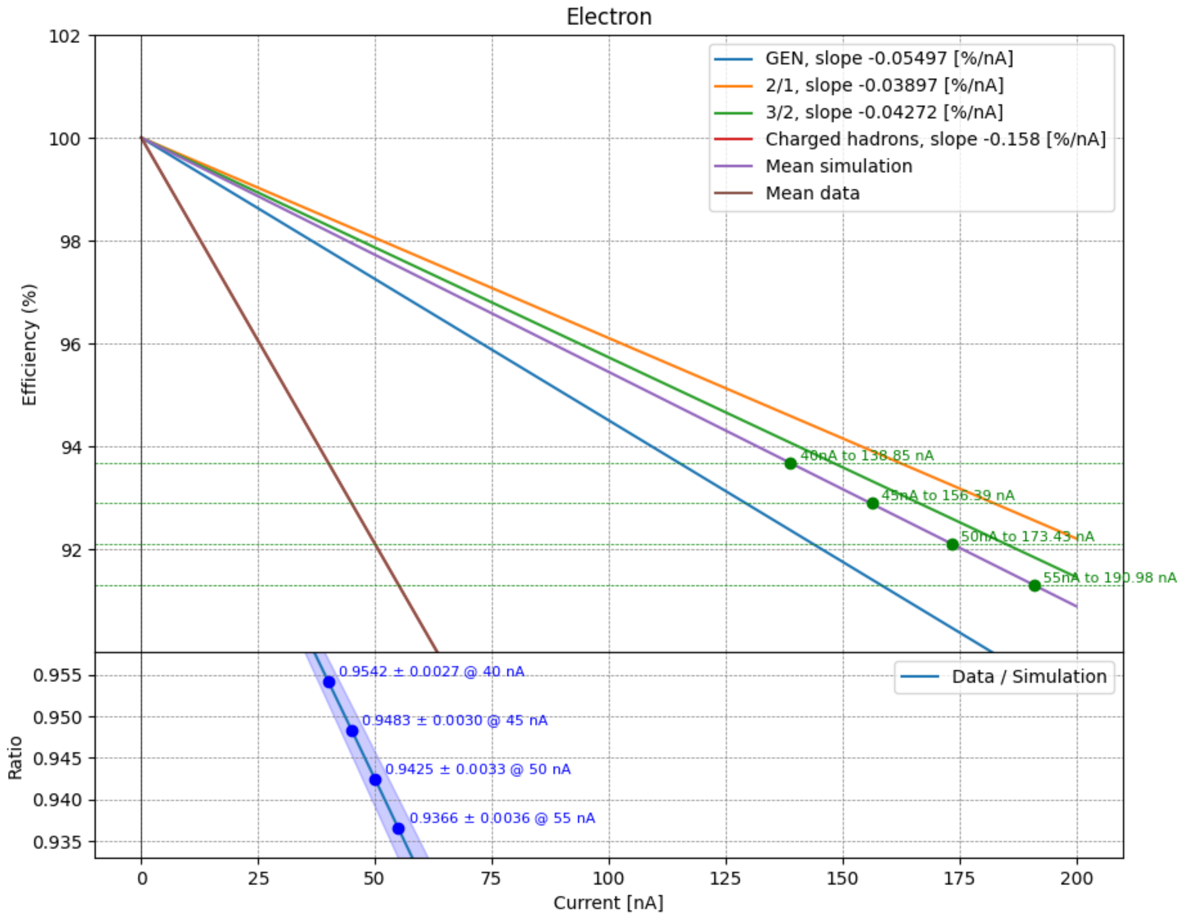

Figure 38: Single particle efficiency of the electrons in a inbending magnetic field, as a function of the beam current for simulation (in blue, orange and green, for the three methods described in this section, and in brown for data). The bottom plots shows the ratio of the average of the MC efficiency, in purple, to the data efficiency, in brown. The red line fit is under the brown one and his the one obtained on data. The green lines (not used in this analysis) indicates the current which should be used in simulation to recover the single particle efficiency, assuming a linear dependence against beam current.

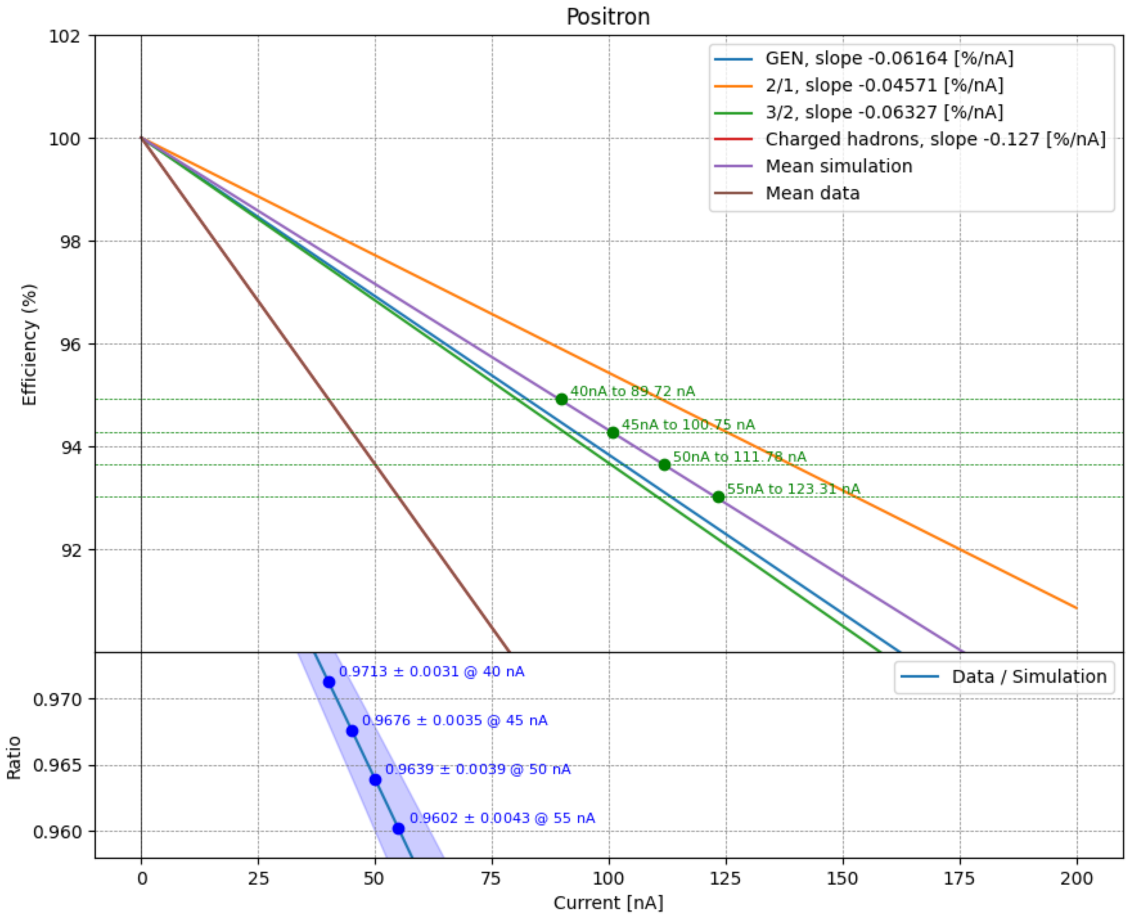

Figure 39: Single particle efficiency of the positrons in a inbending magnetic field, as a function of the beam current for simulation (in blue, orange and green, for the three methods described in this section, and in brown for data).The bottom plots shows the ratio of the average of the MC efficiency, in purple, to the data efficiency, in brown.

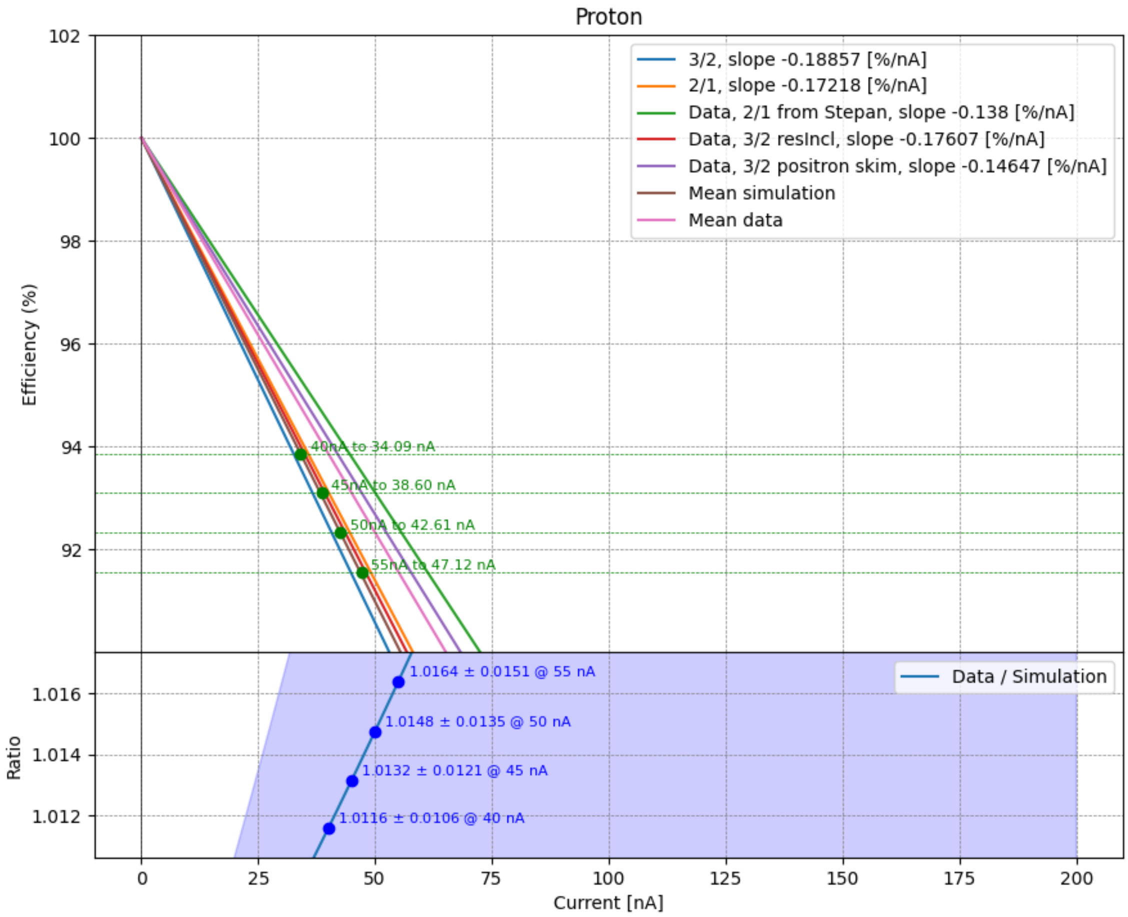

Figure 40: Single particle efficiency of the proton in a inbending magnetic field, as a function of the beam current for simulation (in blue, and orange for the two methods applicable to the proton which are described in this section, and in red, green and purple for data).The bottom plots shows the ratio of the average of the MC efficiency, in purple, to the average of data efficiency, in brown. In the proton case, the MC efficiency can only be done if a MC trigger particle is present thus preventing the use of the reconstructed/generated ratio. For efficiency estimated using data, the ratio $\frac{N_{e^-p}}{N_{e^-}}$ and $\frac{N_{e^-e^+p}}{N_{e^+e^-}}$ (computed both using the 'resincl' and 'positron' skim, were computed.

The data-to-MC normalization factor can then be estimated as:

$$\omega_c = \bar{\epsilon}_{e^+} \cdot \bar{\epsilon}_{e^-} \cdot R^{PID}_{e^+} \cdot R^{PID}_{e^-} \cdot (n_{Std.\ PID} + n_{e^-} R^{BDT}_{e^-} + n_{e^+} R^{BDT}_{e^+} + n_{e^-e^+} R^{BDT}_{e^+} R^{BDT}_{e^-}). \tag{46}$$

$\bar{\epsilon}_{e^x}$ are the efficiency ratios described above. These ratios are assumed symmetric if the magnetic field is inverted as well as the charge of the lepton considered.

$R^{BDT}_{e^x}$ are the BDT efficiency ratios described in section 3.1.2 (they are computed as the inverse of the ratios presented in this section at BDT response of 0.0). The n_{eX} are the fraction of events with exactly one lepton of a given charge with momentum above 4.5 GeV, which is thus identified using the BDT algorithm. $n_{Std.\ PID}$ is the fraction of events where both leptons are identified with standard PID only. The n_{eX} factor are estimated using J/ψ MC samples and summarized in Table 5 (Note that we find the same independent factor for Fall 18 inbending and Spring 2019).

Dataset	Fall 2018 in.	Spring 2019	Fall 2018 out.
$n_{Std.\ PID}$ [%]	39.1	39.1	27.8
n_{e^-} [%]	21.	21.	45.
n_{e^+} [%]	38.7	38.7	24.9
$n_{e^-e^+}$ [%]	2.1	2.1	2.3
$R^{BDT}_{e^+}$	0.96	0.97	0.86
$R^{BDT}_{e^-}$	0.94	0.93	0.89
BDT factor [%]	97.9	98.1	91.11

Table 5: Fraction of events detected with the BDT for each era, and BDT factors. The total BDT normalization factor ($n_{Std.\ PID} + n_{e^-}R^{BDT}_{e^-} + n_{e^+}R^{BDT}_{e^+} + n_{e^-e^+}R^{BDT}_{e^+}R^{BDT}_{e^-}$) is also reported in the last line of the table.

Finally, R^{PID}_{ex} are the ratio of efficiency of the CLAS12 PID taken from the CLAS12 note 2024-004, available here. We use the ratios of efficiency for the PID 11, without DC fiducial cuts and with PCAL cut at 9 cm (Table 1 and 2 of the note). These ratios are assumed symmetric if the magnetic field is inverted as well as the charge of the lepton considered.

For each beam current in the Fall 18 inbending case, the computation yieds:

$$\begin{aligned}
\omega_c^{in/45} &= (0.9483 \cdot 0.9676) \times (\frac{1}{1.03} \cdot 1.0) \times (0.979) = 0.87, \\
\omega_c^{in/50} &= (0.9425 \cdot 0.9639) \times (\frac{1}{1.03} \cdot 1.0) \times (0.979) = 0.863, \\
\omega_c^{in/55} &= (0.9366 \cdot 0.9602) \times (\frac{1}{1.03} \cdot 1.0) \times (0.979) = 0.854, \\
\omega_c^{in/tot} &= 0.867,
\end{aligned}$$

where $\omega_c^{in/tot}$ is the accumulated charge weighted factor. In the Spring 2019 case, the computation yieds:

$$\omega_c^{in/50} = (0.9425 \cdot 0.9639) \times (\frac{1}{1.03} \cdot 1.0) \times (0.981) = 0.864.$$

Finally in the outbending case, one gets:

$$\begin{aligned}
\omega_c^{out/40} &= (0.9542 \cdot 0.9713) \times (\frac{1}{1.03} \cdot 1.0) \times (0.911) = 0.819 \\
\omega_c^{out/50} &= (0.9425 \cdot 0.9639) \times (\frac{1}{1.03} \cdot 1.0) \times (0.911) = 0.803, \\
\omega_c^{out/tot} &= 0.808,
\end{aligned}$$

where $\omega_c^{out/tot}$ is the accumulated charge weighted factor.

Finally, we can get an overall accumulated charge weighted factor using this normalization method:

$$\omega_c^{tot} = 0.849.$$

5 Integrated cross section

This section summarizes the steps involved in the measurement of the total integrated cross-section of the near-threshold photoproduction of J/ψ .

5.1 Kinematic coverage and binning

Figure 41 show the t and E_γ of all events passing the exclusivity cuts with an invariant mass close to the J/ψ peak, in [2.9, 3.3] GeV. The t_{min} and t_{max} boundaries are also shown. Most events are located close to the t_{min} boundary where the cross section is expected to be large. The boundaries of the energy bins used to measured the cross section are also represented in this figure. Additionally, Table 6 summarizes the energy bin boundaries.

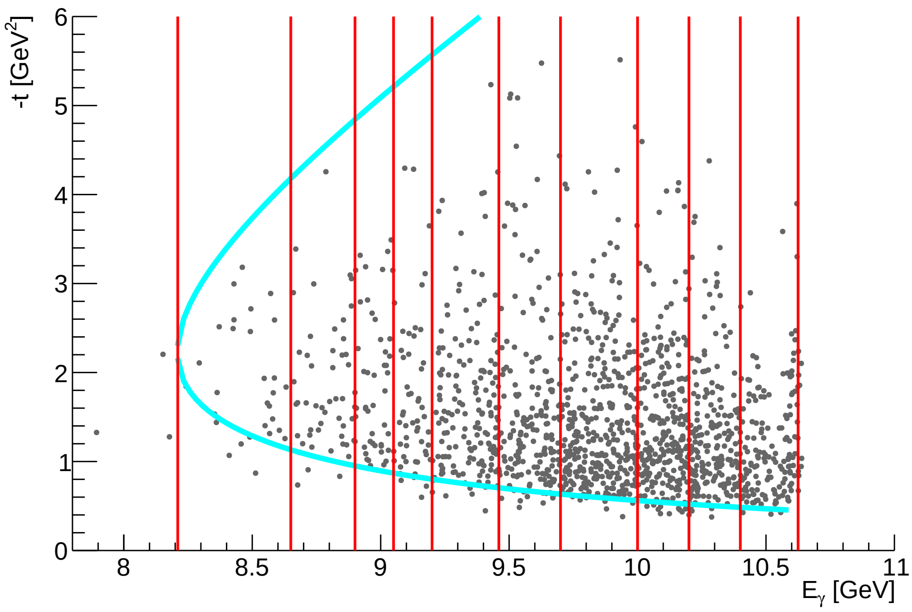

Figure 41: t versus E_γ of quasi-photoproduction events in the [2.9, 3.3] GeV mass region. The t_{min} and t_{max} boundaries are also shown in blue. The energy bin boundaries are shown in red.

Bin	1	2	3	4	5	6	7	8	9	10
Energy min. [GeV]	8.2	8.65	8.9	9.05	9.2	9.46	9.7	10.	10.2	10.4
Energy max. [GeV]	8.65	8.9	9.05	9.2	9.46	9.7	10.	10.2	10.4	10.6

Table 6: Energy bins for the integrated cross section calculation.

5.2 Cross section formula

For each photon energy bin j, the cross section can be express as:

$$\sigma_j = \frac{N_{J/\psi j}}{\mathcal{F}_j \cdot \mathcal{L} \cdot \omega_{cj} \cdot B_r \cdot \epsilon_j \cdot \epsilon_{Rad/j}}, \tag{47}$$

where

- $N_{J/\psi j}$ is the number of J/ψ from data (see section 5.3),
- $\mathcal{F}_j$ is the photon flux (see section 5.4),
- $\mathcal{L}$ is the RG-A luminosity factor (set to 1316.875 mC^{-1} pb^{-1} , see equation 22),

- ω_{cj} is normalization factor (set to 70%, see section 4.3),
- B_r is the branching ratio for the J/ψ to decay in a electron-positron pair (obtained from the PDG and set to 6%),
- ϵ_j is the detection efficiency estimated from MC (see section 5.5),
- $\epsilon_{Rad/j}$ is the radiative correction extracted from MC (see section 5.6).

5.3 J/ψ peak fitting procedure

To extract the raw J/ψ yield, the combined invariant mass spectra (for all three configuration) are fitted in the J/ψ region with gaussian peak and a exponential background. Figure 42 shows one example of such a fit.

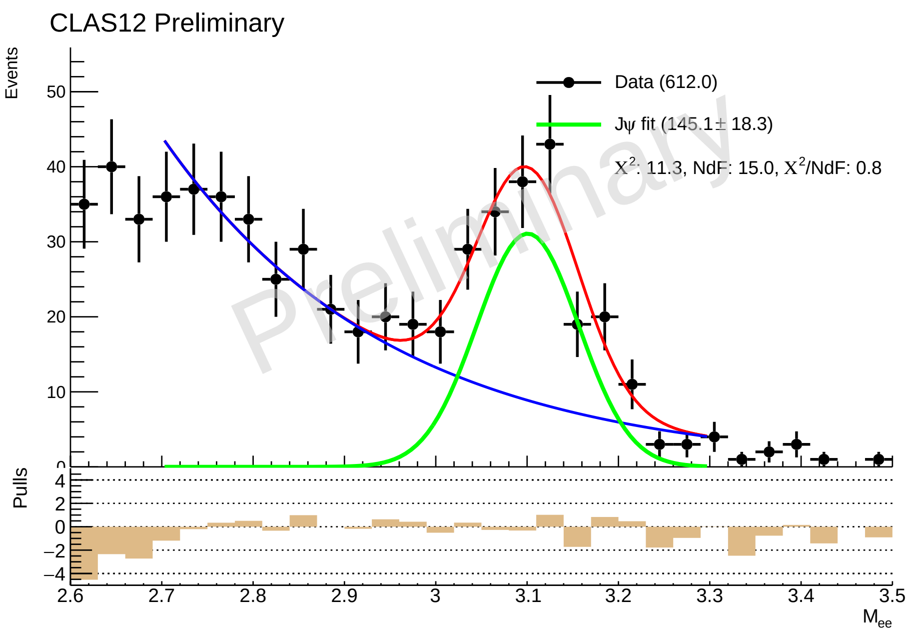

Figure 42: Fit function used to extract the J/ψ yield in the $E_\gamma \in [9.7, 10]$ GeV bin.

Figure 43 shows the measured number of J/ψ per photon energy bins. The fits used to extracted these yields are shown in Appendix E.3.

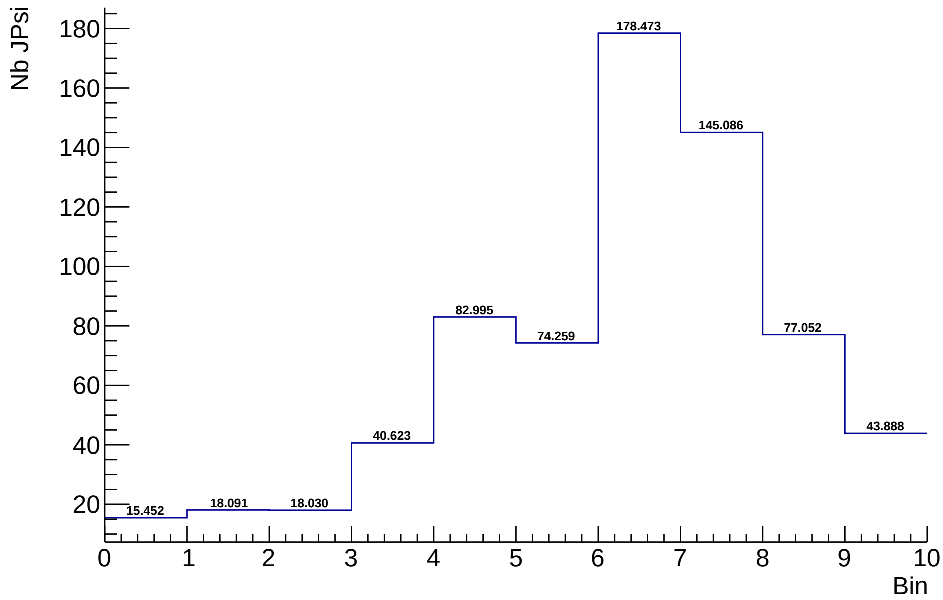

Figure 43: Number of J/ψ per bins

The data fits used to extract the differential cross section can be found in Appendix G.

5.4 Photon flux

5.4.1 Computation

Two contributions for the photon flux are taken into account. The real photon flux can be written as:

$$\mathcal{F}(E_\gamma)|_{real} = \frac{1}{2}\frac{L}{X_0}\frac{1}{E_\gamma}\left(\frac{4}{3} - \frac{4}{3}\frac{E_\gamma}{E_{beam}} + \frac{E_\gamma^2}{E_{beam}^2}\right) \tag{48}$$

where

- L is the target length,
- X_0 is the radiation length of liquid hydrogen,
- E_{beam} is the energy of the incoming electron beam,
- and the initial 1/2 factor account for the fact that real photons are emitted over the whole length of the target.

The virtual photon flux can be expressed as

$$\mathcal{F}(E_\gamma)|_{virtual} = \frac{1}{E_{beam}}\frac{\alpha}{\pi \cdot x}\left(\left(1 - x + \frac{x^2}{2}\right) \cdot \ln\left(\frac{Q^2_{max}}{Q^2_{min}}\right) - (1-x)\right) \tag{49}$$

where

- E_{beam} is the energy of the incoming electron beam,
- α is the fine structure constant (set to 1/137),
- $x = E_\gamma/E_{beam}$,
- $Q^2_{min} = m_e^2 \cdot x^2/(1-x)$,

- Q^2_{max} is a parameter fixed by the experimental setup. In the case of this measurement, it is fixed to 0.02 GeV^2 (see Appendix Q.2 for a justification of this value).

Figure 44 shows the flux functions used for this analysis.

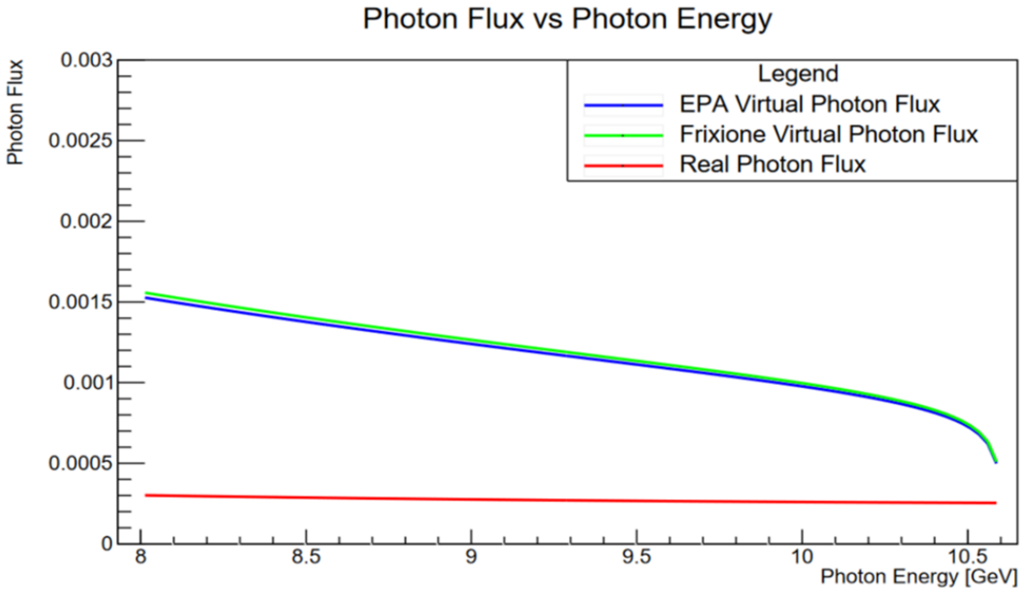

Figure 44: Flux functions for the Fall 2018 dataset. A small scaling factor is introduced to distinguish the otherwise overlapping Frixione and EPA fluxes.

In practice, the total integrated flux is calculated for each bin j and for each dataset configuration c using the non-radiated J/ψ generated event sample and applying the sum/integral correspondence as:

$$\mathcal{F}_{c/j} = \int_j \mathcal{F}_c dE = \Delta E \frac{\sum_{i=1}^{N} \mathcal{F}_c(E_{GEN/i}) \cdot \omega_i}{\sum_{i=1}^{N} \omega_i} \tag{50}$$

where:

- ΔE is the photon energy bin size,
- w_i is the weight of event i include in the calculation (in practice all events which have been generated in a bin of interest are added to the calculation),
- $\mathcal{F}_c(E_{GEN/i}) = \mathcal{F}_c(E_{GEN/i})|_{real} + \alpha_{ISR} \cdot \mathcal{F}_c(E_{GEN/i})|_{virtual}$ is the sum of the real and virtual flux for event i, and where α_{ISR} is defined in the next section.

The total current-weighted flux is then computed as:

$$\mathcal{F}_j = \sum_c C_c \cdot \mathcal{F}_{c/j} \tag{51}$$

where C_c is the total accumulated charge for the dataset c in mC (see Table 1 for numerical values).

5.4.2 Initial state radiation

In the previous section, the constant α_{ISR} is introduced. We add this correction factor in the flux calculation to account for the fact that the initial electron might loose energy before emitting a virtual photon. We computed this factor using GRAPE which include ISR, and computing the ratio of number of event, with and without ISR. The correction factor is $\alpha_{ISR} = 0.83$.

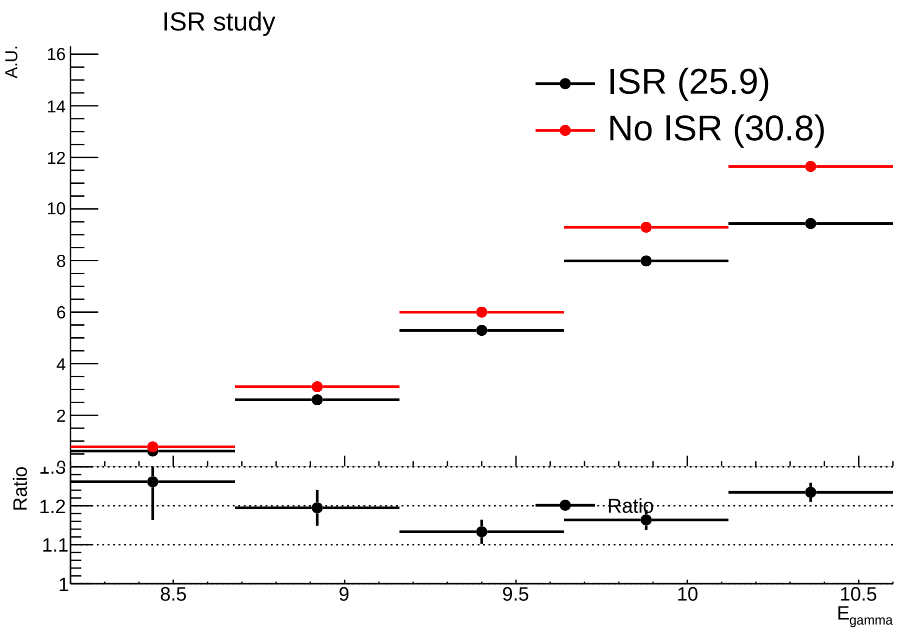

Figure 45: Computation of the ISR correction factor for quasi-real photon flux.

An estimation of the ISR for the real photon flux has also been done (see Appendix Q.2). It is estimated to be of the order of 6% close to the beam energy. However, as the real photon flux account for at most half of the photon flux in this region, we neglected this correction.

5.5 Detection efficiency

The detection efficiency is extracted from the MC samples produced for this analysis. As for the data samples, all MC J/ψ samples are combined together. From this combined sample, a number of events equal to α times the number of J/ψ reconstructed in data in the same bin are randomly drawn. The scaling factor α is set to 4. To approximate the background under the peak, the background fit function obtained in the data fit is used to generate random events. A number of background event equal to the integral of the background fit function is generated. These events are then combined with the random J/ψ MC events described just above. The obtained dataset is fitted with the same functional form as for the data. An example of the fit obtained following this procedure can be seen in Figure 47. This procedure is repeated 1000 times. For each new random drawing and fit, the detection efficiency is then computed as the ratio of the yield obtained by the MC fit to the number of generated events in the bin after radiative effect are applied, adjusting for the scaling factor α and the scaling to the number of fitted events in data:

$$\epsilon_j = \frac{N_{Fit/MC}\big|_j}{\alpha \cdot N_{Fit/Data}\big|_j} \frac{N_{REC/MC}\big|_j}{N_{GEN+RAD/MC}\big|_j}. \tag{52}$$

The average acceptance of the 1000 trials is then used in the following of the analysis.

Two values of α have been tested, with now significant impact on the determination of the cross-section. Figure 46 show the impact of varying the MC scaling factor α between 2 and 4 on the extraction of the integrated cross-section: no impact is seen.

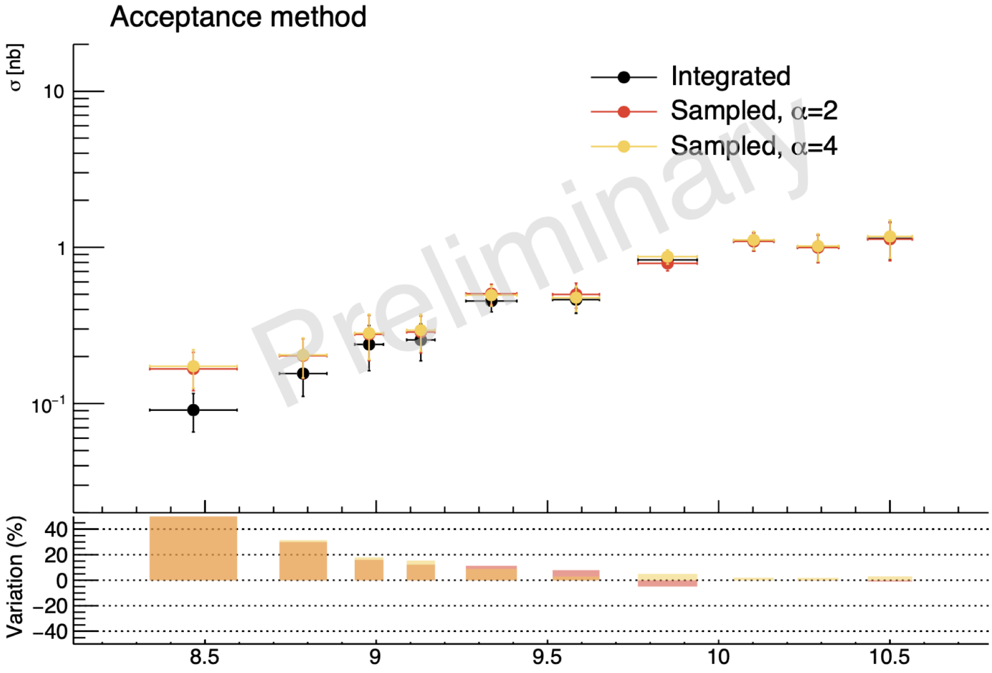

Figure 46: Impact of the acceptance calculation method on the extraction of the integrated cross section. Three method to compute the acceptance have been compared, using $\alpha = 2$ and $\alpha = 4$, and using the full MC dataset. The latest has been ignored as it does not take into account the small statistics available in data and in particular was yielding large χ^2 for the fits.

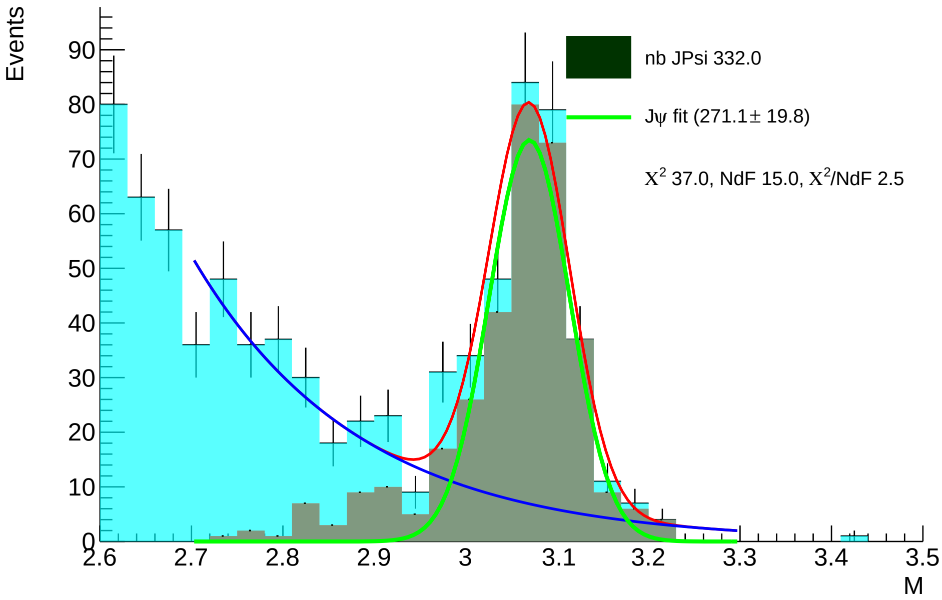

Figure 47: Example of a fit performed on reconstructed MC events, where the background (in blue) has been estimated using the background fit function obtained from the data fit.

Figure 48 shows the efficiency estimated using this method as a function of the bin number used for the extraction of the cross section. Appendix F displays all the MC fits used to extract these efficiencies.

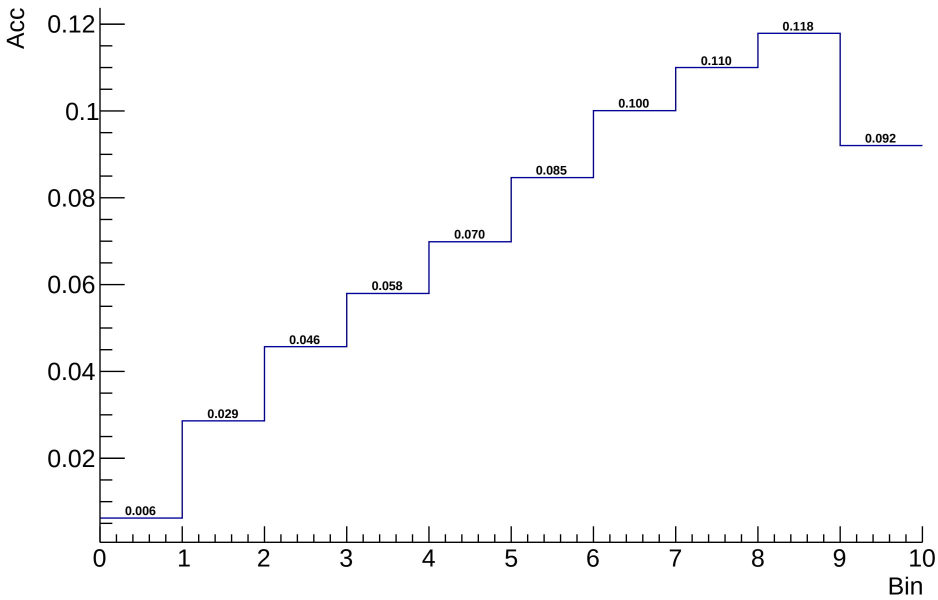

Figure 48: Detection efficiency as a function of the bin number.

5.6 Radiative correction

A radiative correction factor is derived to account for the shift in reconstructed kinematics that occurs when one of the lepton loses energy due to radiative effect. This correction is computed as the ratio of events generated in a given bin with radiative effect and without radiative effect as:

$$\epsilon_{Rad/j} = \frac{N_{J/\psi}\big|_{j/RAD}}{N_{J/\psi}\big|_{j/GEN}}. \tag{53}$$

Figure 49 shows the radiative correction factor as a function of the bin number. As expected, the correction is larger than one at small photon energy and gradually become smaller than one as the energy of the photon gets larger. More events will be measured in the lower energy region as a consequence of the radiative energy loss.

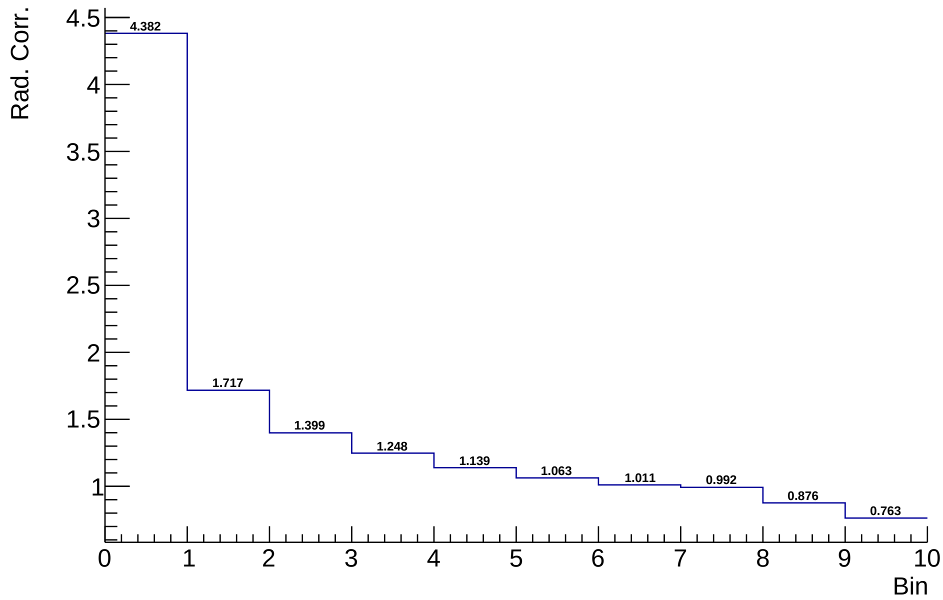

Figure 49: Radiative correction factor

5.7 Determination of the bin center in E_γ and its error bar

For each bin, the average reconstructed photon energy and its RMS are used as bin center and its error bar.

5.8 Results

The results of the computation of the integrated cross section are shown in Figure 50, with the systematic error superimposed. The tabulated results can be found in Appendix A. The computation of the systematic error is detailed in section 7.1.

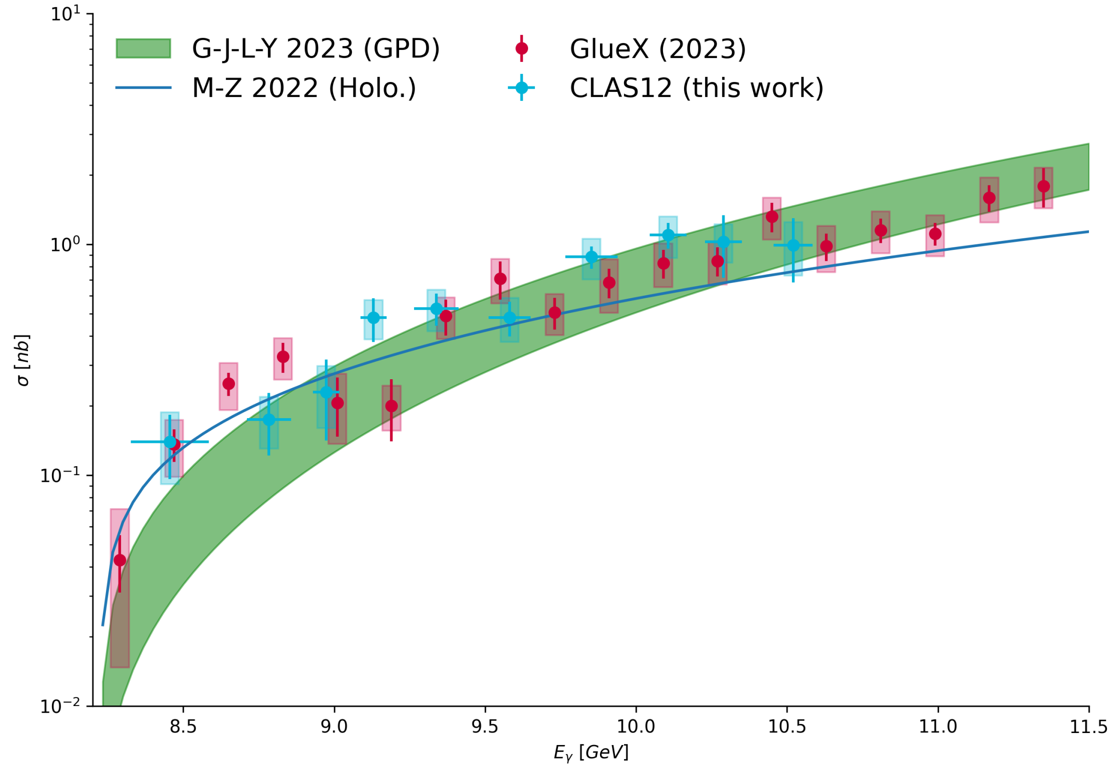

Figure 50: Cross section of the photoproduction of the J/ψ meson near its production threshold as a function of the photon energy in blue. The comparison with previous data and models is done in section 9.2.

6 Differential cross section

This section summarizes the steps involved in the measurement of the differential cross section of the J/ψ photoproduction near threshold as a function of the transferred momentum squared to the proton, t.

6.1 Phase space and binning

The differential cross section is measured in 3 bins of incoming photon energy. For each energy bin, we divided the phase space in t-bins to have similar number of J/ψ in each bins. The table below summarizes the bin limits. Figure 51 shows the bin boundaries super imposed on events in the [2.9, 3.3] GeV mass region.

$E_\gamma \in [8.2, 9.28]$ GeV / Bin	1	2	3	4	5
$-t$ min. [GeV^2]	0.77	1.00	1.5	2.0	2.5
$-t$ max. [GeV^2]	1.00	1.5	2.0	2.5	4.5

$E_\gamma \in [9.28, 10.00]$ GeV / Bin	1	2	3	4	5	6	7	8	9
$-t$ min. [GeV^2]	0.5	0.75	1.0	1.25	1.5	1.75	2.0	2.5	3.0
$-t$ max. [GeV^2]	0.75	1.0	1.25	1.5	1.75	2.0	2.5	3.0	6.0

$E_\gamma \in [10.00, 10.6]$ GeV / Bin	1	2	3	4	5	6	7
$-t$ min. [GeV^2]	0.5	0.7	0.9	1.1	1.3	1.6	2.0
$-t$ max. [GeV^2]	0.7	0.9	1.1	1.3	1.6	2.0	4.5

Table 7: t bins for the differential cross section calculation.

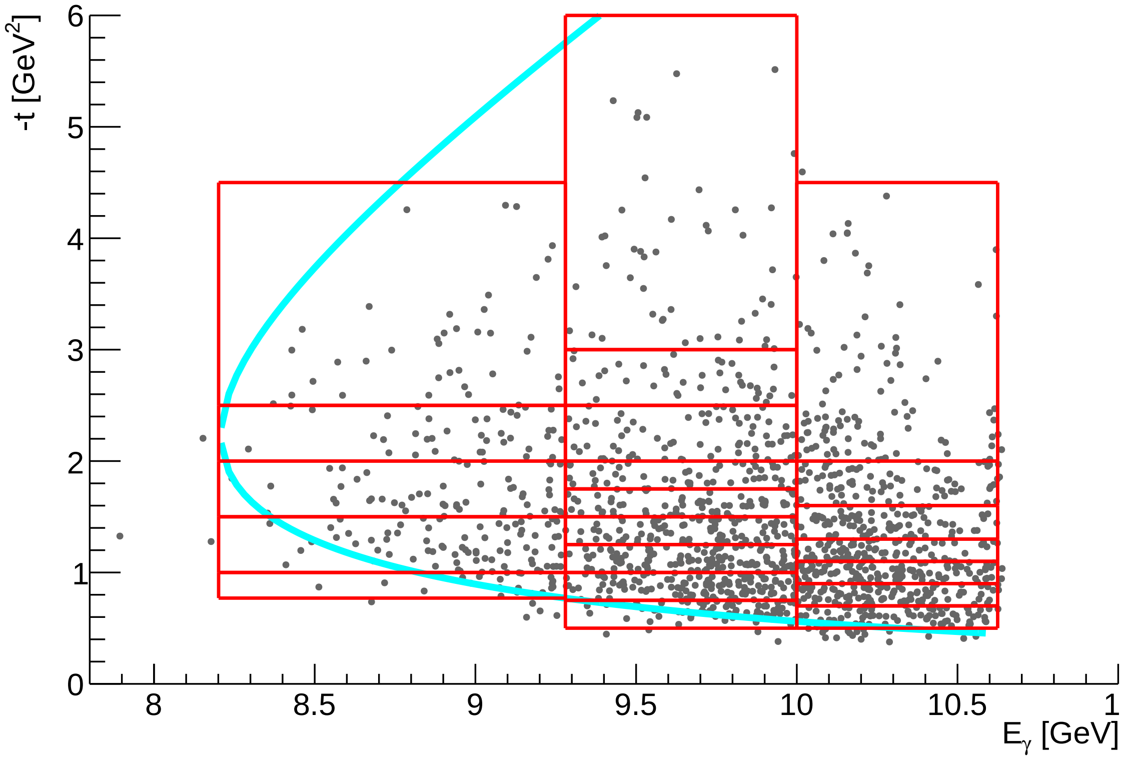

Figure 51: t versus E_γ of quasi-photoproduction events in the [2.9, 3.3] GeV mass region. The t_{min} and t_{max} boundaries are also shown in light blue. The t-E_γ bins boundaries are shown in red.

6.2 Cross section formula

The differential cross section is calculated as:

$$\left.\frac{d\sigma}{dt}\right|_j = \frac{N_{J/\psi/j}}{\mathcal{F}_j \cdot \mathcal{L} \cdot \omega_{c/j} \cdot B_r \cdot \epsilon_j \cdot \epsilon_{Rad/j} \cdot \mathcal{V}_j \cdot \Delta t_j}, \tag{54}$$

where most terms are described in Section 5.2 and

- $\mathcal{V}_j$ is bin volume correction (see section 6.3),
- $\Delta t_j = t_j|_{max} - t_j|_{min}$ is the size of the t bin.

6.3 Bin volume correction

The t-differential cross section is calculated in multiple bins of incident photon energy. Because of kinematic constraints, some values of t are not possible for a given photon energy and t is restricted to a range from t_{min} to t_{max} as illustrated in Figure 52.

To account for the fact that some E_γ-t-bins do not have a rectangular shape, one has to correct for the physical size of the bin. This is done by computing the ratio of the area of the bin within the physical phase space to the rectangular area of the bin. In Figure 52 this corresponds to the hatched area compared to the red rectangular area.

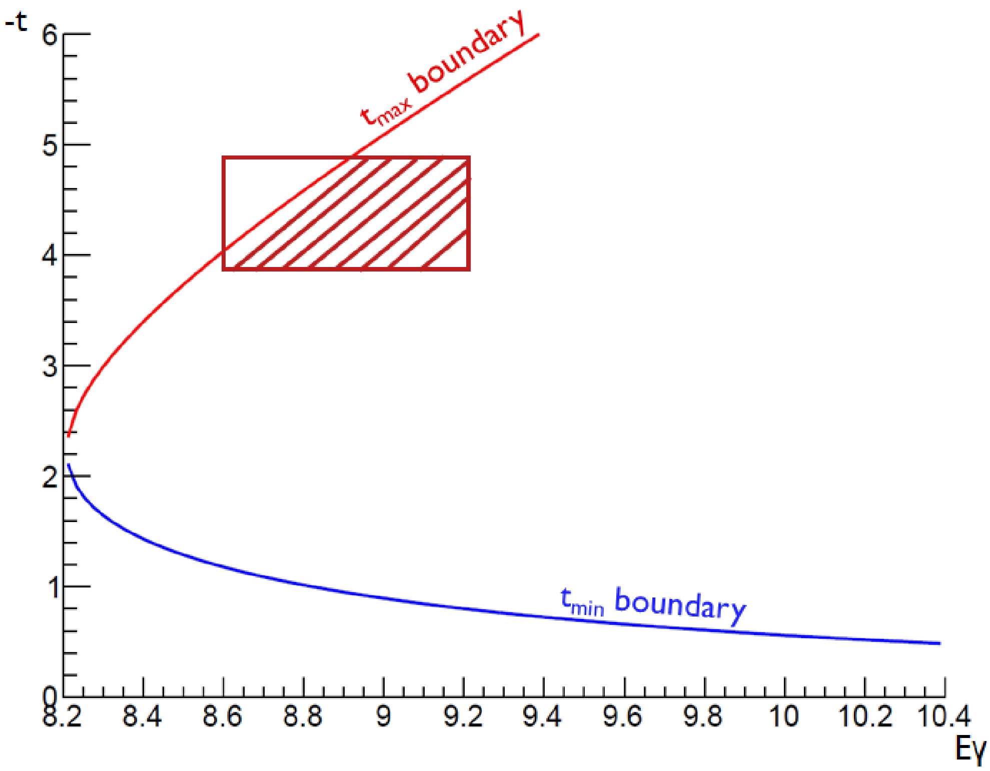

Figure 52: The t_{min} and t_{max} boundaries for the J/ψ production phase space, and an example of the computation of the bin volume correction.

6.4 Determination of the bin center in in E_γ and t and their error bars

For each bin, the average reconstructed photon energy and Mandelstam t and their respective RMS are used as bin center and its error bar.

6.5 Results with systematic uncertainties

The results of the computation of the differential cross section are shown below in Figures 53, 55 and 56, with the systematic error superimposed. The tabulated results can be found in Appendix B. The computation of the systematic error is detailed in section 7.2.

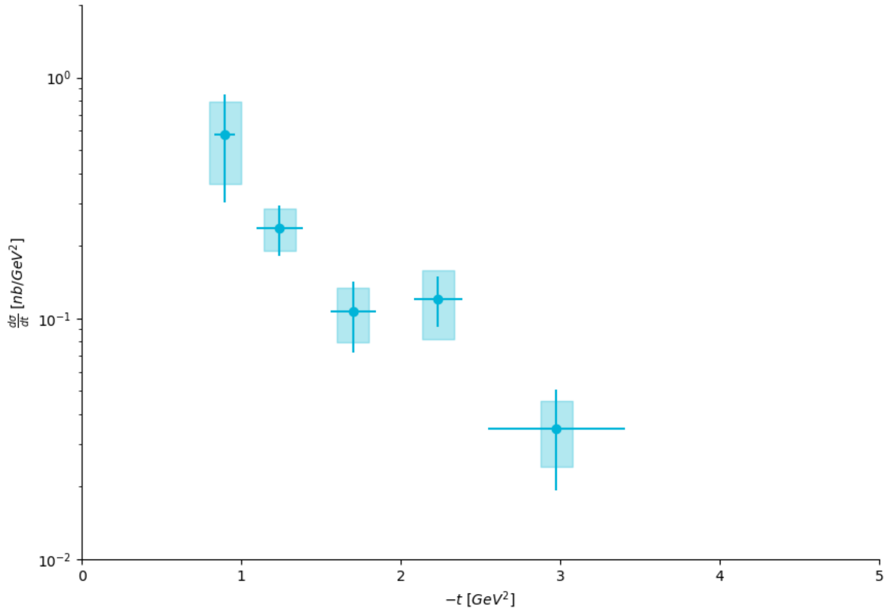

Figure 53: Differential cross-section with systematic uncertainties in bin 1 ($E_\gamma \in [8.2, 9.28]$)

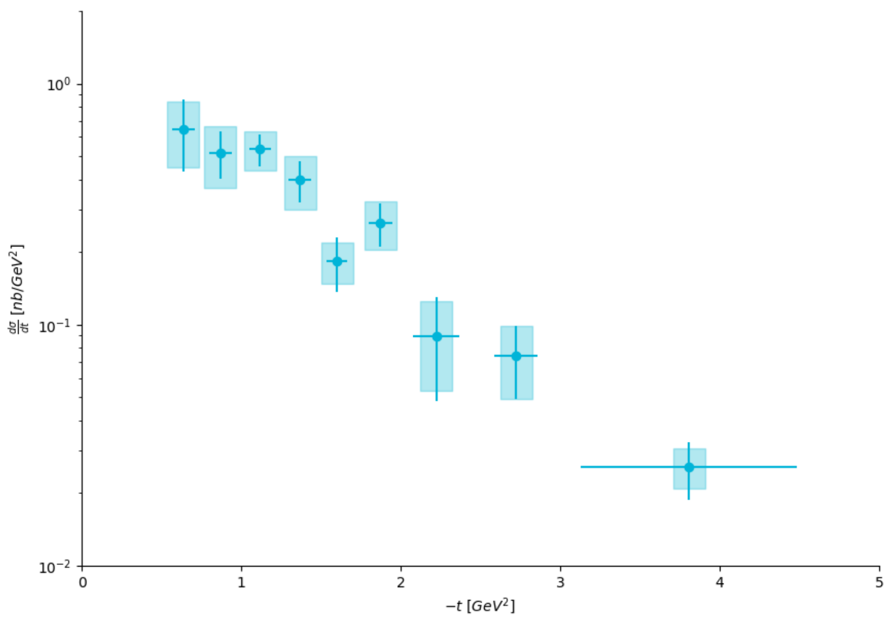

Figure 54

Figure 55: Differential cross-section with systematic uncertainties in bin 2 ($E_\gamma \in [9.28, 10.0]$)

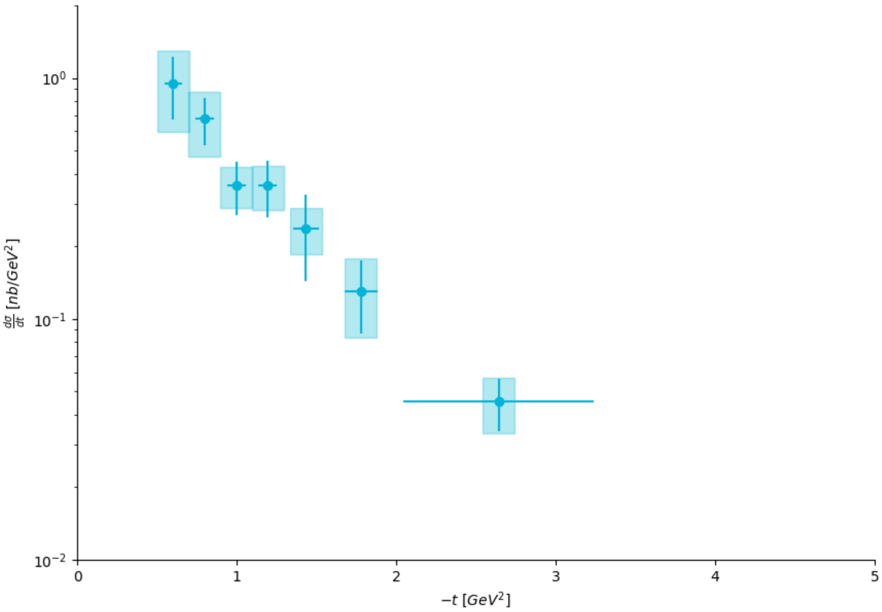

Figure 56: Differential cross-section with systematic uncertainties in bin 3 ($E_\gamma \in [10.0, 10.6]$)

7 Systematic errors study

A complete study of systematic variations have been performed to test the impact of various cuts and corrections used in this analysis. Table 8 summarizes the various variations performed to estimate the systematic error of this analysis. For each variation, the whole analysis is performed. In most cases, the normalization factor is not recomputed, except when explicitly mentioned.

For each source of systematics, the standard deviation of the three variations (standard, down and up) is computed and assigned as systematic error for this source. To compute the total systematic error, all contributions are added in quadrature.

While determining the systematic uncertainty of the cross-section in a given bin, we also compute the average kinematic in this bin. As shown in the following section, the average kinematics does not vary significantly when performing the systematics variations. Thus we did not computed the systematic error on the determination of the mean kinematic of a given bin.

In the following, the computation of the systematic error for each source considered is detailed for both the integrated and differential cross-section.

Variation	$\tilde{Q}^2$ [GeV^2]	MM^2 [GeV^2]	Fit function	AI PID	Prot. PID	Lepton mom. [GeV]
Standard	0.5	0.4	Gauss + Int.	0.0	No cuts	1.7
Down	0.2	0.2	CB + int.	-0.05	2σ	1.5
Up	0.8	0.8	Gauss + Pol.2	0.05	3σ	1.9

Variation	Norm.	Accumulated charge	Radiative correction
Standard	Mixed BG	-	-
Alternative	Single particle eff.	-	-

Table 8: Summary of the variations used to compute the systematics

7.1 Integrated cross section systematics

In this section, the systematic errors for the integrated cross section are estimated. All the tabulated variations can be found in Appendix C.

7.1.1 Measured photon virtuality $\tilde{Q}^2$

The impact of the cut applied on the measured virtuality of the initial photon is tested by varying the cut from 0.5 GeV^2 to 0.2 GeV^2 and 0.8 GeV^2. in both cases, the normalization factor is recomputed. Indeed it was noted that for this cut, the normalization factor varies with the value of the cut. We thus computed the normalization factor for both Fall 2018 inbending and Spring 2019 for the three value of virtuality cut. An average of the normalization factor weighted by the corresponding accumulated charge is then used for each cut. Table 9 summarizes the values of the normalization factors, the associated accumulated charge and the obtained normalization factor for each value of the virtuality cut.

Dataset era (Acc. charge [mC])	Fall 2018 in. (35.667) and Fall 2018 out. (32.451)	Spring 2019 (45.994)	Total (114.112)
Standard: $\tilde{Q}^2 < 0.5$ GeV^2	0.69	0.68	0.69
Down: $\tilde{Q}^2 < 0.2$ GeV^2	0.55	0.77	0.64
Up: $\tilde{Q}^2 < 0.8$ GeV^2	0.74	0.80	0.76

Table 9: Variation of the normalization factor with the cut applied on the reconstructed virtuality of the photon. The charge weighted average of the normalization factor is also given in the last column.

Overall, this systematic is always smaller than 16%, as seen in Figure 57.

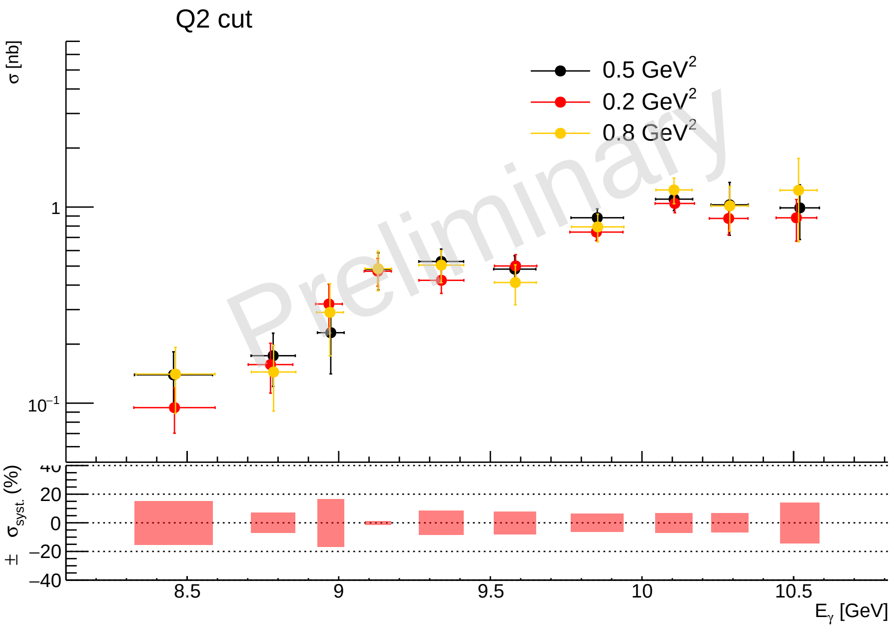

Figure 57: Systematic variation of the integrated cross section for three values of the $\tilde{Q}^2$ cut.

787 ### 7.1.2 Missing mass squared

788 The impact of the cut applied on the missing mass squared is tested by varying the cut from 0.4 GeV^2
789 to 0.2 GeV^2 and 0.8 GeV^2. This can be seen in Figure 58. This systematic is smaller than 6% for all
790 bins, but for the first three, where it reaches up to 12%.

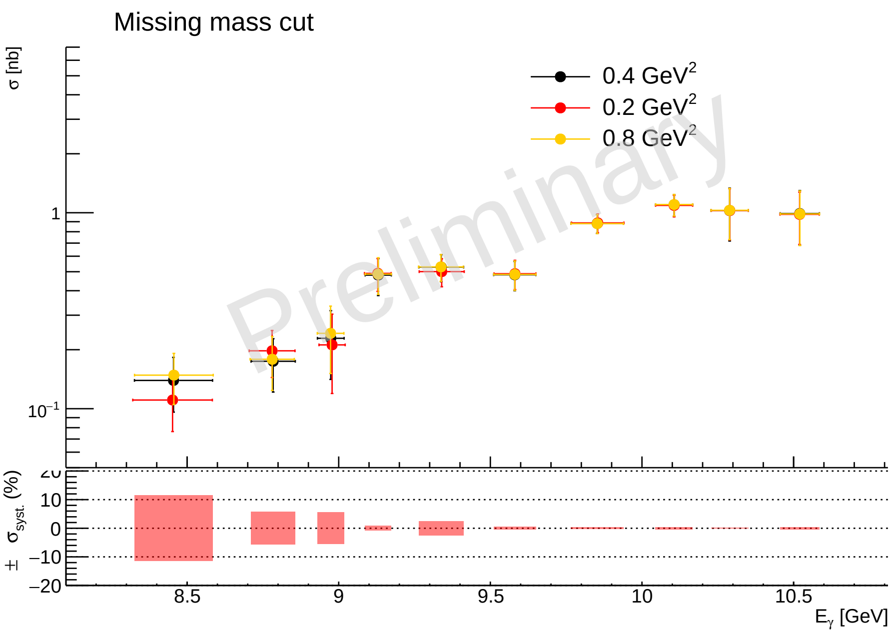

Figure 58: Systematic variation of the integrated cross section for three values of the M_X^2 cut.

791 ### 7.1.3 Fit function

792 The impact of the fit function is tested by performing the analysis with 3 distinct function. For the
793 standard fit, a gaussian is used for the signal and a decaying exponential is used for the background.
794 The variations are performed using, on one side, a crystal-ball for the signal with a decaying expo-

nential background, and on the other side, a gaussian signal with a second order polynomial for the background.

In the case of the crystal-ball signal, the convergence of the fit is difficult to achieve. We thus fixed the parameters describing the left-hand tail (n, the number of standard deviation from the peak value at which the tail starts and α, the decay rate of the power-law tail) using the J/ψ Monte Carlo samples for each dataset (including the radiative effect to account for the radiative tail).

Figure 60 shows the fit of the J/ψ peak for the three MC samples corresponding to the three era of data taking. As the parameters describing the left-hand tail are similar for all three samples, we fixed $n = 4.0$ and $\alpha = 0.84$ for all crystal-ball functions in the rest of the note.

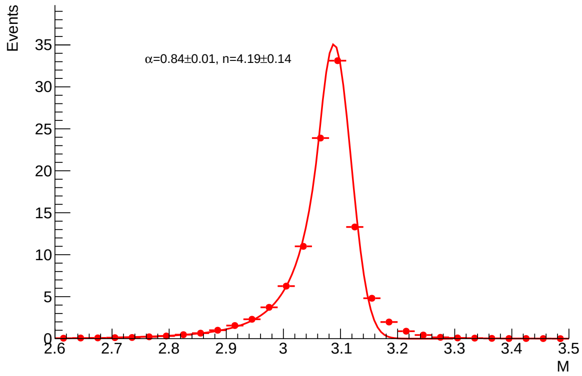

(a) Fall 2018 inbending

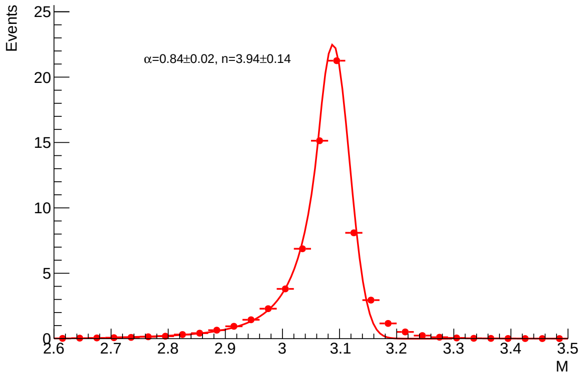

(b) Fall 2018 outbending

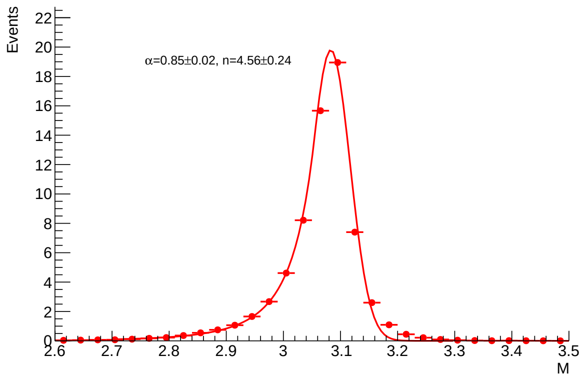

(c) Spring 2019

Figure 59: Crystal-ball fit of the J/ψ peak for the three MC samples used in this analysis.

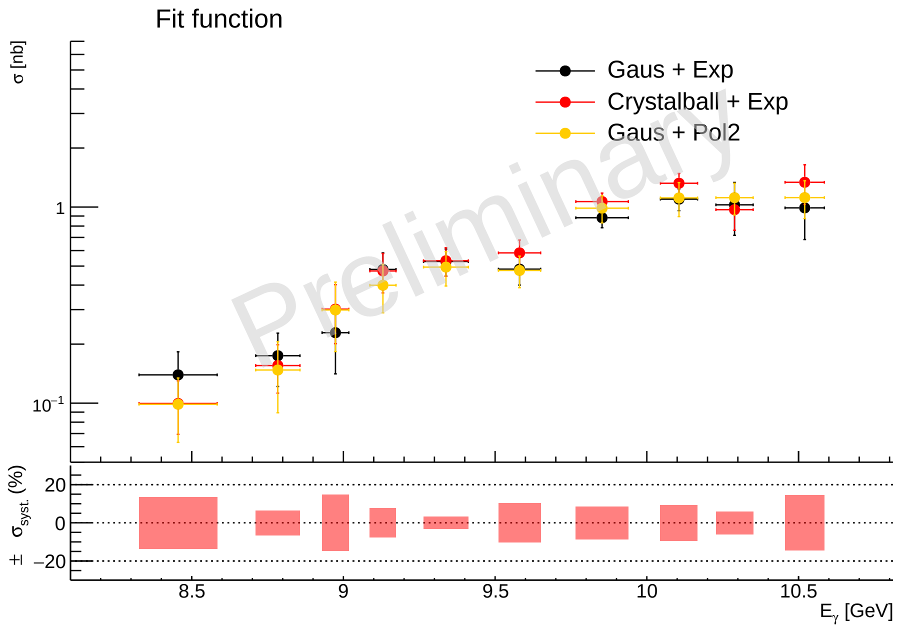

Figure 60: Systematic variation of the integrated cross section for three different fit functions.

The systematic error associated to the choice of fit function is always smaller than 15% as seen in Figure 60.

7.1.4 AI lepton PID score

We assessed the effect of the cut applied on the score provided by the BDT-based Lepton PID by varying it from its nominal value (0.0) to two values in its vicinity (± 0.05).

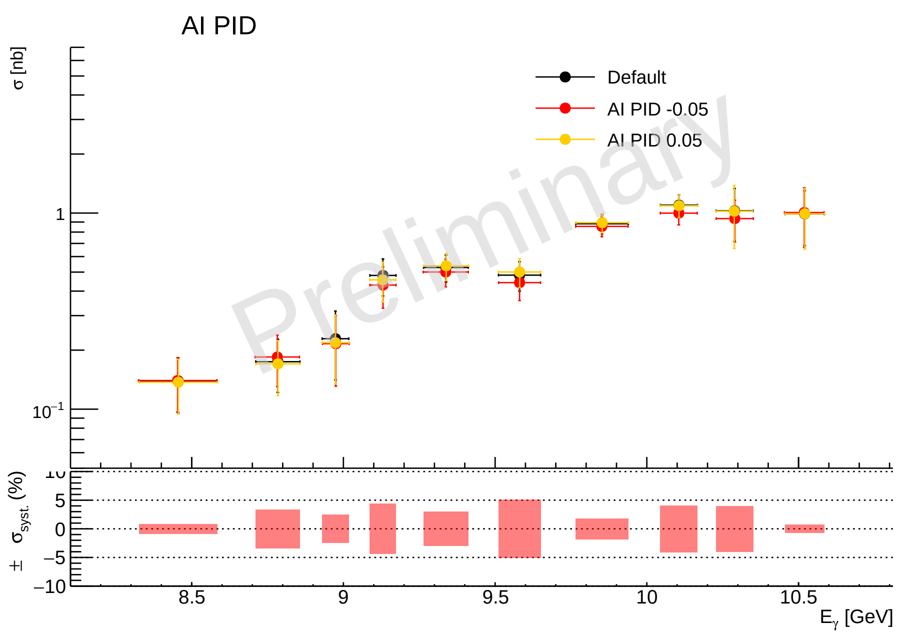

Figure 61: Systematic variation of the integrated cross section for three values of the AI PID cut

For all energy bin, this systematic is always smaller than 5%. Figure 61 display the computation of this systematic.

7.1.5 Proton PID

In the standard analysis, the CLAS12 event builder is used to identified the proton. No further cut is applied. We assessed the potential systematic variation arising from this choice by computing the cross-section with cuts on the PID-χ^2 provided by the EB, with cuts at 2 and 3 standard deviation from the mean value, respectively.

To account for the difference in χ^2 between data and MC samples, as well as between the various dataset, the mean and standard deviation of proton in the FD has been extracted for data and MC, for each era.

Figure 62 and 63 show the χ^2 spectrum for the three datasets and the corresponding three J/ψ MC samples. The peak corresponds to events with invariant mass larger than 2.6 GeV, with all other cut of the analysis applied. It is fitted with a gaussian and the mean and standard deviation are extracted to corrected for the deviation presented before. In the case of the MC sample, a single value of the mean and standard deviation is used for simplicity, set to $\mu = 0.05$ and $\sigma = 1.2$.

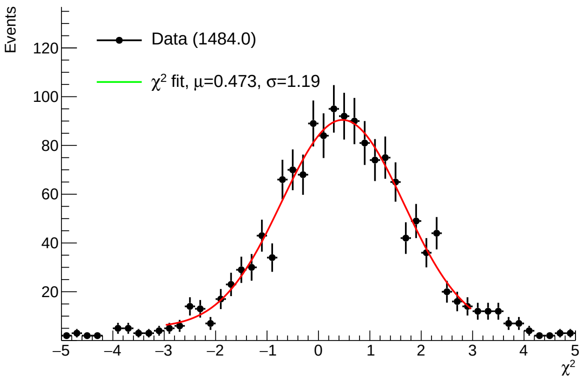

(a) Fall 2018 inbending

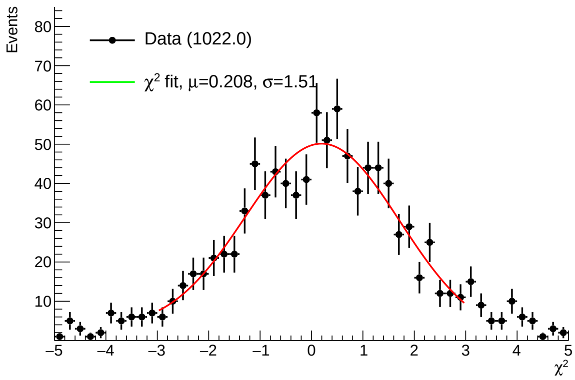

(b) Fall 2018 outbending

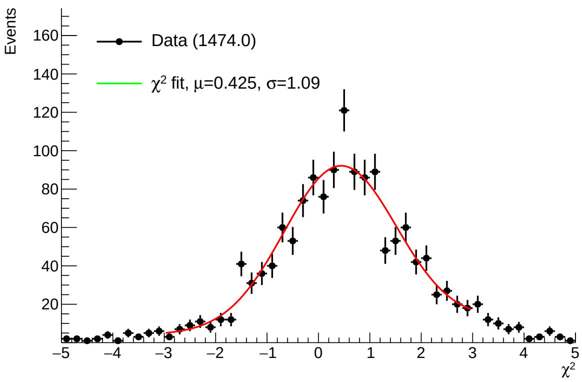

(c) Spring 2019

Figure 62: Gaussian fit of the χ^2 spectrum for proton in the forward detector for the three RGA datasets.

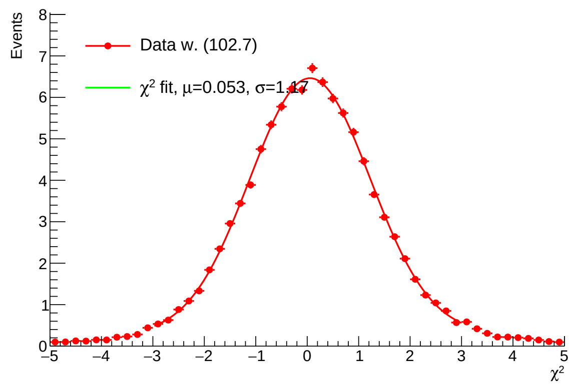

(a) Fall 2018 inbending

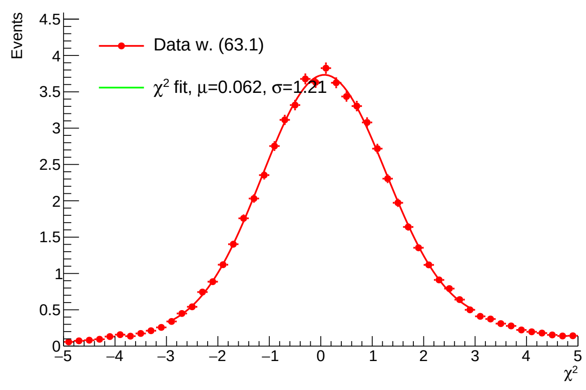

(b) Fall 2018 outbending

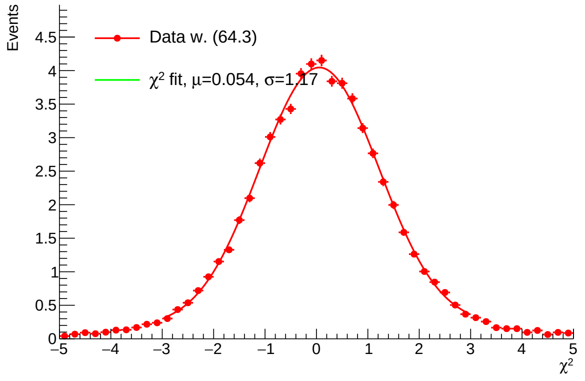

(c) Spring 2019

Figure 63: Gaussian fit of the χ^2 spectrum for proton in the forward detector for the three J/ψ MC samples used in this analysis.

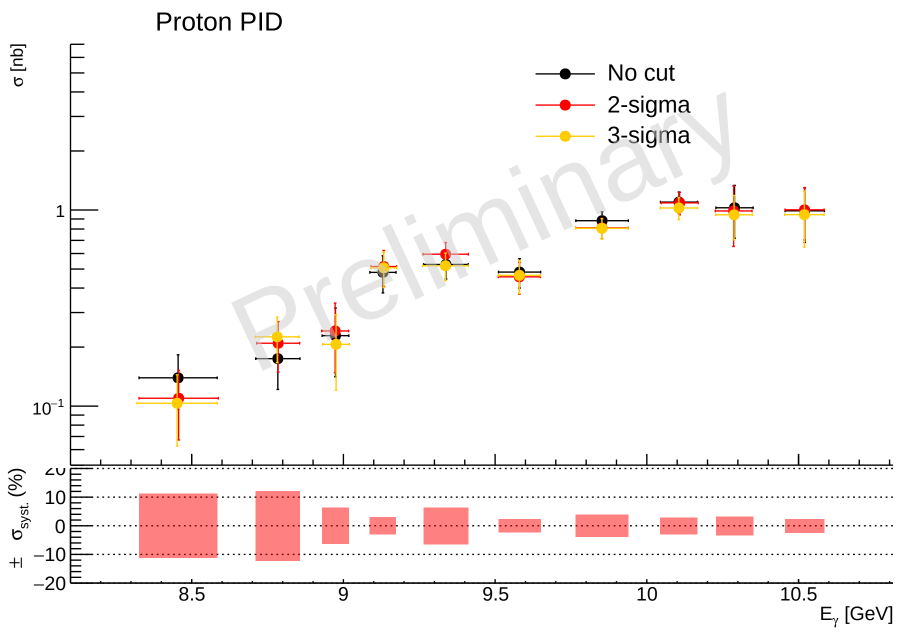

Figure 64: Systematic variation of the integrated cross section for three Proton PID cuts

This systematic error is below 7%, except for the first two energy bins where it reaches up to 12%, as seen in Figure 64.

7.1.6 Lepton momentum cut

To ensure the quality of the momentum reconstruction of the leptons, a cut is applied on their reconstructed momenta. In the standard method, the cut is set at 1.7 GeV for both electrons and positrons. We varied this cut to 1.5 GeV and 1.9 GeV.

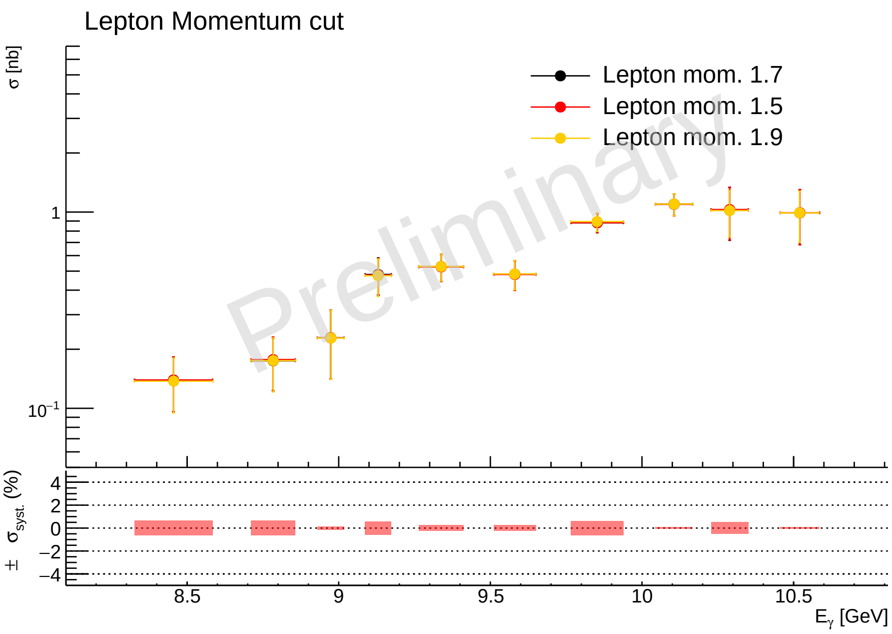

Figure 65: Systematic variation of the integrated cross section for three values of the minimum lepton momentum cut

Overall, the systematic variations for this cut are below 1%, as seen in Figure 65.

7.1.7 Normalization factor

In this analysis, we have derived two normalization factor. An overall normalization factor is derived in section 4.3 to account for the efficiencies mismatch between real data and MC. Another normalization factor is also derived by multiplying the efficiency for each of the final state particle in section 4.4. The systematic error associated to the normalization factor is taken as the difference between the two factors: 16%.

7.1.8 Accumulated charge

The systematic error associated to the determination of the accumulated charge of the whole RG-A dataset has been determined for pass-1 data for the determination of the inclusive cross-section in the resonance region [38]. The corresponding note can be found here.

For pass-1 data, the error, quoted for this approved measurement, is 1.2%. In the current analysis, we will use this number as it constitutes an upper limit for the accuracy of the determination of the integrated charge in pass-2. Note that it is the second smallest systematic in this analysis.

7.1.9 Radiative corrections

In order to validate the computation of the radiative correction factor in sections 5.6, we cross-checked our radiative effect described in Appendix Q with the one produced by the PHOTOS package [39]. In Figure 73, the generated number of event per energy bin is shown for events with and without radiative effect. In the radiative case, both our approach and the PHOTOS code are shown. The ratio of radiative/no-radiative in both cases is shown. This ratio, which is the correction factor used to correct for radiative effect, differs by 16% at most in the first bin, and gets negligible in the following bins. This difference is added in quadrature for each bin to the total systematic.

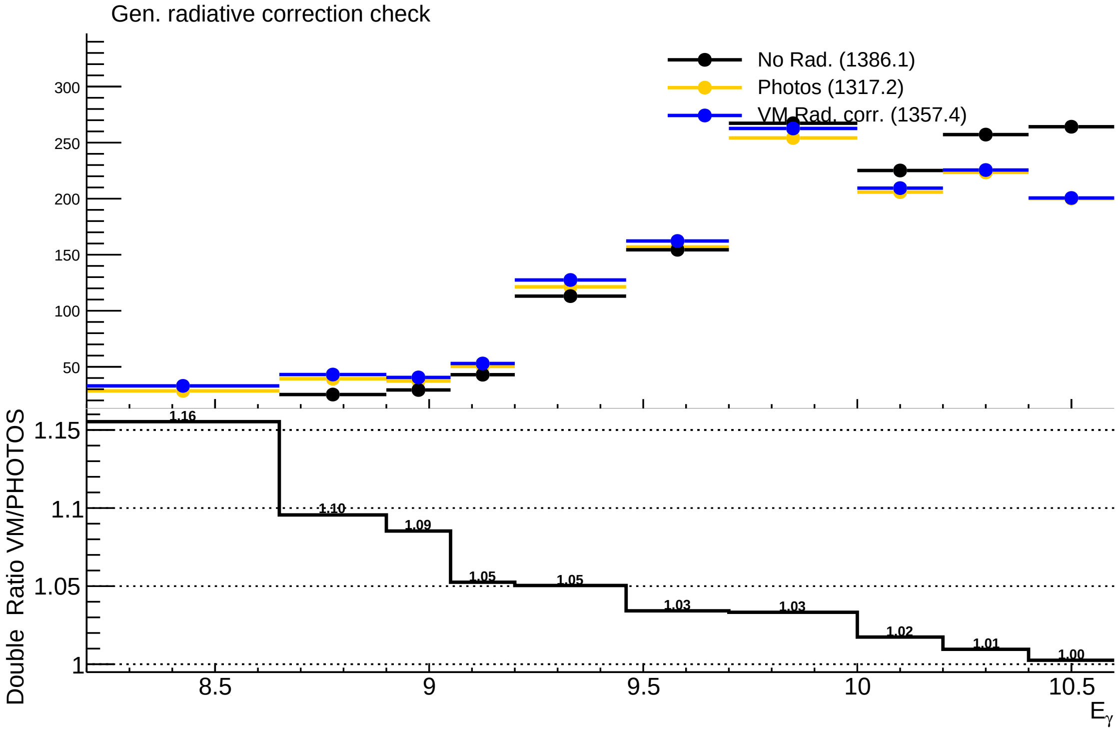

Figure 66: Generated spectra of photon energy for 3 J/ψ samples: one without radiative effect, and two using two different radiative effect approach, the one developed here in Appendix Q and PHOTOS [39]. The energy binning shown is the one of the integrated analysis.

7.2 Differential cross section systematics

In this section, the systematic errors for the differential cross section are estimated. The methods described in the previous section for the integrated case also apply to the following. All the tabulated variations can be found in Appendix D.

7.2.1 Measured photon virtuality $\tilde{Q}^2$

For all energy bins, the systematic variation associated with the $\tilde{Q}^2$ cut is the largest one, but always below 30% (see Figure 67).

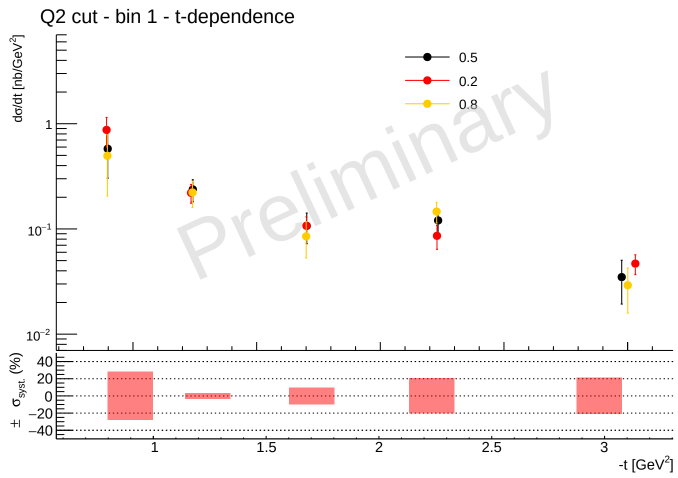

(a) Bin 1: $E_\gamma \in [8.2, 9.28]$

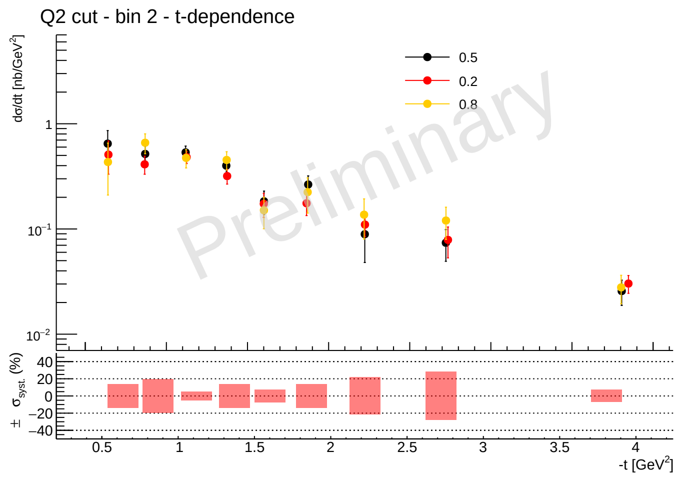

(b) Bin 2: $E_\gamma \in [9.28, 10.0]$

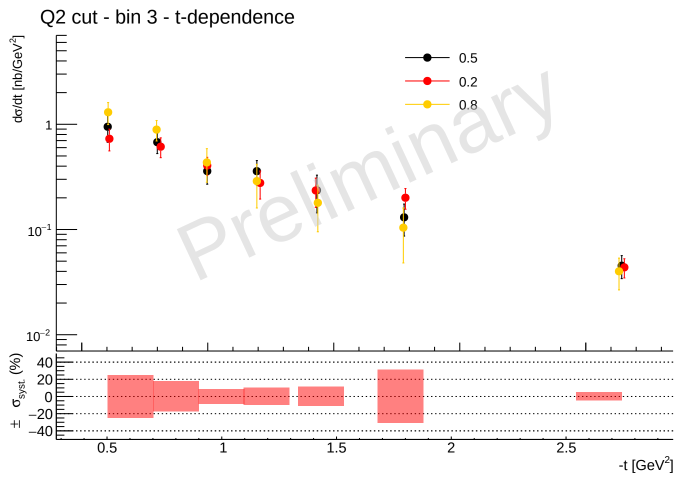

(c) Bin 3: $E_\gamma \in [10.0, 10.6]$

Figure 67: Systematic variation of the differential cross section for three values of the $\tilde{Q}^2$ cut.

7.2.2 Missing mass squared

For the first energy bin, the systematic variation associated with the missing mass cut reaches 15%. However, for all other bin it is always smaller than 5% (see Figure 68).

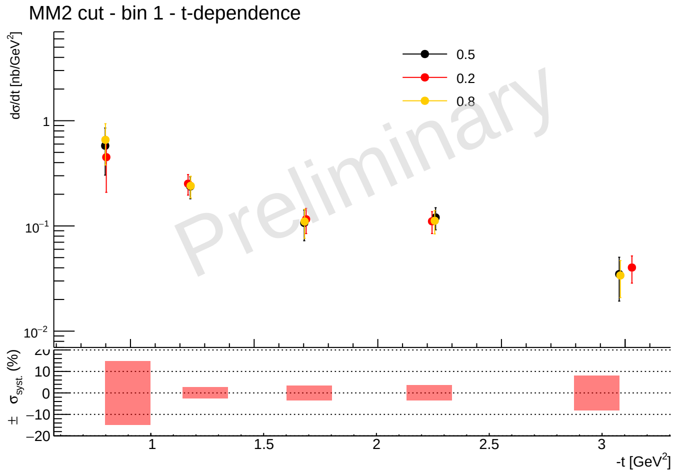

(a) Bin 1: $E_\gamma \in [8.2, 9.28]$

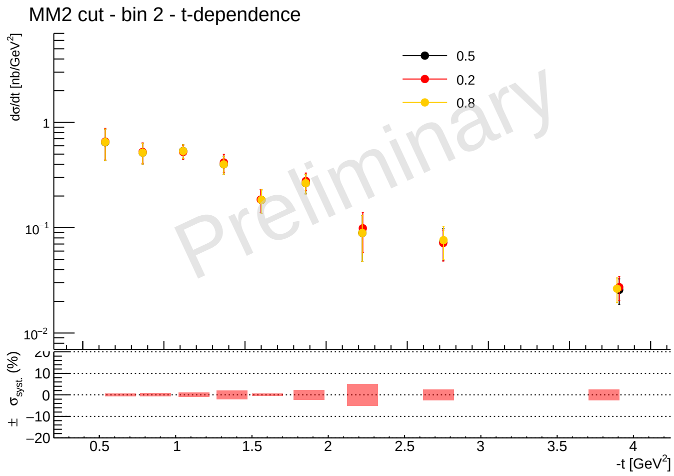

(b) Bin 2: $E_\gamma \in [9.28, 10.0]$

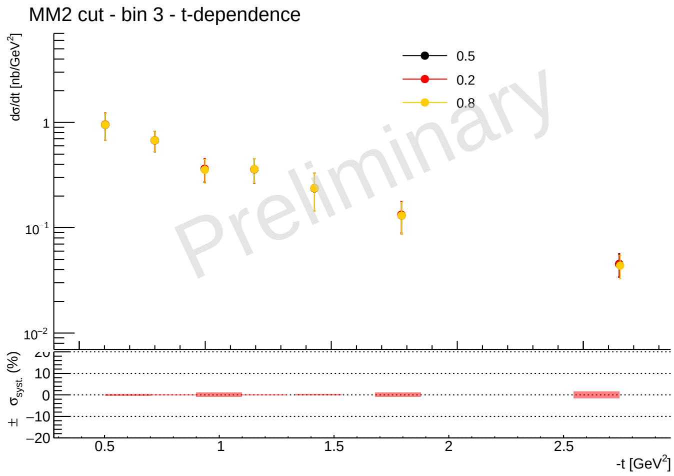

(c) Bin 3: $E_\gamma \in [10.0, 10.6]$

Figure 68: Systematic variation of the differential cross section for three values of the M_X^2 cut.

7.2.3 Fit function

The systematic variation associated with the choice of fitting function is above 14% for three bins. For all other bin it is always smaller than 11% (see Figure 69).

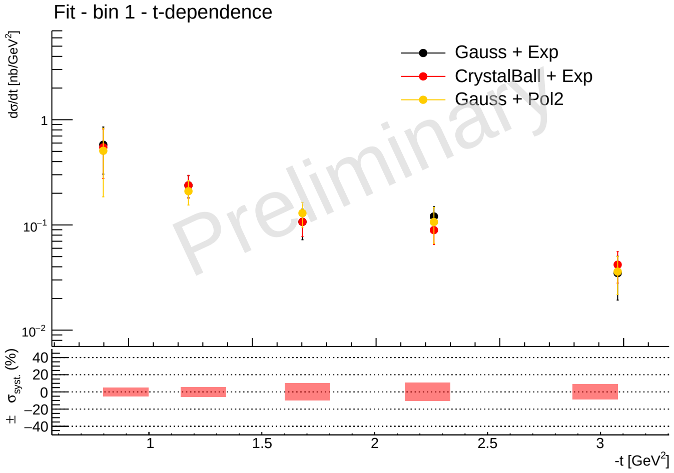

(a) Bin 1: $E_\gamma \in [8.2, 9.28]$

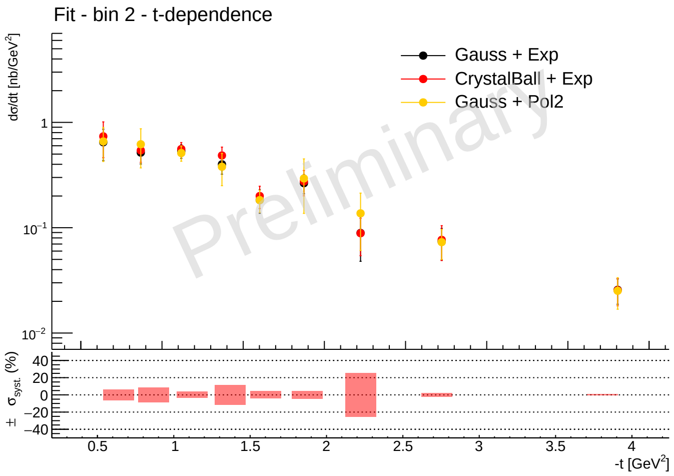

(b) Bin 2: $E_\gamma \in [9.28, 10.0]$

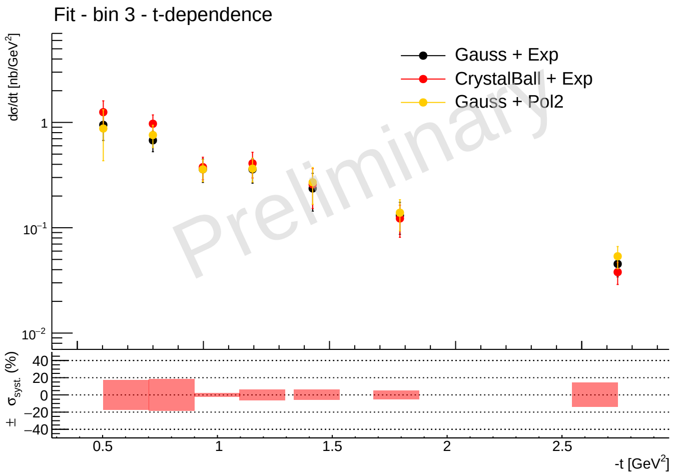

(c) Bin 3: $E_\gamma \in [10.0, 10.6]$

Figure 69: Systematic variation of the differential cross section for three fit functions.

7.2.4 AI lepton PID score

For all energy bins, the systematic variation associated with AI PID for lepton is always smaller than 7.5% (see Figure 70).

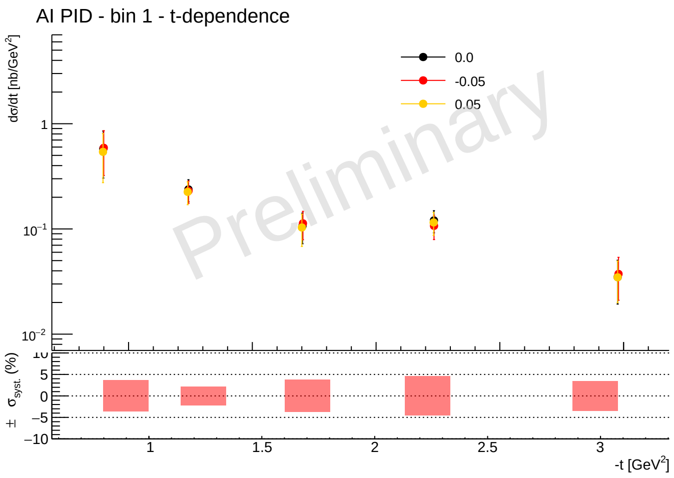

(a) Bin 1: $E_\gamma \in [8.2, 9.28]$

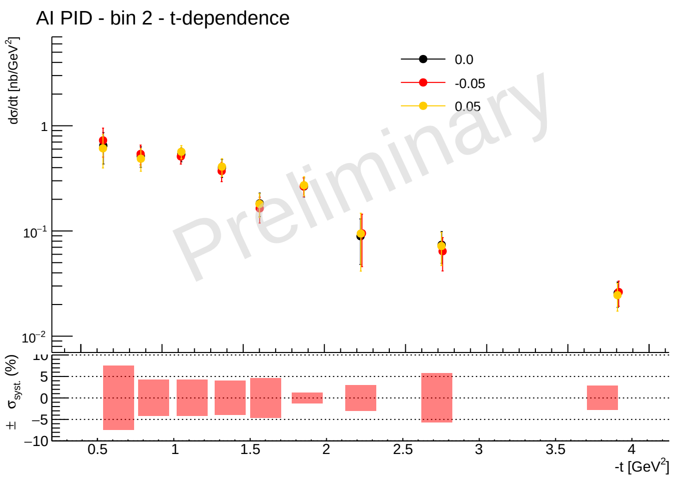

(b) Bin 2: $E_\gamma \in [9.28, 10.0]$

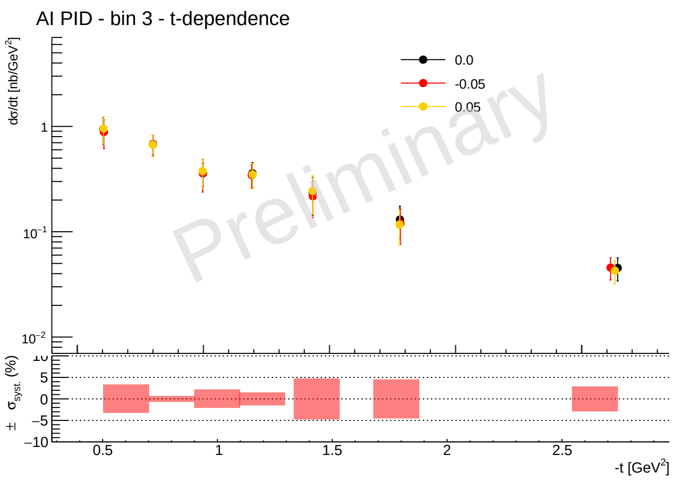

(c) Bin 3: $E_\gamma \in [10.0, 10.6]$

Figure 70: Systematic variation of the differential cross section for three cuts on the AI PID score.

7.2.5 Proton PID

The systematic variation associated with the proton PID reaches almost 20% for a single bin. For all other bins, it is always smaller than 15% (see Figure 71).

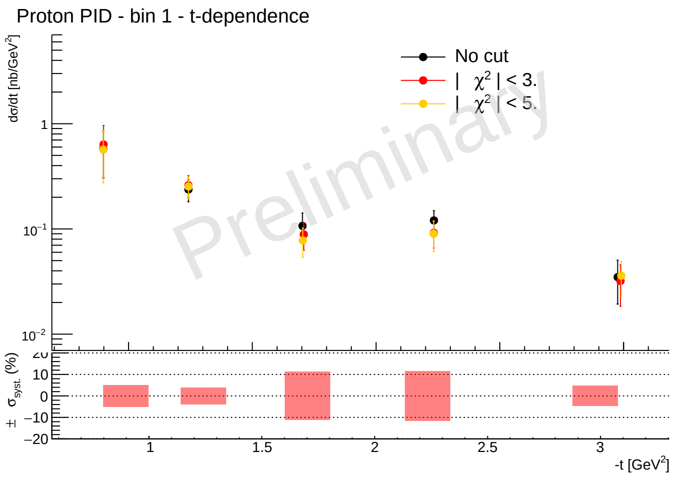

(a) Bin 1: $E_\gamma \in [8.2, 9.28]$

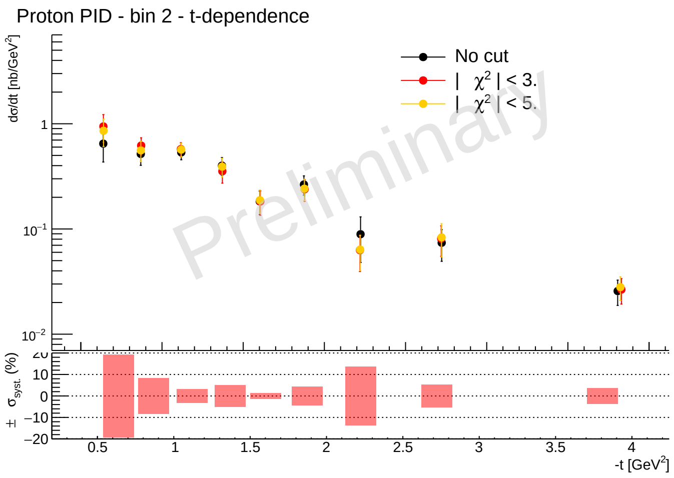

(b) Bin 2: $E_\gamma \in [9.28, 10.0]$

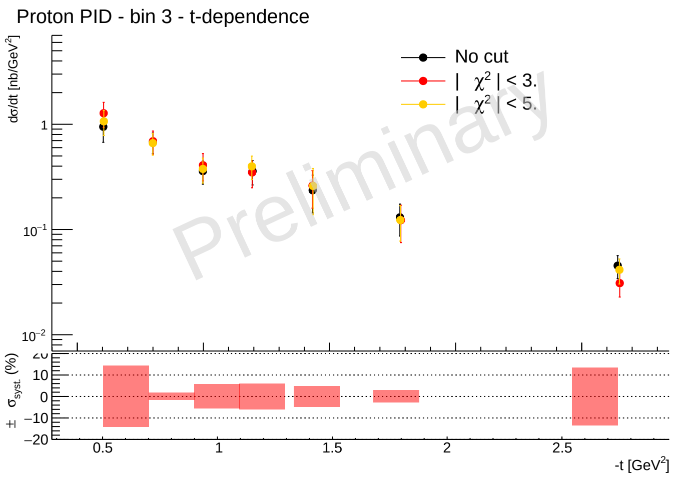

(c) Bin 3: $E_\gamma \in [10.0, 10.6]$

Figure 71: Systematic variation of the differential cross section for three cuts on the proton χ^2

7.2.6 Lepton momentum cut

The systematic variation associated with the lepton momentum cut is always below 2%, except for a single bin where it reaches almost 4% (see Figure 72).

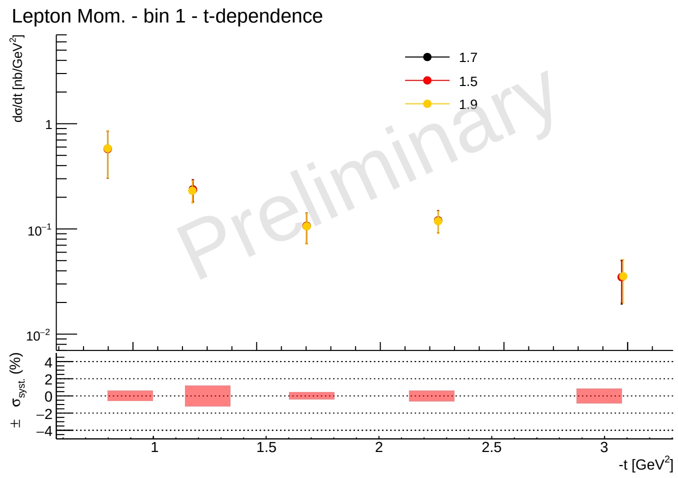

(a) Bin 1: $E_\gamma \in [8.2, 9.28]$

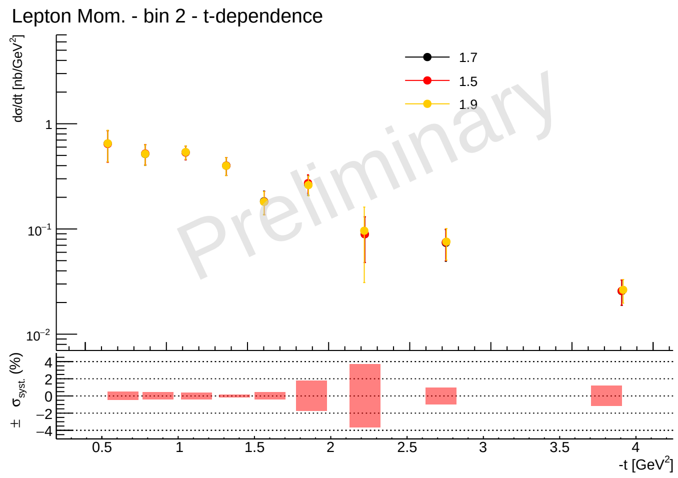

(b) Bin 2: $E_\gamma \in [9.28, 10.0]$

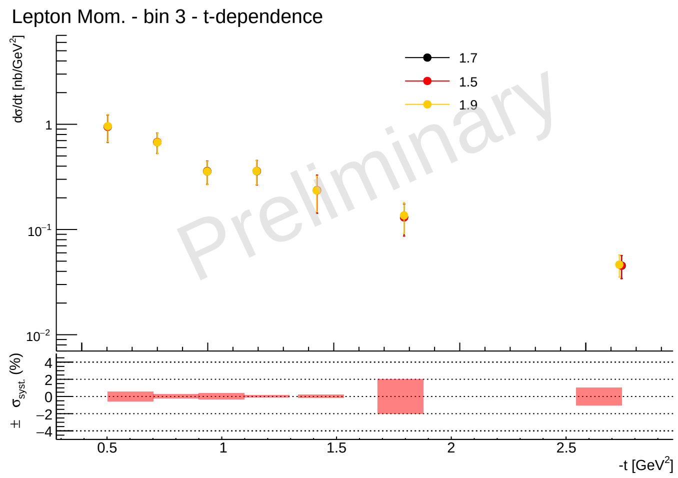

(c) Bin 3: $E_\gamma \in [10.0, 10.6]$

Figure 72: Systematic variation of the differential cross section for three values of the minimal lepton momentum.

7.2.7 Normalization factor

The systematic error associated with the normalization factor for the differential cross section is set to 16% as for the integrated cross section.

7.2.8 Accumulated charge

The systematic error discussed for the integrated case (1.2%) is also used for the differential case.

7.2.9 Radiative corrections

The double ratio between the correction obtained using the ad-hoc radiative effect and the one using Photos is computed for each energy bin of the differential analysis and added in quadrature to the total systematic calculation. Note that the radiative correction does not vary much as a function of t allowing to perform the computation decribed above.

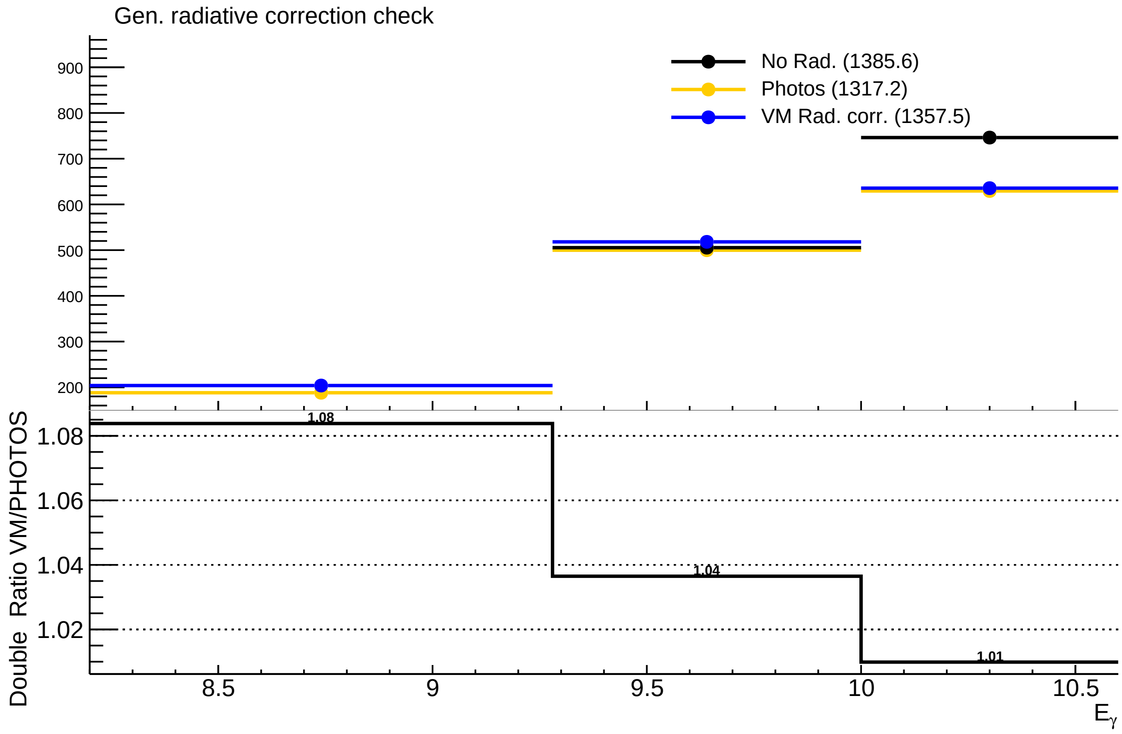

Figure 73: Generated spectra of photon energy for three J/ψ samples: one without radiative effect, and two using two different radiative effect approach, the one developed here in Appendix Q and PHOTOS [39]. The energy binning shown is the one of the differential analysis.

8 Additional checks

This section regroups additional checks. The results shown here are not used in the following of the analysis. They are displayed to answers questions that have been raised during the analysis.

8.1 Impact of radiative effect

We also tested the impact of the radiative effect on the extraction of the cross section. The effect of this correction is of the order of 10% which is of the same order of magnitude quoted by the GlueX collaboration (8%).

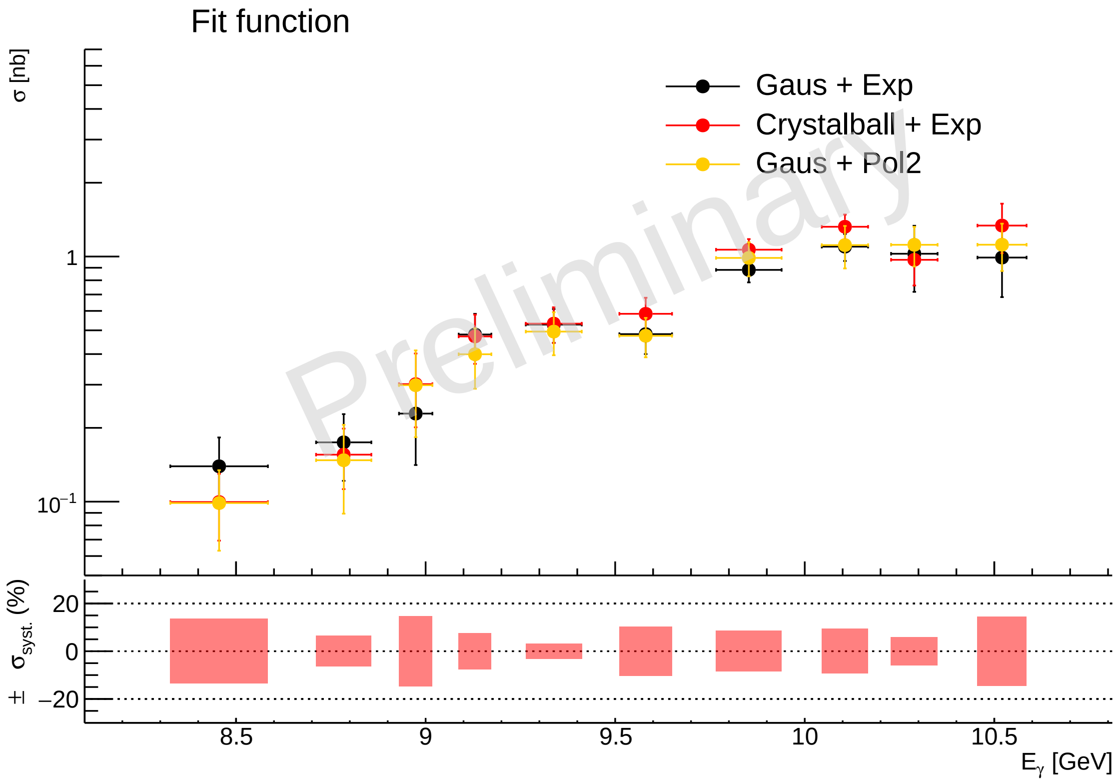

Figure 74: Study of the effect of including radiative correction on the integrated cross section.

8.2 Resolution on the initial photon energy

The observation of features in the energy dependance of the total cross section is limited by the initial photon energy resolution of CLAS12. In Figure 75, the initial photon energy difference between MC and data is fitted with a Gaussian and the standard deviation is reported as a function of energy. For the energy range accessible by CLAS12, the resolution is always at least three time as small as the bin size. Following this conclusion, bin migration between energy bins has been ignored in the analysis.

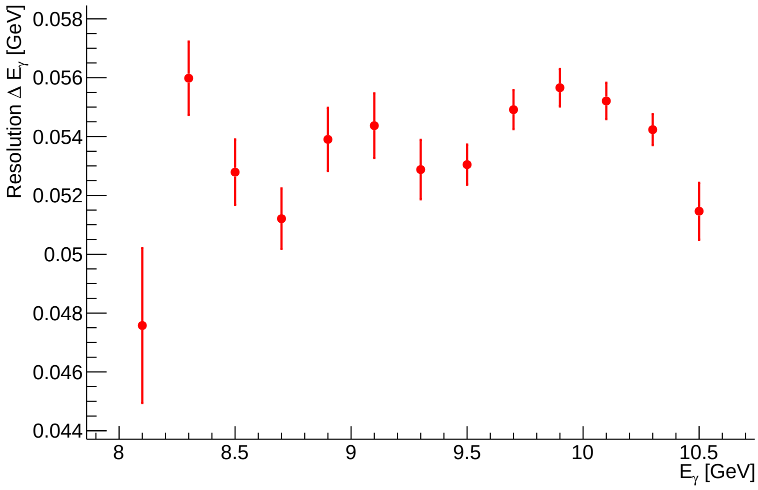

(a) Resolution of the initial photon energy for the Fall 2018 inbending configuration.

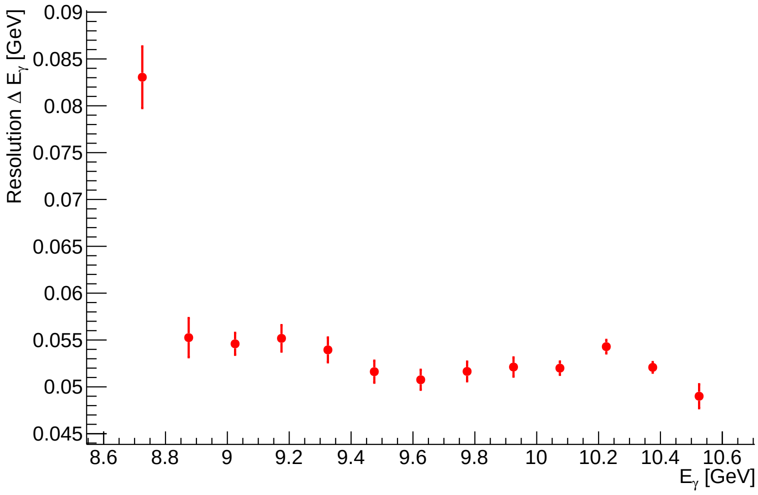

(b) Resolution of the initial photon energy for the Fall 2018 outbending configuration.

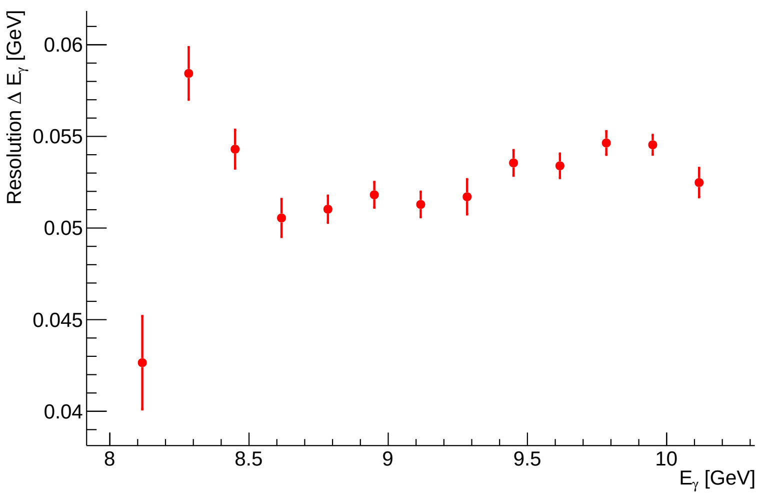

(c) Resolution of the initial photon energy for the Spring 2019 configuration.

Figure 75: Resolution of the initial photon energy for the all configuration. These resolutions are obtained from J/ψ Monte-Carlo sample, using the highest possible current for background merging.

8.3 Consistency between fitted number of J/ψ in the differential and integrated cross-sections cases

The consistency between the number of J/ψ extracted in the integrated cross-section and the differential cases has been verified. In the integrated case, we found a total number of J/ψ of 694.1$\pm$ 44.2, with a bin-by-bin breakup summarized in Table 10. In the differential case, we found a total number of J/ψ of 682.4$\pm$ 40.2, with a bin-by-bin breakup summarized in Table 11. These two numbers are consistent well within 1-sigma. Additionally, if we sum the number of J/ψ of the integrated case according to the energy binning of the differential case, we find the that the number of J/ψ are consistent:

- Integrated case bin 1+2+3+4: 92.2 $\pm$ 13.3 J/ψ , Differential case energy bin 1: 112$\pm$ 15.7 J/ψ . Note that in this case, the energy range of the differential case bin is slightly larger than the one covered by the four first bin of the integrated case,
- Integrated case bin 5+6+7: 335.8 $\pm$ 26.9 J/ψ , Differential case energy bin 2: 325$\pm$ 26.3 J/ψ ,
- Integrated case bin 8+9+10: 266.1 $\pm$ 32.5 J/ψ , Differential case energy bin 3: 245.4$\pm$ 26.0 J/ψ .

Bin nb.	1	2	3	4	5	6	7
Energy (GeV)	[8.2,8.65]	[8.65,8.9]	[8.9,9.05]	[9.05,9.2]	[9.2,9.46]	[9.46,9.7]	[9.7,10.]
Nb. J/ψ	15.5$\pm$ 4.8	18.1$\pm$ 5.5	18$\pm$ 6.9	40.6$\pm$ 8.7	83.0$\pm$ 13.1	74.3$\pm$ 12.7	178.5$\pm$ 19.7

Bin nb.	8	9	10	1+2+3+4	5+6+7	8+9+10	Total
Energy (GeV)	[10,10.2]	[10.2,10.4]	[10.4,10.6]	[8.2,9.2]	[9.2,10.]	[10.,10.6]	[8.2,10.6]
Nb. J/ψ	145.1$\pm$18.3	77.1$\pm$23.2	43.9$\pm$13.6	92.2 $\pm$13.3	335.8$\pm$26.9	266.1$\pm$32.5	694.1$\pm$44.2

Table 10: Number of fitted J/ψ per bin, in the integrated case. Each bin is reference as 'energy bin' and the integration range is also given. Sub-total and total number of events are also provided.

Bin nb.	1/1	1/2	1/3	1/4	1/5	Total energy bin 1
Energy (GeV)	[8.2, 9.28]					[8.2, 9.28]
Nb. J/ψ	6.9$\pm$ 3.3	32.7$\pm$ 7.7	24.6$\pm$ 8.0	28.7$\pm$ 6.8	19.1$\pm$ 8.1	112$\pm$ 15.7

Bin nb.	2/1	2/2	2/3	2/4	2/5	2/6	2/7
Energy (GeV)	[9.28, 10]						
Nb. J/ψ	15.5$\pm$ 5.1	53.6$\pm$ 11.8	68.1$\pm$ 10.1	58.5$\pm$ 11.4	25.9$\pm$ 6.5	36.6$\pm$ 7.6	22.9 $\pm$ 10.4

Bin nb.	2/8	2/9	Total energy bin 2
Energy (GeV)	[9.28, 10]		[9.28, 10]
Nb. J/ψ	17.3$\pm$ 5.8	26.6$\pm$ 7.2	325$\pm$ 26.3

Bin nb.	3/1	3/2	3/3	3/4	3/5
Energy (GeV)	[10, 10.6]				
Nb. J/ψ	39.2$\pm$ 11.3	47.9$\pm$ 10.6	31.7$\pm$ 8.0	32.3$\pm$ 8.4	31.1$\pm$ 12.1

Bin nb.	3/6	3/7	Total energy bin 3	Total
Energy (GeV)	[10, 10.6]		[10, 10.6]	[8.2, 10.6]
Nb. J/ψ	22.4$\pm$ 7.6	40.8$\pm$ 10	245.4$\pm$ 26	682.4$\pm$ 40.2

Table 11: Number of fitted J/ψ per bin, in the differential case. Each bin is reference as 'energy bin'/'$-t$ bin' and the integration range is also given. The total number of events is given per bin and overall.

8.4 Consistency between measured differential and integrated cross-sections

A consistency check is also performed on the cross-section measurement itself. For this check, we use the dipole and exponential model fitted on data which are respectively presented in sections 9.3.1 and 9.3.2. For each model, and for each energy bin of the differential computation, we use the fitted parameters and computed the integrated cross-section. Figure 76 shows the measured total integrated cross-section compared to the uncertainty bands of the model integrals for each of the three bin of the differential analysis. One can verify that, for each model, the integrated data are compatible with the integrated differential cross-sections.

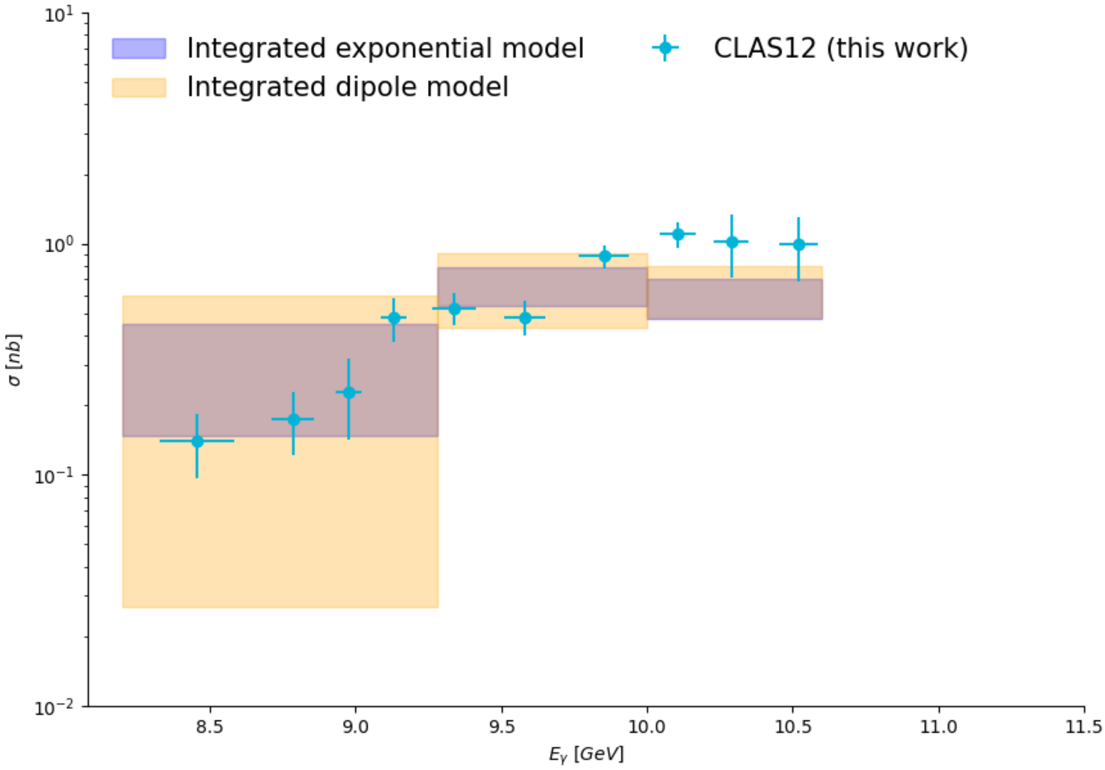

Figure 76: Integrated differential cross section compared with the measured total cross section obtained from the integration of dipole and exponential models fitted on the measured differential cross-section.

9 Physical interpretation of the measured cross-sections

In this section, the comparisons of our results with theoretical model prediction and with existing data are presented. We also attempted to extract mass radii as well as the impact of our data on the extraction of gluonic GFFs.

9.1 Comparison with previous measurements and with model predictions

9.2 Interpretation of the integrated cross-section

The measured integrated cross-section is compared with the one measured by GlueX in Figure 77. We also compare our results to two model predictions, one using a GPD-based model in [6] and one using an holographic QCD model. Our results are in good agreement with the GlueX measurements. We cannot make any quantitative conclusion on a potential dip of the cross-section in the $D - \Lambda_C$ threshold region around 9 GeV.

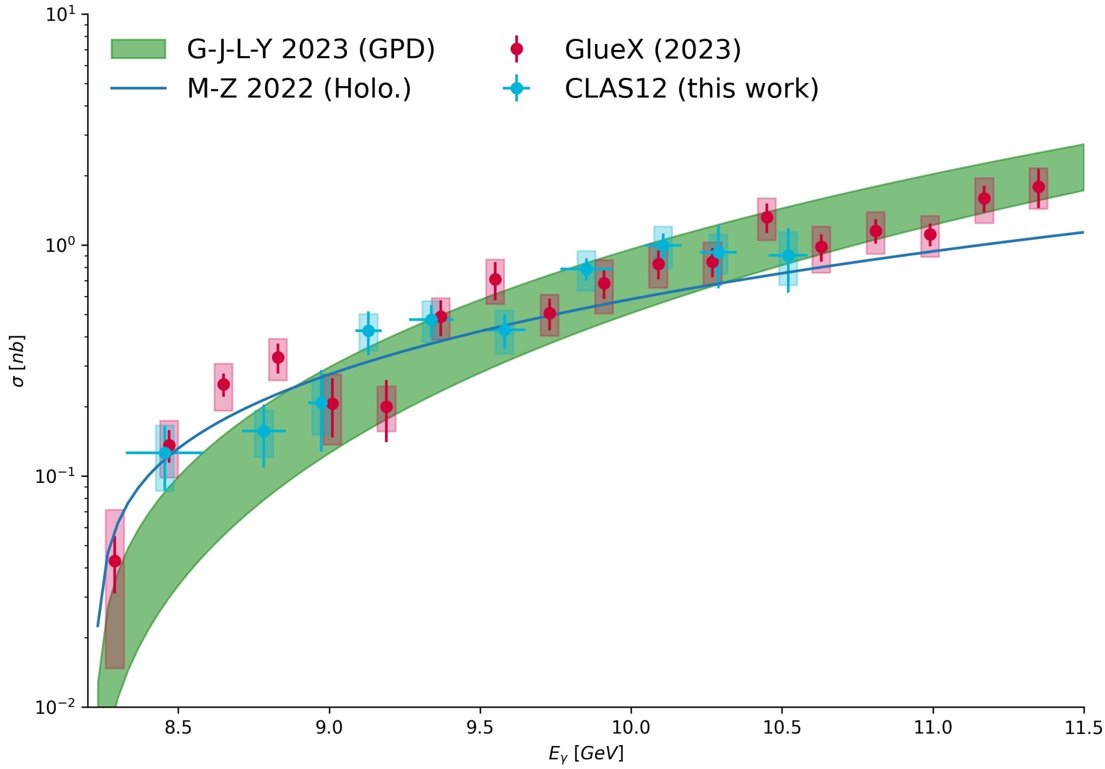

Figure 77: Comparison of the integrated cross-section measured in this work, with the results of the GlueX experiment. Two model predictions (the GPD model from [6] and and holographic model from [5]) are also shown.

9.3 Interpretation of the differential cross-section

Before comparing the measured cross-section, a comparison of the covered phase-sace is presented in Figure 78, where the average photon energy and t is shown for these results, the GlueX and Hall C results. One can see that the results of this analysis cover a very similar phase sace as the one of Hall C. However these results do not reach very large t like the GlueX ones.

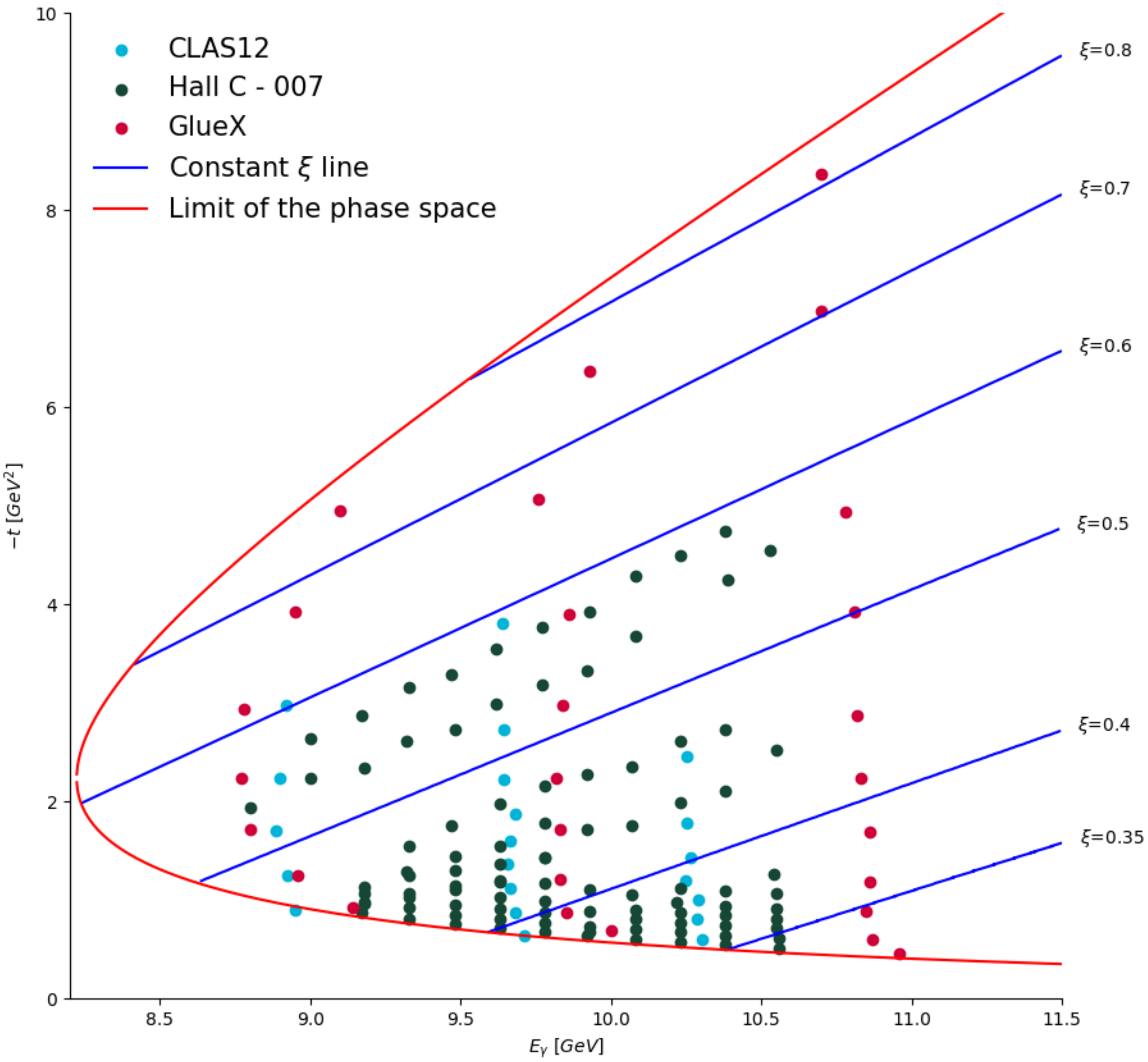

Figure 78: Phase space diagram (t versus photon energy) of the near threshold photo-production of J/ψ . The points computed in this analysis are displayed in light blue. The existing GlueX and Hall C results are shown in red and green respectively. The accessible phase space is located inside the red line. The blue lines represents constant line of ξ, which is the gluon momentum imbalance in the GPD model.

In Figure 79, all the available differential data in the threshold region are shown. The energy binning from the Nature paper [19] is used. One can see that our measurement agrees qualitatively with the previous GlueX and Hall C measurements. In Figure 79, four models from [19, 6, 5] are compared to these data.

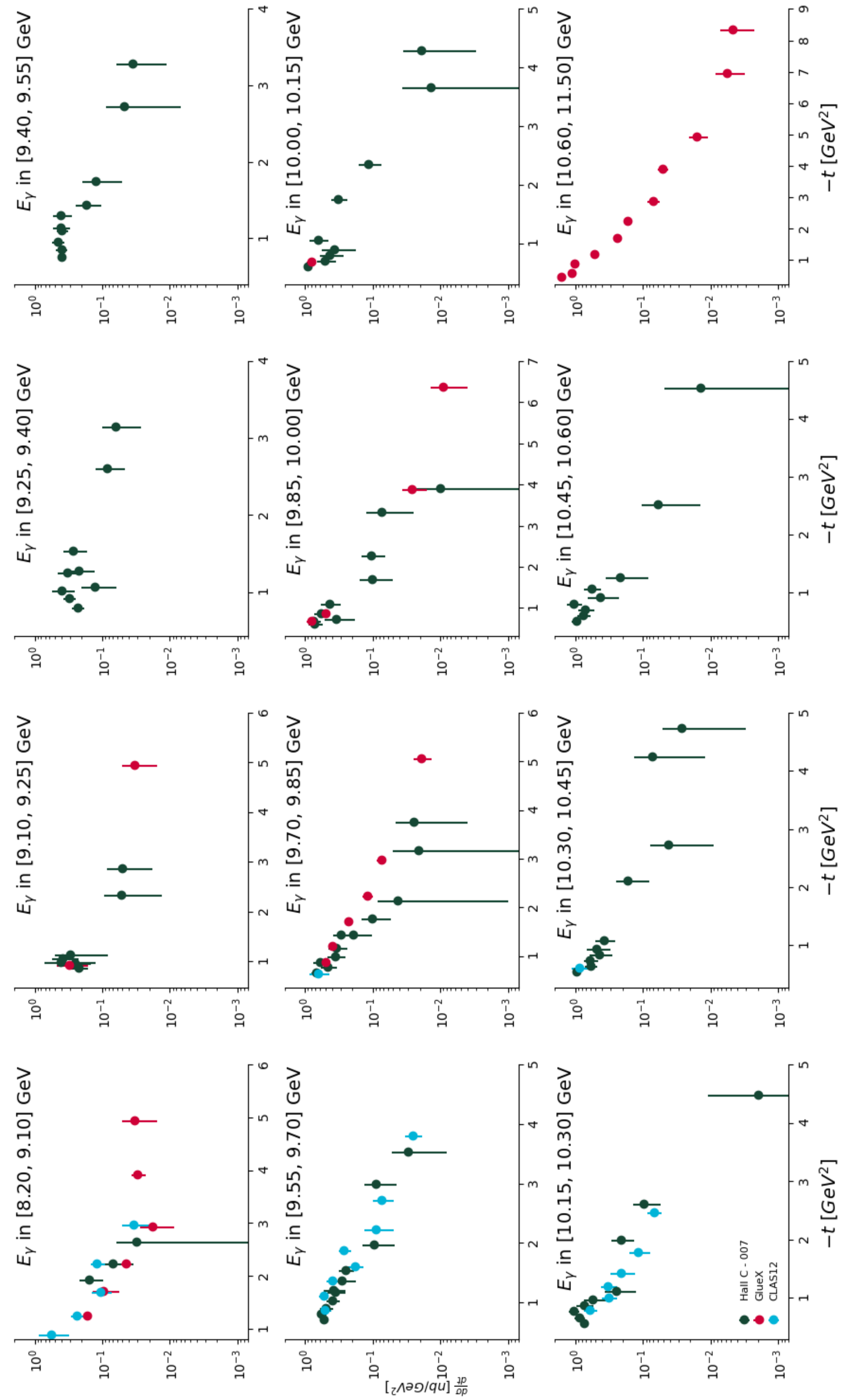

Figure 79: Comparison of all the available differential cross section data. The CLAS12 data are in light blue, the GlueX data are in red, and the Hall C data are in green.

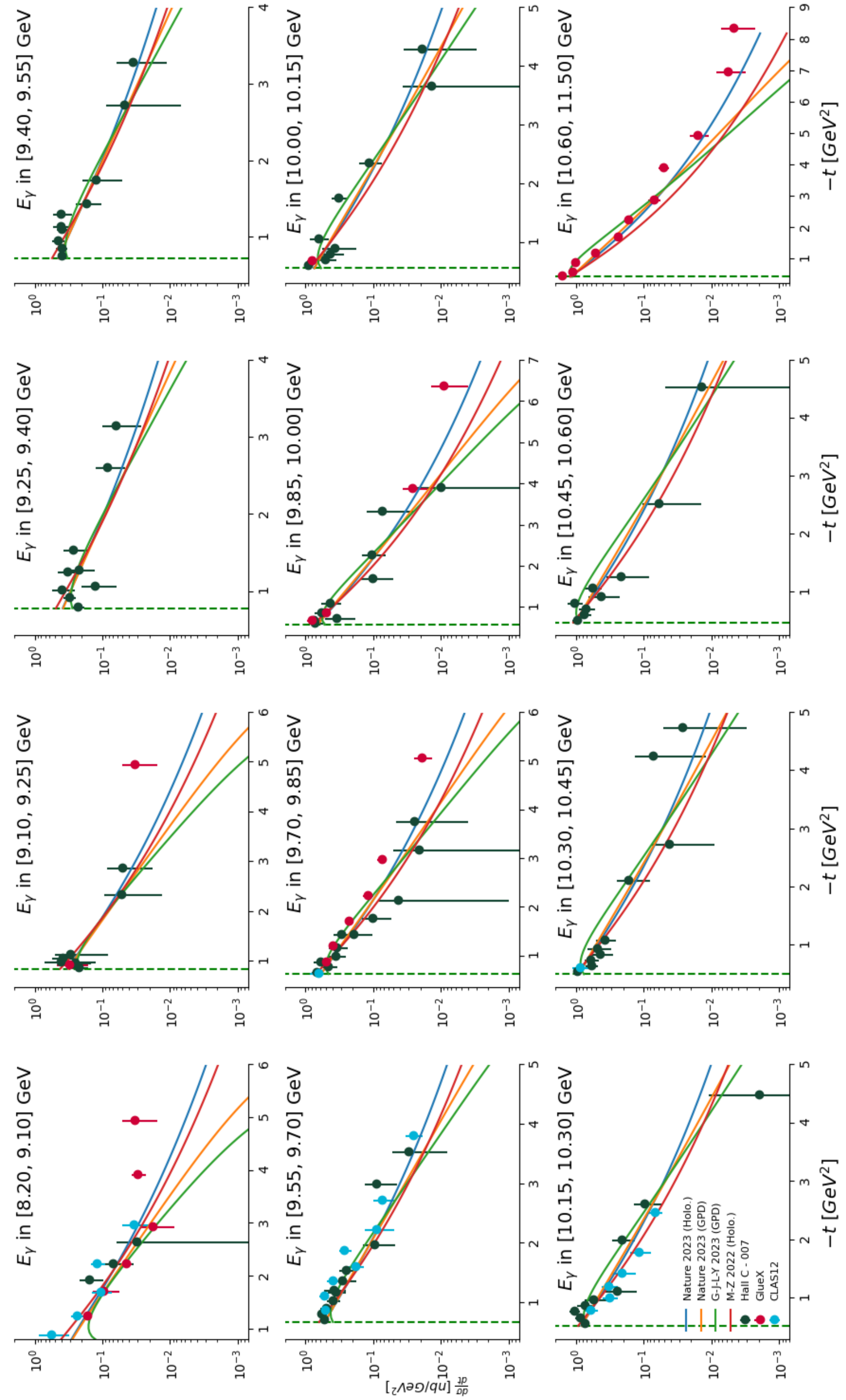

Figure 80: Comparison of all the available differential cross section data. The CLAS12 data are in light blue, the GlueX data are in red, and the Hall C data are in green. Four model predictions are also displayed: the GPD model and the holographic model of the Hall C paper [19] (Note that we use the uncorrected model from [3] for the GPD prediction), and the models from [6] (GPD-based) and [5] (holographic).

9.3.1 Dipole fit and interpretation in terms of mass radius

Following the work in [1], the t-dependant cross section is fitted with a dipole function:

$$\frac{d\sigma}{dt} = \left.\frac{d\sigma}{dt}\right|_0 \cdot \frac{1}{(1 - t/m_S^2)^4} \tag{55}$$

where the m_S parameter can be related to the mass radius of the proton as:

$$\sqrt{\langle r_m^2 \rangle} = \frac{\sqrt{12}}{m_S}. \tag{56}$$

Figure 81 displays the dipole fits of the CLAS12 data in energy bins. Figure 82 shows the mass radius extracted in this analysis compared to the one extracted by the E12-16-007 experiment in Hall C [19] and by the GlueX collaboration [18]. One can see that our data are compatible with the previous extracted radius using Hall C and Hall D data. Close to threshold, the model is expected to be more reliable and only Hall D data were available previous to this work. Our data is compatible in this bin with the fit of GlueX data, and point toward a mass radius of the order of half a fermi, smaller than the charge radius of the proton.

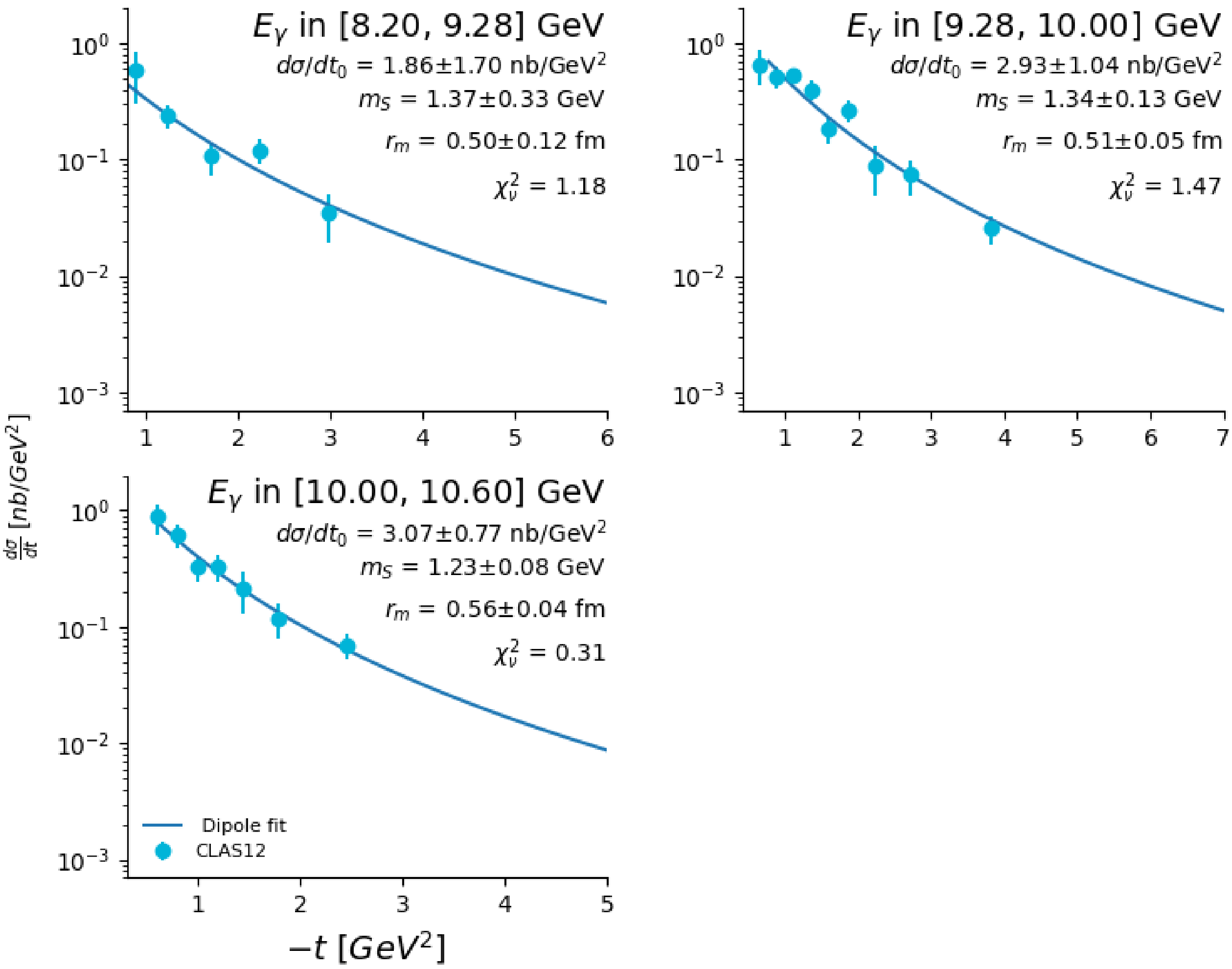

Figure 81: Dipole fits of the CLAS12 differential cross-section.

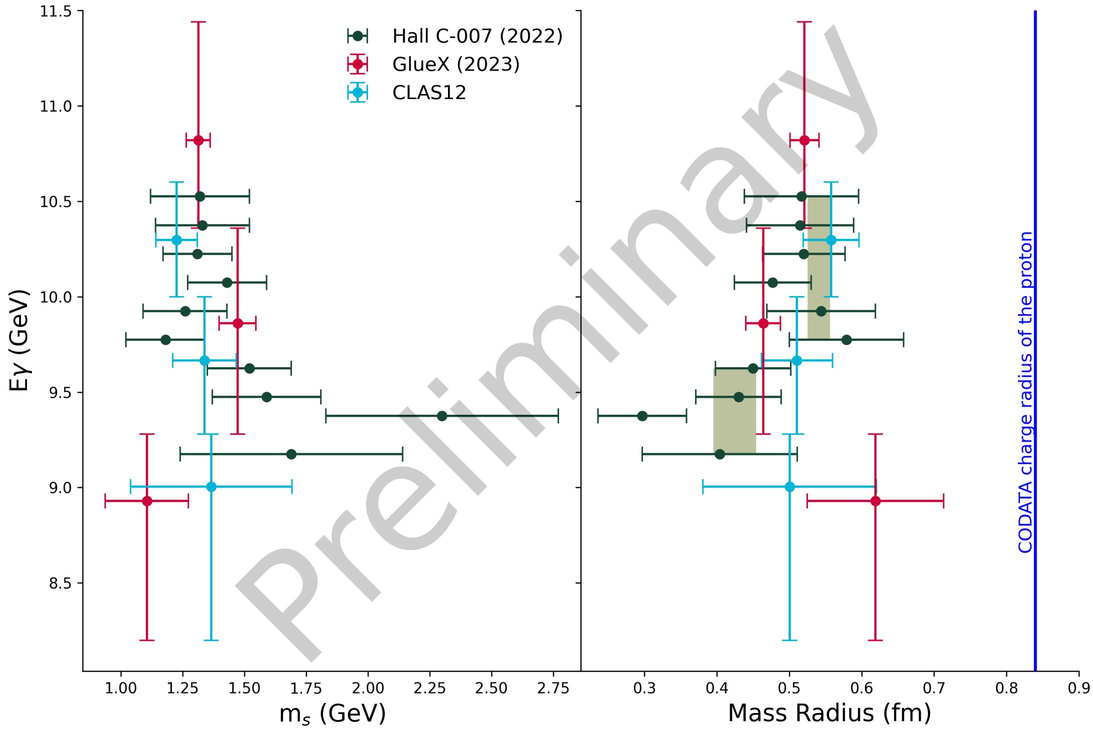

Figure 82: Mass radius of the proton extracted by three experiments: Hall C (E12-16-007), GlueX and CLAS12, as a function of the incoming photon energy. In the case of the Hall C results, the average value of the radius in two energy bins is shown, as reported in [19].

9.3.2 Exponential fit and comparison with HERA results

The J/ψ photoproduction measurements of HERA [15, 16] have been interpreted in terms of gluonic transverse radius (see [40] for exemple). This is done by fitting the differential cross-section with an exponentially decaying function. For a one-to-one comparison with these results, a exponential function is fitted to the CLAS12 data:

$$\frac{d\sigma}{dt} = \left.\frac{d\sigma}{dt}\right|_0 \cdot e^{-B_G \cdot |t|}. \tag{57}$$

Figure 83 shows the fits which have been obtained. The extracted slopes are then compared to the one obtained by HERA in Figure 84, as a function of the center of mass energy W. The slopes derived in this work are smaller than the one extracted by HERA. This can be understood as a shrinking of the size of the proton with diminishing c-o-m energy.

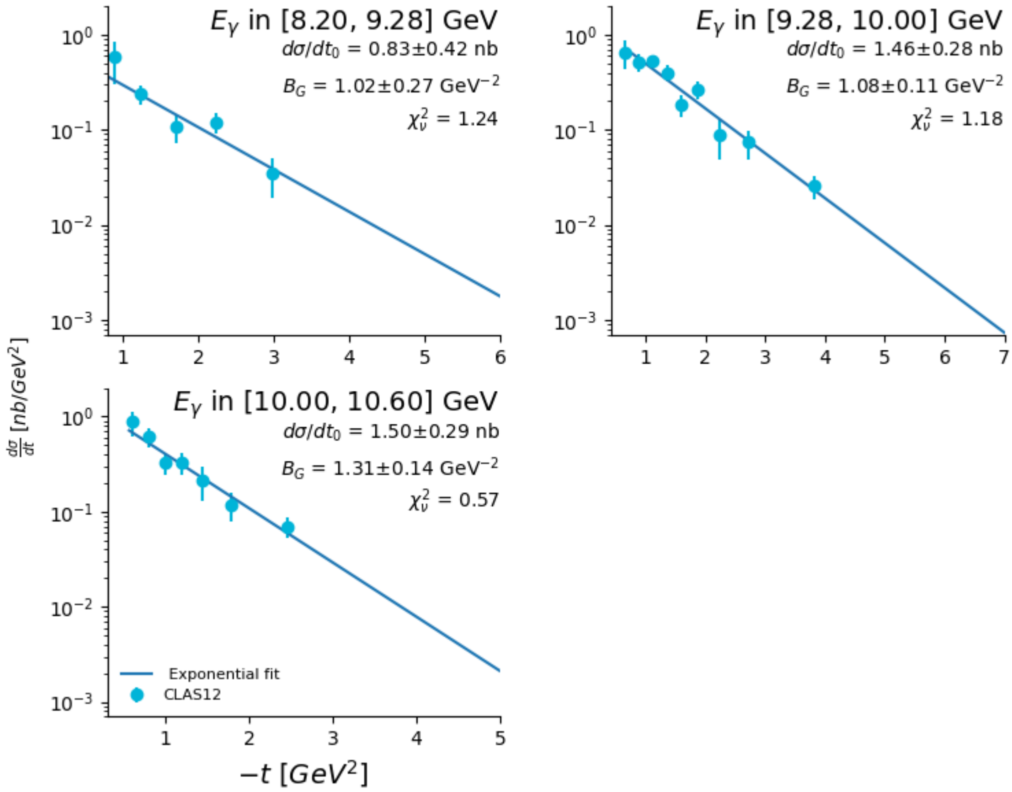

Figure 83: Exponential fits of the CLAS12 differential cross-section.

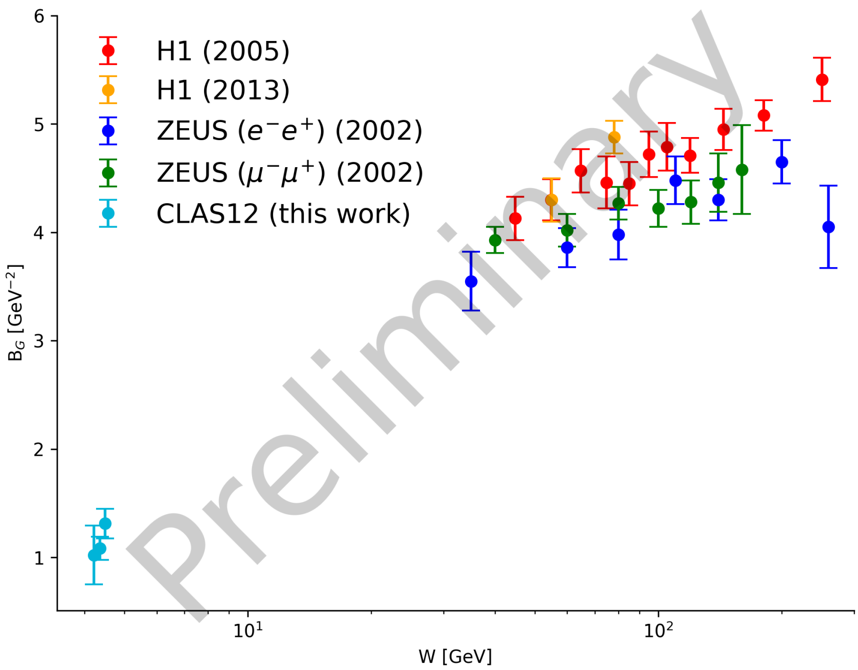

Figure 84: Exponential slopes extracted from the t dependence of the cross-section of the photoproduction of J/ψ at HERA and for CLAS12.

To make the previous statement more striking, the slope is displayed as a function of x_B in Figure

85, where

$$x_B = \frac{M_{J/\psi}^2}{W^2 - m_p^2}. \tag{58}$$

The slope can also be converted in a gluonic transverse radius as:

$$r_g = \sqrt{2B_G}. \tag{59}$$

Figure 85 shows that the extracted gluonic radius from CLAS12 using this approach is of the order of 0.3 fm and smaller than the one obtained for small x_B.

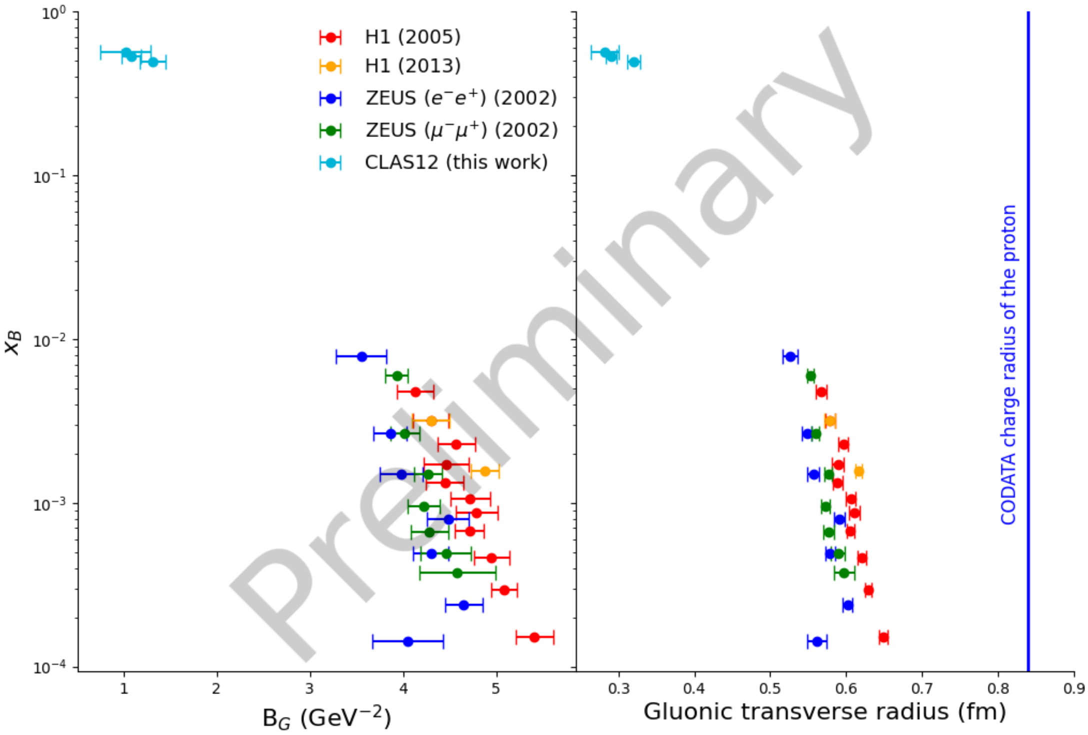

Figure 85: Exponential slope of the t-dependent cross-section of the photoproduction of J/ψ as a function of x_B (left). The corresponding gluonic transverse radius is also shown as a function of x_B (right).

9.3.3 GFFs extraction using the GPD and Holographic models, and interpretation in terms of mass and scalar radius

Using the cross-section models presented in section 1.2, a fit to the data is done with the aim to extract the A_g and C_g GFFs. These is done under the assumptions which are presented in section 1.2. Especially, it is assumed that Vector Meson Dominance is fulfilled and that these models are applicable. In more details, the B_g and $\bar{C}_g$ GFFs are ignored and we used a tripole function for the A_g and C_g GFFs. The fits have three free parameters: m_A, $C(0)$ and m_C. In the case of the GPD-model, the approach followed in [6] consisting in applying a cut of $\xi < 0.4$ is also applied to this analysis.

Four fits are done, two per models, respectively combining Hall B and D data and Hall B,D, and C data. In the cases where we use only the Hall B data, the m_C parameter is fixed to allow the fit to converge. In the case of the GPD model, we fix $m_C = 0.91 \pm 0.10$ GeV following the results reported in [6]. For the holographic model fitted on Hall B data only, we use $m_C = 1.12 \pm 0.21$ GeV as reported in [19]. Figure 86 shows the fits which have been performed in this analysis.

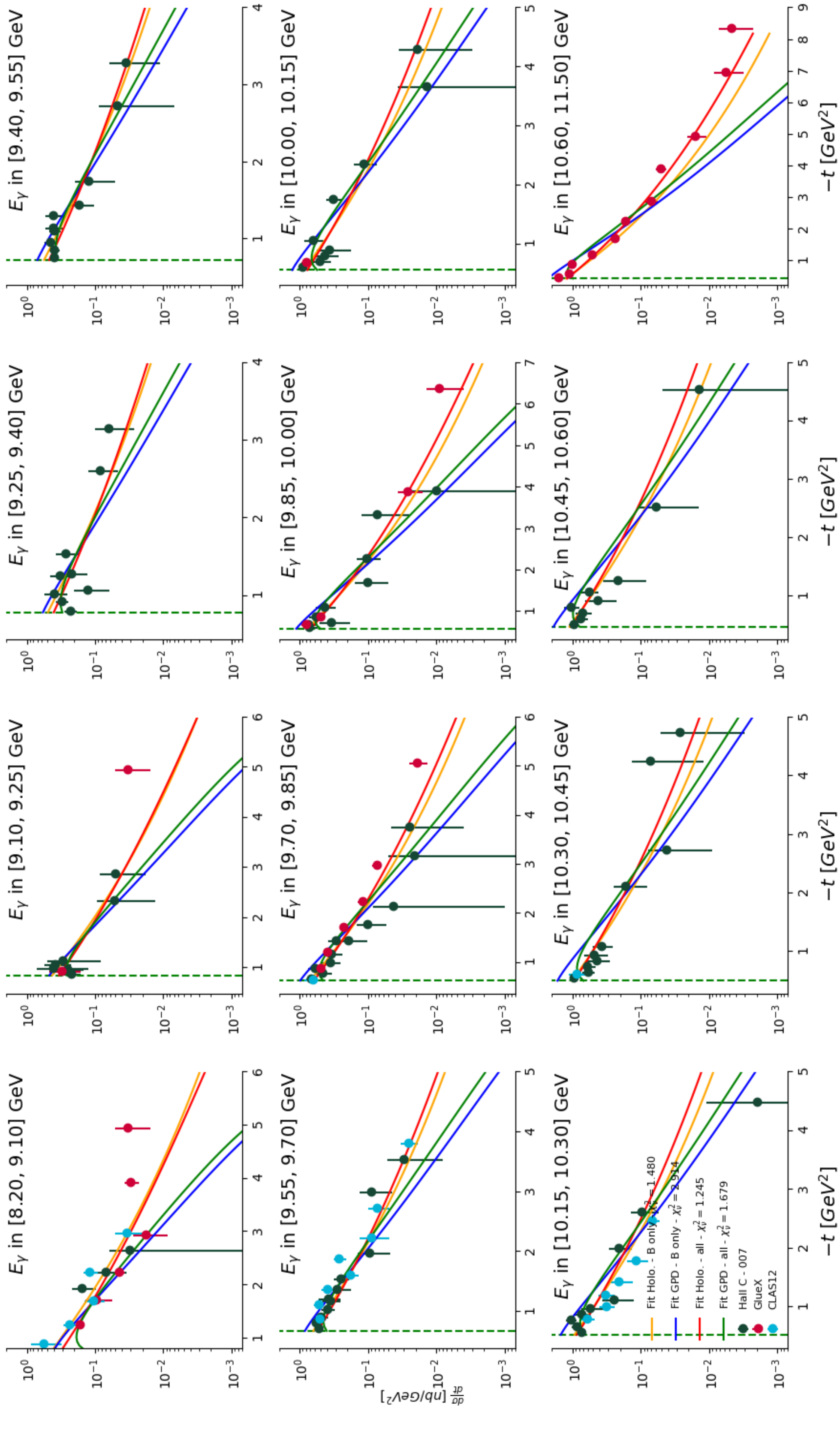

Figure 86: The four fits to the data which have been performed in this analysis. We used both the GPD and holographic models, combining data from Hall B and D, and Hall B,D and C.

In Table 12 summarizes the fitted parameters from this analysis for the different models and datasets. The correlations between the parameters, which appear in the computations of the error bars later reported, are reported in Table 13.

Model / Dataset	χ^2_ν	$A(0)$	m_A [GeV]	$C(0)$	m_C [GeV]
GPD / Hall B	2,914	0.414±0.008*	1.872±0.110	-0.587±0.309	0.91±0.10*
GPD / All data	1.68	0.414±0.008*	2.014±0.060	-1.707±1.025	0.794±0.148
Holographic / Hall B	1.480	0.414±0.008*	1.722±0.0590	-0.288±0.136	1.12±0.21*
Holographic / All data	1.245	0.414±0.008*	1.971±0.051	-0.294±0.020	1.744±0.135

Table 12: Summary of the fit parameters for the GFFs extraction of this analysis. Fixed parameters are identified with a *.

Model / Dataset	$\rho(m_A, C(0))$	$\rho(m_C, C(0))$
GPD / Hall B	-0.893	-
GPD / All data	0.8270	0.9950
Holographic / Hall B	-0.891	-
Holographic / All data	0.05027	0.5065

Table 13: Summary of the fit parameters correlations entering in the computations of the error bars of the GFFs, pressure profiles and radii shown in the following

Finally, from these fitted, the GFFs can be plotted as a function of t. Similarly, One can use the fitted parameters to plot the pressure and shear force profiles defined in Equations 16 and 17. This is done for the GPD model in Figure 87 and for the holographic model in Figure 88. The results obtained using the Hall C data only in [19, 25] are also superimposed to our results. While, fixing m_C was needed for the fit one the Hall B data only to converge, we find GFFs which are in agreement with what has been extracted in [19, 25]. In the case of the holographic model, the C_g form factor does vary significantly with the inclusion of the data from GlueX. This effect could be done by the larger t coverage of this experiment.

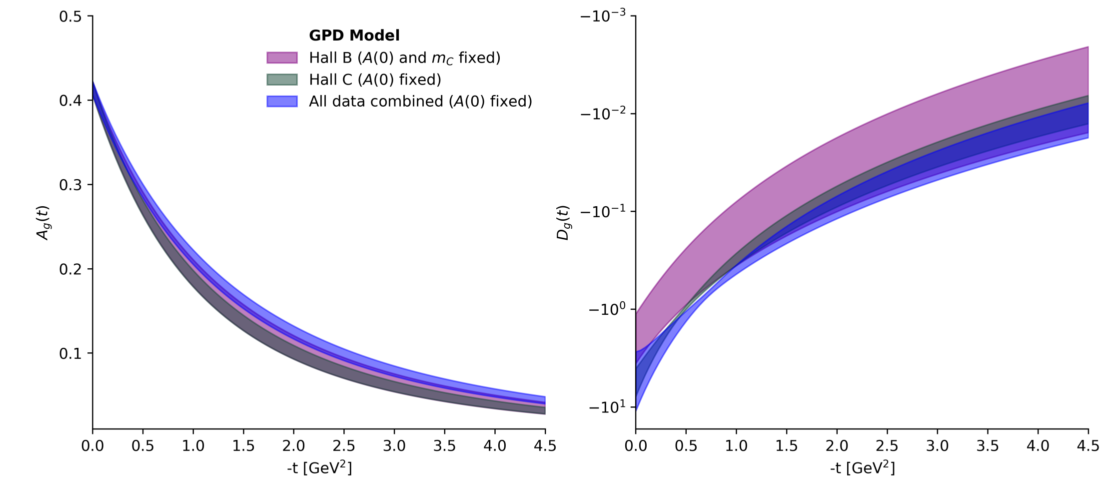

(a) Gravitational Form Factors, derived using the GPD model.

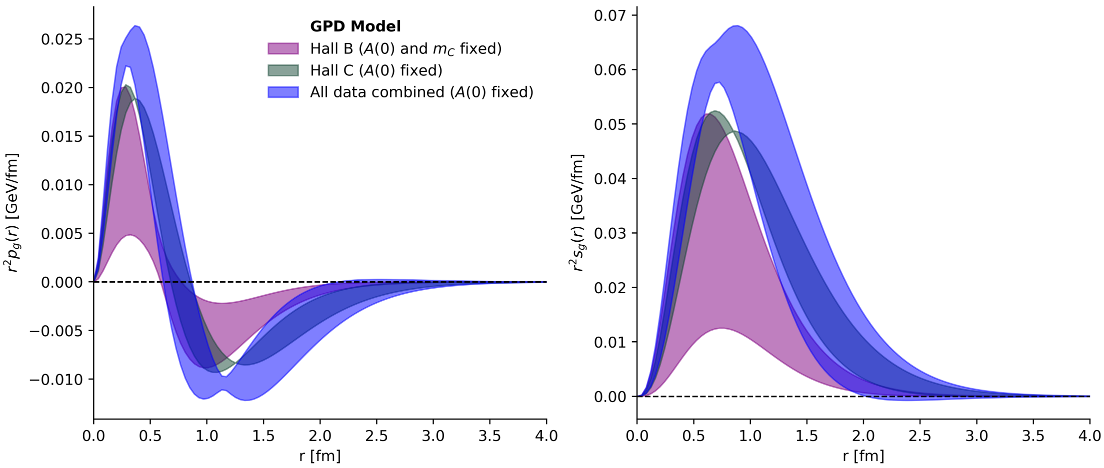

(b) Transverse and shear pressure profile, derived using the GPD model.

Figure 87: Gravitational Form Factors and pressure profiles from the GPD model. The gray band shows the results from [19, 25], where we assumed $\rho(m_C, C(0)) = 1.0$ to reproduced the error band reported in this paper. The results using only the Hall B data are shown in purple, and our extraction using all available data is shown in blue.

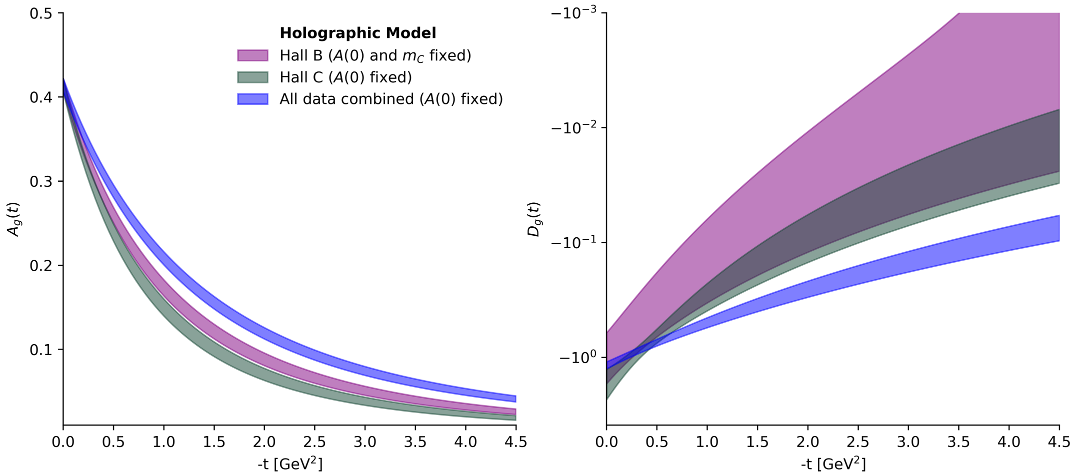

(a) Gravitational Form Factors, derived using the holographic model.

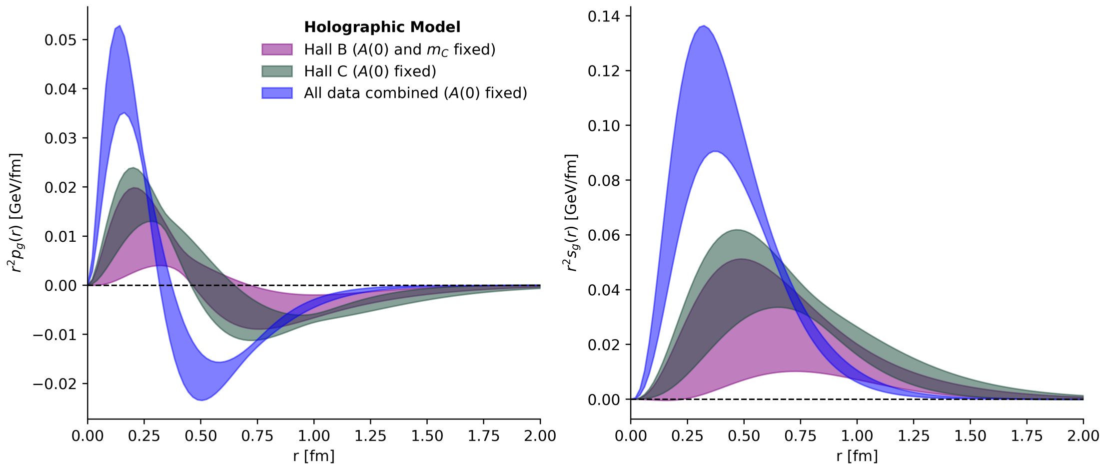

(b) Transverse and shear pressure profile, derived using the holographic model.

Figure 88: Gravitational Form Factors and pressure profiles from the holographic model. The gray band shows the results from [19, 25], where we assumed $\rho(m_C, C(0)) = 0.9$ to reproduced the error band reported in this paper. The results using only the Hall B data are shown in purple, and our extraction using all available data is shown in blue.

Finally, the mass and scalar radii defined in 18 and 19 have been extracted. Figure 89 shows the extracted radii, which are also reported in Table 14. The radius found using Hall B data only and fixing m_c are compatible with what was extracted in [19, 25]. The agreement is quantitatively less good for the GPD model, but these results shoudl be taken with care as the χ^2_ν for this fit is fairly large. When including all available data in the fit, we find compatible radii for the GPD model with large error bars. These error bars arise from the large error on the value of $C(0)$ for this fit. For the holographic model, the error bars are greatly reduced in the case where all data are included.

Model / Dataset	$\sqrt{< r_m^2 >_g}$ [fm]	$\sqrt{< r_s^2 >_g}$ [fm]
GPD / Hall B	0.759±0.115	1.153±0.248
GPD / All data	1.126±0.297	1.859±0.533
Holographic / Hall B	0.649±0.055	0.889±0.138
Holographic / All data	0.607±0.019	0.863±0.029

Table 14: Extracted mass and scalar radii from Hall B data alone and combining all available data.

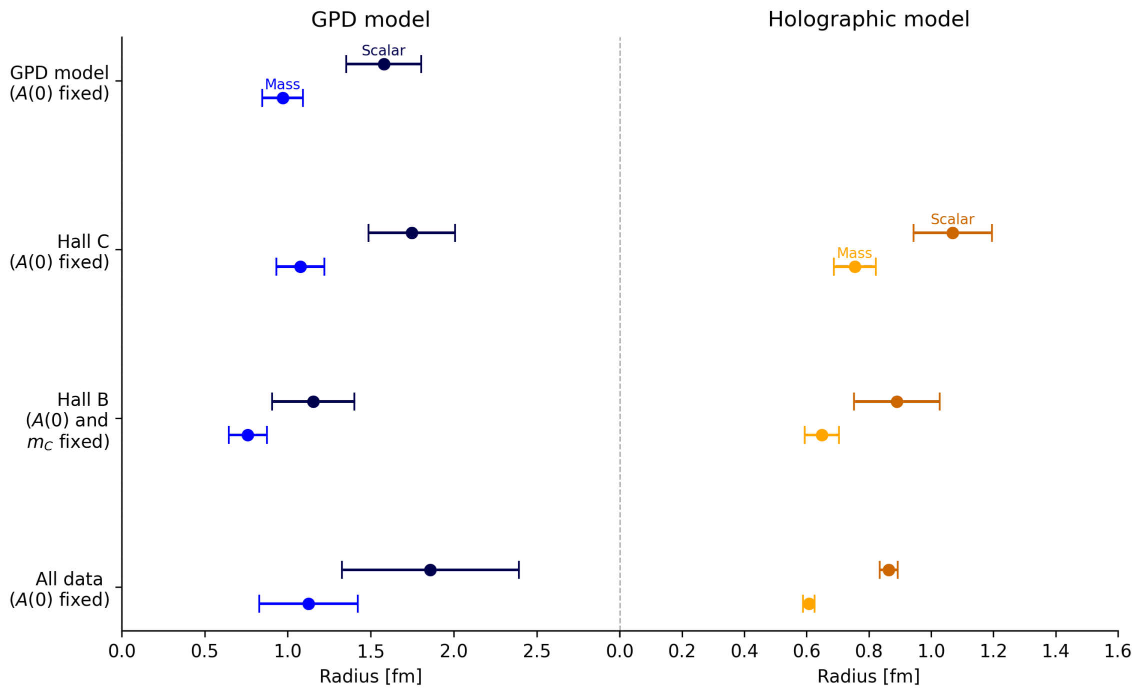

Figure 89: Mass and scalar radii defined in Equations 18 and 19. The radii extracted in [6] and [19, 25] are shown in the first and second line respectively. We extracted these radii using Hall D and B data combined, as well as the whole available dataset.

End of the core analysis

References

[1] D. Kharzeev, H. Satz, A. Syamtomov, and G. Zinovjev. J/ψ-photoproduction and the gluon structure of the nucleon. *Nuclear Physics A*, 661(1):568–572, 1999.

[2] Yoshitaka Hatta, Abha Rajan, and Di-Lun Yang. Near threshold j/ψ and Υ photoproduction at jlab and rhic. *Phys. Rev. D*, 100:014032, Jul 2019.

[3] Yuxun Guo, Xiangdong Ji, and Yizhuang Liu. Qcd analysis of near-threshold photon-proton production of heavy quarkonium. *Phys. Rev. D*, 103:096010, May 2021.

[4] Dmitri E. Kharzeev. Mass radius of the proton. *Phys. Rev. D*, 104:054015, Sep 2021.

[5] Kiminad A. Mamo and Ismail Zahed. J/ψ near threshold in holographic QCD: A and D gravitational form factors. *Phys. Rev. D*, 106(8):086004, 2022.

[6] Yuxun Guo, Xiangdong Ji, Yizhuang Liu, and Jinghong Yang. Updated analysis of near-threshold heavy quarkonium production for probe of proton's gluonic gravitational form factors. *Phys. Rev. D*, 108(3):034003, 2023.

[7] I. Yu. Kobzarev and L. B. Okun. GRAVITATIONAL INTERACTION OF FERMIONS. *Zh. Eksp. Teor. Fiz.*, 43:1904–1909, 1962.

[8] Heinz Pagels. Energy-Momentum Structure Form Factors of Particles. *Phys. Rev.*, 144:1250–1260, 1966.

[9] P. E. Shanahan and W. Detmold. Gluon gravitational form factors of the nucleon and the pion from lattice QCD. *Phys. Rev. D*, 99(1):014511, 2019.

[10] Dimitra A. Pefkou, Daniel C. Hackett, and Phiala E. Shanahan. Gluon gravitational structure of hadrons of different spin. *Phys. Rev. D*, 105(5):054509, 2022.

[11] Daniel C. Hackett, Dimitra A. Pefkou, and Phiala E. Shanahan. Gravitational Form Factors of the Proton from Lattice QCD. *Phys. Rev. Lett.*, 132(25):251904, 2024.

[12] Maxim V. Polyakov and Peter Schweitzer. Forces inside hadrons: pressure, surface tension, mechanical radius, and all that. *Int. J. Mod. Phys. A*, 33(26):1830025, 2018.

[13] Cédric Lorcé, Andreas Metz, Barbara Pasquini, and Simone Rodini. Energy-momentum tensor in QCD: nucleon mass decomposition and mechanical equilibrium. *JHEP*, 11:121, 2021.

[14] V. D. Burkert, L. Elouadrhiri, F. X. Girod, C. Lorcé, P. Schweitzer, and P. E. Shanahan. Colloquium: Gravitational form factors of the proton. *Rev. Mod. Phys.*, 95(4):041002, 2023.

[15] S. Chekanov et al. Exclusive photoproduction of J / psi mesons at HERA. *Eur. Phys. J.*, C24:345–360, 2002.

[16] C. Alexa et al. Elastic and Proton-Dissociative Photoproduction of J/psi Mesons at HERA. *Eur. Phys. J. C*, 73(6):2466, 2013.

[17] P. A. Adderley et al. The Continuous Electron Beam Accelerator Facility at 12 GeV. *Phys. Rev. Accel. Beams*, 27(8):084802, 2024.

[18] S. Adhikari et al. Measurement of the j/ψ photoproduction cross section over the full near-threshold kinematic region. *Phys. Rev. C*, 108:025201, Aug 2023.

[19] B. Duran, Z.-E. Meziani, S. Joosten, et al. Determining the gluonic gravitational form factors of the proton. *Nature*, 615(7954):813–816, Mar 2023.

[20] Kazuhiro Tanaka. Three-loop formula for quark and gluon contributions to the QCD trace anomaly. *JHEP*, 01:120, 2019.

[21] Kazuhiro Tanaka. Twist-four gravitational form factor at NNLO QCD from trace anomaly constraints. *JHEP*, 03:013, 2023.

[22] Kiminad A. Mamo and Ismail Zahed. Electroproduction of heavy vector mesons using holographic qcd: From near threshold to high energy regimes. *Phys. Rev. D*, 104:066023, Sep 2021.

[23] Kiminad A. Mamo and Ismail Zahed. Diffractive photoproduction of j/ψ and Υ using holographic qcd: Gravitational form factors and gpd of gluons in the proton. *Phys. Rev. D*, 101:086003, Apr 2020.

[24] Kiminad A. Mamo and Ismail Zahed. Nucleon mass radii and distribution: Holographic qcd, lattice qcd, and gluex data. *Phys. Rev. D*, 103:094010, May 2021.

[25] Zein-Eddine Meziani. Gluonic gravitational form factors of the proton, 2024.

[26] Meng-Lin Du, Vadim Baru, Feng-Kun Guo, Christoph Hanhart, Ulf-G Meißner, Alexey Nefediev, and Igor Strakovsky. Deciphering the mechanism of near-threshold J/ψ photoproduction. *Eur. Phys. J. C*, 80(11):1053, 2020.

[27] D. Winney, C. Fernández-Ramírez, A. Pilloni, A. N. Hiller Blin, M. Albaladejo, Ł. Bibrzycki, N. Hammoud, J. Liao, V. Mathieu, G. Montaña, R. J. Perry, V. Shastry, W. A. Smith, and A. P. Szczepaniak. Dynamics in near-threshold j/ψ photoproduction. *Phys. Rev. D*, 108:054018, Sep 2023.

[28] Michael I. Eides, Victor Yu. Petrov, and Maxim V. Polyakov. Narrow nucleon-$\psi(2S)$ bound state and LHCb pentaquarks. *Phys. Rev.*, D93(5):054039, 2016.

[29] V. Kubarovsky and M. B. Voloshin. Formation of hidden-charm pentaquarks in photon-nucleon collisions. *Phys. Rev.*, D92(3):031502, 2015.

[30] Feng-Kun Guo, Ulf-G. Meißner, Wei Wang, and Zhi Yang. How to reveal the exotic nature of the $P_c(4450)$. *Phys. Rev.*, D92(7):071502, 2015.

[31] A. N. Hiller Blin, C. Fernández-Ramírez, A. Jackura, V. Mathieu, V. I. Mokeev, A. Pilloni, and A. P. Szczepaniak. Studying the $P_c(4450)$ resonance in $J\psi$ photoproduction off protons. *Phys. Rev.*, D94(3):034002, 2016.

[32] Igor Strakovsky, William J. Briscoe, Eugene Chudakov, Ilya Larin, Lubomir Pentchev, Axel Schmidt, and Ronald L. Workman. Plausibility of the LHCb Pc in the GlueX total cross sections. *Phys. Rev. C*, 108(1):015202, 2023.

[33] Tetsuo Abe. Grape-dilepton (version 1.1): A generator for dilepton production in ep collisions. *Computer Physics Communications*, 136(1):126–147, 2001.

[34] M. Ungaro et al. The clas12 geant4 simulation. *Nuclear Instruments and Methods in Physics Research Section A: Accelerators, Spectrometers, Detectors and Associated Equipment*, 959:163422, 2020.

[35] S. Agostinelli et al. Geant4—a simulation toolkit. *Nuclear Instruments and Methods in Physics Research Section A: Accelerators, Spectrometers, Detectors and Associated Equipment*, 506(3):250–303, 2003.

[36] V. Ziegler et al. The clas12 software framework and event reconstruction. *Nuclear Instruments and Methods in Physics Research Section A: Accelerators, Spectrometers, Detectors and Associated Equipment*, 959:163472, 2020.

[37] A. Rogozhnikov. Reweighting with Boosted Decision Trees. *J. Phys. Conf. Ser.*, 762(1):012036, 2016.

[38] V. Klimenko. Differential cross sections from clas12 rg-a inclusive electron scattering, 2024.

[39] Elisabetta Barberio and Zbigniew Was. PHOTOS: A Universal Monte Carlo for QED radiative corrections. Version 2.0. *Comput. Phys. Commun.*, 79:291–308, 1994.

[40] Heikki Mäntysaari and Björn Schenke. Confronting impact parameter dependent JIMWLK evolution with HERA data. *Phys. Rev. D*, 98(3):034013, 2018.

[41] Matthias Heller, Oleksandr Tomalak, and Marc Vanderhaeghen. Soft-photon corrections to the Bethe-Heitler process in the $\gamma p \to l^+ l^- p$ reaction. *Phys. Rev. D*, 97(7):076012, 2018.

[42] F. Ehlotzky and H. Mitter. Radiative corrections to the leptonic-decay modes of the neutral vector mesons $\rho 0$, ω, ϕ. *Il Nuovo Cimento A (1965-1970)*, 55(1):181–192, May 1968.

[43] S. Navas et al. Review of particle physics. *Phys. Rev. D*, 110(3):030001, 2024.

[44] Yung-Su Tsai. Pair Production and Bremsstrahlung of Charged Leptons. *Rev. Mod. Phys.*, 46:815, 1974. [Erratum: Rev.Mod.Phys. 49, 421–423 (1977)].

[45] Kjell Mork and Haakon Olsen. Radiative corrections. i. high-energy bremsstrahlung and pair production. *Phys. Rev.*, 140:B1661–B1674, Dec 1965.

[46] H. D. Schulz and G. Lutz. Experimental confirmation of radiative corrections to bremsstrahlung and pair production at high energies. *Phys. Rev.*, 167:1280–1283, Mar 1968.

Appendix

1099 # A Tabulated results for the integrated cross-section

Bin	1	2	3	4	5
$E_\gamma[GeV]$	8.455251	8.783893	8.973826	9.130290	9.338019
$\delta(E_\gamma)[GeV]$	0.128787	0.072953	0.044045	0.043109	0.073841
$\sigma[nb]$	0.139410	0.174572	0.228733	0.480779	0.527697
$\delta(\sigma)[nb]$	0.043367	0.052965	0.087674	0.103028	0.083029

Bin	6	7	8	9	10
$E_\gamma[GeV]$	9.580518	9.852534	10.106003	10.289055	10.520365
$\delta(E_\gamma)[GeV]$	0.069500	0.086529	0.061118	0.061377	0.064777
$\sigma[nb]$	0.482492	0.881968	1.097364	1.026451	0.990492
$\delta(\sigma)[nb]$	0.082528	0.097535	0.138431	0.308741	0.307483

Table 15: Tabulated results of the integrated cross-section.

1100 # B Tabulated results for the differential cross-section

$E_\gamma \in [8.2, 9.28]$ GeV / Bin	1	2	3	4	5
$-t[GeV^2]$	0.897794	1.241885	1.702589	2.233740	2.976116
$\delta(-t)[GeV^2]$	0.063470	0.143868	0.141560	0.152451	0.428174
$E_\gamma[GeV]$	8.950678	8.921866	8.883788	8.897524	8.920611
$\delta(E_\gamma)[GeV]$	0.263666	0.264286	0.272308	0.283335	0.245572
$\frac{d\sigma}{dt}[nb \cdot GeV^{-2}]$	0.578384	0.237497	0.106935	0.120434	0.034852
$\delta(\frac{d\sigma}{dt})[nb \cdot GeV^{-2}]$	0.274360	0.056286	0.034605	0.028586	0.015539

Table 16: Tabulated results of the differential cross-section in the first energy bin.

$E_\gamma \in [9.28, 10.0]$ GeV / Bin	1	2	3	4	5
$-t[GeV^2]$	0.638364	0.869347	1.118700	1.369231	1.601855
$\delta(-t)[GeV^2]$	0.069408	0.069904	0.067353	0.070731	0.065839
$E_\gamma[GeV]$	9.711591	9.681540	9.666771	9.657326	9.664881
$\delta(E_\gamma)[GeV]$	0.184376	0.209981	0.202378	0.195307	0.206044
$\frac{d\sigma}{dt}[nb \cdot GeV^{-2}]$	0.647196	0.516595	0.534277	0.399949	0.183071
$\delta(\frac{d\sigma}{dt})[nb \cdot GeV^{-2}]$	0.214338	0.113967	0.079447	0.077679	0.046047

$E_\gamma \in [9.28, 10.0]$ GeV / Bin	6	7	8	9
$-t[GeV^2]$	1.874082	2.222924	2.722623	3.806569
$\delta(-t)[GeV^2]$	0.077079	0.146622	0.137175	0.675477
$E_\gamma[GeV]$	9.679761	9.644904	9.641957	9.641022
$\delta(E_\gamma)[GeV]$	0.186172	0.213992	0.215558	0.193663
$\frac{d\sigma}{dt}[nb \cdot GeV^{-2}]$	0.264695	0.089165	0.073938	0.025705
$\delta(\frac{d\sigma}{dt})[nb \cdot GeV^{-2}]$	0.055046	0.041153	0.024669	0.006936

Table 17: Tabulated results of the differential cross-section in the second energy bin.

$E_\gamma \in [10.0, 10.6]$ GeV / Bin	1	2	3	4
$-t[GeV^2]$	0.603028	0.799744	0.997887	1.194783
$\delta(-t)[GeV^2]$	0.057292	0.057068	0.057827	0.056768
$E_\gamma[GeV]$	10.304637	10.285980	10.291438	10.247728
$\delta(E_\gamma)[GeV]$	0.185474	0.173143	0.189569	0.173065
$\frac{d\sigma}{dt}[nb \cdot GeV^{-2}]$	0.947718	0.676014	0.358979	0.358672
$\delta(\frac{d\sigma}{dt})[nb \cdot GeV^{-2}]$	0.273956	0.149186	0.089571	0.093503

$E_\gamma \in [10.0, 10.6]$ GeV / Bin	5	6	7
$-t[GeV^2]$	1.433268	1.779149	2.642590
$\delta(-t)[GeV^2]$	0.081499	0.102220	0.595131
$E_\gamma[GeV]$	10.265659	10.252512	10.244344
$\delta(E_\gamma)[GeV]$	0.184433	0.178602	0.167123
$\frac{d\sigma}{dt}[nb \cdot GeV^{-2}]$	0.236087	0.130531	0.045315
$\delta(\frac{d\sigma}{dt})[nb \cdot GeV^{-2}]$	0.092430	0.043924	0.011184

Table 18: Tabulated results of the differential cross-section in the third energy bin.

C Tabulated systematics for the integrated cross-section

Bin	1	2	3	4	5
$E_\gamma[GeV]$	8.455251	8.783893	8.973826	9.130290	9.338019
$\tilde{Q}^2$ cut syst. [%]	15.2623	7.12544	16.6759	1.22668	8.53409
Missing mass cut syst. [%]	11.5078	5.69875	5.50693	0.827488	2.49655
Fit function syst. [%]	13.6051	6.48846	14.725	7.59433	3.23004
AI PID cut syst. [%]	0.830795	3.39863	2.4525	4.36833	3.00934
Lepton momenta cut syst. [%]	0.64161	0.654621	0.131991	0.573095	0.253077
Proton PID cut syst. [%]	11.2581	12.18	6.32923	3.04228	6.40981
Total bin-by-bin [%]	26.0444	16.9021	23.9025	9.40902	11.8196
Normalization [%]			16.		
Accumulated charge [%]			1.2		
Radiative correction [%]	16.	10.	9.	5.	5.
Total [%]	34.52	25.34	30.16	19.26	20.55

Bin	6	7	8	9	10
$E_\gamma[GeV]$	9.580518	9.852534	10.106003	10.289055	10.520365
$\tilde{Q}^2$ cut syst. [%]	7.89663	6.42553	6.85951	6.70166	14.1579
Missing mass cut syst. [%]	0.506499	0.343491	0.405982	0.119847	0.374545
Fit function syst. [%]	10.2895	8.56513	9.35056	5.89271	14.4803
AI PID cut syst. [%]	5.09871	1.8137	4.07374	3.99243	0.711531
Lepton momenta cut syst. [%]	0.252514	0.628994	0.0825364	0.508277	0.0863656
Proton PID cut syst. [%]	2.27357	3.91011	2.96632	3.23282	2.4019
Total bin-by-bin [%]	14.1321	11.5646	12.6512	10.3102	20.4096
Normalization [%]			16.		
Accumulated charge [%]			1.2		
Radiative correction [%]	3.	3.	2.	1.	0.
Total [%]	21.59	20.0	20.53	19.10	25.96

Table 19: Tabulated systematic variation for integrated cross-section. The total sytematic reported here only referes to the one displayed in the table. One has to add in quadrature the normalization, accumulated charge and radiative effects systematics to get the final total systematics.

D Tabulated systematics for the differential cross-section

$E_\gamma \in [8.2, 9.28]$ GeV / Bin	1	2	3	4	5
$-t[GeV^2]$	0.897794	1.241885	1.702589	2.233740	2.976116
$E_\gamma[GeV]$	8.950678	8.921866	8.883788	8.897524	8.920611
Missing mass cut syst. [%]	14.8086	2.6515	3.40865	3.58774	8.04232
$\tilde{Q}^2$ cut syst. [%]	28.0509	3.2372	9.72357	20.5135	21.0884
AI PID cut syst. [%]	3.6648	2.15592	3.73481	4.56985	3.45675
Proton PID cut syst. [%]	5.08958	3.94441	11.2473	11.5651	4.68777
Lepton momenta cut syst. [%]	0.592603	1.19544	0.421141	0.623669	0.85257
Fit function syst. [%]	5.05541	5.63527	9.93107	10.5775	8.83051
Total bin-by-bin [%]	32.7321	8.42031	18.5855	26.4685	24.9405
Normalization [%]	16.				
Accumulated charge [%]	1.2				
Radiative correction [%]	8.				
Total [%]	37.32	19.81	25.82	31.97	30.72

Table 20: Tabulated systematic variation of the differential cross-section in the first energy bin. One has to add in quadrature the normalization, accumulated charge and radiative effects systematics to get the final total systematics.

$E_\gamma \in [9.28, 10.0]$ GeV / Bin	1	2	3	4	5
$-t[GeV^2]$	0.638364	0.869347	1.118700	1.369231	1.601855
$E_\gamma[GeV]$	9.711591	9.681540	9.666771	9.657326	9.664881
Missing mass cut syst. [%]	0.683588	0.708655	0.938708	1.99144	0.480201
$\tilde{Q}^2$ cut syst. [%]	13.7007	19.7187	5.02389	13.8435	7.45981
AI PID cut syst. [%]	7.47879	4.20043	4.22222	3.99516	4.6348
Proton PID cut syst. [%]	19.242	8.26652	3.25234	5.03751	1.2919
Lepton momenta cut syst. [%]	0.485057	0.41029	0.385507	0.157433	0.42416
Fit function syst. [%]	6.11467	8.49365	3.54232	11.4683	4.34159
Total bin-by-bin [%]	25.534	23.4012	8.19891	19.1962	9.90248
Normalization [%]	16				
Accumulated charge [%]	1.2				
Radiative correction [%]	4.				
Total [%]	30.42	28.65	18.46	25.34	19.27

$E_\gamma \in [9.28, 10.0]$ GeV / Bin	6	7	8	9
$-t[GeV^2]$	1.874082	2.222924	2.722623	3.806569
$E_\gamma[GeV]$	9.679761	9.644904	9.641957	9.641022
Missing mass cut syst. [%]	2.28538	5.11117	2.53361	2.48517
$\tilde{Q}^2$ cut syst. [%]	13.7676	21.8154	28.1282	7.26208
AI PID cut syst. [%]	4.40799	13.6803	5.33368	3.70458
Proton PID cut syst. [%]	4.37069	13.8257	5.00637	3.62788
Lepton momenta cut syst. [%]	1.76113	3.68511	0.977806	1.18569
Fit function syst. [%]	4.4848	25.3964	2.12173	0.827228
Total bin-by-bin [%]	15.459	36.8322	29.3957	9.09458
Normalization [%]	16			
Accumulated charge [%]	1.2			
Radiative correction [%]	4.			
Total [%]	22.64	40.37	33.73	18.87

Table 21: Tabulated systematic variation of the differential cross-section in the second energy bin. One has to add in quadrature the normalization, accumulated charge and radiative effects systematics to get the final total systematics.

$E_\gamma \in [10.0, 10.6]$ GeV / Bin	1	2	3	4
$-t[GeV^2]$	0.603028	0.799744	0.997887	1.194783
$E_\gamma[GeV]$	10.304637	10.285980	10.291438	10.247728
Missing mass cut syst. [%]	0.390639	0.170699	1.02658	0.178225
$\tilde{Q}^2$ cut syst. [%]	24.9002	17.5911	8.62308	10.0637
AI PID cut syst. [%]	3.30112	0.670091	2.09577	1.50156
Proton PID cut syst. [%]	14.2236	1.69626	5.67602	5.98689
Lepton momenta cut syst. [%]	0.560885	0.237967	0.362265	0.144846
Fit function syst. [%]	17.1773	18.3953	2.30222	6.23854
Total bin-by-bin [%]	33.5969	25.5195	10.8375	13.3547
Normalization [%]	16			
Accumulated charge [%]	1.2			
Radiative correction [%]	1.			
Total [%]	37.25	30.16	19.39	20.90

$E_\gamma \in [10.0, 10.6]$ GeV / Bin	5	6	7
$-t[GeV^2]$	1.433268	1.779149	2.642590
$E_\gamma[GeV]$	10.265659	10.252512	10.244344
Missing mass cut syst. [%]	0.266901	0.983997	1.54568
$\tilde{Q}^2$ cut syst. [%]	11.2181	31.1301	4.84548
AI PID cut syst. [%]	4.72545	4.49564	2.87388
Proton PID cut syst. [%]	4.82943	2.79884	13.4113
Lepton momenta cut syst. [%]	0.196958	2.03263	1.04243
Fit function syst. [%]	5.95217	5.1239	14.1225
Total bin-by-bin [%]	14.3888	32.07	20.3599
Normalization [%]	16		
Accumulated charge [%]	1.2		
Radiative correction [%]	1.		
Total [%]	21.57	35.87	25.94

Table 22: Tabulated systematic variation of the differential cross-section in the third energy bin. One has to add in quadrature the normalization, accumulated charge and radiative effects systematics to get the final total systematics.

E List of runs and associated accumulated charge

E.1 Fall 2018 Inbending

Beam Current (nA)	Run Numbers	Associated Charge (nC)
55	5368	327150.00
	5369	94684.20
	5372	369081.00
	5373	361669.00
	5374	382198.00
	5375	387490.00
	5376	290796.00
	5377	12941.50
	5378	36996.30
	5379	387531.00
	5380	357707.00
	5381	371711.00
	5382	284935.00
	5383	281662.00
	5386	187210.00
	5390	26329.60
	5391	365707.00
	5398	42407.60
	5400	34099.10
	5401	31765.70
	5403	110510.00
	5404	14970.50
	5406	179818.00
	5407	416414.00

Table 23: Summary of Run Numbers and Associated Charge for Each Beam Current (1/1)

Beam Current (nA)	Run Numbers	Associated Charge (nC)
45	5032	34245.60
	5036	114022.00
	5038	378709.00
	5039	96850.50
	5040	147343.00
	5041	175940.00
	5043	140423.00
	5045	137370.00
	5046	394408.00
	5047	16445.20
	5051	288303.00
	5052	34382.70
	5053	52192.90
	5116	38416.60
	5117	393660.00
	5119	12884.60
	5120	78582.20
	5124	395035.00
	5125	397571.00
	5126	397503.00
	5127	57527.10
	5128	397371.00
	5129	167882.00
	5130	398070.00
	5139	139615.00
	5153	69038.40
	5158	39550.80
	5159	248129.00
	5160	174660.00
	5162	80069.80
	5163	401403.00
	5164	5041.72
	5165	271204.00
	5166	404803.00
	5167	398386.00
	5168	200402.00
	5169	407935.00
	5180	222796.00
	5181	368857.00
	5182	74984.80
	5183	328041.00
	5191	86529.90
	5193	154744.00
	5195	75158.60
	5196	411810.00
	5197	414557.00
	5198	411532.00
	5199	412208.00
	5200	154042.00
	5201	80925.50
	5202	410589.00
	5203	414655.00
	5204	398399.00
	5205	90713.70
	5206	289584.00
	5208	333470.00
	5211	87206.40
	5212	391124.00

Table 24: Summary of Run Numbers and Associated Charge for Each Beam Current (1/2)

Beam Current (nA)	Run Numbers	Associated Charge (nC)
	5215	386497.00
	5216	165194.00
	5219	385594.00
	5220	350442.00
	5221	389766.00
	5222	388895.00
	5223	135114.00
	5230	371039.00
	5231	390388.00
	5232	391028.00
	5233	389224.00
	5234	391996.00
	5235	145449.00
	5237	156465.00
	5238	310085.00
	5247	81018.70
	5248	401352.00
	5249	434539.00
	5252	272836.00
	5253	98629.50
	5257	430276.00
	5258	429167.00
45	5259	161727.00
	5261	430571.00
	5262	202647.00
	5303	420564.00
	5304	406558.00
	5305	157358.00
	5306	401701.00
	5307	47816.40
	5310	105109.00
	5311	138911.00
	5315	97427.70
	5317	401966.00
	5318	400666.00
	5319	405694.00
	5320	200445.00
	5323	27479.10
	5324	33812.90
	5333	99299.90
	5334	72452.30
	5346	379346.00
	5347	178928.00
	5349	242454.00
	5351	52604.30
	5354	377576.00
	5355	170245.00
	5367	373381.00

Table 25: Summary of Run Numbers and Associated Charge for Each Beam Current (2/2)

Beam Current (nA)	Run Numbers	Associated Charge (nC)
	5335	13391.90
40	5339	95397.90
	5341	124227.00

Table 26: Summary of Run Numbers and Associated Charge for Each Beam Current (1/1)

Beam Current (nA)	Run Numbers	Associated Charge (nC)
50	5340	35553.80
	5342	115739.00
	5343	60278.60
	5344	152308.00
	5345	382028.00
	5356	377070.00
	5357	377122.00
	5358	382403.00
	5359	382255.00
	5360	378618.00
	5361	372562.00
	5362	28149.70
	5366	393710.00
	5392	198954.00
	5393	363850.00

Table 27: Summary of Run Numbers and Associated Charge for Each Beam Current (1/1)

E.2 Fall 2018 Outbending

Beam Current (nA)	Run Numbers	Associated Charge (nC)
	5423	112980.00
	5424	264486.00
	5425	267255.00
	5426	68942.80
	5428	139909.00
	5429	247113.00
	5430	266452.00
	5432	267451.00
	5434	265513.00
	5435	265439.00
	5436	274392.00
	5437	110764.00
	5438	240984.00
	5440	268080.00
	5441	263971.00
	5442	172651.00
	5445	266277.00
	5447	277844.00
	5448	313069.00
	5449	261028.00
	5450	14483.70
	5451	219754.00
	5452	269934.00
	5453	223794.00
40	5454	279375.00
	5455	260691.00
	5460	235280.00
	5464	291683.00
	5465	102147.00
	5466	109989.00
	5467	292428.00
	5468	266584.00
	5469	143783.00
	5470	94898.30
	5471	220916.00
	5472	169560.00
	5473	75652.60
	5474	267543.00
	5475	267462.00
	5476	132327.00
	5478	267366.00
	5479	269173.00
	5480	135958.00
	5481	274804.00
	5482	266653.00
	5483	287530.00
	5485	269152.00
	5486	269163.00
	5487	203926.00
	5495	50398.80
	5496	2838.39
	5497	284746.00
	5498	123275.00
	5499	266609.00
	5500	286430.00
	5504	19713.50

Table 28: Summary of Run Numbers and Associated Charge for Each Beam Current (1/1)

Beam Current (nA)	Run Numbers	Associated Charge (nC)
50	5505	139380.00
	5507	249718.00
	5516	258148.00
	5517	264240.00
	5518	94151.10
	5519	252087.00
	5520	256258.00
	5521	69842.10
	5522	167539.00
	5523	255325.00
	5524	163887.00
	5525	269679.00
	5526	259544.00
	5527	276489.00
	5528	267212.00
	5530	258755.00
	5532	257154.00
	5533	76048.90
	5534	251081.00
	5535	281328.00
	5536	215670.00
	5537	262880.00
	5538	276008.00
	5540	266045.00
	5541	231565.00
	5543	285812.00
	5544	282757.00
	5545	72226.20
	5546	15066.00
	5547	258592.00
	5548	287255.00
	5549	277389.00
	5550	257720.00
	5551	258887.00
	5552	262001.00
	5555	261225.00
	5556	290141.00
	5557	275467.00
	5558	262254.00
	5559	219761.00
	5562	8095.72
	5567	70463.60
	5569	283466.00
	5570	269549.00
	5571	142724.00
	5572	99451.10
	5573	293319.00
	5574	253885.00
	5577	256631.00
	5578	172260.00
	5591	285997.00
	5592	114444.00
	5594	11681.80
	5597	95529.30
	5598	106461.00
	5600	5279.14

Table 29: Summary of Run Numbers and Associated Charge for Each Beam Current (1/2)

Beam Current (nA)	Run Numbers	Associated Charge (nC)
50	5601	211068.00
	5602	259107.00
	5603	259836.00
	5604	17561.20
	5606	265711.00
	5607	56099.60
	5611	256931.00
	5612	285714.00
	5613	273183.00
	5614	210533.00
	5616	35980.80
	5617	6775.56
	5618	35846.80
	5619	156520.00
	5621	42793.90
	5623	43244.90
	5624	258722.00
	5625	258502.00
	5626	258820.00
	5627	16849.40
	5628	275311.00
	5629	205783.00
	5630	272102.00
	5631	257041.00
	5632	266949.00
	5633	66156.10
	5635	267154.00
	5637	160175.00
	5638	233715.00
	5639	222118.00
	5641	254416.00
	5643	74896.10
	5644	130154.00
	5645	89489.50
	5646	274376.00
	5647	271177.00
	5648	259397.00
	5649	260185.00
	5650	19105.60
	5651	121138.00
	5652	38820.90
	5654	262466.00
	5655	260122.00
	5656	156393.00
	5662	226460.00
	5663	259759.00
	5664	269589.00
	5665	13574.80
	5666	286251.00

Table 30: Summary of Run Numbers and Associated Charge for Each Beam Current (2/2)

E.3 Spring 2019 Inbending

Beam Current (nA)	Run Numbers	Associated Charge (nC)
50	6619	561457.00
	6620	643089.00
	6632	204373.00
	6636	622174.00
	6637	267280.00
	6638	151209.00
	6639	172046.00
	6640	556465.00
	6642	220667.00
	6645	393439.00
	6647	560164.00
	6648	161958.00
	6650	27065.50
	6651	379068.00
	6652	81755.10
	6654	105743.00
	6655	488416.00
	6656	625794.00
	6657	570031.00
	6658	72815.10
	6660	538270.00
	6661	597381.00
	6662	568126.00
	6663	385429.00
	6664	487043.00
	6665	218738.00
	6666	269647.00
	6667	596382.00
	6668	553007.00
	6669	298259.00
	6670	236095.00
	6672	642085.00
	6673	275658.00
	6677	554223.00
	6678	527390.00
	6680	442762.00
	6682	234153.00
	6683	626955.00
	6684	335669.00
	6685	579668.00
	6687	200926.00
	6688	539434.00
	6689	620071.00
	6691	604244.00
	6692	603502.00
	6693	217143.00
	6694	628618.00
	6695	321818.00
	6696	53021.80
	6697	628941.00
	6698	501188.00
	6699	143383.00
	6704	580833.00
	6705	620115.00
	6706	586632.00

Table 31: Summary of Run Numbers and Associated Charge for Each Beam Current (1/2)

Beam Current (nA)	Run Numbers	Associated Charge (nC)
50	6707	159064.00
	6708	376579.00
	6709	443418.00
	6710	499652.00
	6711	612557.00
	6712	612725.00
	6713	509857.00
	6714	310608.00
	6715	624800.00
	6716	562852.00
	6717	610758.00
	6718	614315.00
	6719	232845.00
	6729	453328.00
	6730	14857.80
	6731	503292.00
	6732	203490.00
	6733	590084.00
	6734	299947.00
	6736	595320.00
	6737	596860.00
	6738	571835.00
	6739	533640.00
	6740	614879.00
	6741	651068.00
	6742	54308.20
	6743	588115.00
	6744	454551.00
	6746	630807.00
	6747	612094.00
	6748	587984.00
	6749	122685.00
	6750	392232.00
	6753	165571.00
	6754	86864.30
	6755	68965.10
	6756	367406.00
	6759	320793.00
	6760	553734.00
	6762	630245.00
	6763	29160.50
	6764	146760.00
	6765	572577.00
	6767	590503.00
	6768	555960.00
	6769	209629.00
	6775	636468.00
	6776	535981.00
	6777	636299.00
	6778	473077.00
	6779	478333.00
	6780	598856.00
	6781	373498.00
	6783	39713.10

Table 32: Summary of Run Numbers and Associated Charge for Each Beam Current (2/2)

F Data fits for the integrated cross section

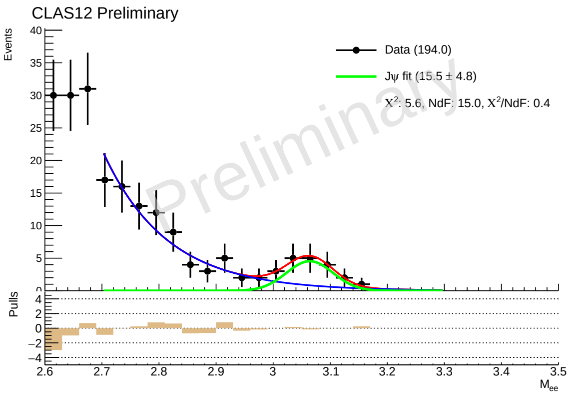

(a) $E_\gamma \in [8.2, 8.65]$ GeV

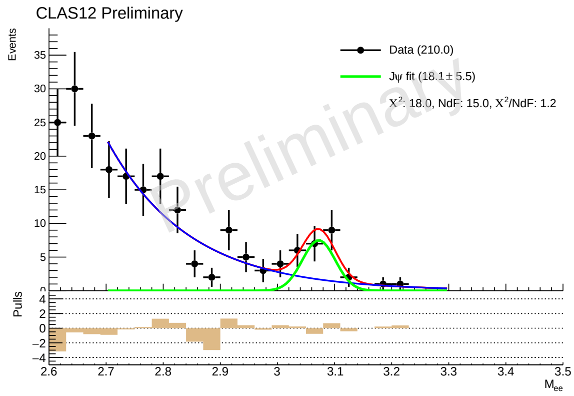

(b) $E_\gamma \in [8.65, 8.9]$ GeV

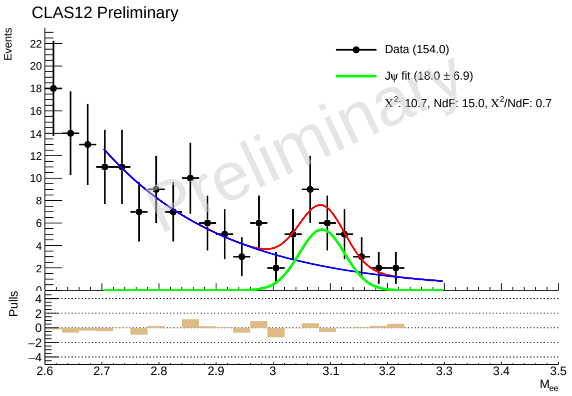

(c) $E_\gamma \in [8.9, 9.05]$ GeV

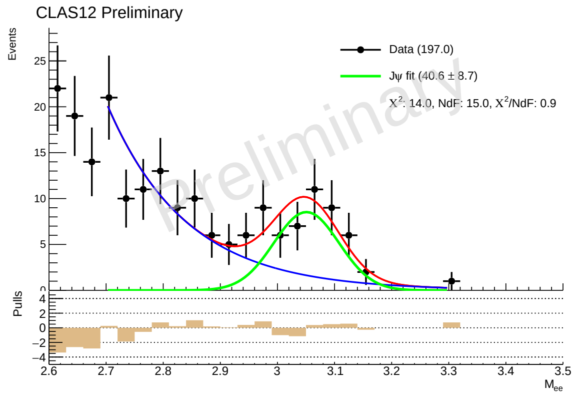

(d) $E_\gamma \in [9.05, 9.2]$ GeV

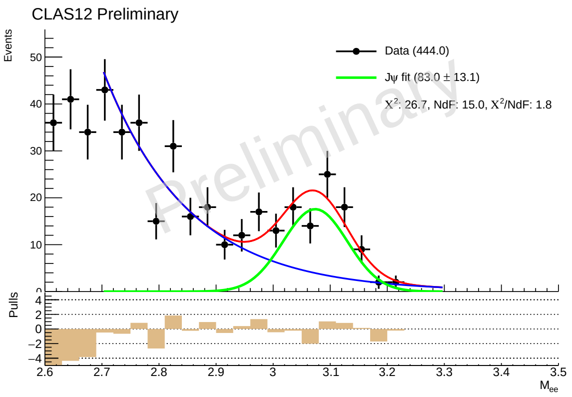

(e) $E_\gamma \in [9.2, 9.46]$ GeV

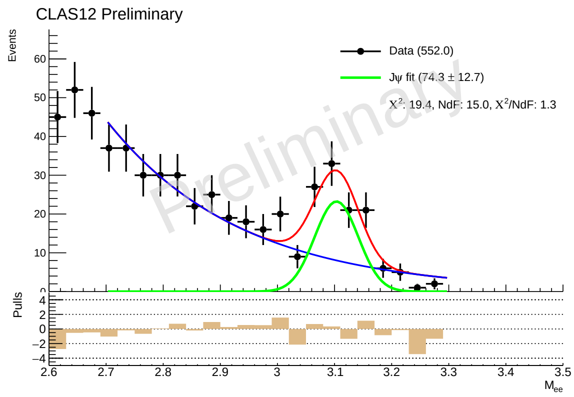

(f) $E_\gamma \in [9.46, 9.7]$ GeV

Figure 90: Data fits for the integrated cross section

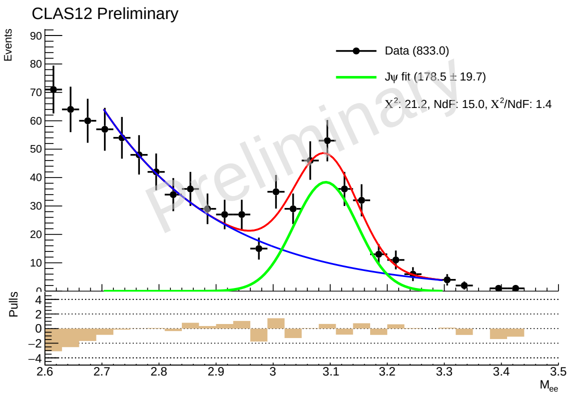

(a) $E_\gamma \in [9.7, 10.0]$ GeV

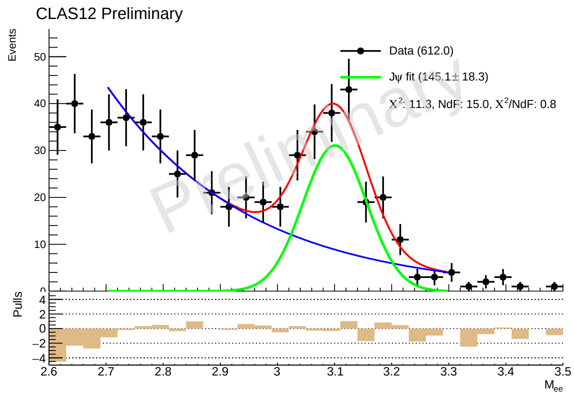

(b) $E_\gamma \in [10.0, 10.2]$ GeV

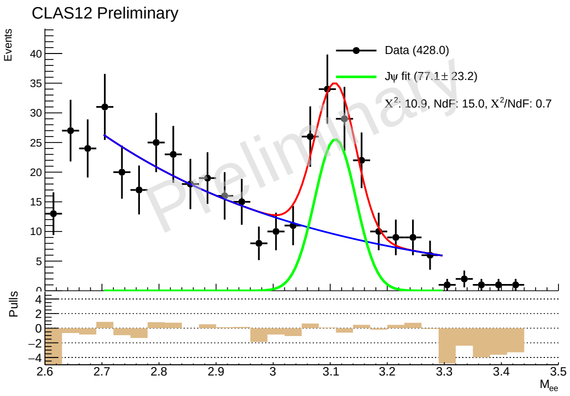

(c) $E_\gamma \in [10.2, 10.4]$ GeV

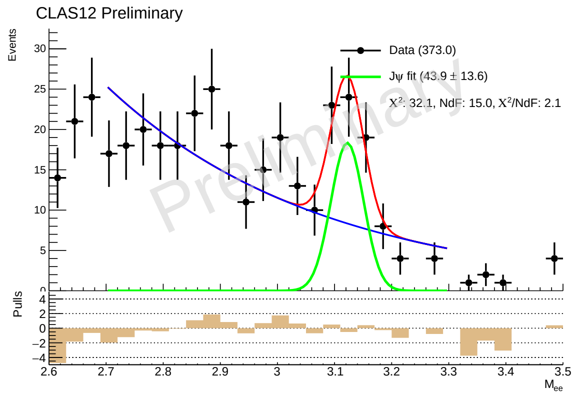

(d) $E_\gamma \in [10.4, 10.6]$ GeV

Figure 91: Data fits for the integrated cross section

G Acceptance fits for the integrated cross section

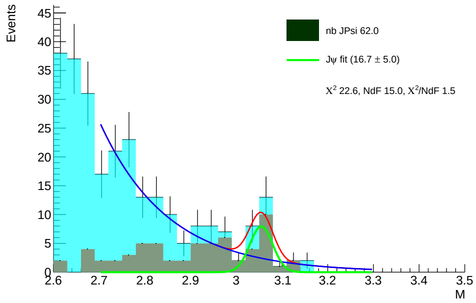

(a) $E_\gamma \in [8.2, 8.65]$ GeV

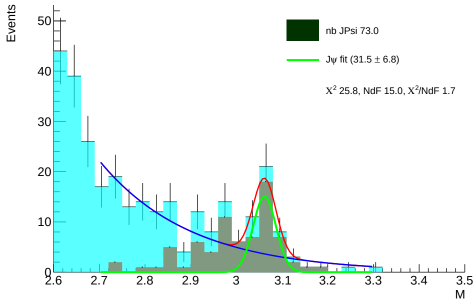

(b) $E_\gamma \in [8.65, 8.9]$ GeV

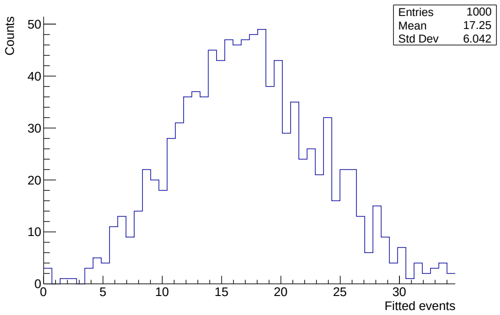

(c) $E_\gamma \in [8.2, 8.65]$ GeV

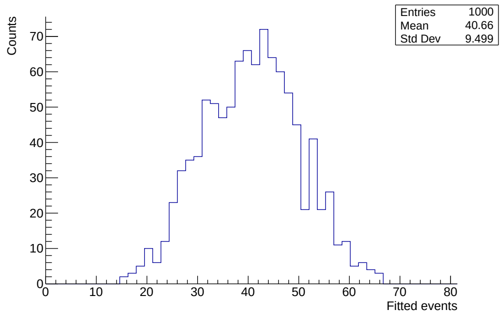

(d) $E_\gamma \in [8.65, 8.9]$ GeV

Figure 92: Acceptance fits for the integrated cross section

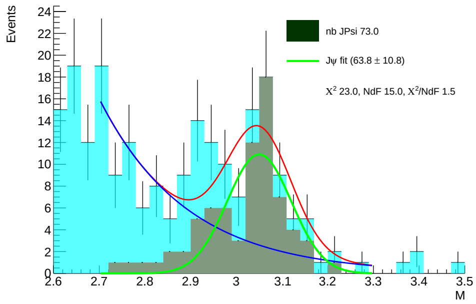

(a) $E_\gamma \in [8.9, 9.05]$ GeV

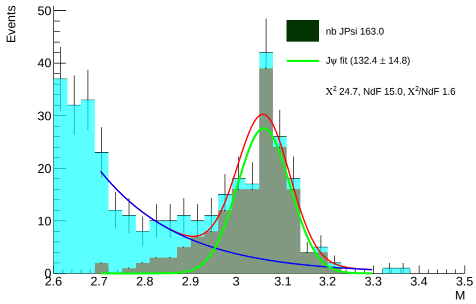

(b) $E_\gamma \in [9.05, 9.2]$ GeV

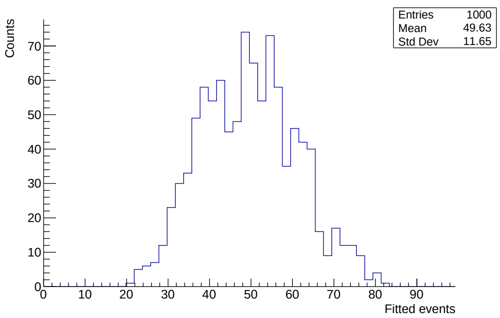

(c) $E_\gamma \in [8.9, 9.05]$ GeV

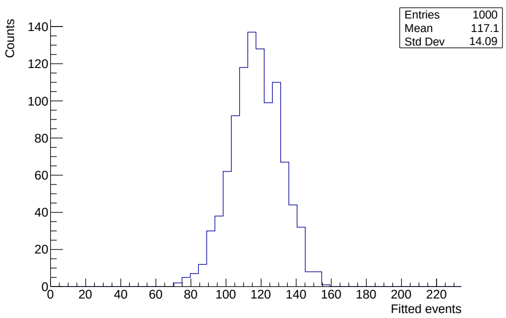

(d) $E_\gamma \in [9.05, 9.2]$ GeV

Figure 93: Acceptance fits for the integrated cross section

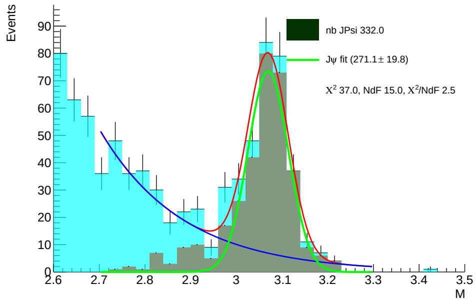

(a) $E_\gamma \in [9.2, 9.46]$ GeV

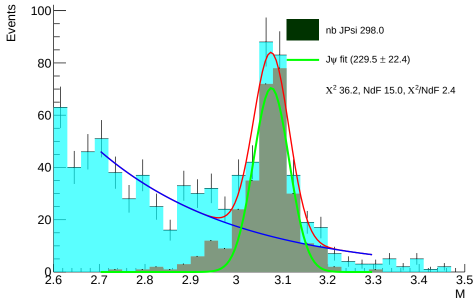

(b) $E_\gamma \in [9.46, 9.7]$ GeV

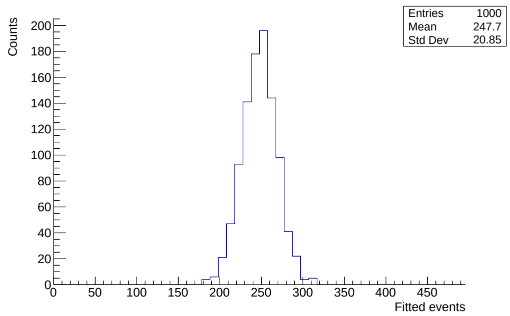

(c) $E_\gamma \in [9.2, 9.46]$ GeV

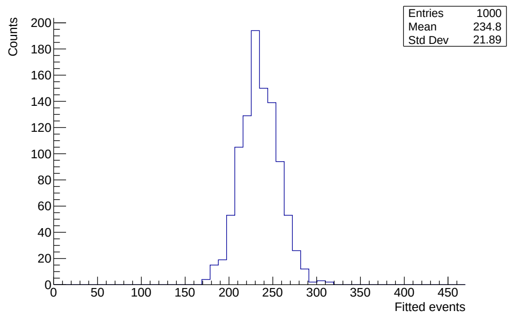

(d) $E_\gamma \in [9.46, 9.7]$ GeV

Figure 94: Acceptance fits for the integrated cross section

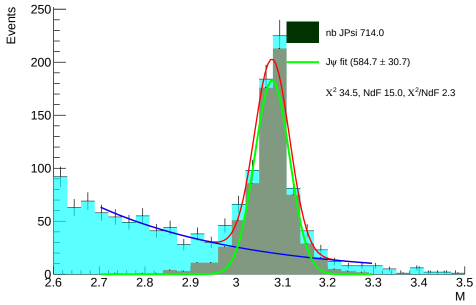

(a) $E_\gamma \in [9.7, 10.0]$ GeV

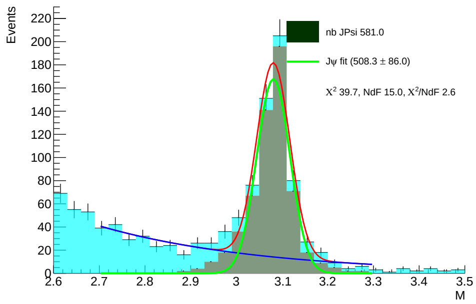

(b) $E_\gamma \in [10.0, 10.2]$ GeV

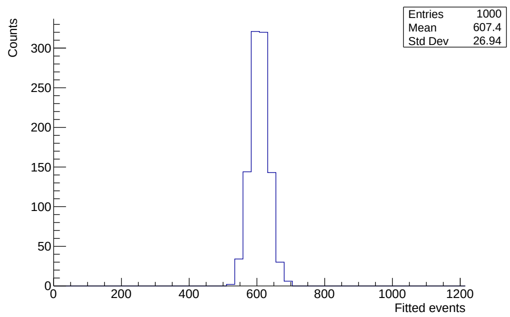

(c) $E_\gamma \in [9.7, 10.0]$ GeV

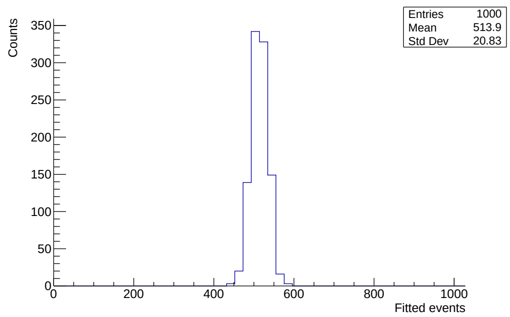

(d) $E_\gamma \in [10.0, 10.2]$ GeV

Figure 95: Acceptance fits for the integrated cross section

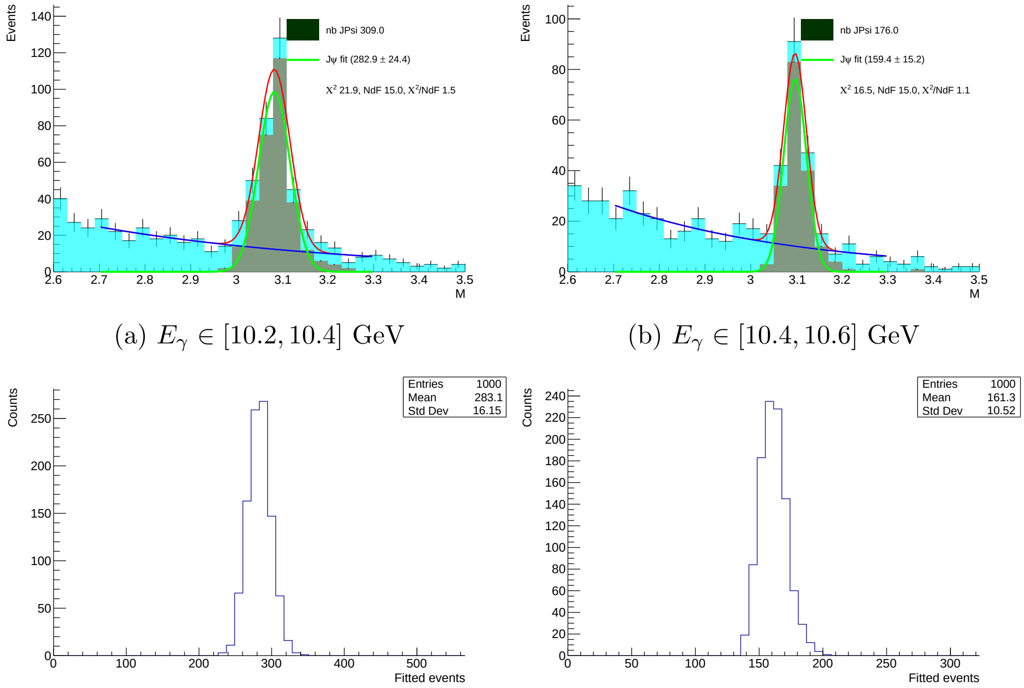

(a) $E_\gamma \in [10.2, 10.4]$ GeV

(b) $E_\gamma \in [10.4, 10.6]$ GeV

(c) $E_\gamma \in [10.2, 10.4]$ GeV

(d) $E_\gamma \in [10.4, 10.6]$ GeV

Figure 96: Acceptance fits for the integrated cross section

H Data fits for the differential cross section

H.1 $E_\gamma \in [8.20, 9.28]$ GeV

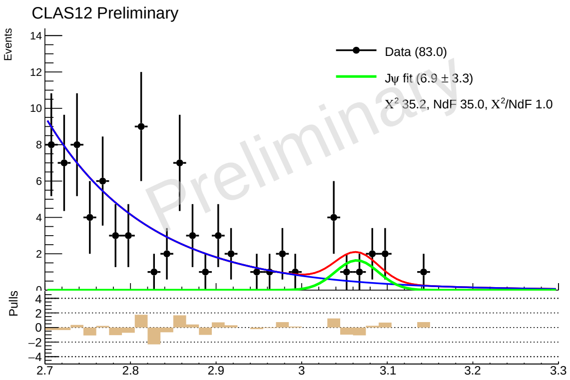

(a) $-t \in [0.77, 1.0]$ GeV^2

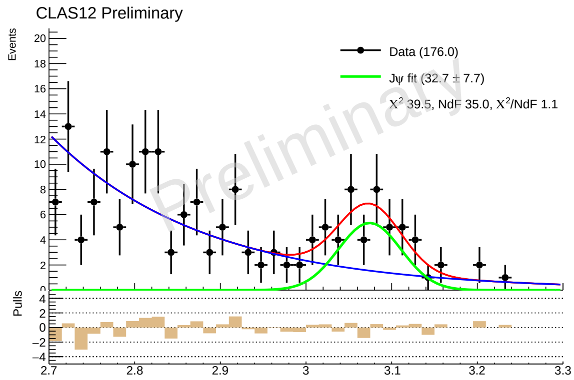

(b) $-t \in [1.0, 1.5]$ GeV^2

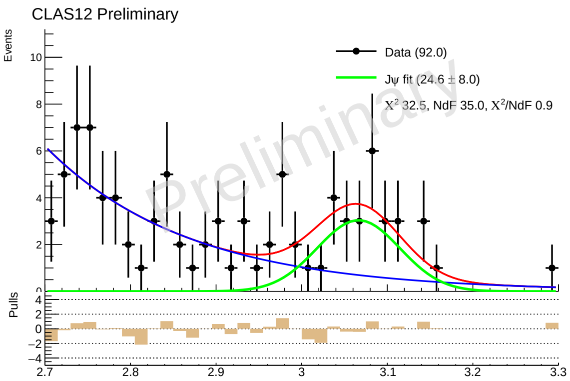

(c) $-t \in [1.5, 2.0]$ GeV^2

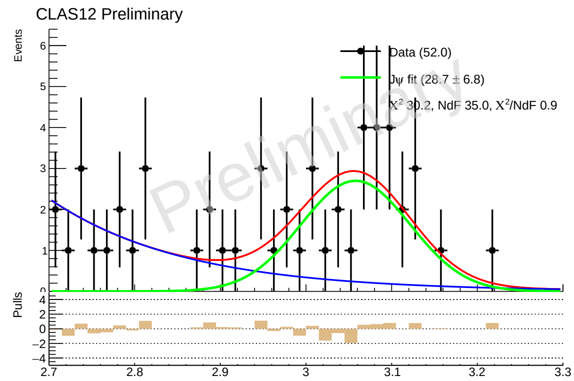

(d) $-t \in [2.0, 2.5]$ GeV^2

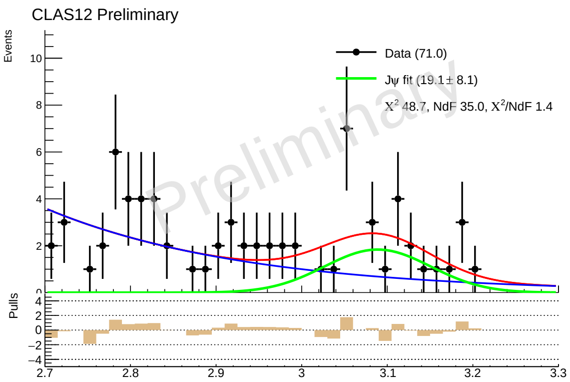

(e) $-t \in [2.5, 4.5]$ GeV^2

Figure 97: Data fits for the differential cross section

H.2 $E_\gamma \in [9.28, 10.00]$ GeV

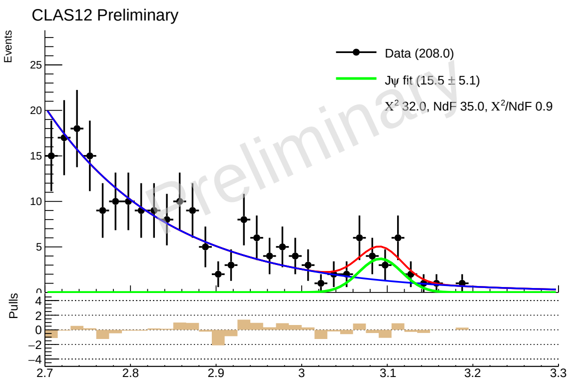

(a) $-t \in [0.5, 0.75]$ GeV^2

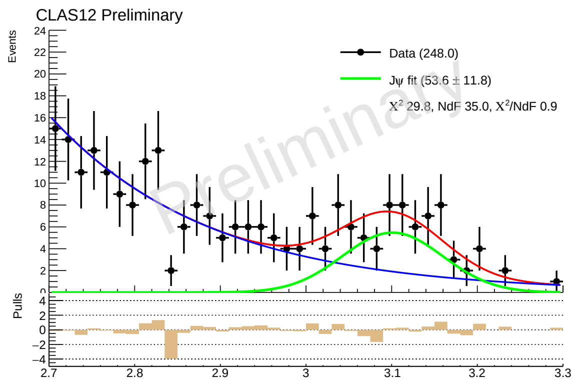

(b) $-t \in [0.75, 1.0]$ GeV^2

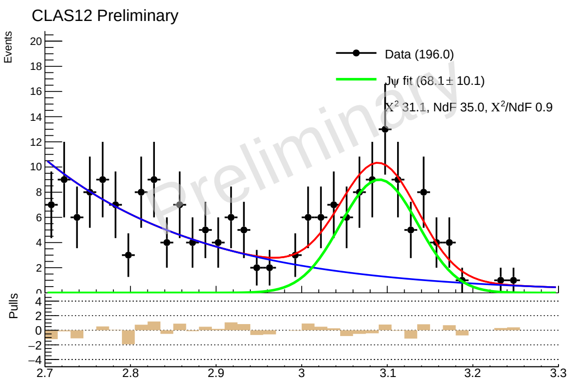

(c) $-t \in [1.0, 1.25]$ GeV^2

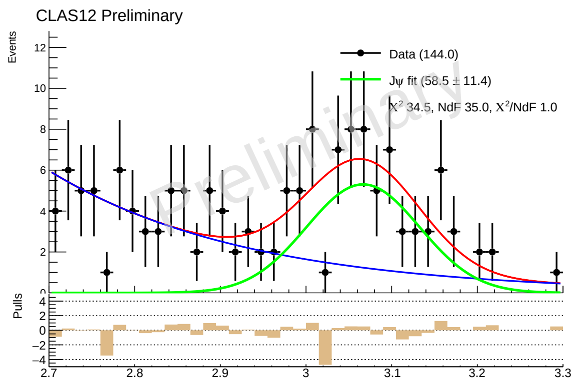

(d) $-t \in [1.25, 1.5]$ GeV^2

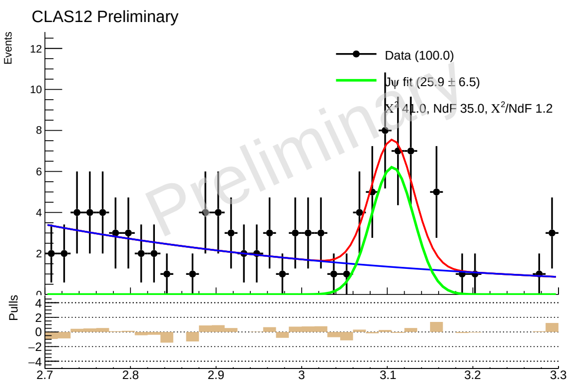

(e) $-t \in [1.5, 1.75]$ GeV^2

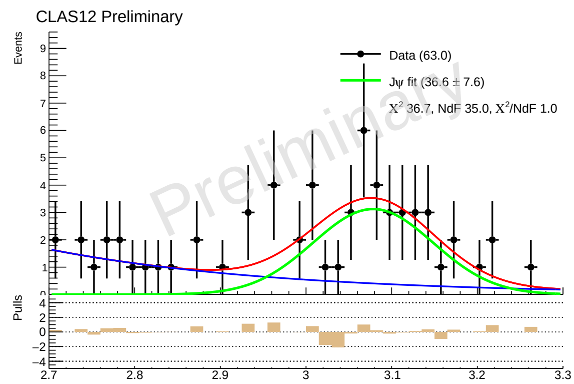

(f) $-t \in [1.75, 2.0]$ GeV^2

Figure 98: Data fits for the integrated cross section

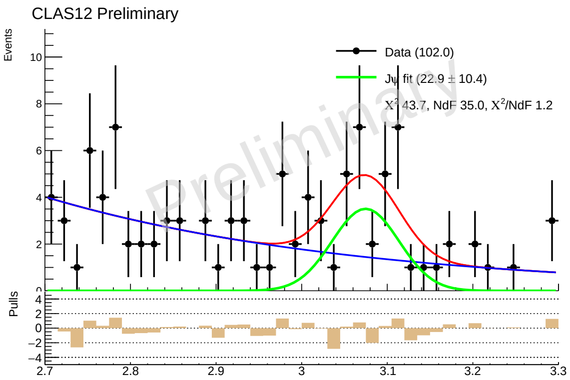

(a) $-t \in [2.0, 2.5]$ GeV^2

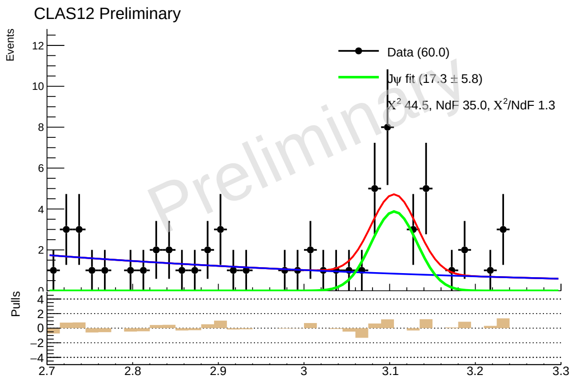

(b) $-t \in [2.5, 3.0]$ GeV^2

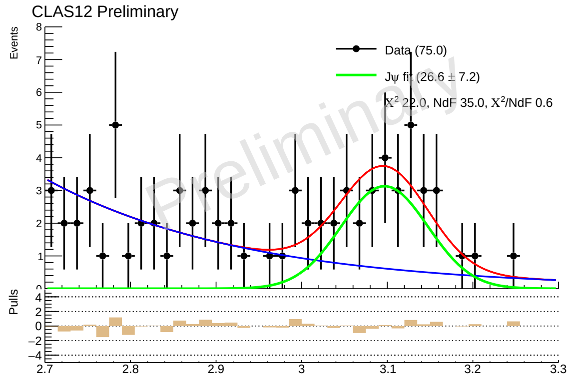

(c) $-t \in [3.0, 6.0]$ GeV^2

Figure 99: Data fits for the integrated cross section

1112 H.3 $E_\gamma \in [10.00, 10.60]$ GeV

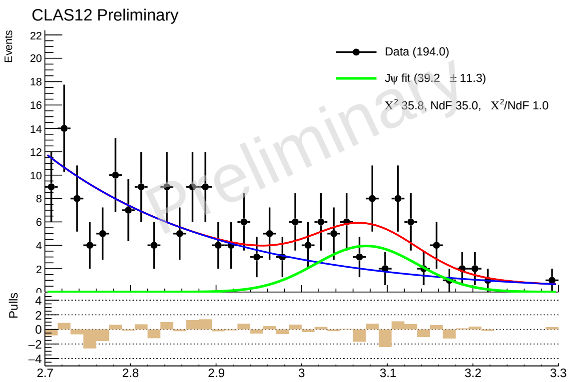

(a) $-t \in [0.5, 0.7]$ GeV^2

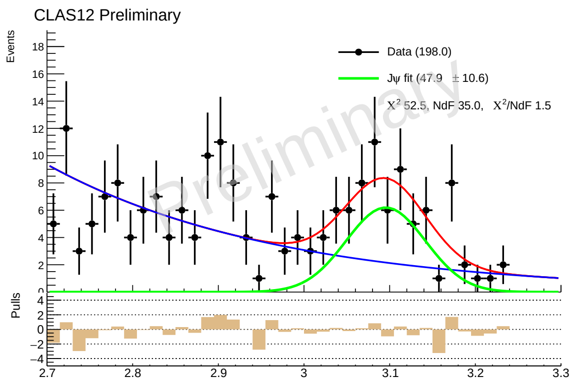

(b) $-t \in [0.7, 0.9]$ GeV^2

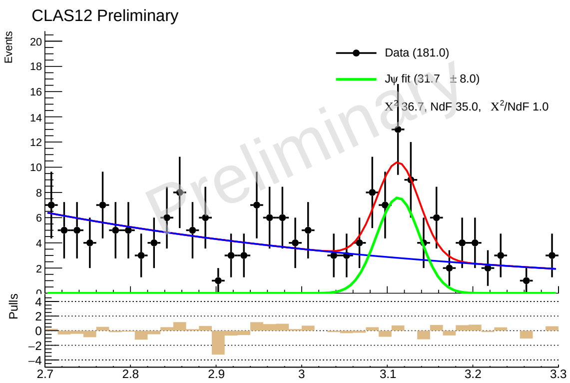

(c) $-t \in [0.9, 1.1]$ GeV^2

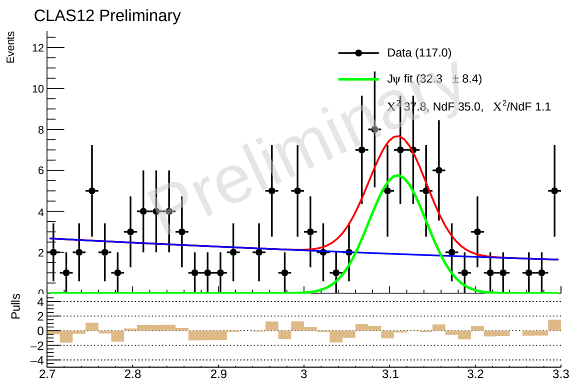

(d) $-t \in [1.1, 1.3]$ GeV^2

Figure 100: Data fits for the differential cross section

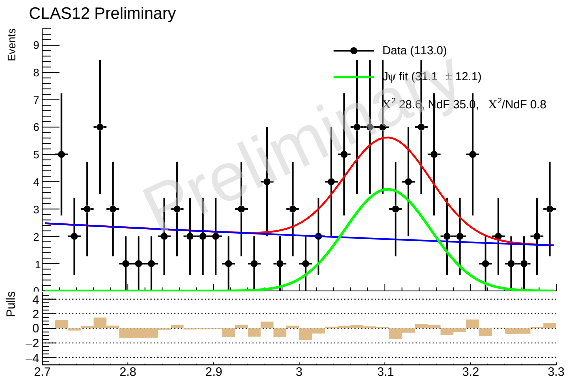

(a) $-t \in [1.3, 1.6]$ GeV^2

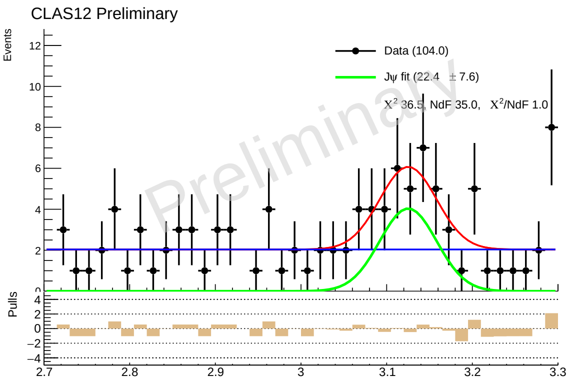

(b) $-t \in [1.6, 2.0]$ GeV^2

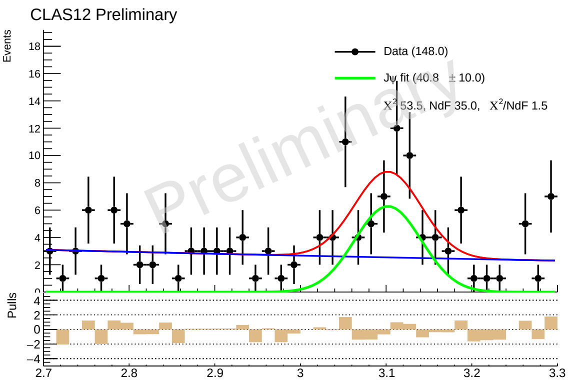

(c) $-t \in [2.0, 4.5]$ GeV^2

Figure 101: Data fits for the differential cross section

I Acceptance fits for the differential cross section

I.1 $E_\gamma \in [8.20, 9.28]$ GeV

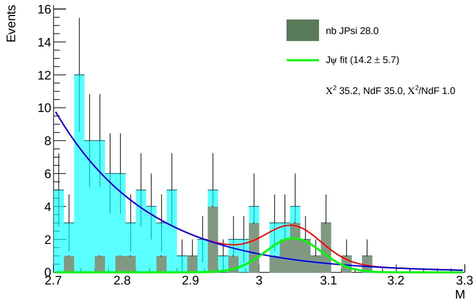

(a) $-t \in [0.77, 1.0]$ GeV^2

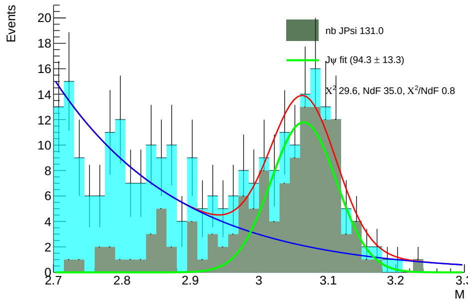

(b) $-t \in [1.0, 1.5]$ GeV^2

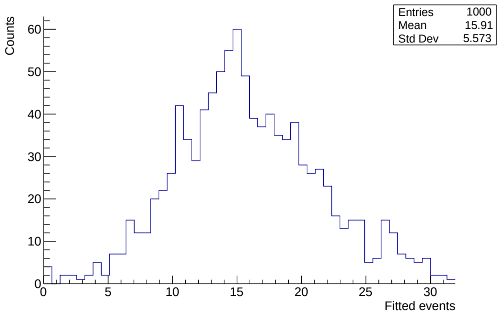

(c) $-t \in [0.77, 1.0]$ GeV^2

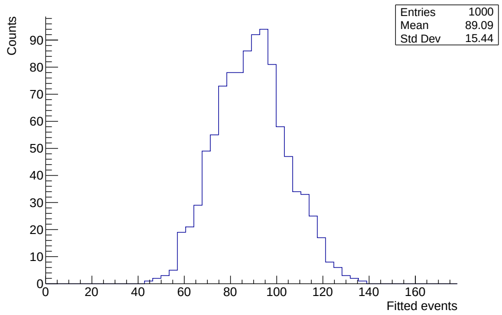

(d) $-t \in [1.0, 1.5]$ GeV^2

Figure 102: Acceptance fits for the differential cross section

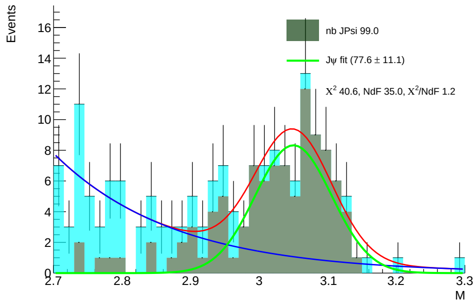

(a) $-t \in [1.5, 2.0]$ GeV^2

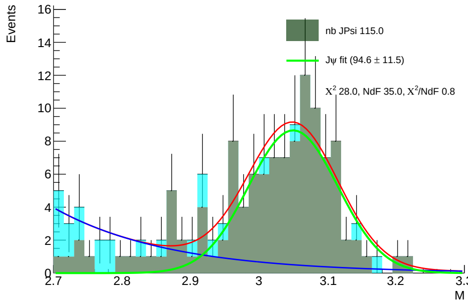

(b) $-t \in [2.0, 2.5]$ GeV^2

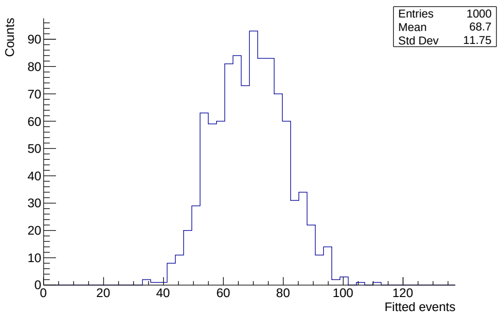

(c) $-t \in [1.5, 2.0]$ GeV^2

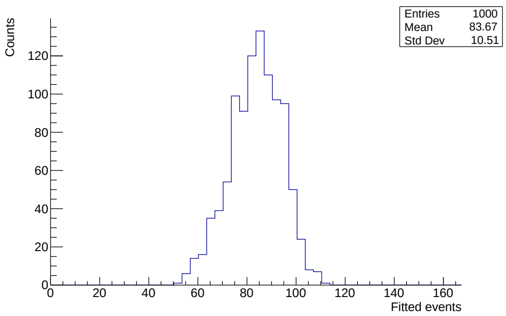

(d) $-t \in [2.0, 2.5]$ GeV^2

Figure 103: Acceptance fits for the differential cross section

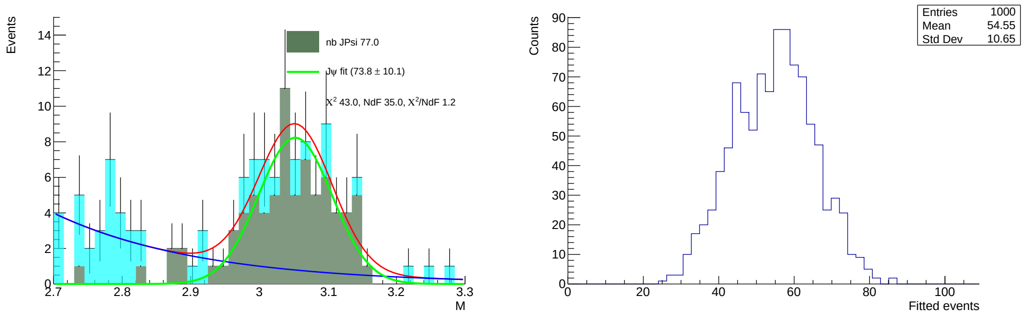

(a) $-t \in [2.5, 4.5]$ GeV^2 (b) $-t \in [2.5, 4.5]$ GeV^2

Figure 104: Acceptance fits for the differential cross section

I.2 $E_\gamma \in [9.28, 10.00]$ GeV

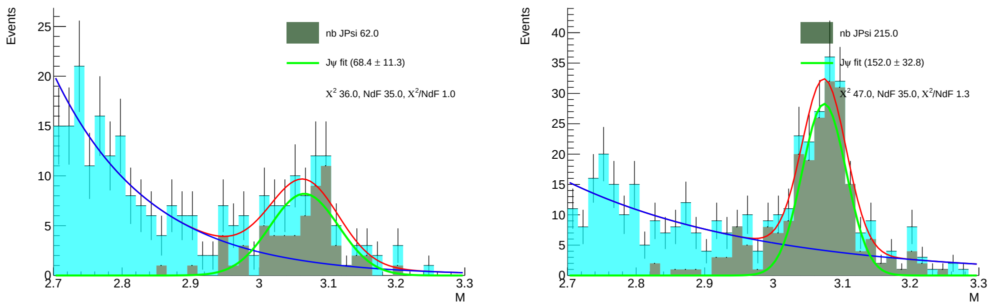

(a) $-t \in [0.5, 0.75]$ GeV^2 (b) $-t \in [0.75, 1.0]$ GeV^2

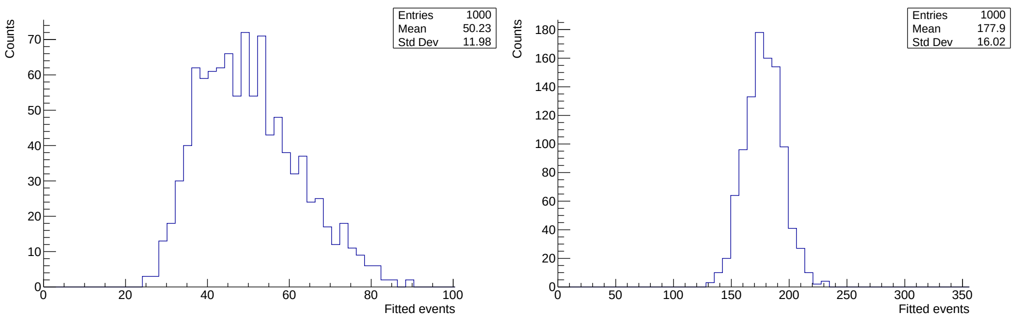

(c) $-t \in [0.5, 0.75]$ GeV^2 (d) $-t \in [0.75, 1.0]$ GeV^2

Figure 105: Acceptance fits for the differential cross section

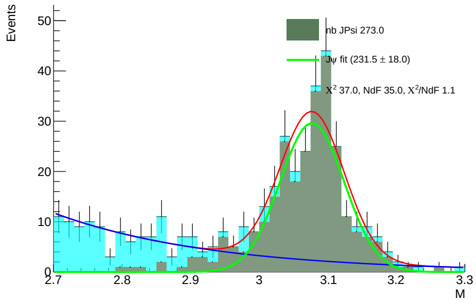

(a) $-t \in [1.0, 1.25]$ GeV^2

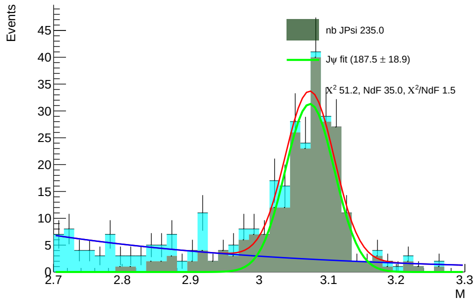

(b) $-t \in [1.25, 1.5]$ GeV^2

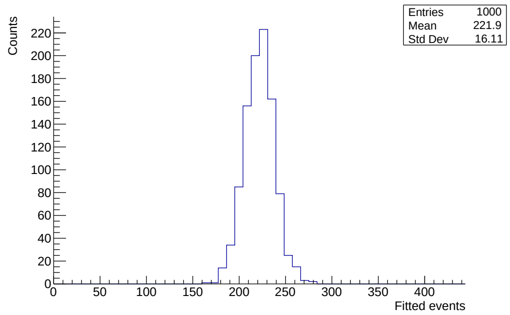

(c) $-t \in [1.O, 1.25]$ GeV^2

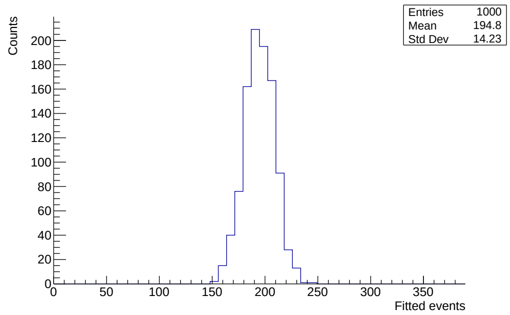

(d) $-t \in [1.25, 1.5]$ GeV^2

Figure 106: Acceptance fits for the differential cross section

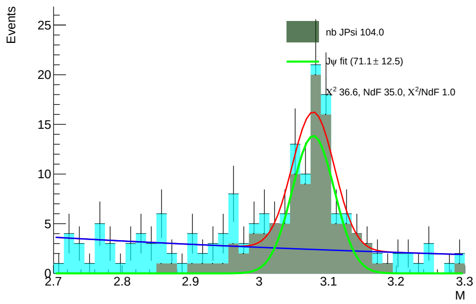

(a) $-t \in [1.5, 1.75]$ GeV^2

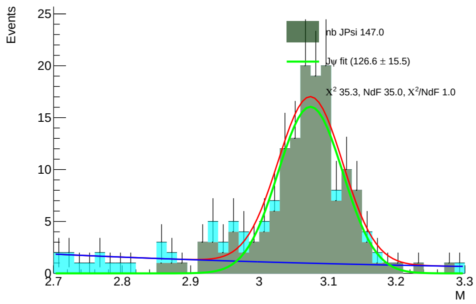

(b) $-t \in [1.75, 2.0]$ GeV^2

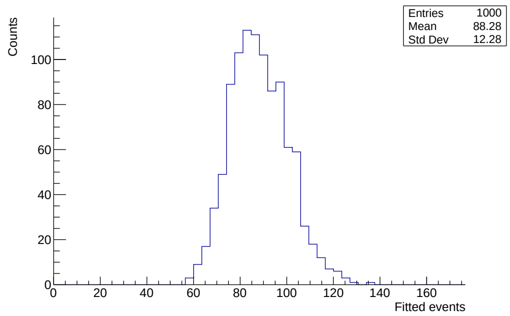

(c) $-t \in [1.5, 1.75]$ GeV^2

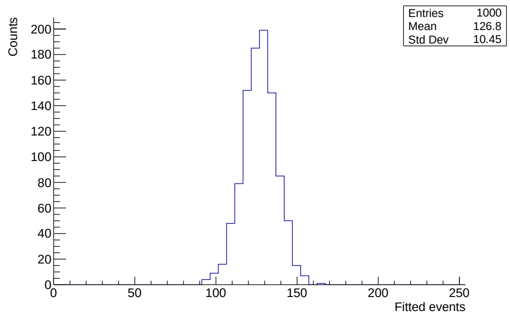

(d) $-t \in [1.75, 2.0]$ GeV^2

Figure 107: Acceptance fits for the differential cross section

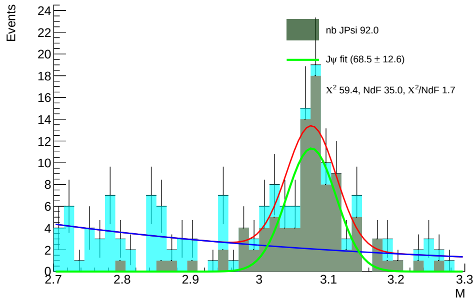

(a) $-t \in [2.0, 2.5]$ GeV^2

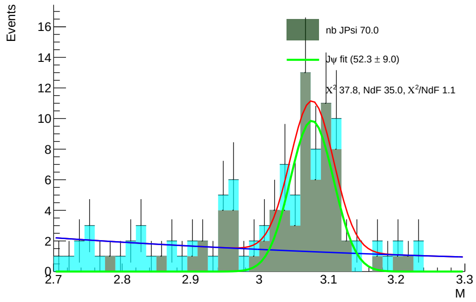

(b) $-t \in [2.5, 3.0]$ GeV^2

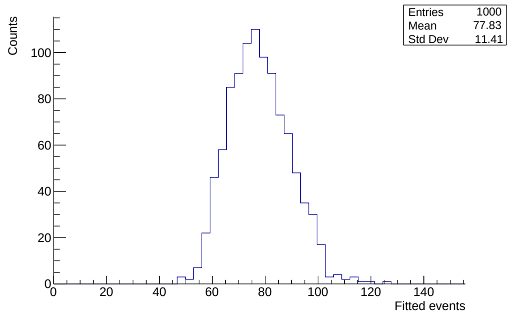

(c) $-t \in [2.0, 2.5]$ GeV^2

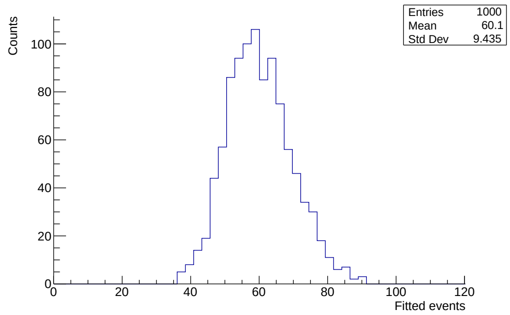

(d) $-t \in [2.5, 3.0]$ GeV^2

Figure 108: Acceptance fits for the differential cross section

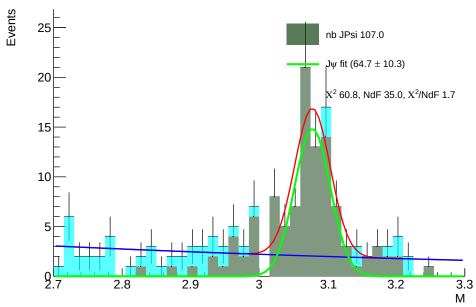

(a) $-t \in [3.0, 6.0]$ GeV^2

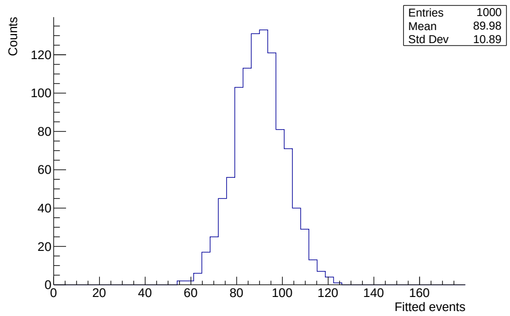

(b) $-t \in [3.0, 6.0]$ GeV^2

Figure 109: Acceptance fits for the differential cross section

1116 I.3 $E_\gamma \in [10.00, 10.60]$ GeV

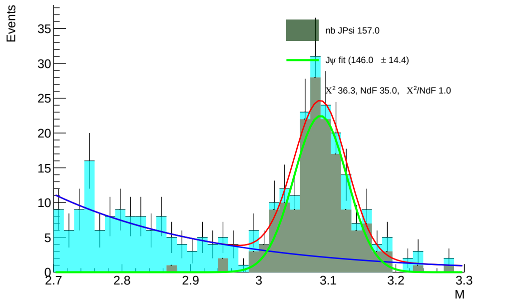

(a) $-t \in [0.5, 0.7]$ GeV^2

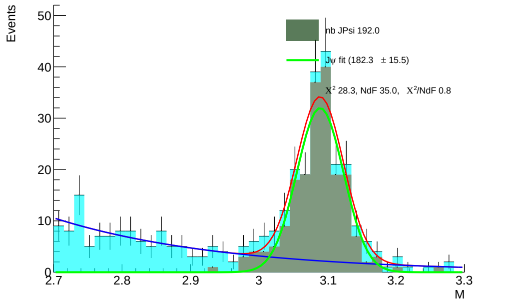

(b) $-t \in [0.7, 0.9]$ GeV^2

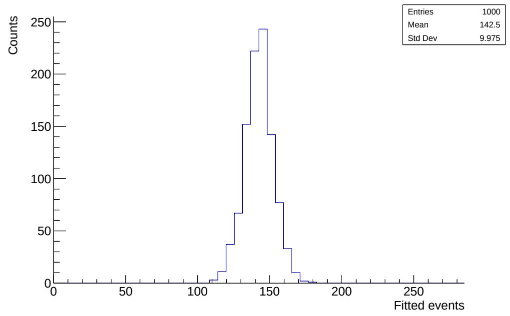

(c) $-t \in [0.5, 0.7]$ GeV^2

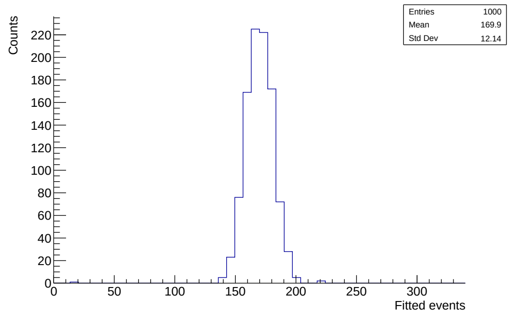

(d) $-t \in [0.7, 0.9]$ GeV^2

Figure 110: Acceptance fits for the differential cross section

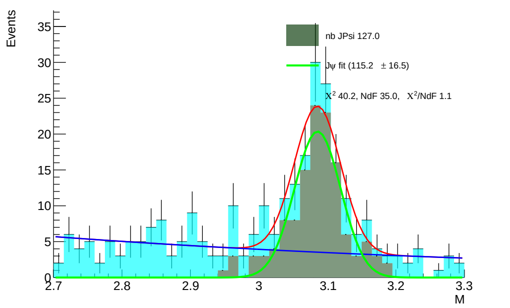

(a) $-t \in [0.9, 1.1]$ GeV^2

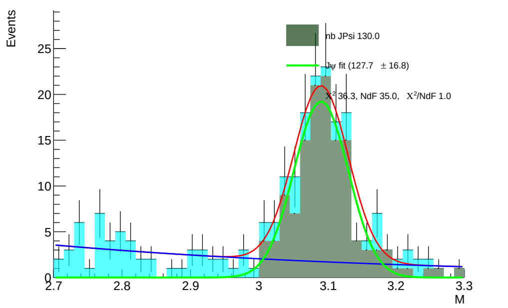

(b) $-t \in [1.1, 1.3]$ GeV^2

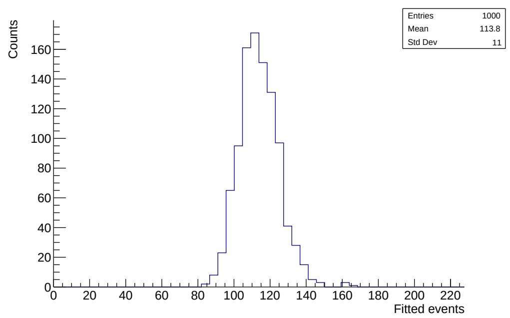

(c) $-t \in [0.9, 1.1]$ GeV^2

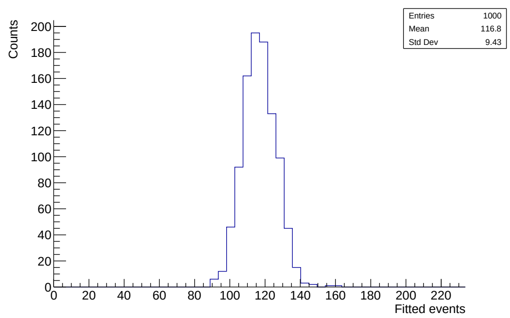

(d) $-t \in [1.1, 1.3]$ GeV^2

Figure 111: Acceptance fits for the differential cross section

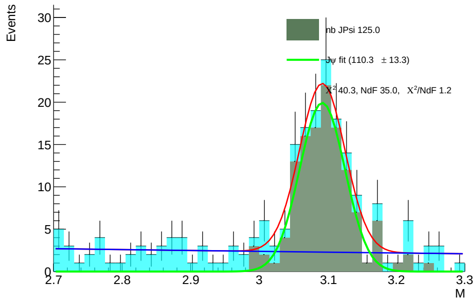

(a) $-t \in [1.3, 1.6]$ GeV^2

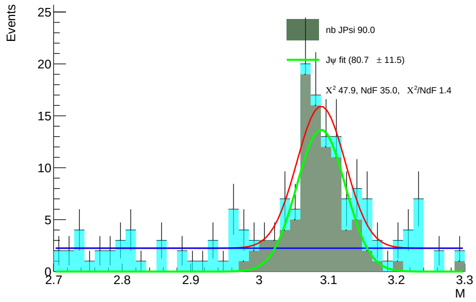

(b) $-t \in [1.6, 2.0]$ GeV^2

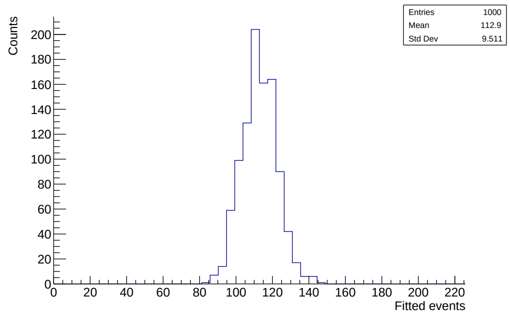

(c) $-t \in [1.3, 1.6]$ GeV^2

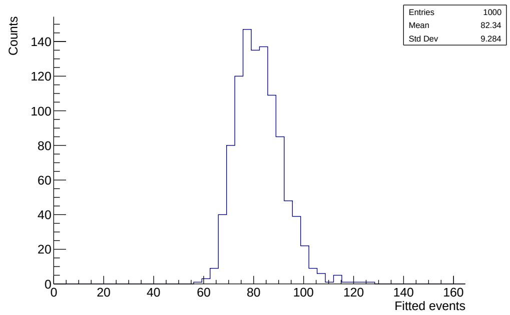

(d) $-t \in [1.6, 2.0]$ GeV^2

Figure 112: Acceptance fits for the differential cross section

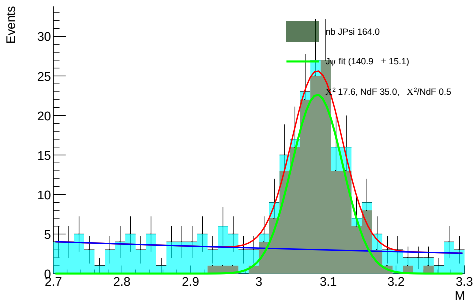

(a) $-t \in [2.0, 4.5]$ GeV^2

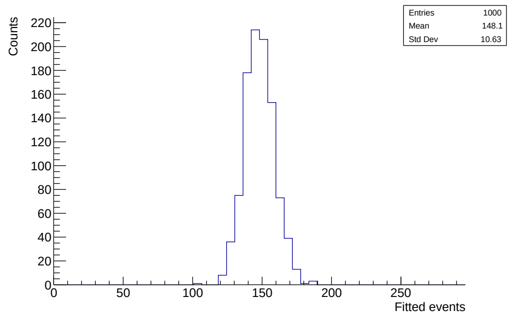

(b) $-t \in [2.0, 4.5]$ GeV^2

Figure 113: Acceptance fits for the differential cross section

J Fall 2018 inbending dataset: 1D comparison in the training region

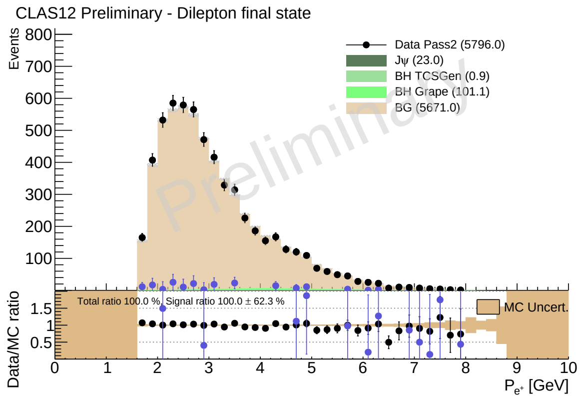

(a) Positron momentum

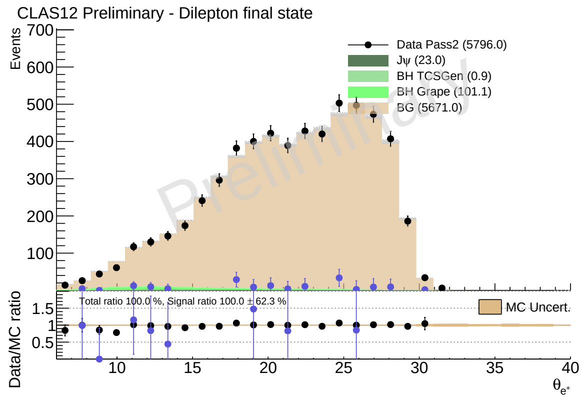

(b) Positron polar angle

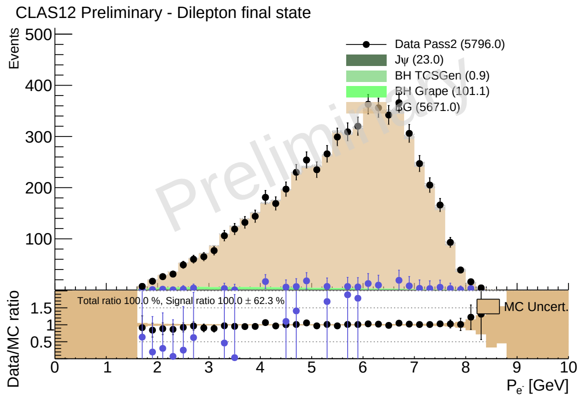

(c) Electron momentum

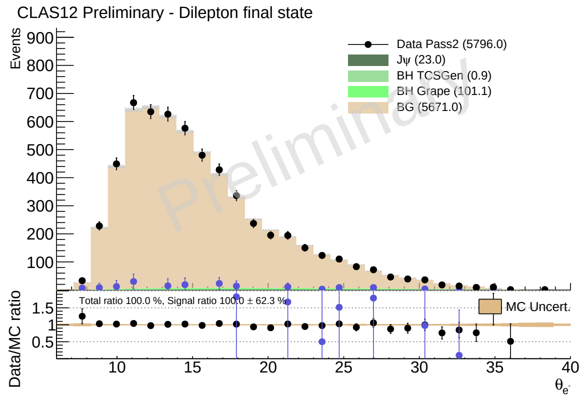

(d) Electron polar angle

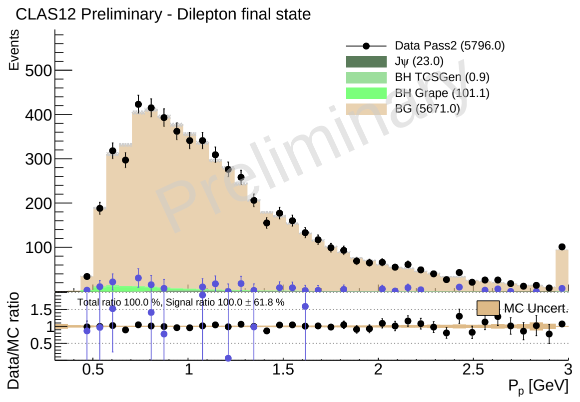

(e) Proton momentum

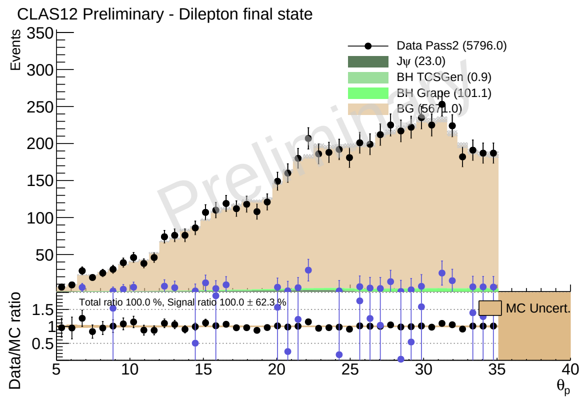

(f) Proton polar angle

Figure 114: Inbending Fall 2018, training region: Particle kinematics

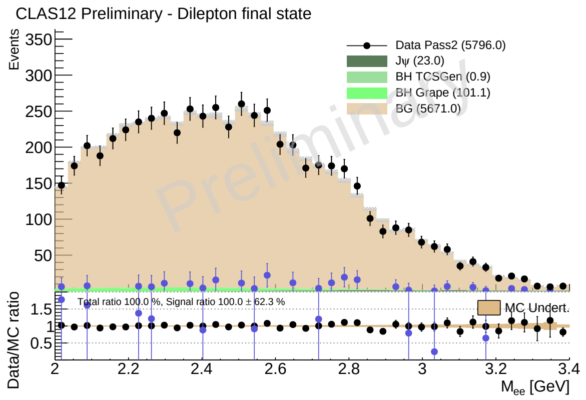

(a) Lepton invariant mass

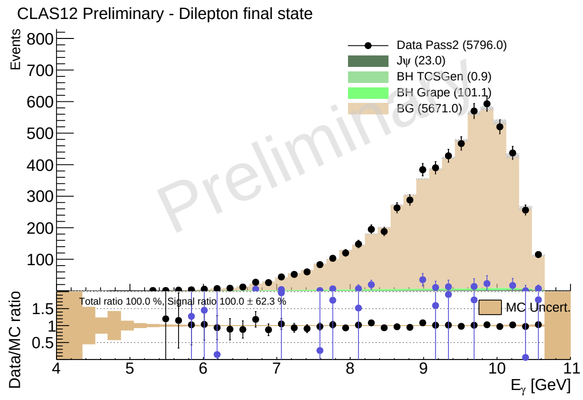

(b) Photon energy

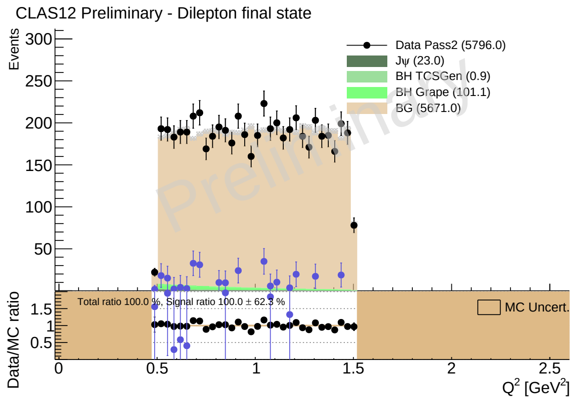

(c) Reconstructed virtuality of the photon

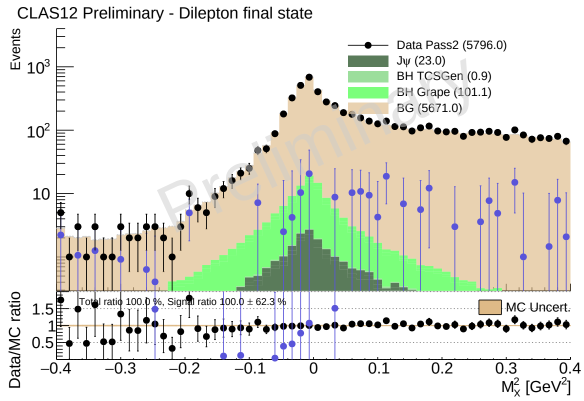

(d) Missing mass squared

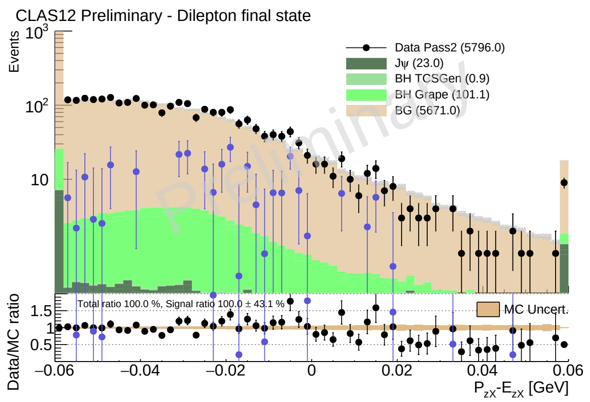

(e) Momentum-Energy imbalance of the missing particlecle

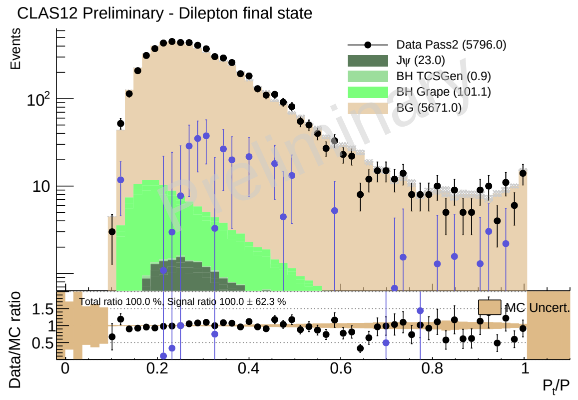

(f) Transverse momentum fraction of the missing parti-

Figure 115: Inbending Fall 2018, training region: reaction kinematics

K Fall 2018 inbending dataset: 1D comparison in the signal region

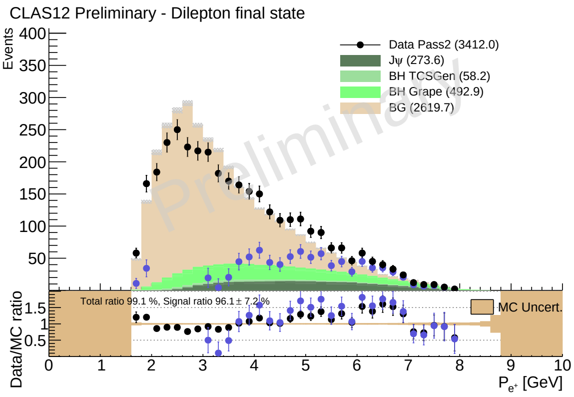

(a) Positron momentum

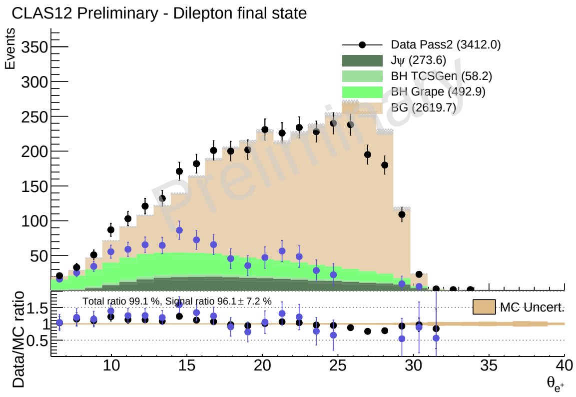

(b) Positron polar angle

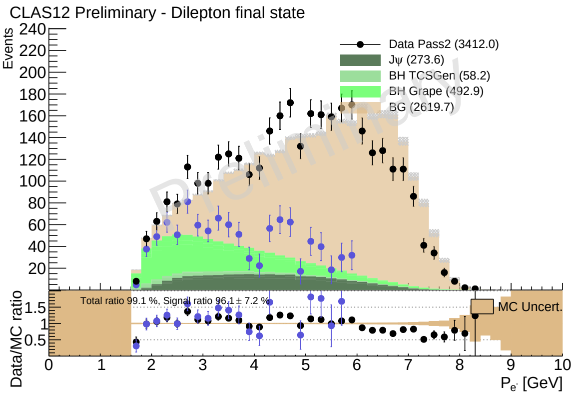

(c) Electron momentum

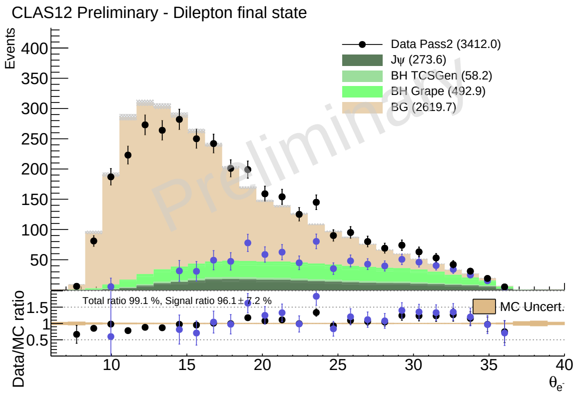

(d) Electron polar angle

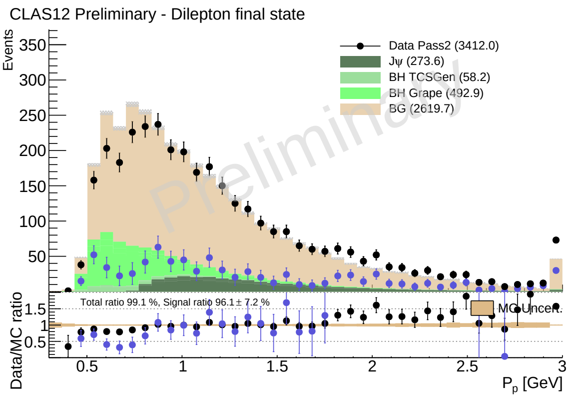

(e) Proton momentum

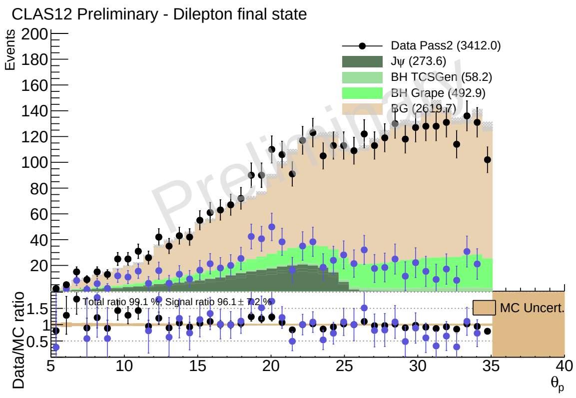

(f) Proton polar angle

Figure 116: Inbending Fall 2018, signal region: Particle kinematics

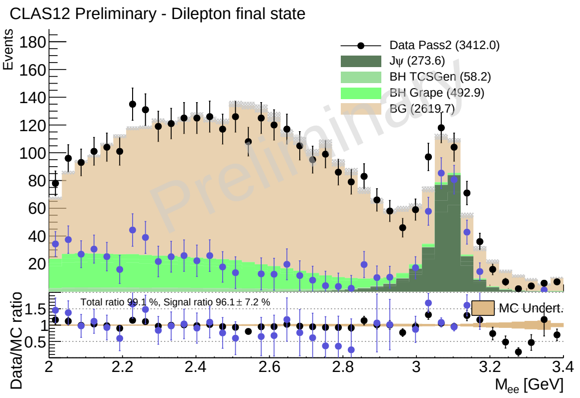

(a) Lepton invariant mass

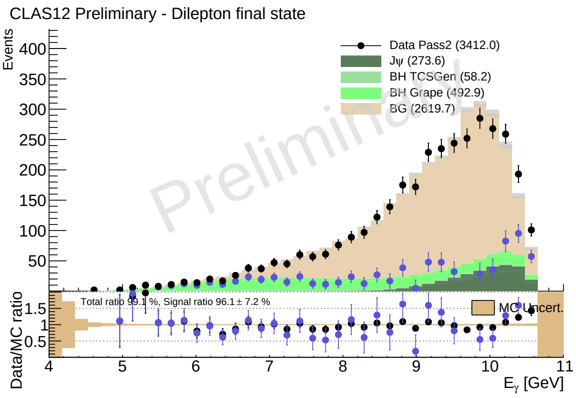

(b) Photon energy

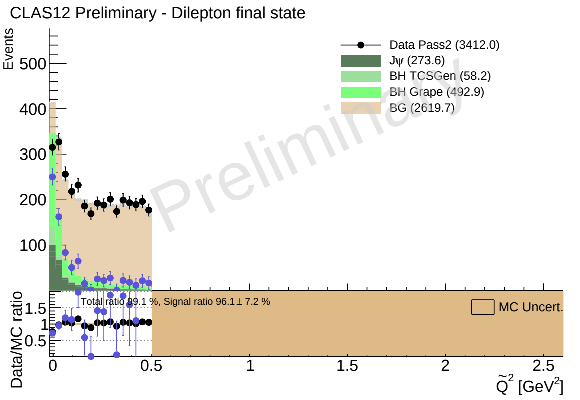

(c) Reconstructed virtuality of the photon

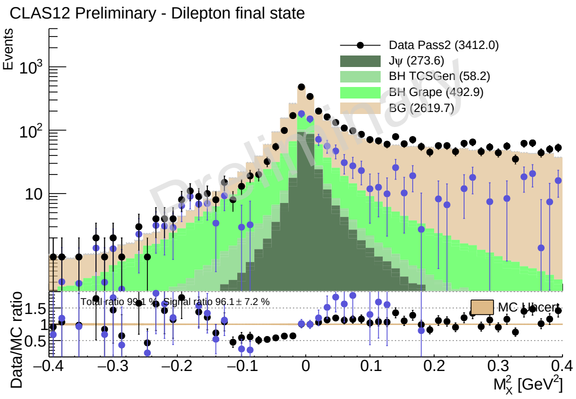

(d) Missing mass squared

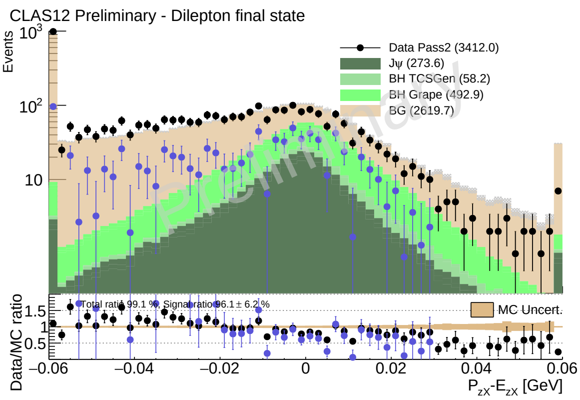

(e) Momentum-Energy imbalance of the missing particlecle

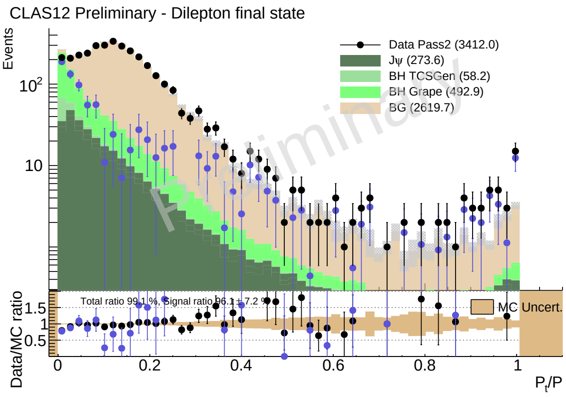

(f) Transverse momentum fraction of the missing parti-

Figure 117: Inbending Fall 2018, signal region: reaction kinematics

L Fall 2018 inbending dataset: 1D comparison in the validation region

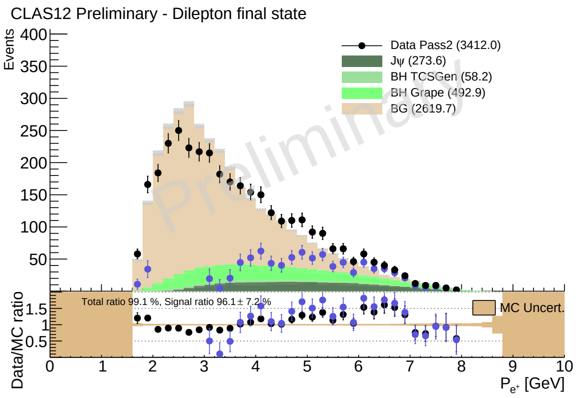

(a) Positron momentum

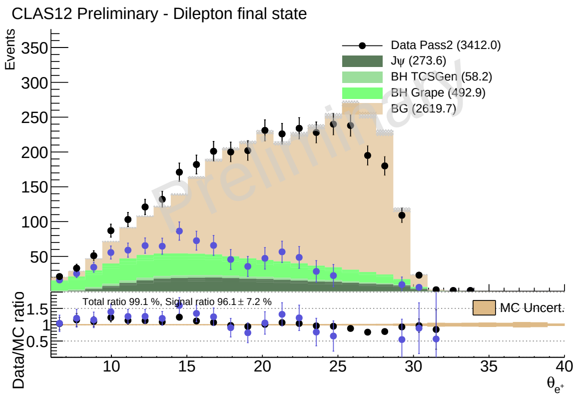

(b) Positron polar angle

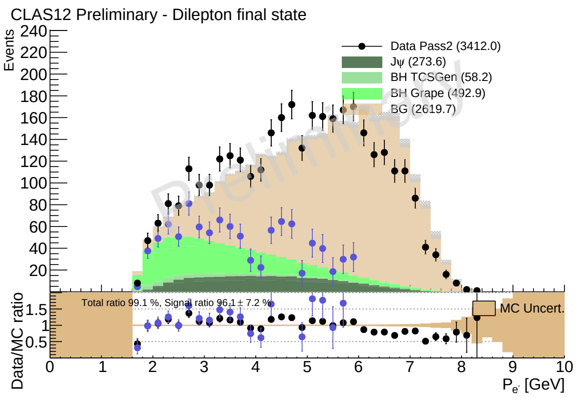

(c) Electron momentum

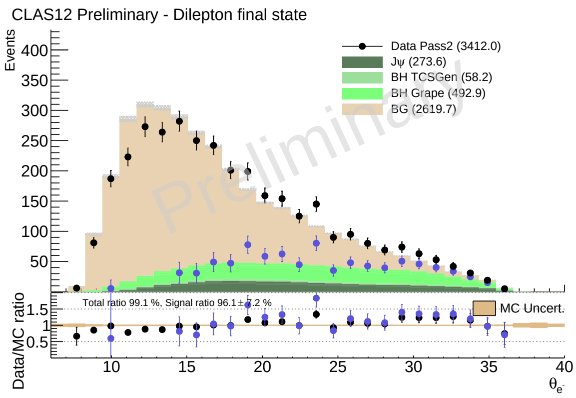

(d) Electron polar angle

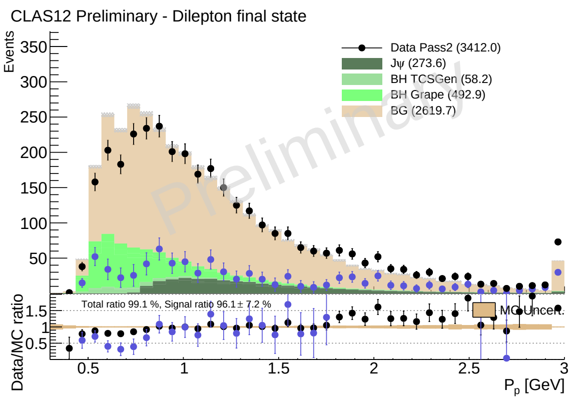

(e) Proton momentum

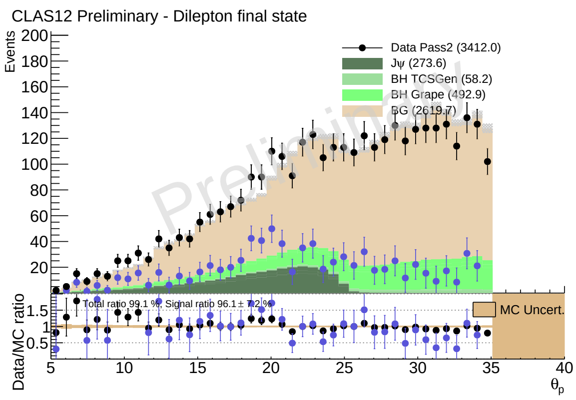

(f) Proton polar angle

Figure 118: Inbending Fall 2018, validation region: Particle kinematics

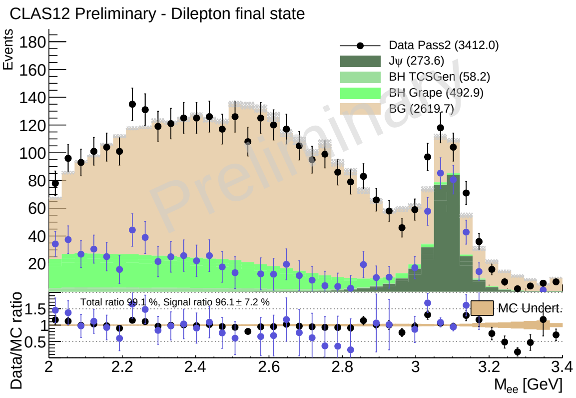

(a) Lepton invariant mass

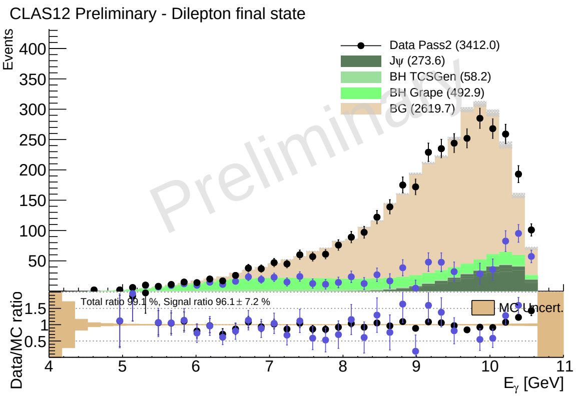

(b) Photon energy

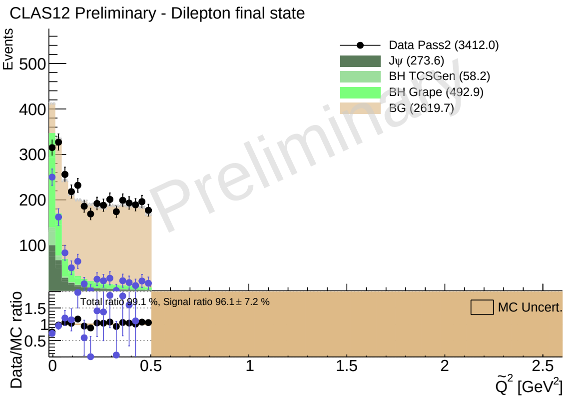

(c) Reconstructed virtuality of the photon

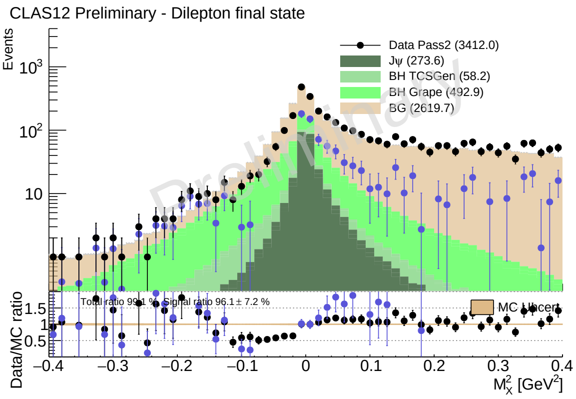

(d) Missing mass squared

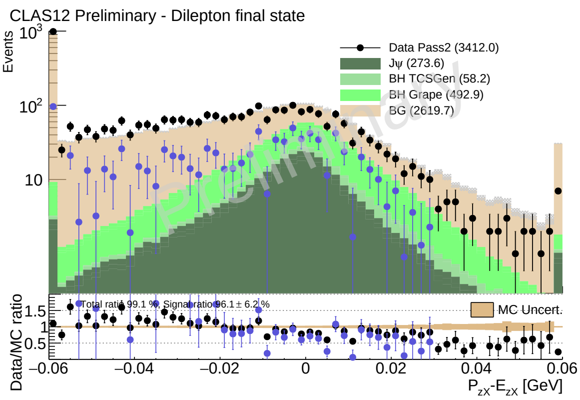

(e) Momentum-Energy imbalance of the missing particlecle

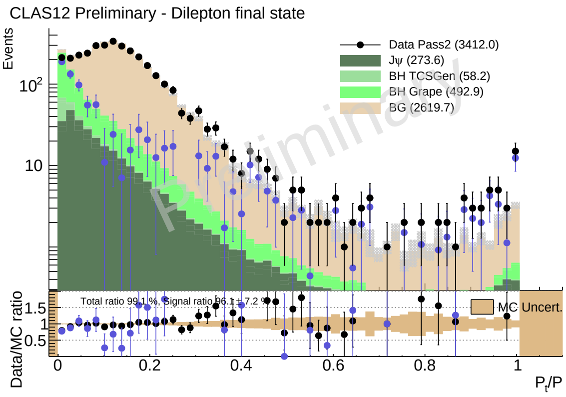

(f) Transverse momentum fraction of the missing parti-

Figure 119: Inbending Fall 2018, validation region: reaction kinematics

M Fall 2018 outbending dataset: 1D comparison in the signal region

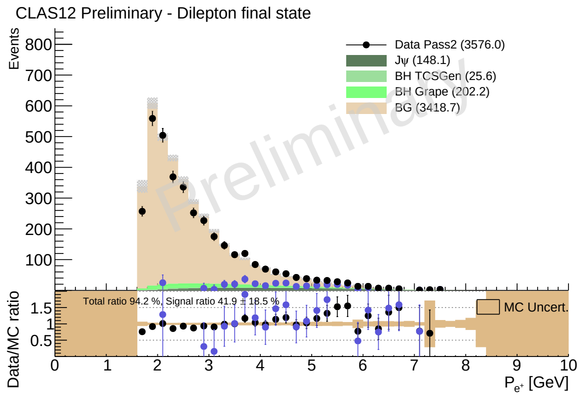

(a) Positron momentum

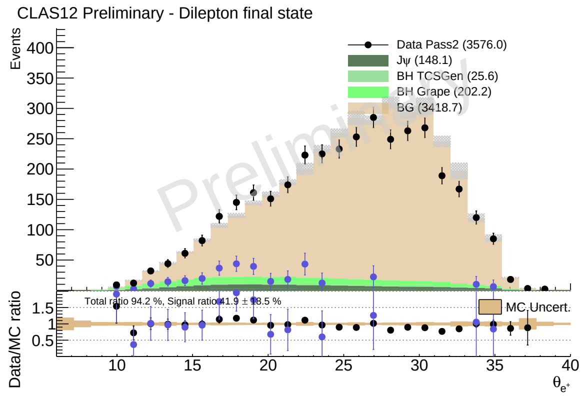

(b) Positron polar angle

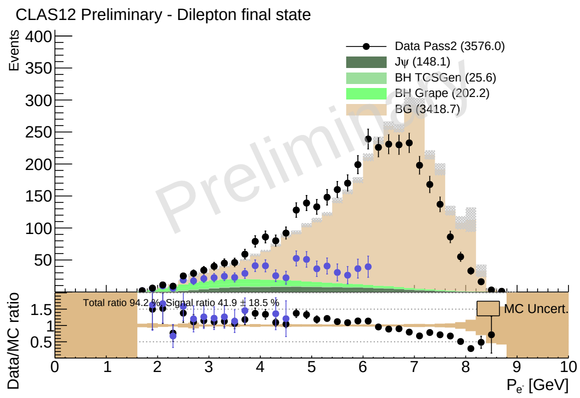

(c) Electron momentum

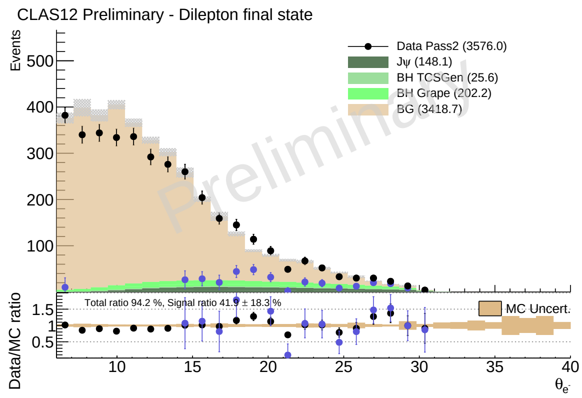

(d) Electron polar angle

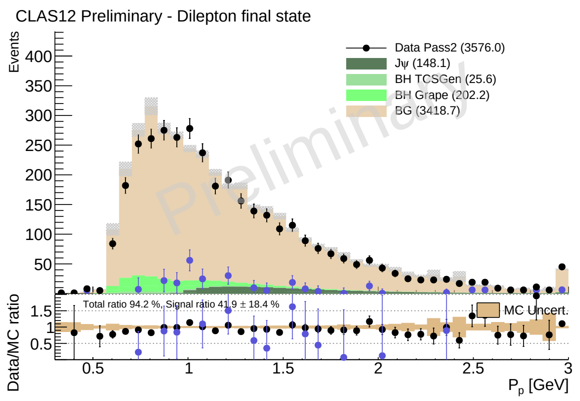

(e) Proton momentum

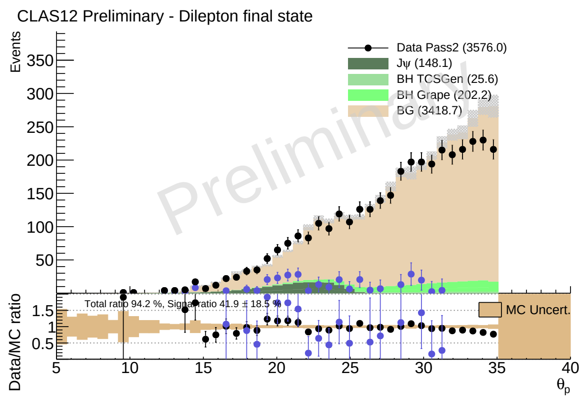

(f) Proton polar angle

Figure 120: Outbending Fall 2018, signal region: Particle kinematics

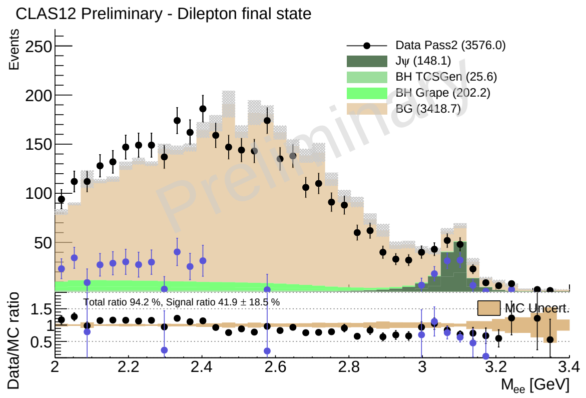

(a) Lepton invariant mass

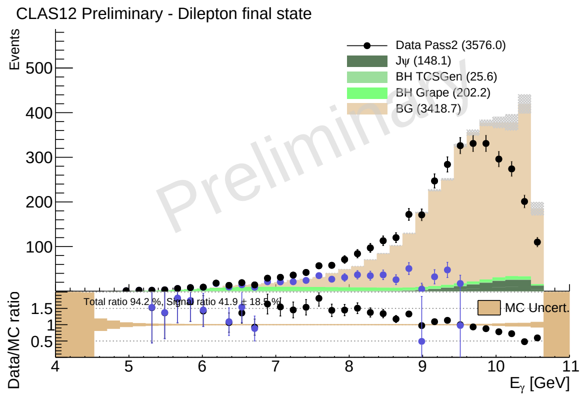

(b) Photon energy

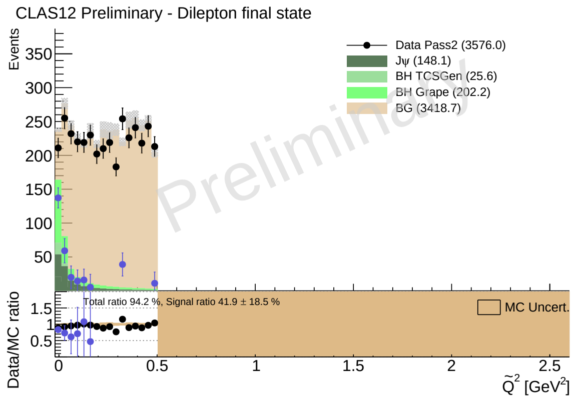

(c) Reconstructed virtuality of the photon

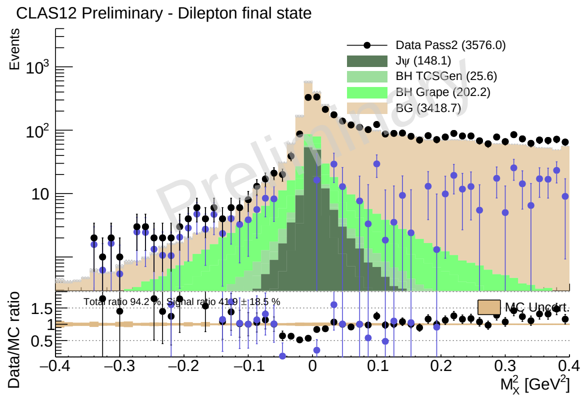

(d) Missing mass squared

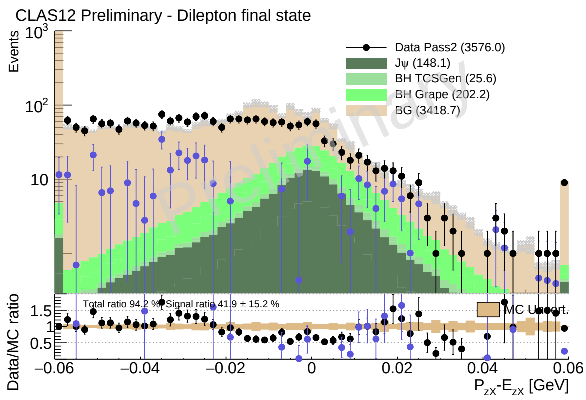

(e) Momentum-Energy imbalance of the missing particlecle

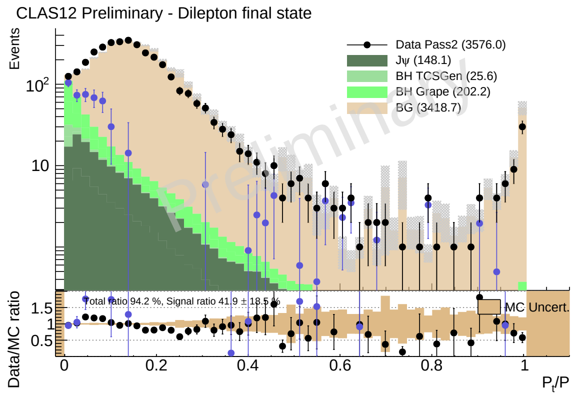

(f) Transverse momentum fraction of the missing parti-

Figure 121: Outbending Fall 2018, signal region: reaction kinematics

N Spring 2019 inbending dataset: 1D comparison in the signal region

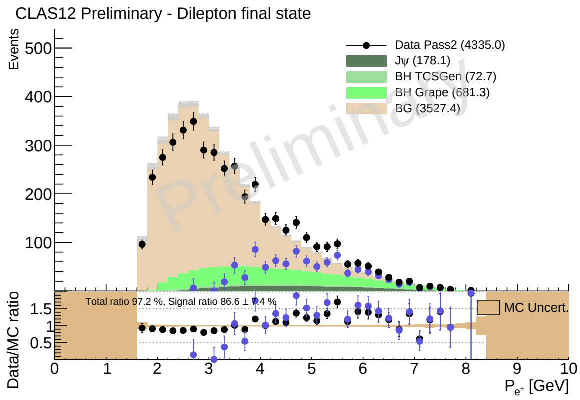

(a) Positron momentum

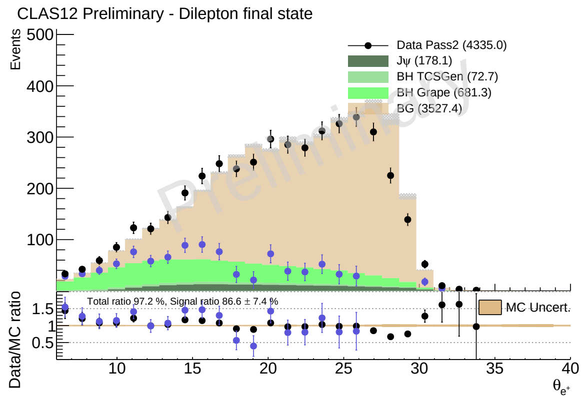

(b) Positron polar angle

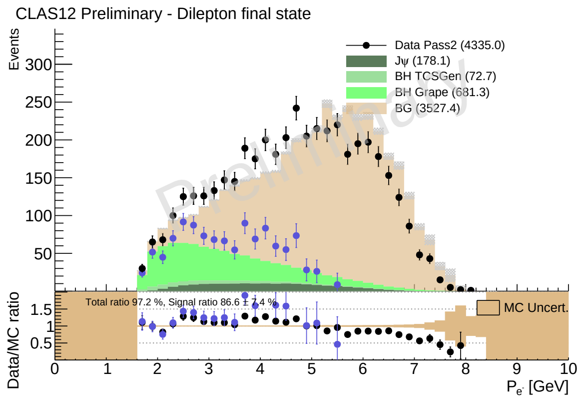

(c) Electron momentum

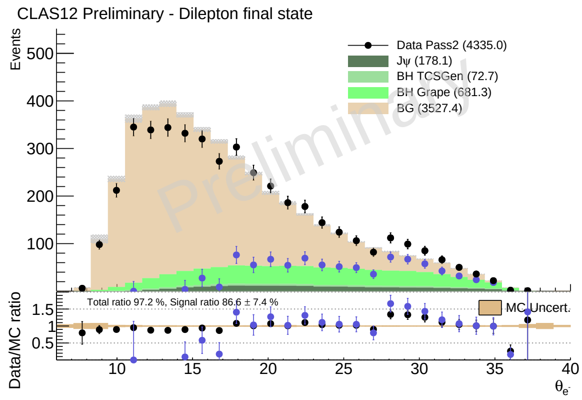

(d) Electron polar angle

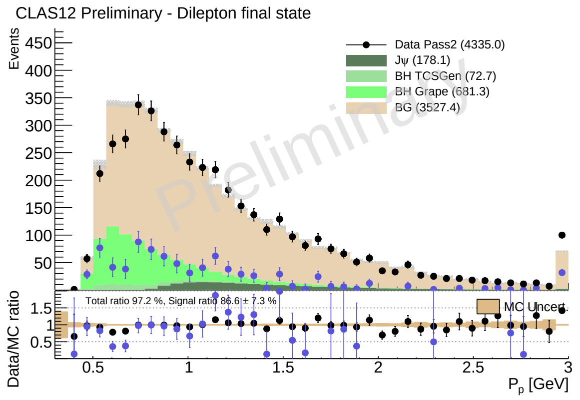

(e) Proton momentum

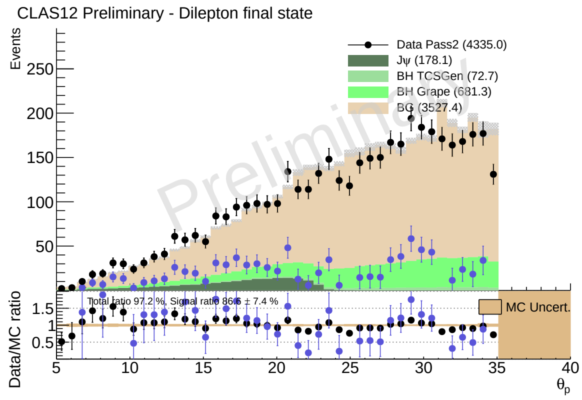

(f) Proton polar angle

Figure 122: Spring 2019, signal region: Particle kinematics

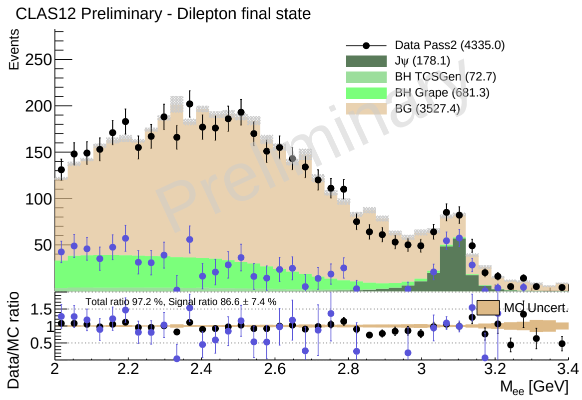

(a) Lepton invariant mass

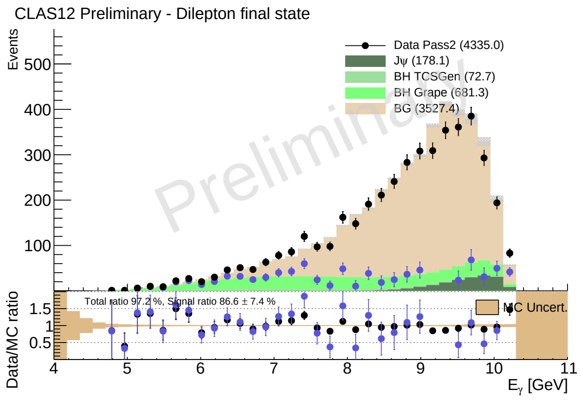

(b) Photon energy

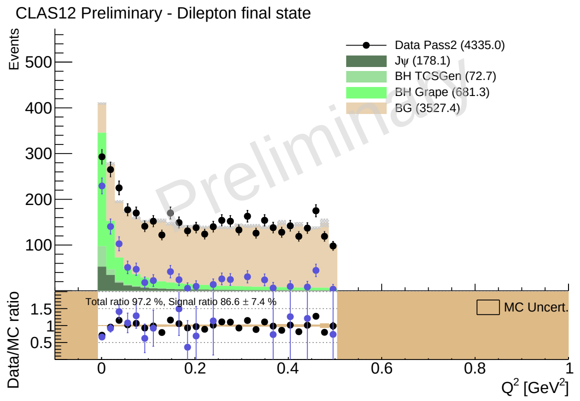

(c) Reconstructed virtuality of the photon

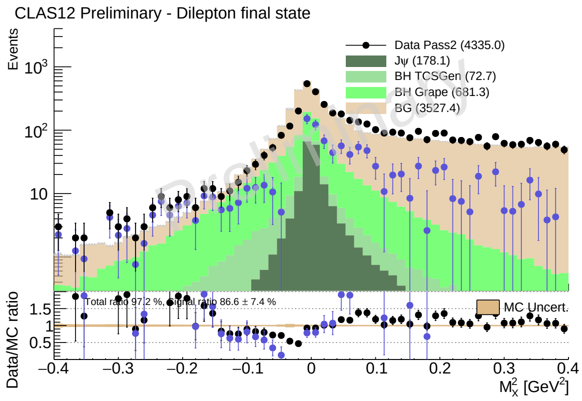

(d) Missing mass squared

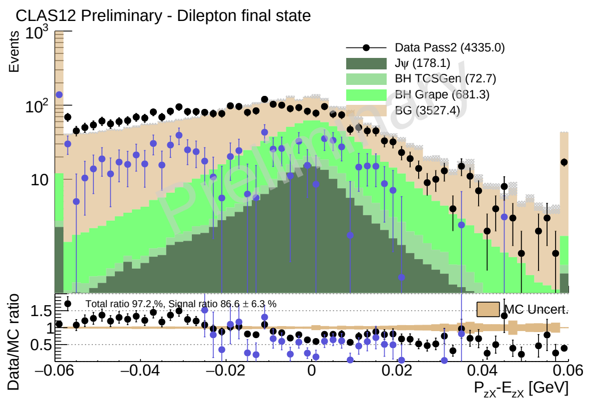

(e) Momentum-Energy imbalance of the missing particlecle

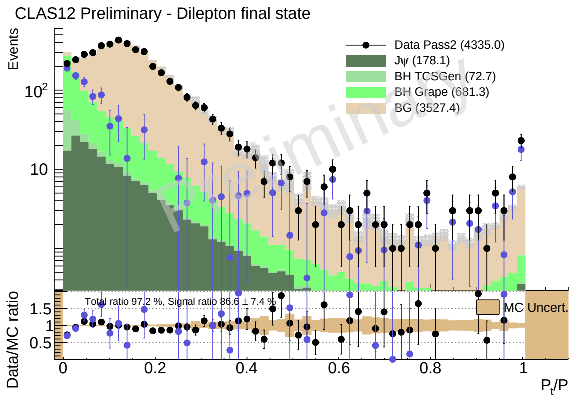

(f) Transverse momentum fraction of the missing parti-

Figure 123: Spring 2019, signal region: reaction kinematics

1124 # O Lepton identification based on Boosted Decision Trees

1125 ## O.1 Ratios MC/data

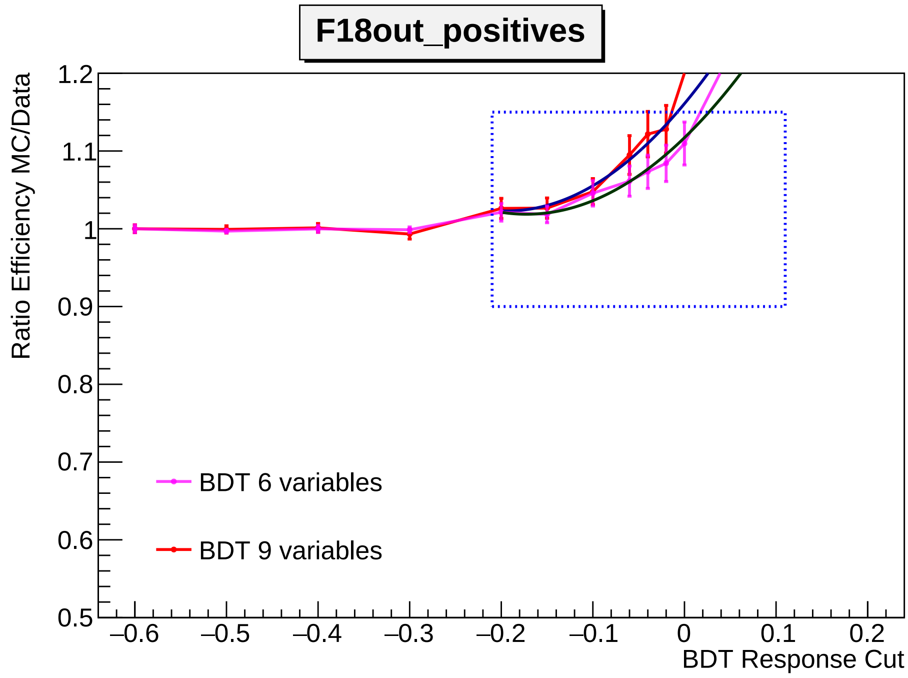

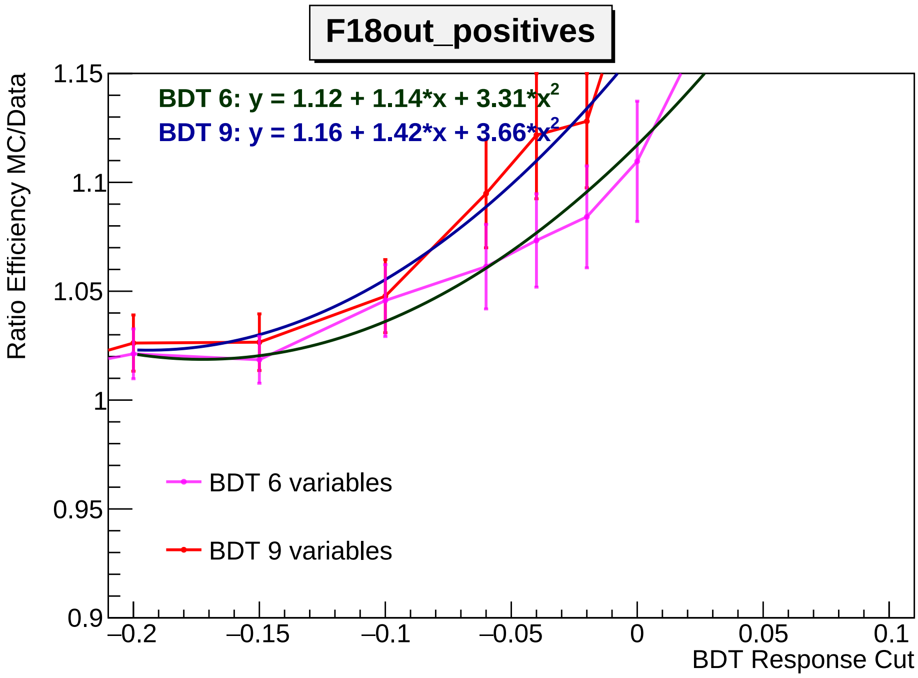

Figure 124: Ratios of efficiencies MC to data for positron identification classifiers for the Fall 2018 outbending data sets as a function of the cut in the response. The lower plot is a zoom in the region of the cut value at 0.0. The BDT used in this analysis is referenced as 'BDT 9 variables'.

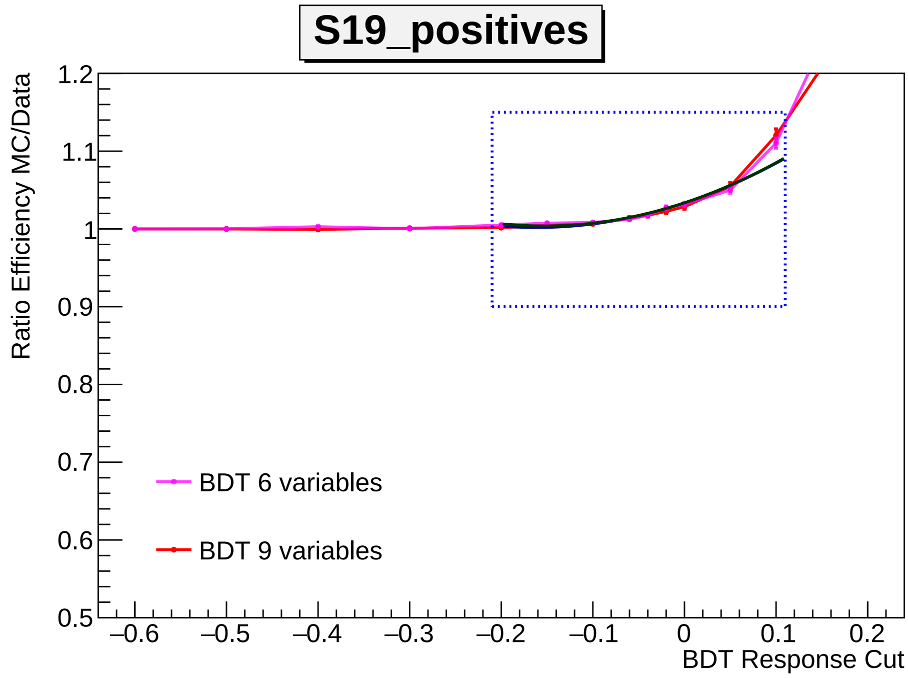

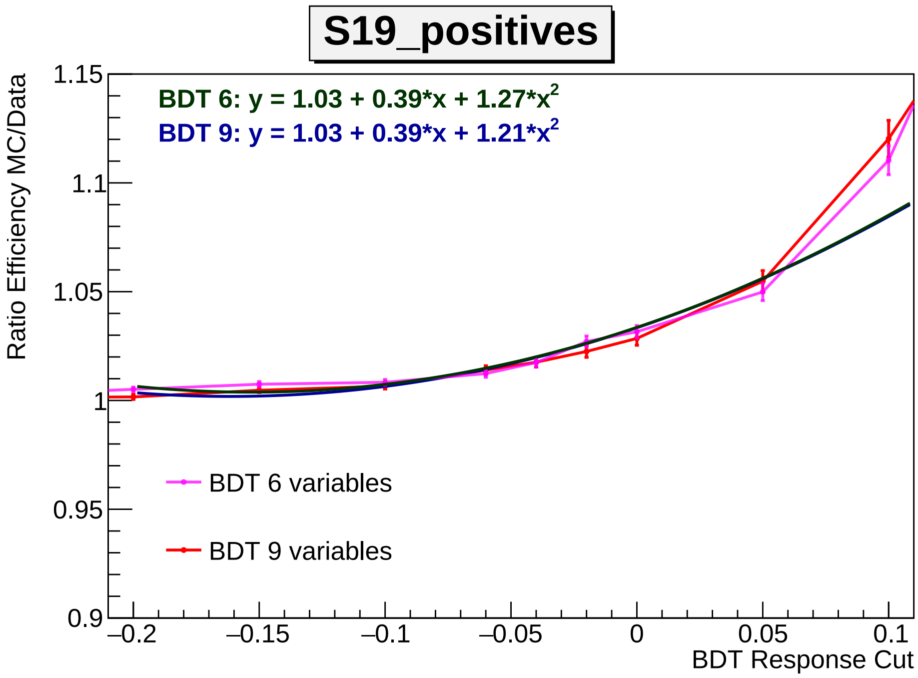

Figure 125: Ratios of efficiencies MC to data for positron identification classifiers for the Spring 2019 data sets as a function of the cut in the response. The lower plot is a zoom in the region of the cut value at 0.0.

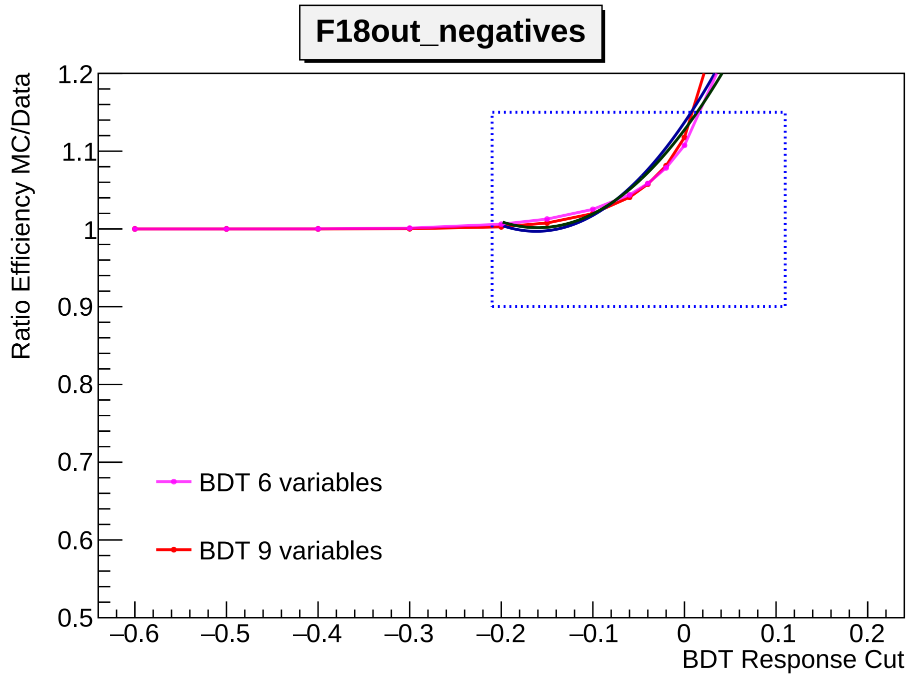

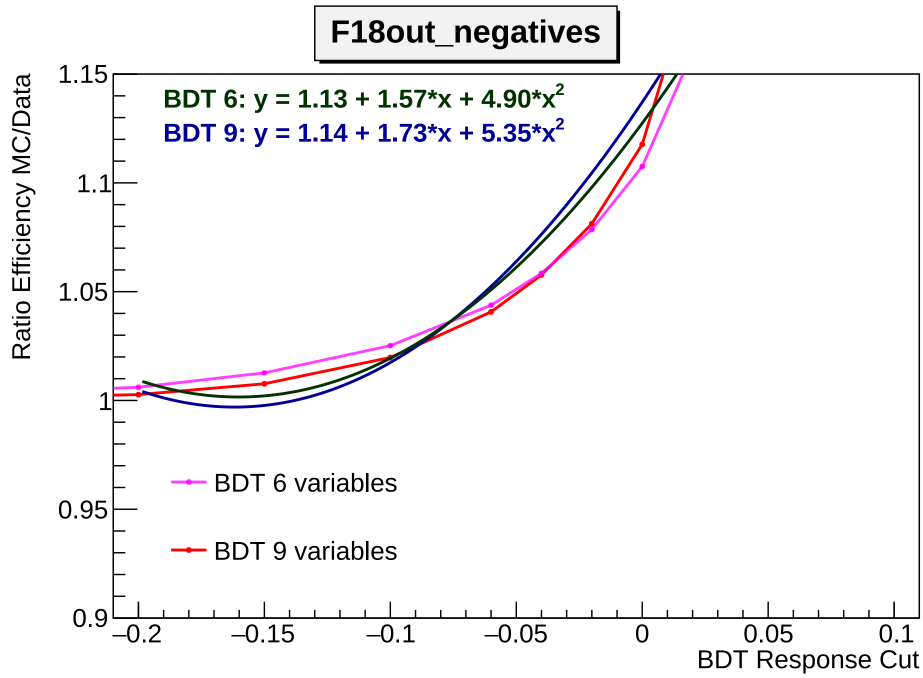

Figure 126: Ratios of efficiencies MC to data for electron identification classifiers for the Fall 2018 outbending data sets as a function of the cut in the response. The lower plot is a zoom in the region of the cut value at 0.0. The BDT used in this analysis is referenced as 'BDT 9 variables'.

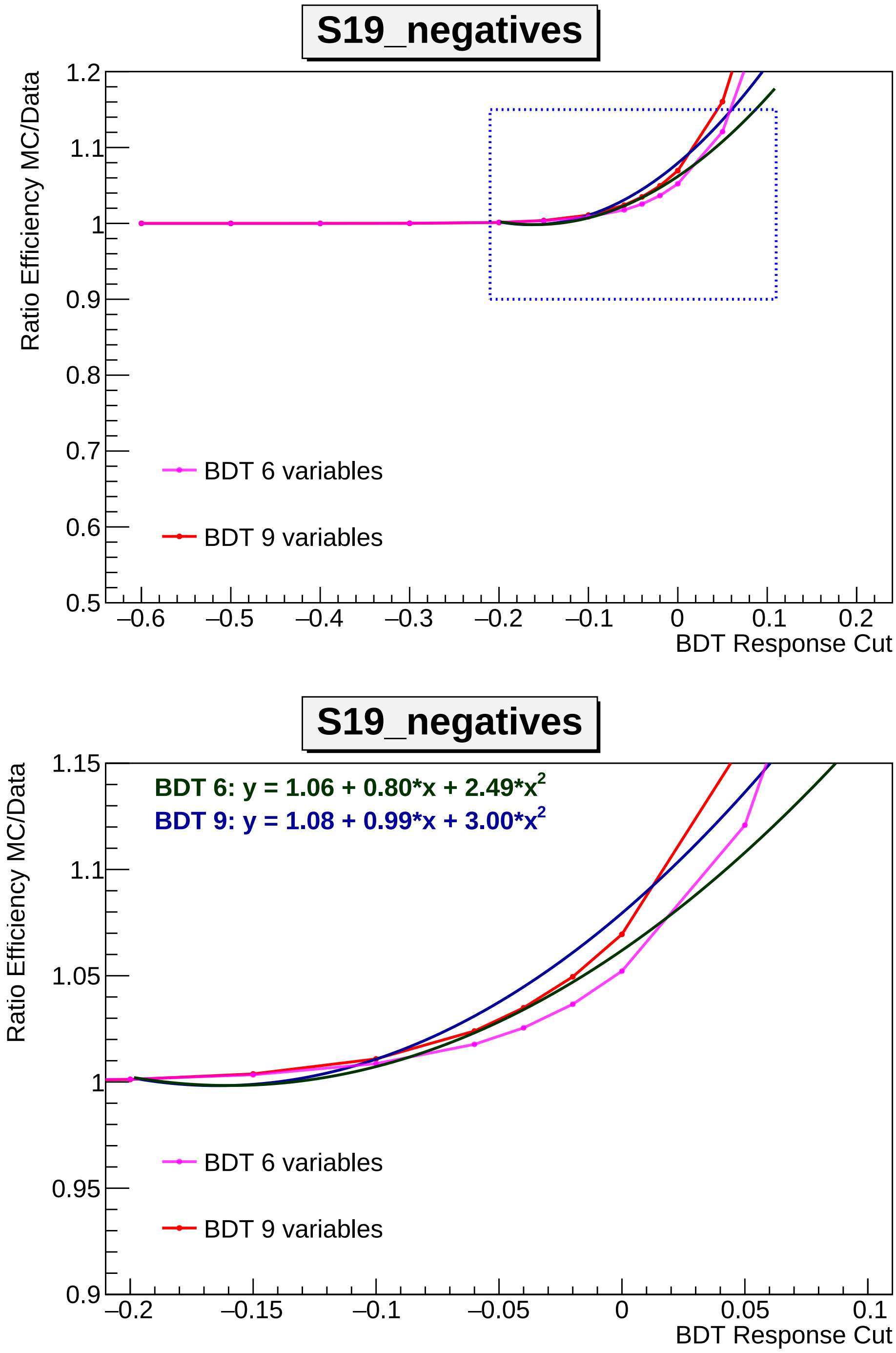

Figure 127: Ratios of efficiencies MC to data for electron identification classifiers for the Spring 2019 data sets as a function of the cut in the response. The lower plot is a zoom in the region of the cut value at 0.0.

P Radiative effects for Bethe-Heitler events

P.1 Formulae for the raditive effect in Bethe-Heitler

The cross-section of the BH process with soft photon emmission $\left(\frac{d\sigma}{dt\, ds_{ll}}\right)_{rad}$ is related to the Born-level cross section $\left(\frac{d\sigma}{dt\, ds_{ll}}\right)_0$ by the relation:

$$\left(\frac{d\sigma}{dt\, ds_{ll}}\right)_{rad} = \left(\frac{d\sigma}{dt\, ds_{ll}}\right)_0 (1+\delta). \tag{60}$$

The correction factor δ depends on the maximum energy of the radiative photon. It is given by the formula (64) of [41]:

$$\begin{aligned}\delta = -\left(\frac{\alpha}{\pi}\right)\Bigg\{&\left[\ln\left(\frac{4\Delta E_s^2}{m^2}\right) + \ln\left(\frac{1-\beta}{1+\beta}\right)\right]\left[1 + \left(\frac{1+\beta^2}{2\beta}\right)\ln\left(\frac{1-\beta}{1+\beta}\right)\right] \\ &+ \left(\frac{1-\beta}{\beta}\right)\ln\left(\frac{1-\beta}{1+\beta}\right) + \left(\frac{1+\beta^2}{2\beta}\right)\left[4\,\mathrm{Li}_2\left(\frac{2\beta}{1+\beta}\right) - \pi^2\right]\Bigg\},\end{aligned} \tag{61}$$

which reduces in the limit $s_{ll} >> 4m^2$ to:

$$\delta = -\left(\frac{\alpha}{\pi}\right)\left\{\ln\left(\frac{4\Delta E_s^2}{s_{ll}}\right)\left[1 + \ln\left(\frac{m^2}{s_{ll}}\right)\right] - \frac{\pi^2}{3}\right\}. \tag{62}$$

To account for the emission of multiple photons and higher order correction, on can exponentiate δ as in Equation (66) of [41]:

$$\begin{aligned}\left(\frac{d\sigma}{dt\, ds_{ll}}\right)_{\mathrm{s;tot}} &= \left(\frac{d\sigma}{dt\, ds_{ll}}\right)_0 \cdot F \exp\left\{-\frac{\alpha}{\pi}\left[\ln\left(\frac{4\Delta E_s^2}{m^2}\right) + \ln\left(\frac{1-\beta}{1+\beta}\right)\right]\left[1 + \left(\frac{1+\beta^2}{2\beta}\right)\ln\left(\frac{1-\beta}{1+\beta}\right)\right]\right\} \\ &\times\left\{1 - \frac{\alpha}{\pi}\left[\left(\frac{1-\beta}{\beta}\right)\ln\left(\frac{1-\beta}{1+\beta}\right) + \left(\frac{1+\beta^2}{2\beta}\right)\left[4\,\mathrm{Li}_2\left(\frac{2\beta}{1+\beta}\right) - \pi^2\right]\right]\right\} \\ &\equiv \left(\frac{d\sigma}{dt\, ds_{ll}}\right)_0 (1+\delta_{\mathrm{exp}}),\end{aligned} \tag{63}$$

where the factor F is given by:

$$F = 1 - \frac{\alpha^2}{3}\left[1 + \left(\frac{1+\beta^2}{2\beta}\right)\ln\left(\frac{1-\beta}{1+\beta}\right)\right]^2 + \ldots \tag{64}$$

In the case of Jlab kinematics, the factor F is equal to 1 at the sub-percent level. Furthermore Eq. 63 can be approximated using the formula for δ in Eq. 62. This lead to the following equation for the corrected cross-section once all approximation have been used:

$$\left(\frac{d\sigma}{dt\, ds_{ll}}\right)_{\mathrm{s;tot}} = \left(\frac{d\sigma}{dt\, ds_{ll}}\right)_0 \cdot \exp\left\{-\left(\frac{\alpha}{\pi}\right)\left\{\ln\left(\frac{4\Delta E_s^2}{s_{ll}}\right)\left[1 + \ln\left(\frac{m^2}{s_{ll}}\right)\right] - \frac{\pi^2}{3}\right\}\right\} \tag{65}$$

$$= \left(\frac{d\sigma}{dt\, ds_{ll}}\right)_0 (1 + \delta_{\mathrm{exp.\ approx.}}). \tag{66}$$

We can now derive the differential cross-section against the energy of the radiated photon E_s using:

$$\frac{d(1+\delta_{exp})}{dE_s} = \frac{d}{dE_s} exp\left\{-\left(\frac{\alpha}{\pi}\right)\left\{\ln\left(\frac{4\Delta E_s^2}{s_{ll}}\right)\left[1 + \ln\left(\frac{m^2}{s_{ll}}\right)\right] - \frac{\pi^2}{3}\right\}\right\} \tag{67}$$

$$= \frac{-\alpha}{\pi}\left[1 + \ln\left(\frac{m^2}{s_{ll}}\right)\right]\left(\frac{2}{E_s}\right) exp(\delta). \tag{68}$$

One can see that this formula diverges as $1/E_s^3$ in zero. However the integral is finite and equal to $1+\delta$.

P.2 Various checks and comparison with published results

In this section, we demonstrate that we can reproduce the results of [41]. Furthermore some validations are made of the various approximations discussed earlier. We also studied the various dependencies of the radiative correction factor δ.

In Figure 128 and 129, the results from Fig. 7 and Fig. 8 of [41] are reproduced. In this case, the invariant mass of the lepton pair ($M_{ee} = \sqrt{s_{ll}} = \sqrt{0.077}\ GeV$) is smaller than what we can measure with CLAS12. We also investigated the approximation made in Eq. 62 and Eq. 66 (ie, the first order approximation assuming . In both cases, the curve for the full formula and for the approximated ones match.

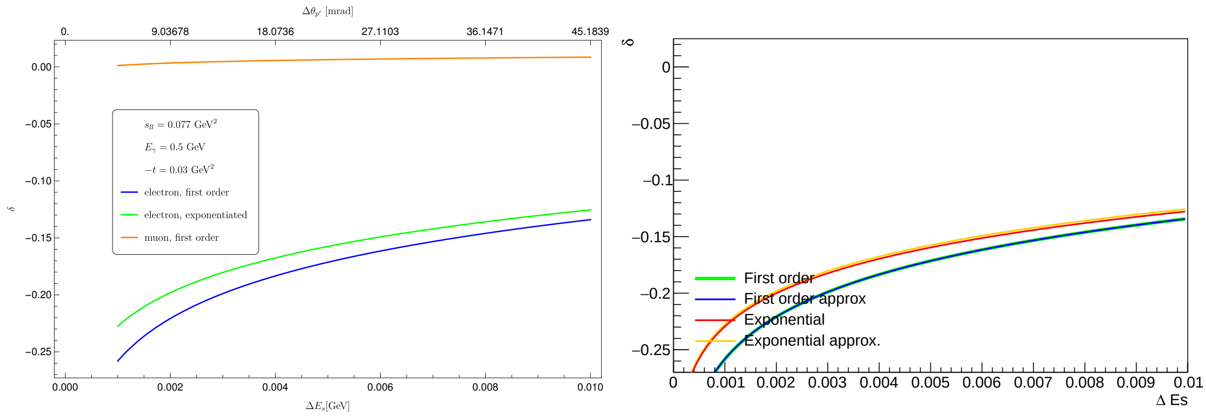

(a) (b)

Figure 128: Radiative correction factor calculation done in [41] a) and our calculation for the same hypothesis using various approximations b). We compared the computation of δ using the first order formula of Eq. 61, the first order approximated formula in Eq. 62, the exponential formula in Eq. 63 and the approximated exponential formula in Eq. 66.

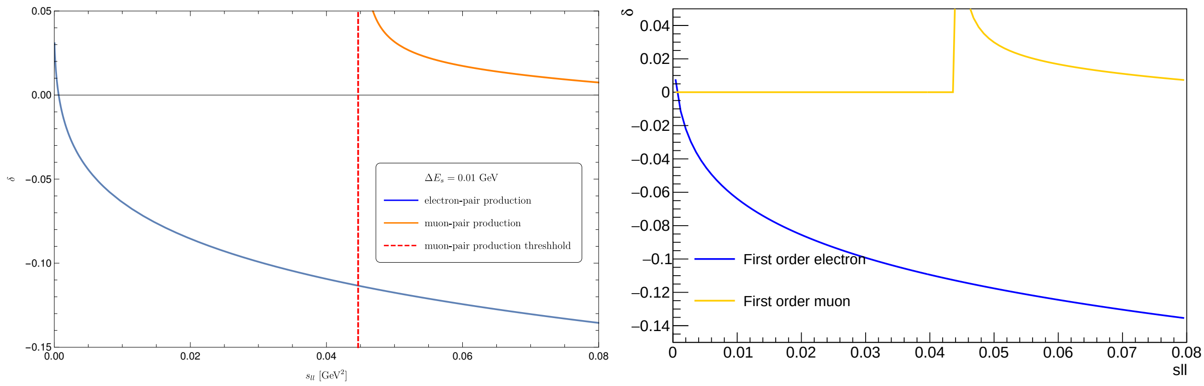

(a) (b)

Figure 129: Radiative correction factor calculation done in [?] a) and our calculation for the same hypothesis using various approximations b).

We further explore the dependence of δ in the range of invariant masses accessible by CLAS12 and for maximum energies of photons within reasonable values (see section **??**, where the energy of the radiated photons are extracted from data and are shown to be within the range 0.5 GeV to 0.01 GeV). In Figure 130, δ is calculated for invariant masses between 1 and 3.5 GeV for different values of ΔE_S. As expected from the formula, the radiative correction factor δ becomes larger in size as the maximum energy of the considered radiated photons decreases. For the case $\Delta E_S = 0.10\ GeV$, the 4 ways to calculate δ are compared. The first order calculation and its approximation are matching. This is also the case for the exponential formula and its approximation.

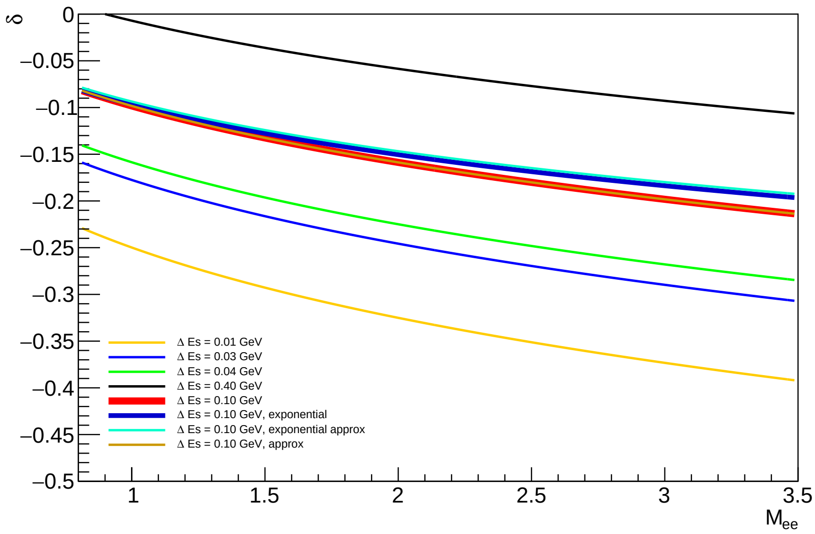

Figure 130: Study of the invariant mass dependence of radiative correction factor δ for various values of the maximum radiated photon energy ΔE_S. For the case $\Delta E_S = 0.10\ GeV$, the first order formula, the exponential formula and their approximation are used. For other cases, only the first order formula is plotted.

In Figure 131, the dependence of δ as a function of ΔE_S is explored. For the invariant mass of 3 GeV, the various ways to calculate δ are compared. Especially, the full exponential and approximate exponential computation of δ are compared. Both methods yield very close numbers. In Figure 132, the ΔE_S-dependence of δ is studied further, for invariant masses 1.5 GeV and 3 GeV. Again, we conclude that the approximated formula match the exact formulae. Thus based on these various results presented so far, we use in the following the approximated exponential formula.

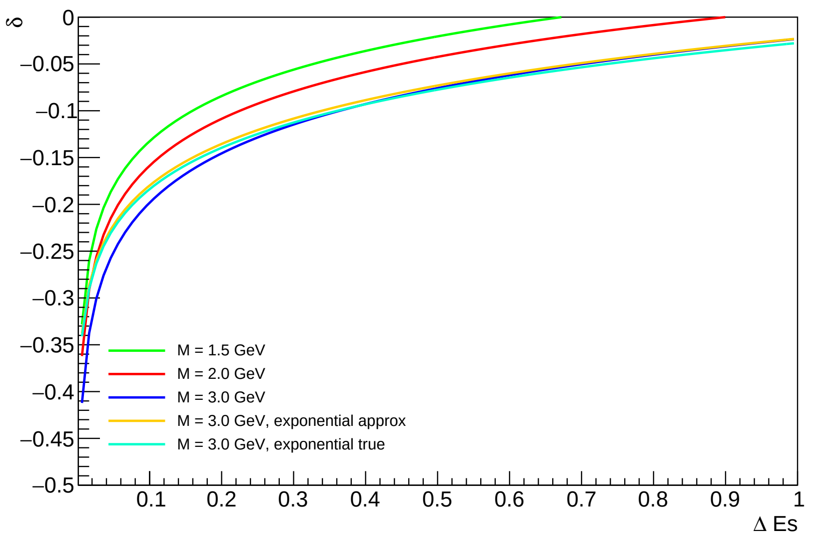

Figure 131: Study of the dependence on the maximum energy of the radiated photon on the radiative correction factor δ for various values of the invariant mass. For the invariant mass 3.0 GeV, the first order formula, the exponential formula and its approximation are shown. For other cases, only the first order formula is plotted.

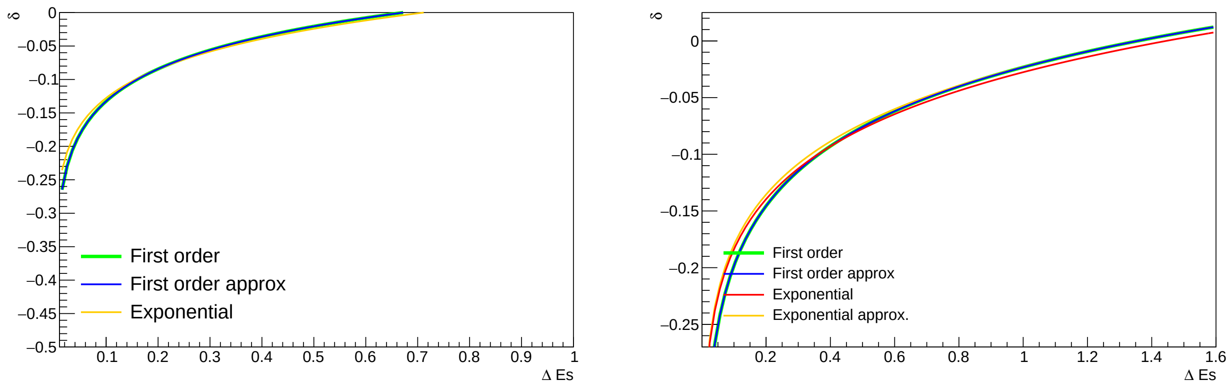

(a) (b)

Figure 132: Further study of the dependence on the maximum energy of the radiated photon on the radiative correction factor δ for two values of the invariant mass a) 1.5 GeV and b) 3.0 GeV. For the invariant mass 3.0 GeV, the exponential formula and its approximation are shown.

Finally, in order to validate the procedure to implement radiative effect in Monte-Carlo described in section P.3, we verify that δ vanishes for ΔE_S equal to its maximum, ie the energy of the leptons in the COM frame of the lepton pair $\Delta E_S = \sqrt{s}/2$. In Figure 133, *delta* is computed as a function of ΔE_S. In subfigure a), δ is calculated for the invariant mass 3.0 GeV and the value at $\Delta E_S = 1.5 GeV$ is computed. At this value of ΔE_S, $\delta = 0$. This is expected as all energy possible of radiated photons are taken into account in the calculation of the total cross-section. In subfigure b), the variation of δ is explored at small values of ΔE_S. The value of δ is always above -1. Thus δ can be considered as the fraction of events with radiated photon energy between 0 and ΔE_S.

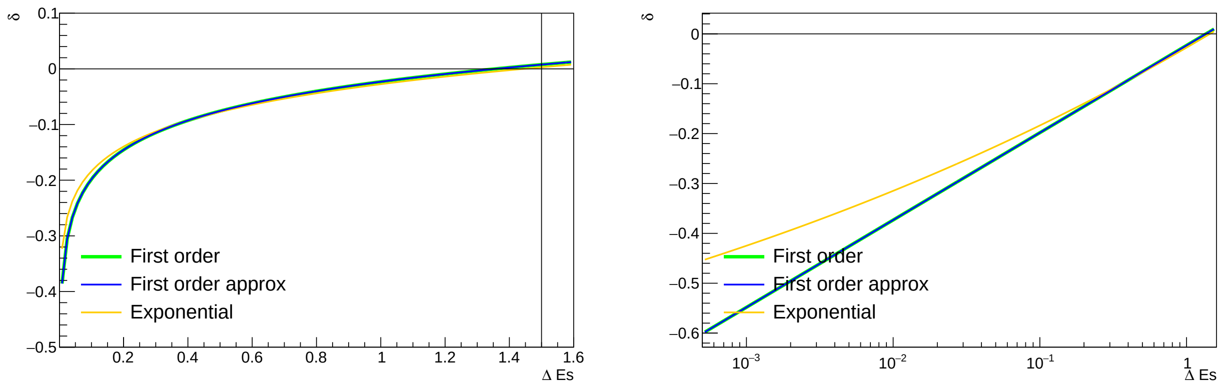

(a) (b)

Figure 133: Variation of *delta* as a function of ΔE_S for invariant mass of 3 GeV. On subfigure a), the line indicates $\delta = 0$ and $\Delta E_S = 1.5\ GeV$. On subfigure b) the x-axis is using log-scale to further study the lower range of ΔE_S.

P.3 Implementation of radiative photon in event generators

In the previous section, we derived the radiative correction factor based on data. In this approach, the maximum radiated photon energy is derived using the 4-momenta of the measured final state particles. One issue arises from this approach: the intrinsic resolution of CLAS12 is not taken into account and thus might bias our extraction of the radiative correction factor. In this section, the implementation of the radiative correction in the various MC generator used in this analysis is presented.

P.3.1 General considerations

The radiative factor δ can be interpreted in terms of probability for an event to have the emission of a soft photon in a certain range of energy. Especially, the factor $(1 + \delta_{exp})$ represents the probability to have the emission of soft photons carrying up to ΔE_S energy. Thus the derivative of $(1 + \delta_{exp})$ with respect to E_S, given in Eq. 68 give the probability to emit an energy within a range $E_S \pm dE_S$. We will refer to it as $\sigma_{\gamma R} = \frac{d}{dE_S}(1 + \delta_{exp})$. As already, mentioned in section P.1, the formula for $\sigma_{\gamma R}$ diverges as $1/E_S^3$ in zero, but additional diagrams are canceling the divergence of its integral $(1+\delta_{exp})$ as explained in [41]. Figure 134 shows $\sigma_{\gamma R}$ as a function of E_S for two invariant masses.

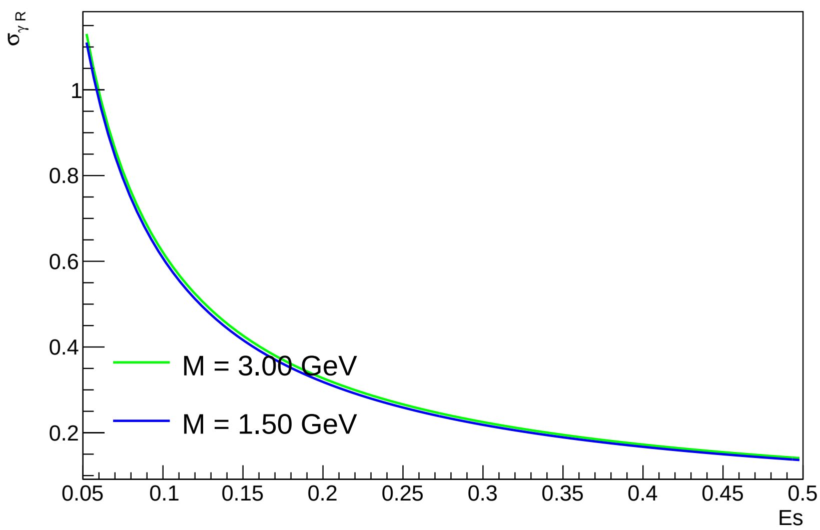

Figure 134: Probability $(1 + \delta_{exp})$ to radiate a photon as a function of the radiated energy. The distribution is diverging at small energy, thus we apply a cut-off on the minimum radiated energy and study its effect at a later stage.

P.3.2 Description of the algorithm

In order to implement the emission of soft photon in the ee-final state generator (JPsiGen, TCSGen and Grape), the following algorithm has been developed.

1 The range of soft photon energy is initial defined. The maximum energy of the soft photon in $\mathcal{S}$ is limited by half the invariant mass of the lepton pair $E_{S\ max} = \sqrt{s_{ll}}/2$ (For this value of photon energy, $(1 + \delta_{exp})$ is very close to 1). The minimum energy defines the lowest energy of soft photons that can be emitted. In theory, this energy cannot reach zero and the integral of $\sigma_{\gamma R}$ is finite. In practice, we test multiple value of $E_{S\ min}$ and use one where no effect of this cut off as impact on the analysis.

2 $(1+\delta_{exp})(E_{S\ min})$ is computed. This represents the probability to emit a soft photon with energy smaller than $E_{S\ min}$.

3 For each generated event:

- A random number $x \in [0, 1]$ is drawn.
- If $x < 1 + \delta$, then we consider that the soft photon emmited in this event has an energy smaller than $E_{S\ min}$. In this case, no soft photon is written by the algorithm.
- If $x > 1 + \delta$, then we consider that a soft photon with an energy larger than $E_{S\ min}$ is emitted.
  * An energy E_S randomly distributed between $E_{S\ min}$ and $E_{S\ max}$ according to $\sigma_{\gamma R}$ is drawn. Technically this is done using the *GetRandom* method of the Root TF1 class.

  - $*$ In the lepton pair CoM, soft photons must be emmited along the direction of the leptons. Two ways to emit the energy E_S have been implemented. In the first method, referred as V0, only one lepton (chosen randomly) emits a photon of energy E_S. In the second method, referred as V1, each lepton radiated a fraction of E_S.
  - $*$ The energy of the lepton in the CoM are recalculated according to the energy of the emmited sof photon.

  Figure 135 shows a schematic description of the algorithm used to determined if an event radiated a photon and which energy was radiated. Figure 136 shows the two ways to share the radiated energy between both final state leptons.

- The 4-momemta of the final state particles, including leptons and soft photons, are boosted to the Lab frame.

This algorithm is implemented in TCSGen and as a post-generation stage for Grape events.

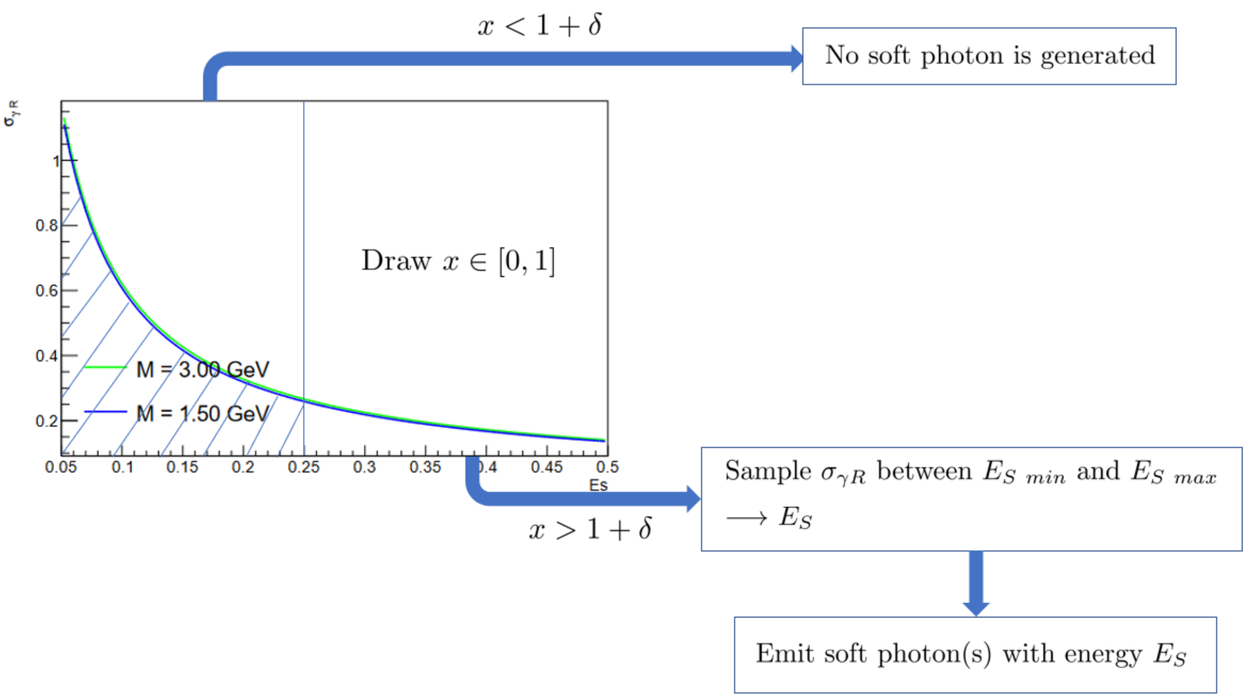

Figure 135: Schematic description of the algorythm used for each event to determined if the soft photon energy is large enough to be considered and how it is determined otherwise.

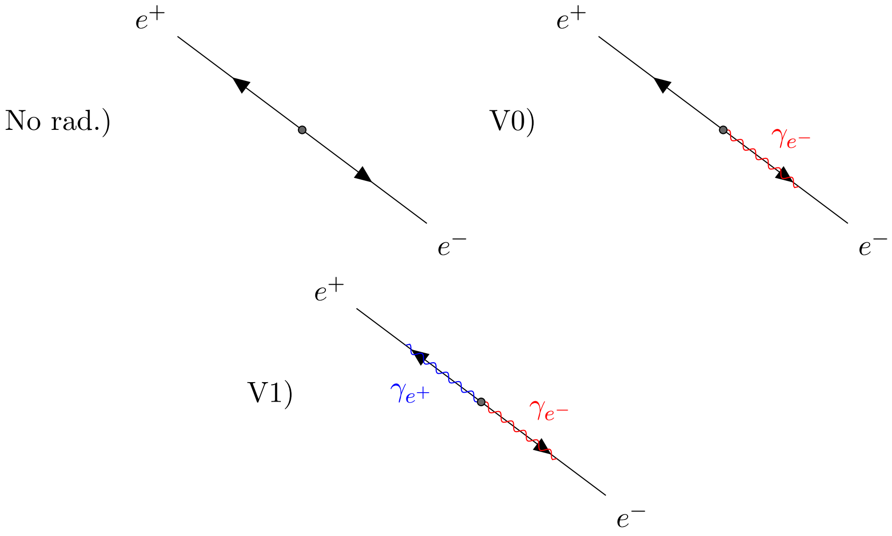

Figure 136: Diagrams representing the various soft-photon emission procedure used. The case where no radiative photon is emitted is represented in the diagram No rad.). In the first skim V0), only one photon with energy E_γ is emitted along the direction of one of the two lepton chosen randomly. In the second skim V1), two photons are emitted in both lepton directions. Each photon then carries a fraction of the total emitted energy E_γ. In all cases, the momenta of the leptons are recalculated to account for the momenta of the emitted photons.

1218 P.3.3 Implementation in TCSGen

1219 The algorithm of section P.3.2 is applied to the TCSGen generator. The effects of the implementation
1220 of this corrections to generated and reconstructed kinematics are presented in this section.

1221 ### P.3.4 Generated TCSGen sample with soft photon emission

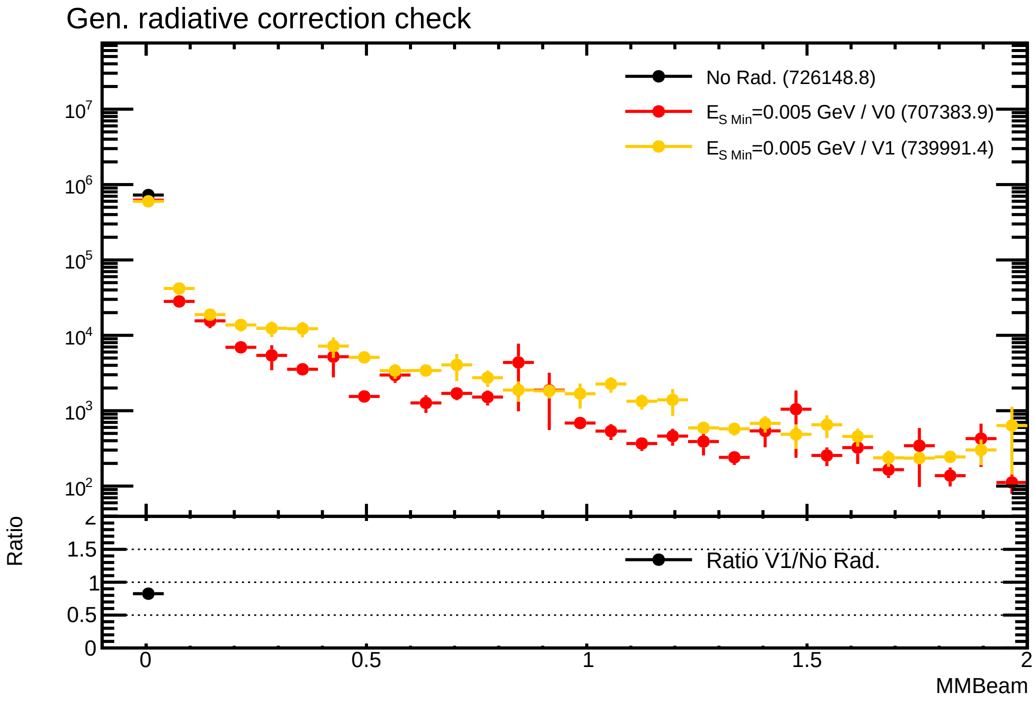

(a)

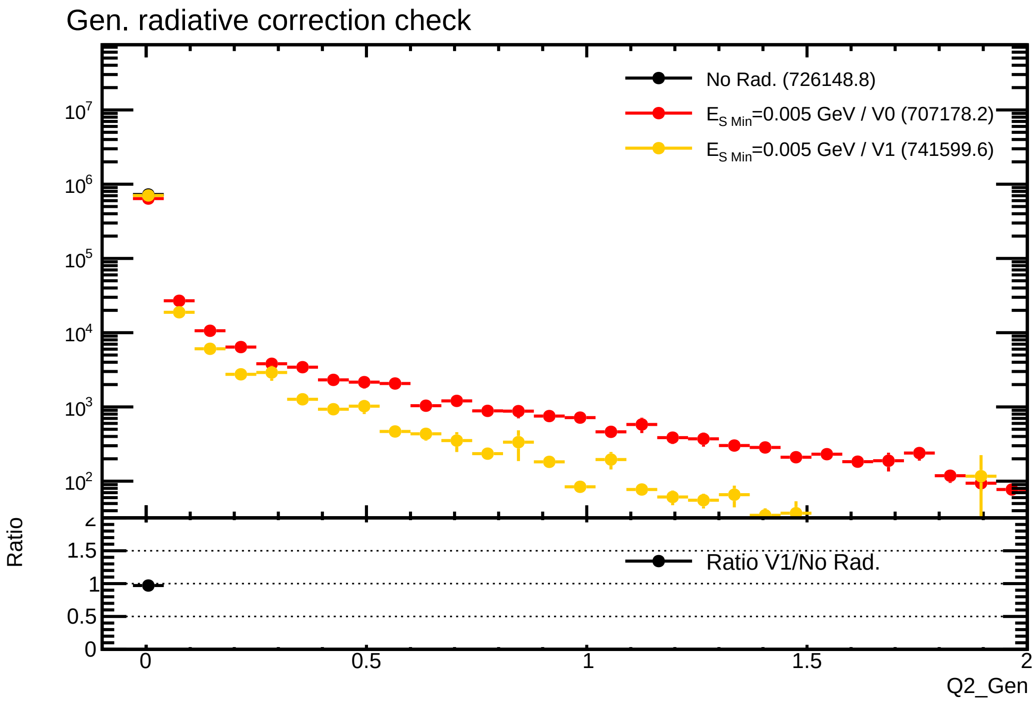

(b)

Figure 137: Generated missing mass of the scattered electron a) and generated virtuality of the real photon calculated using the final state particles momenta. In the non-radiated case, all events are in a single bin at 0. Both version of the radiation algorithm lead to a tail at large missing mass and large virtuality.

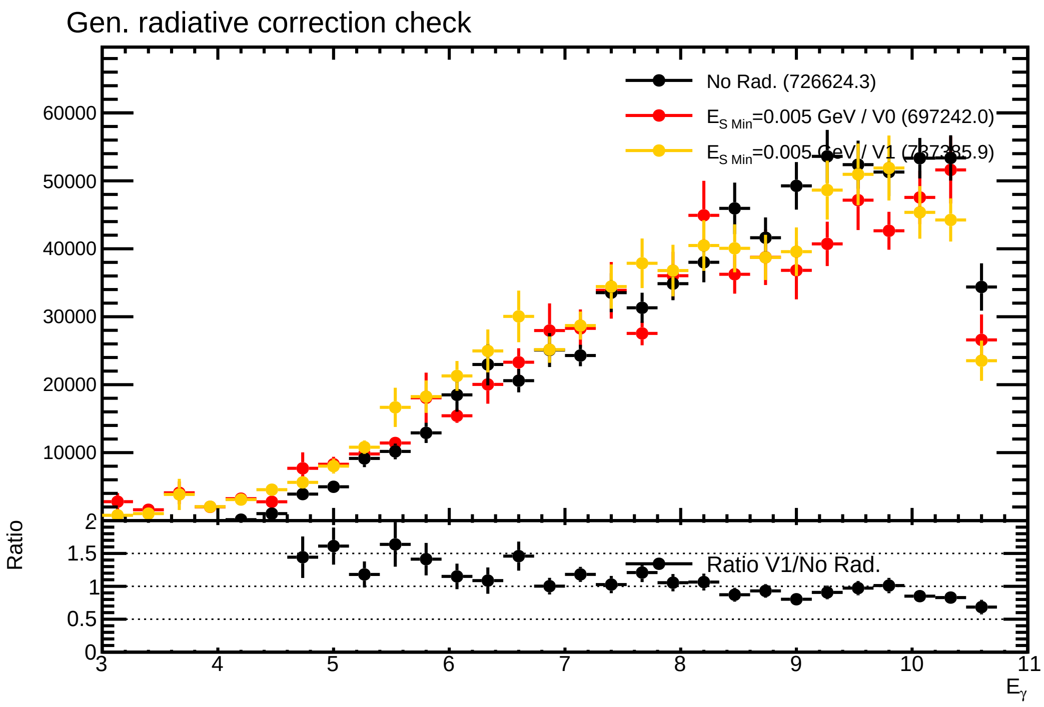

(a)

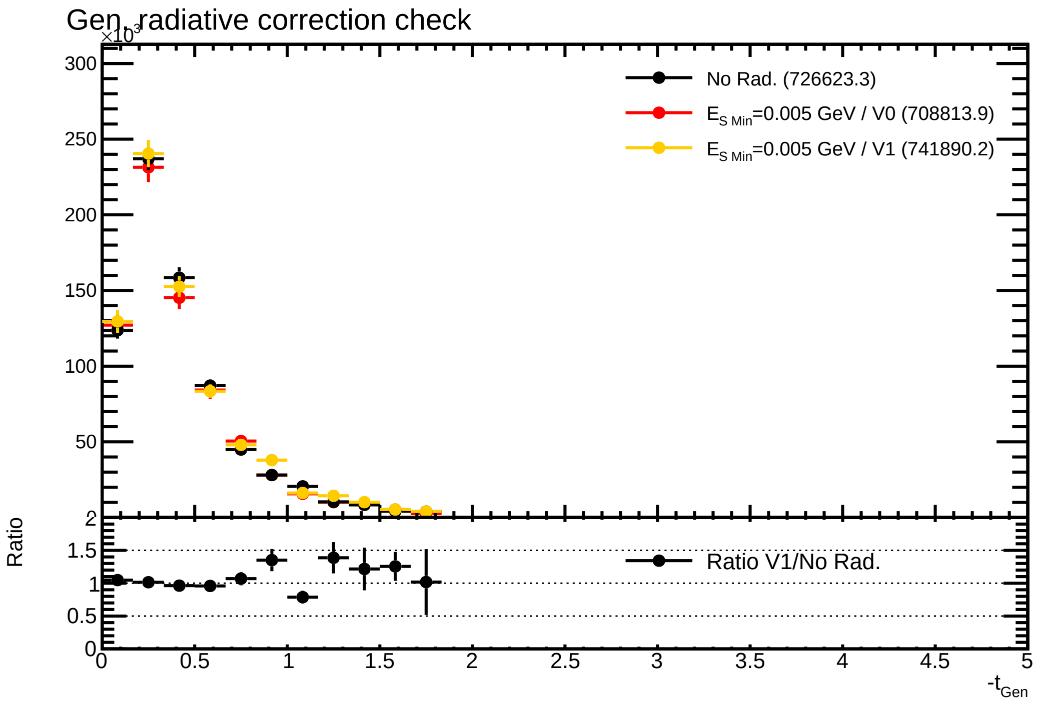

(b)

Figure 138: Generated energy of the real photon calculated using the final state particle momenta a) and square of the momentum transferred to the proton (-t) b).

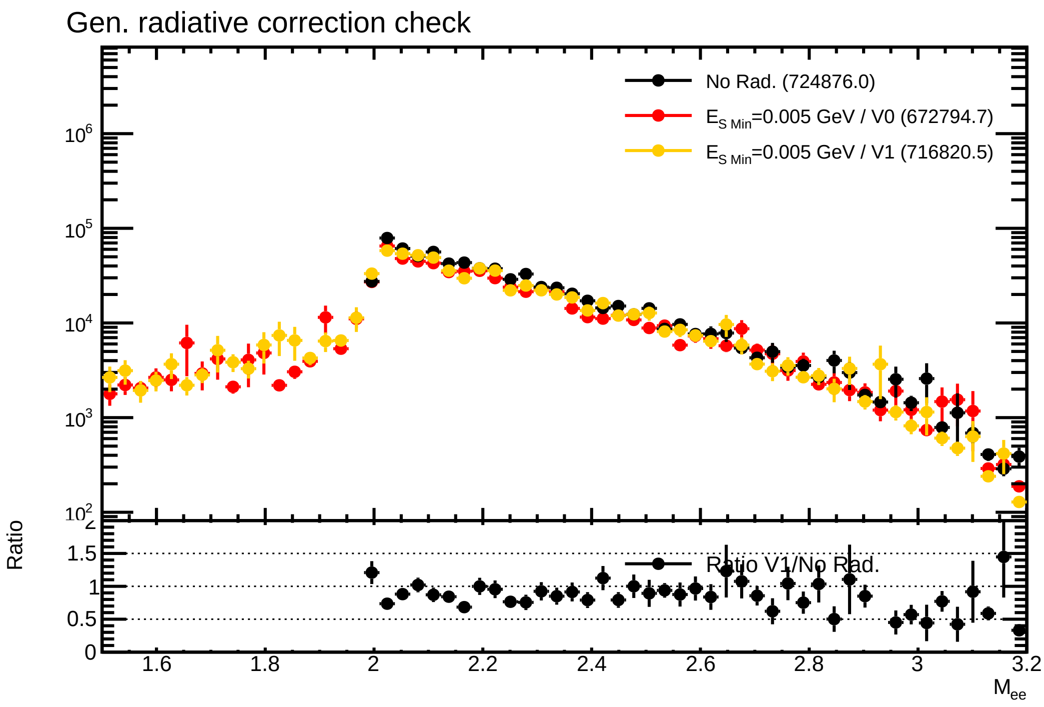

Figure 139: Generated invariant mass of the lepton pair. The generated events have a minimal invariant mass of 2 GeV. In case the radiative algorithm is in use, the generated mass can shift toward lower mass. This is visible in the tails of the distributions on the left hand side for both version of the radiative algorithm.

1222 #### P.3.4.1 Reconstructed TCSGen sample with soft photon emission

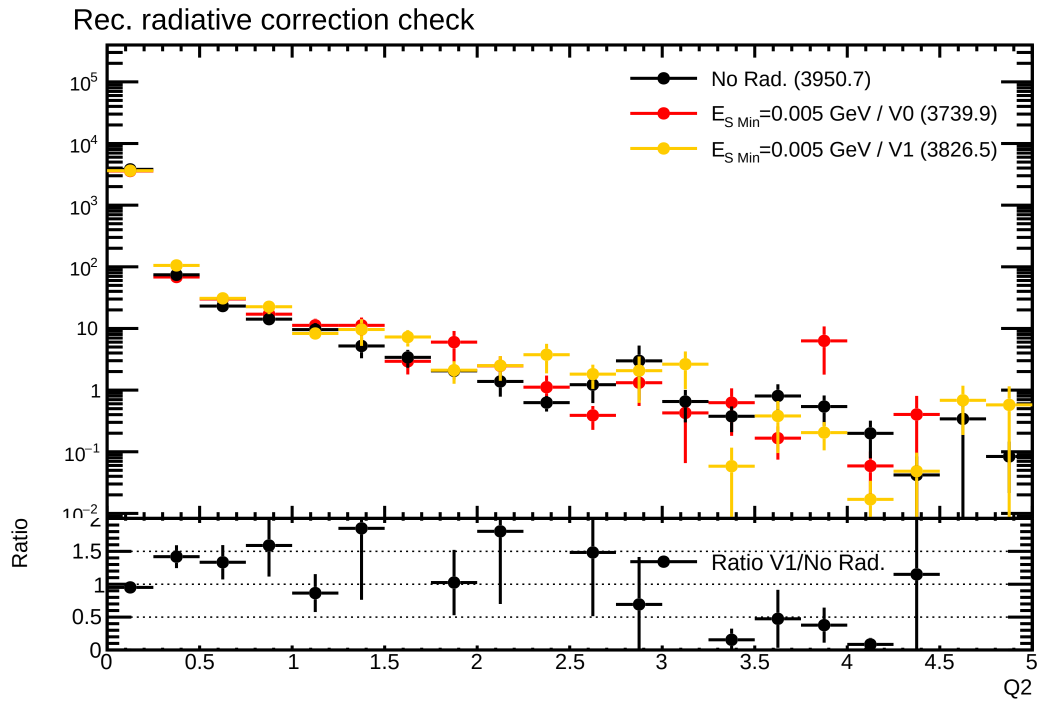

(a)

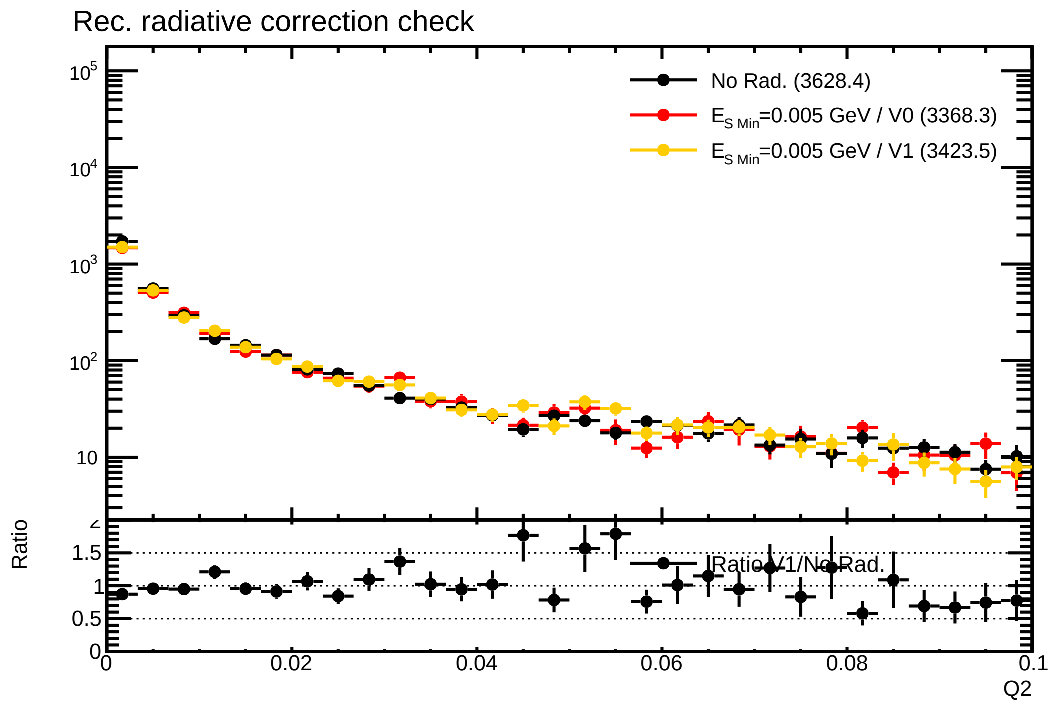

(b)

Figure 140: Reconstructed virtuality of the real photon, a) up to 5 GeV and b) in the region selected for the J/ψ analysis. A tail is observed in all cases including the non radiated case. In both cases, a cut on the missing mass is applied $|MM^2| < 0.4\ GeV^2$.

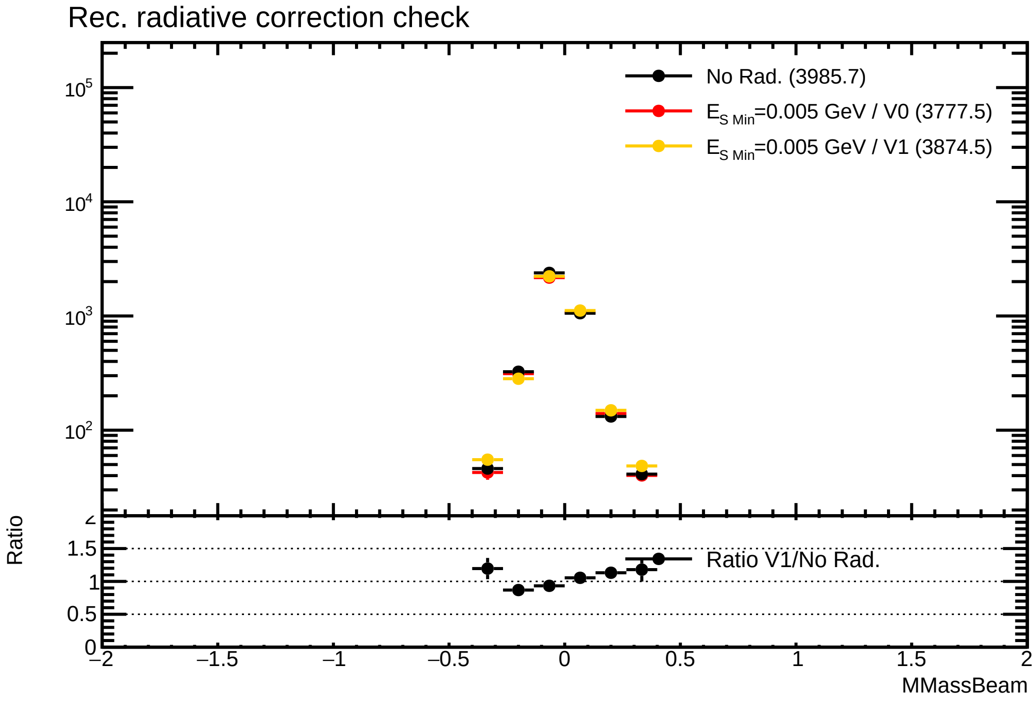

(a)

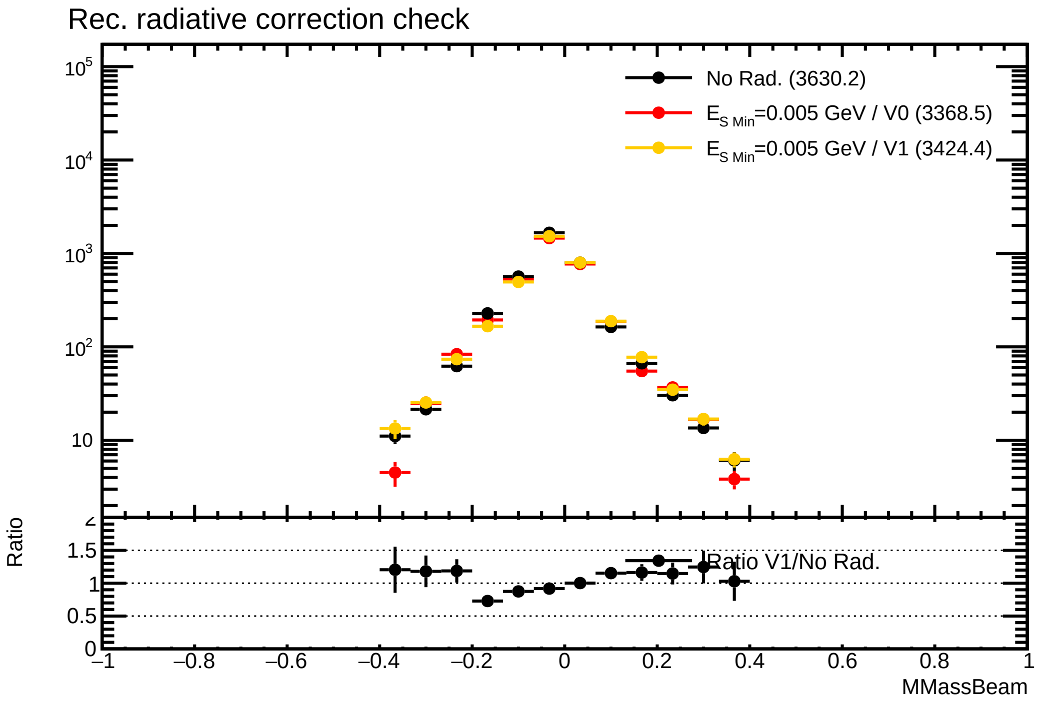

(b)

Figure 141: Reconstructed missing mass, a) without any virtuality cut and b) with a virtuality cut as $|Q^2| < 0.1GeV^2$. In both cases, a cut on the missing mass is applied $|MM^2| < 0.4\ GeV^2$.

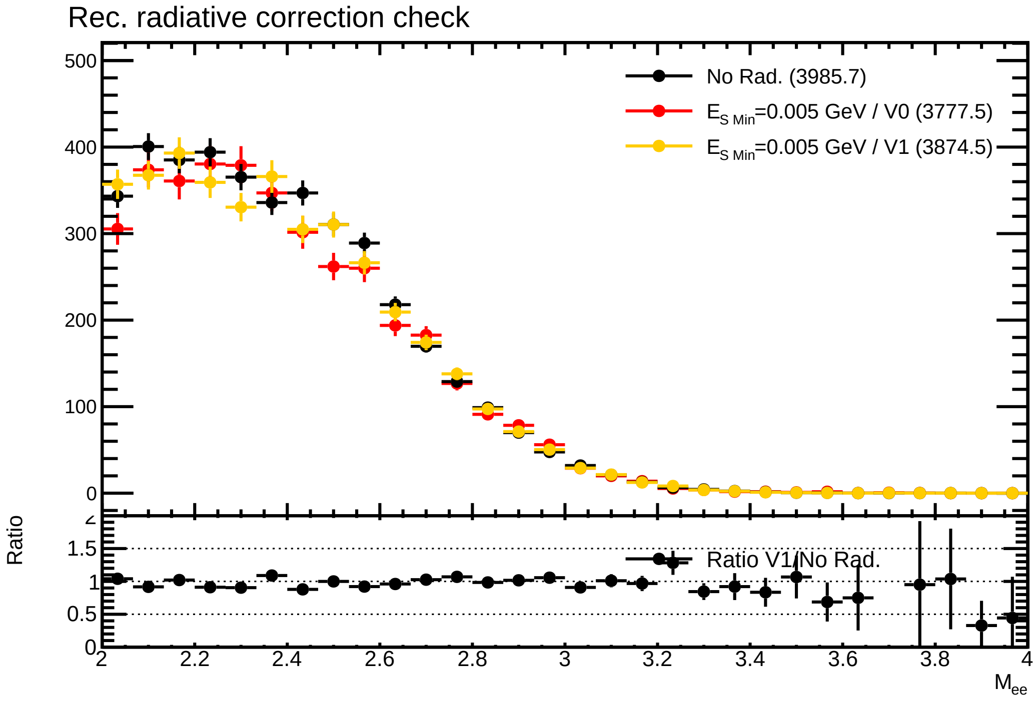

(a)

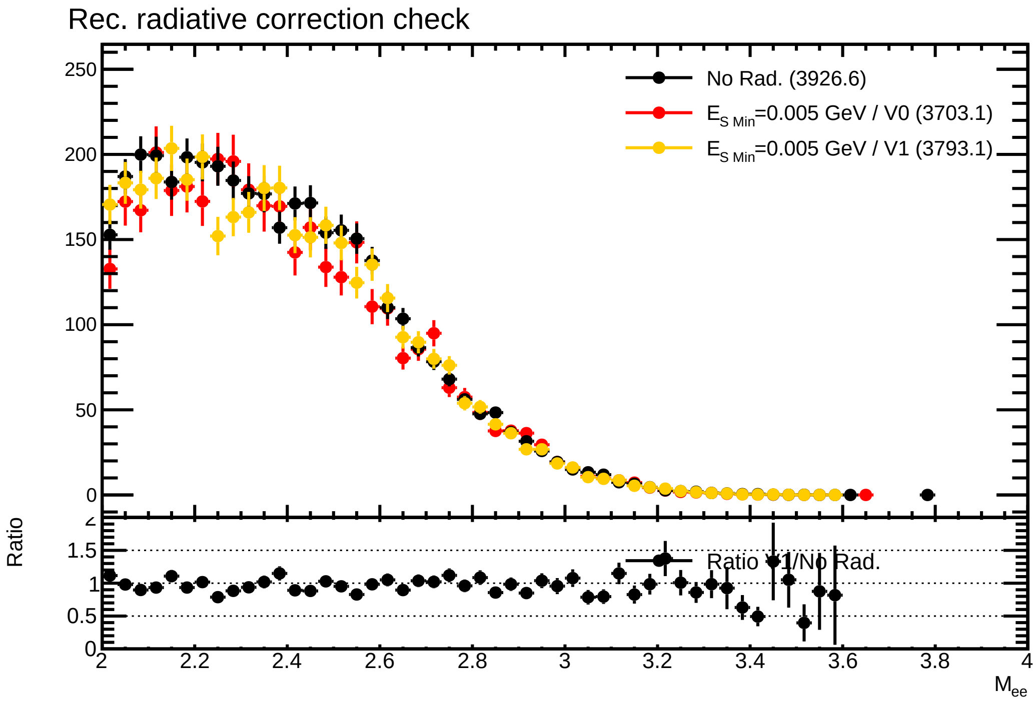

(b)

Figure 142: Reconstructed invariant mass of the lepton pair a) applying only a missing mass cut $|MM^2| < 0.4\ GeV^2$ and b) applying an additional virtuality cut $|Q^2| < 0.1 GeV^2$.

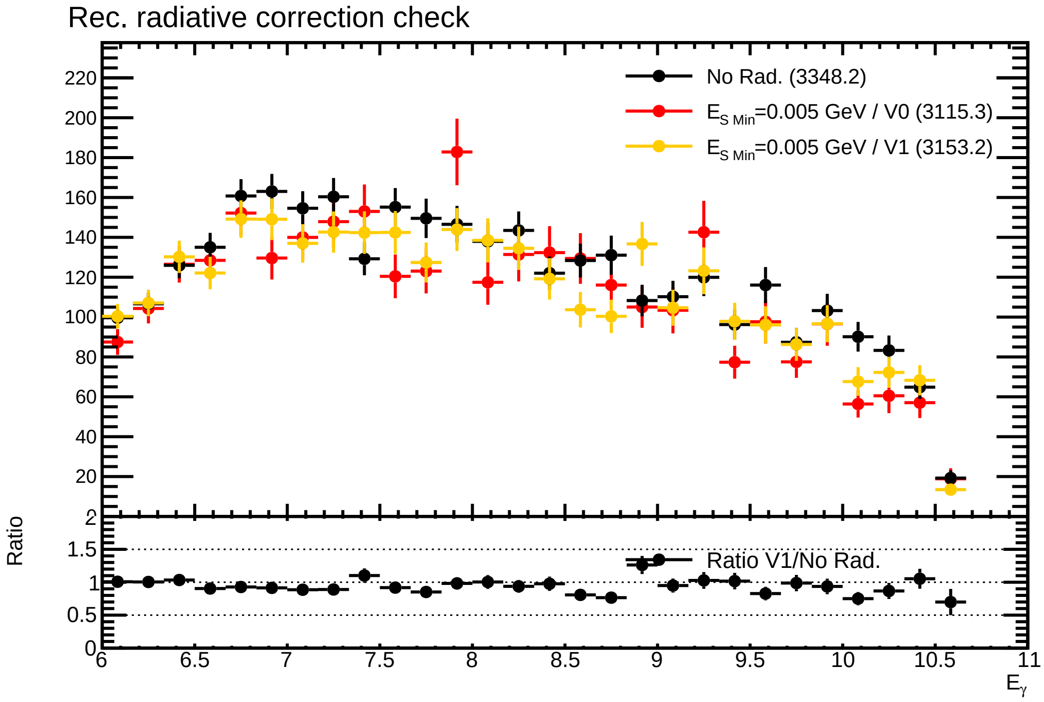

(a)

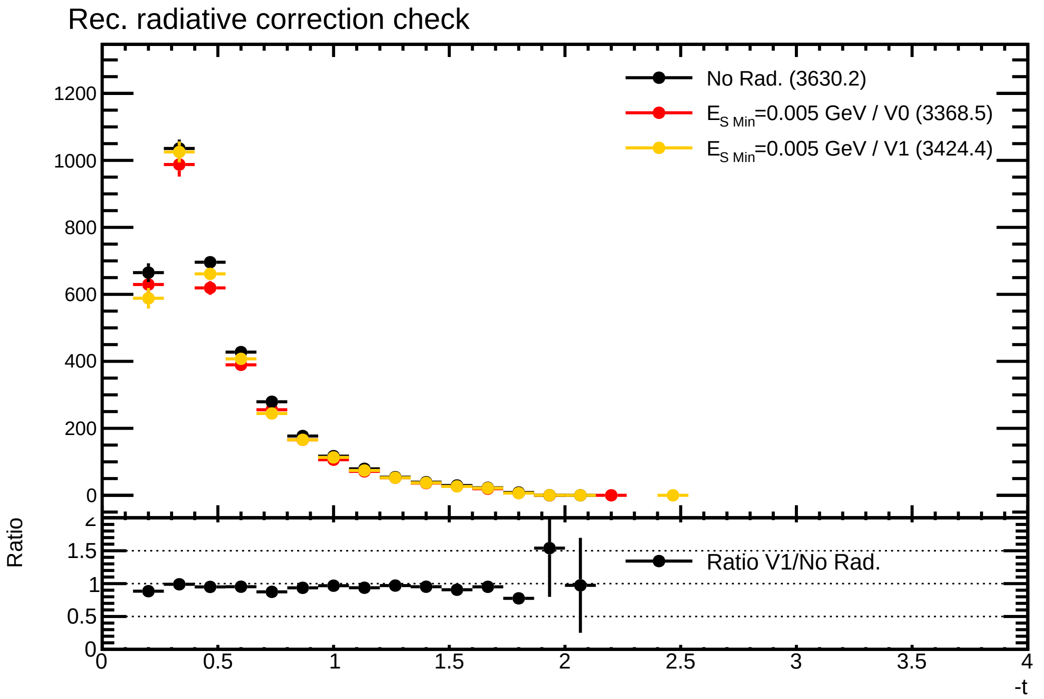

(b)

Figure 143: Reconstructed a) energy of the real photon and b) square of the transferred momentum to the proton. In both cases the usual selection cuts are applied: $|MM^2| < 0.4\,GeV^2$ and $|Q^2| < 0.1 GeV^2$.

1223 P.3.5 Implementation in Grape

1224 The algorithm of section P.3.2 is applied to the Grape generator. The effects of the implementation
1225 of this corrections to generated and reconstructed kinematics are presented in this section.

1226 #### P.3.5.1 Generated Grape sample with soft photon emission

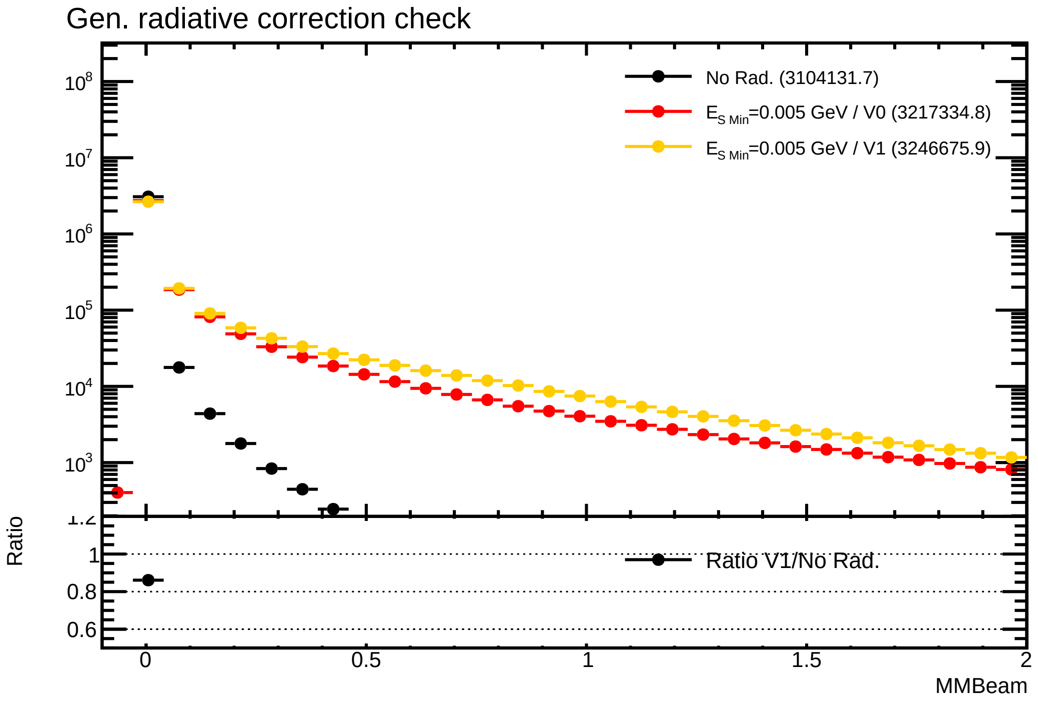

(a)

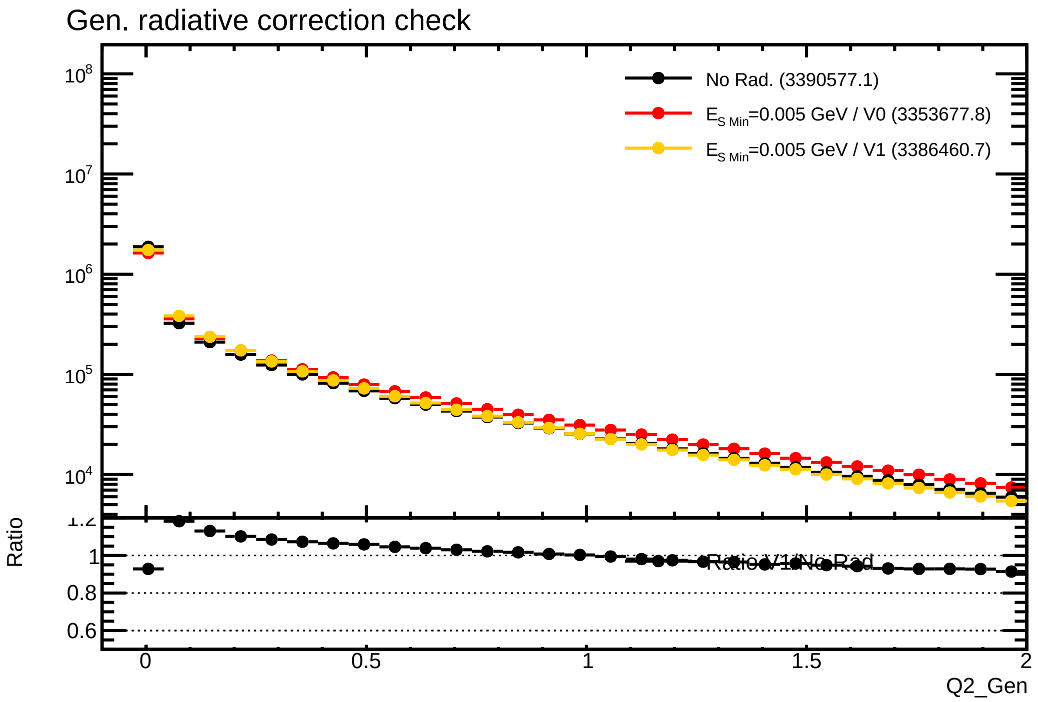

(b)

Figure 144: Generated missing mass of the scattered electron a) and generated virtuality of the real photon calculated using the final state particles momenta. In the non-radiated case, all events are in a single bin at 0. Both version of the radiation algorithm lead to a tail at large missing mass and large virtuality.

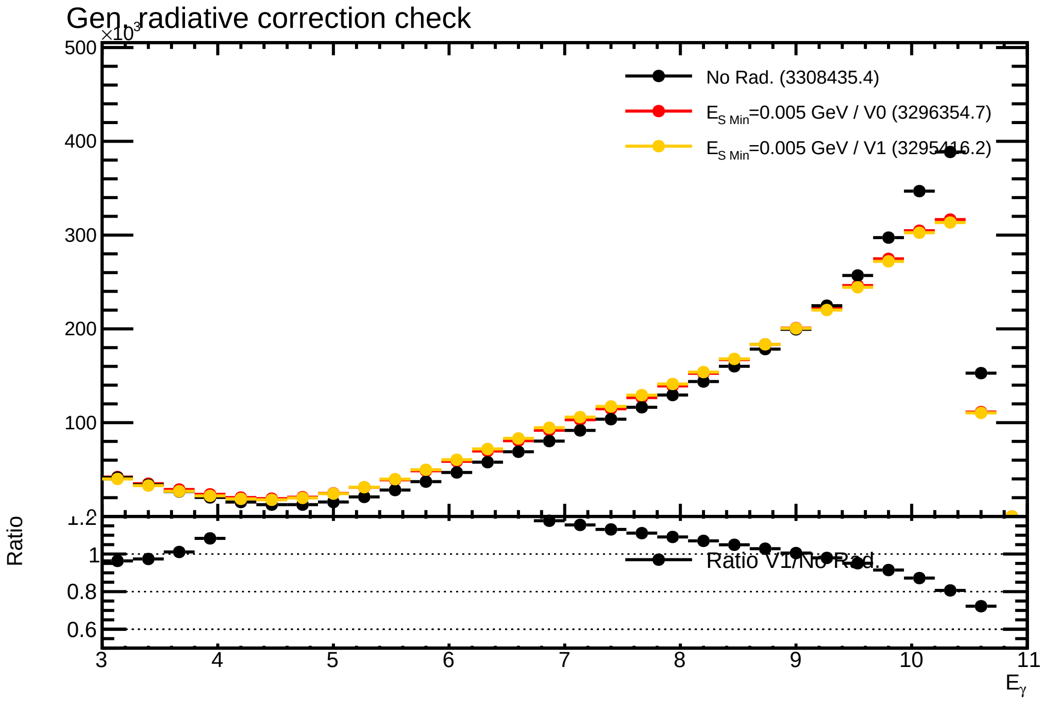

(a)

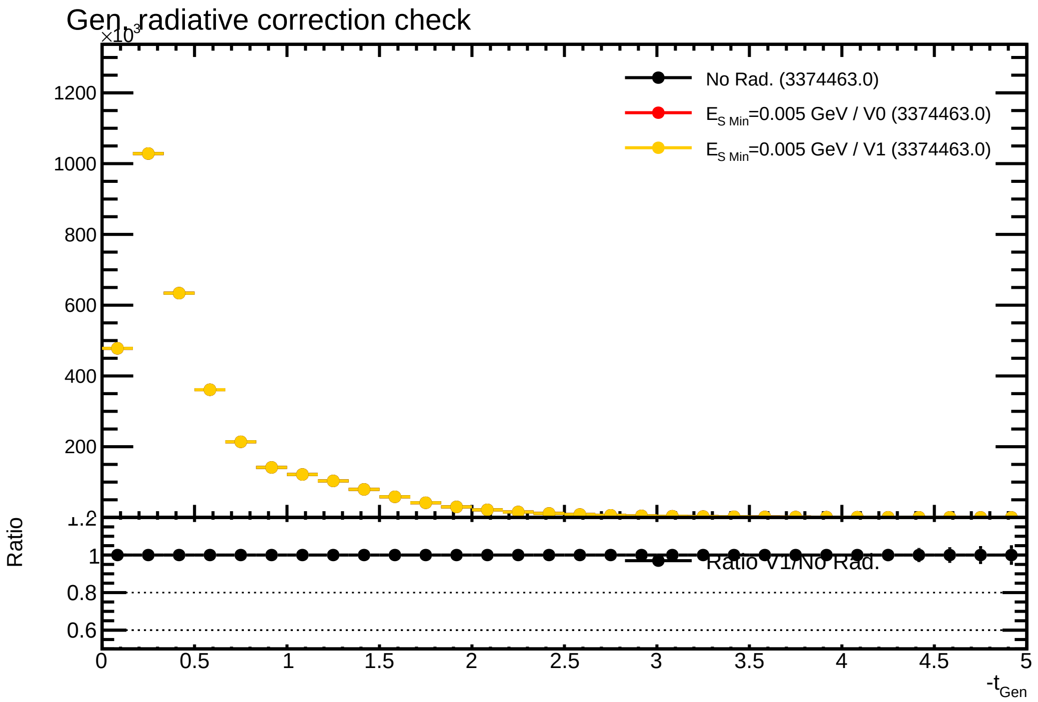

(b)

Figure 145: Generated energy of the real photon calculated using the final state particle momenta a) and square of the momentum transferred to the proton (-t) b).

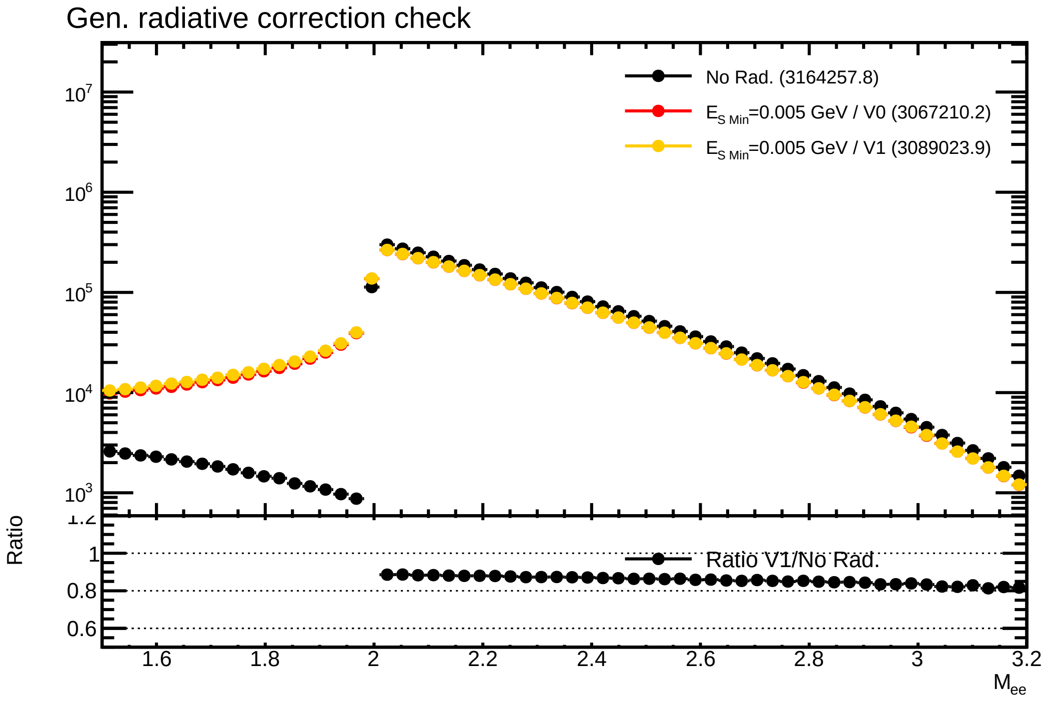

Figure 146: Generated invariant mass of the lepton pair. The generated events have a minimal invariant mass of 2 GeV. In case the radiative algorithm is in use, the generated mass can shift toward lower mass. This is visible in the tails of the distributions on the left hand side for both version of the radiative algorithm.

P.3.5.2 Reconstructed Grape sample with soft photon emission

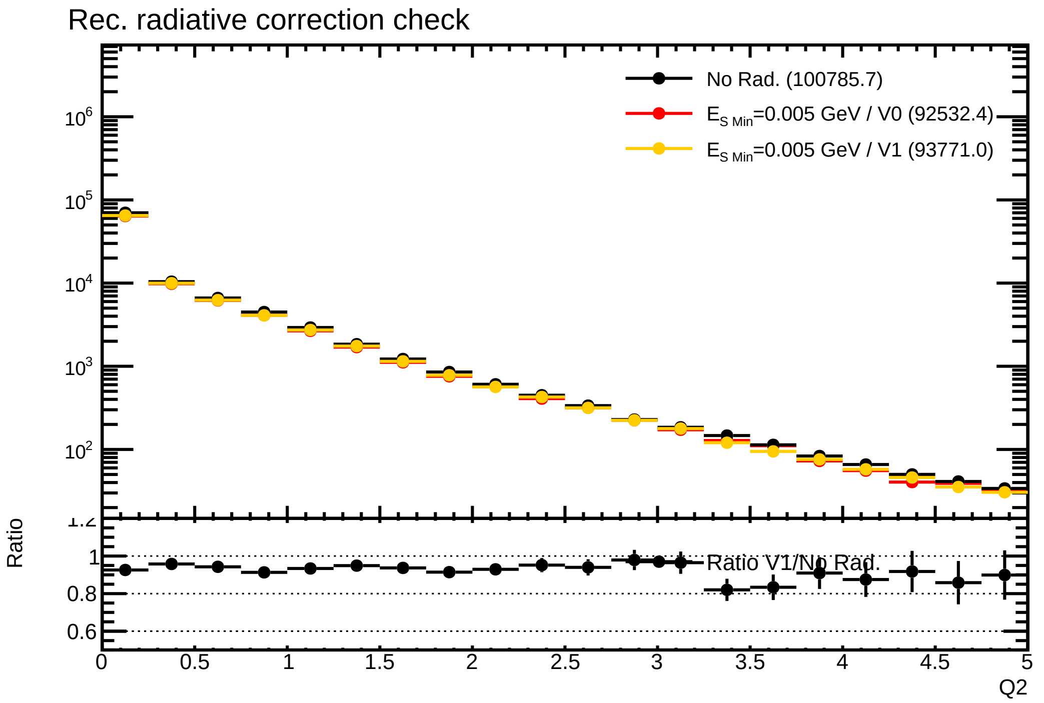

(a)

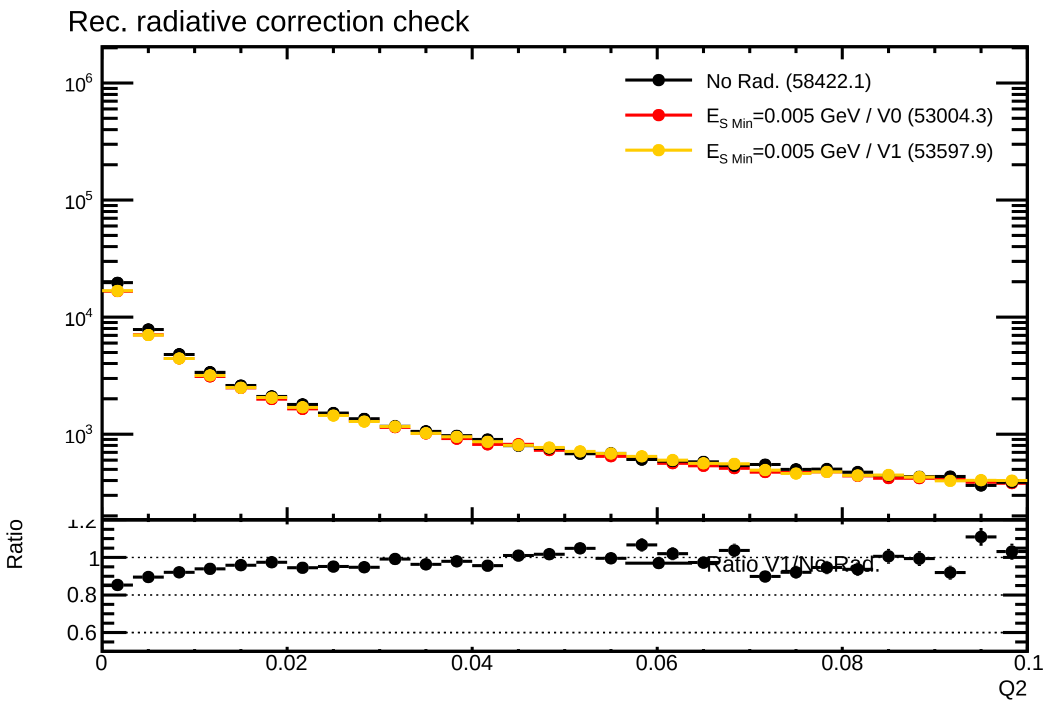

(b)

Figure 147: Reconstructed virtuality of the real photon, a) up to 5 GeV and b) in the region selected for the J/ψ analysis. A tail is observed in all cases including the non radiated case. In both cases, a cut on the missing mass is applied $|MM^2| < 0.4\ GeV^2$.

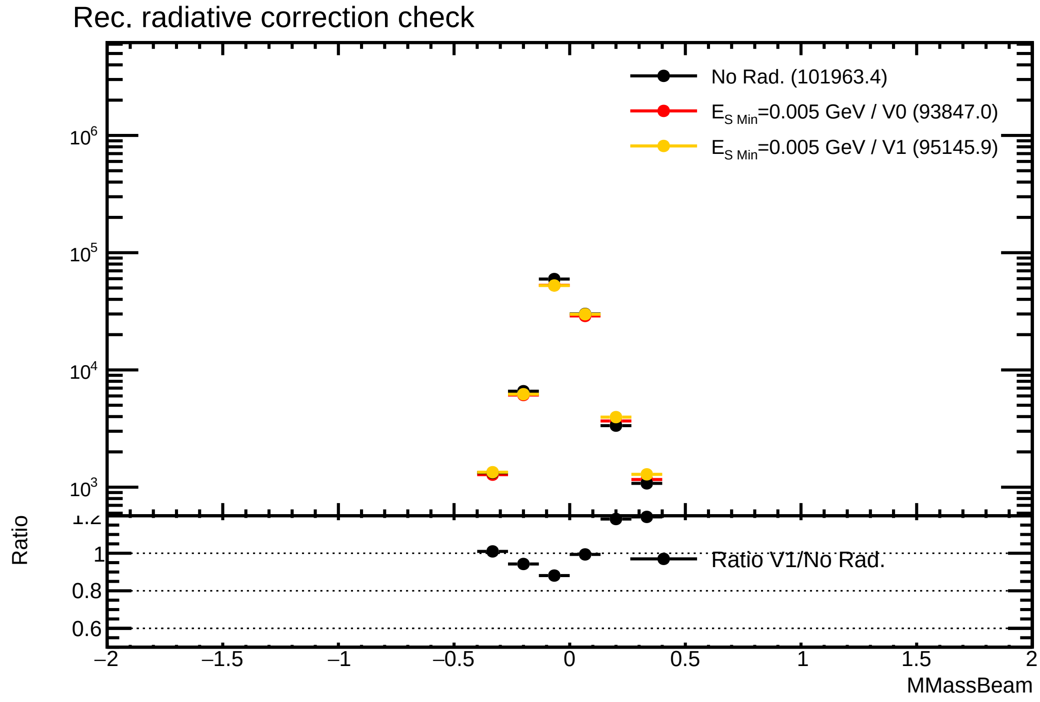

(a)

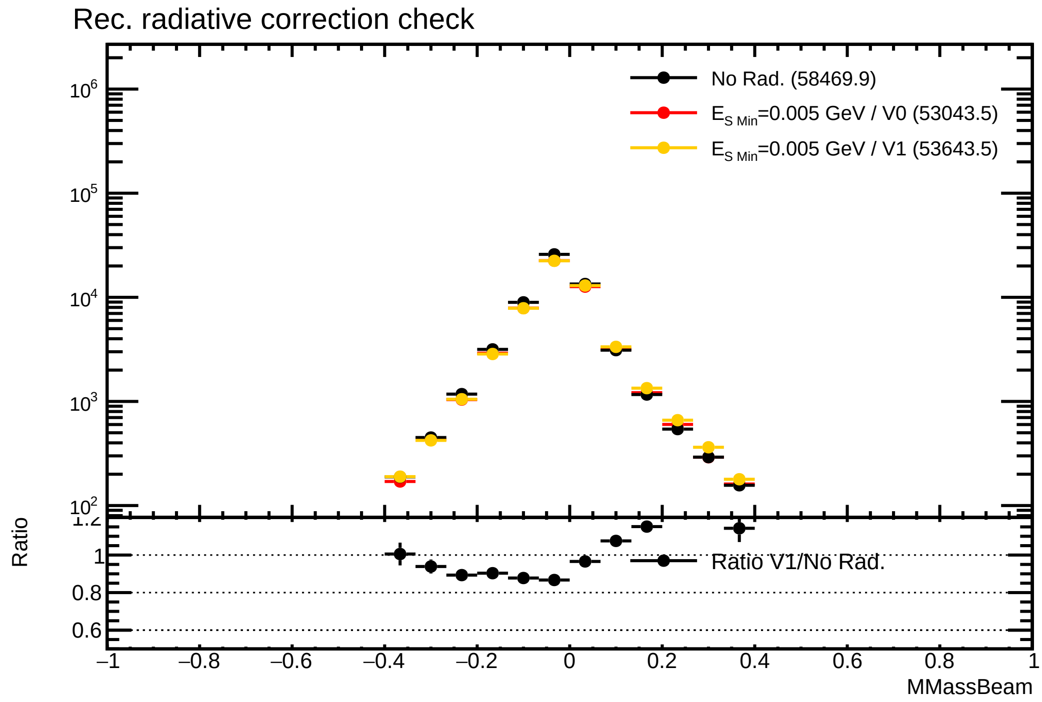

(b)

Figure 148: Reconstructed missing mass, a) without any virtuality cut and b) with a virtuality cut as $|Q^2| < 0.1 GeV^2$. In both cases, a cut on the missing mass is applied $|MM^2| < 0.4\ GeV^2$.

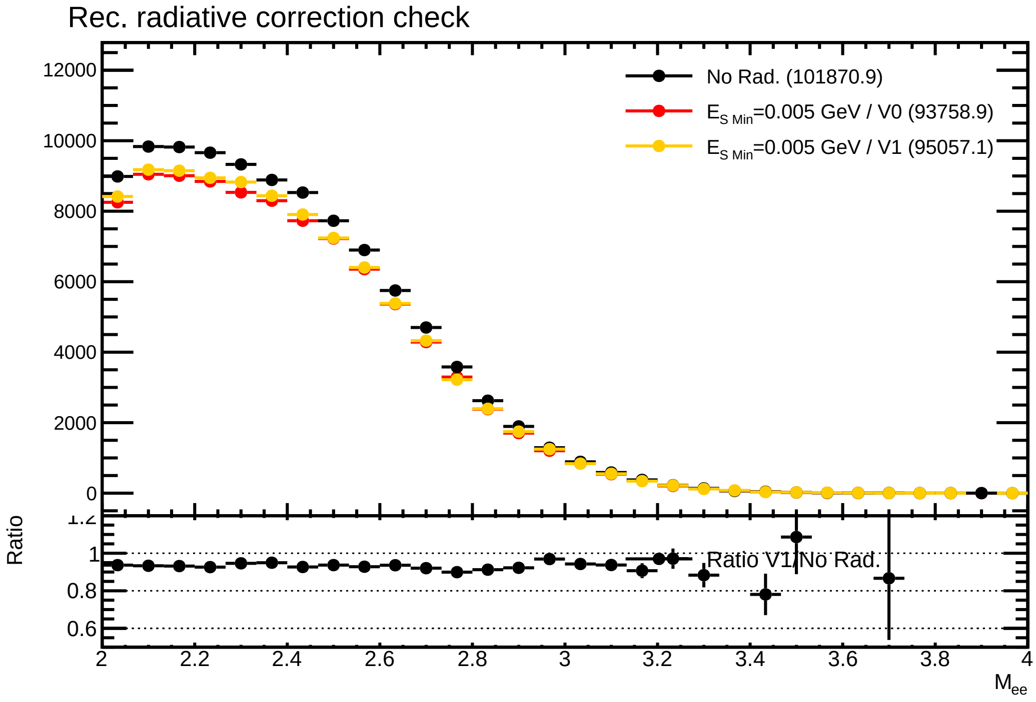

(a)

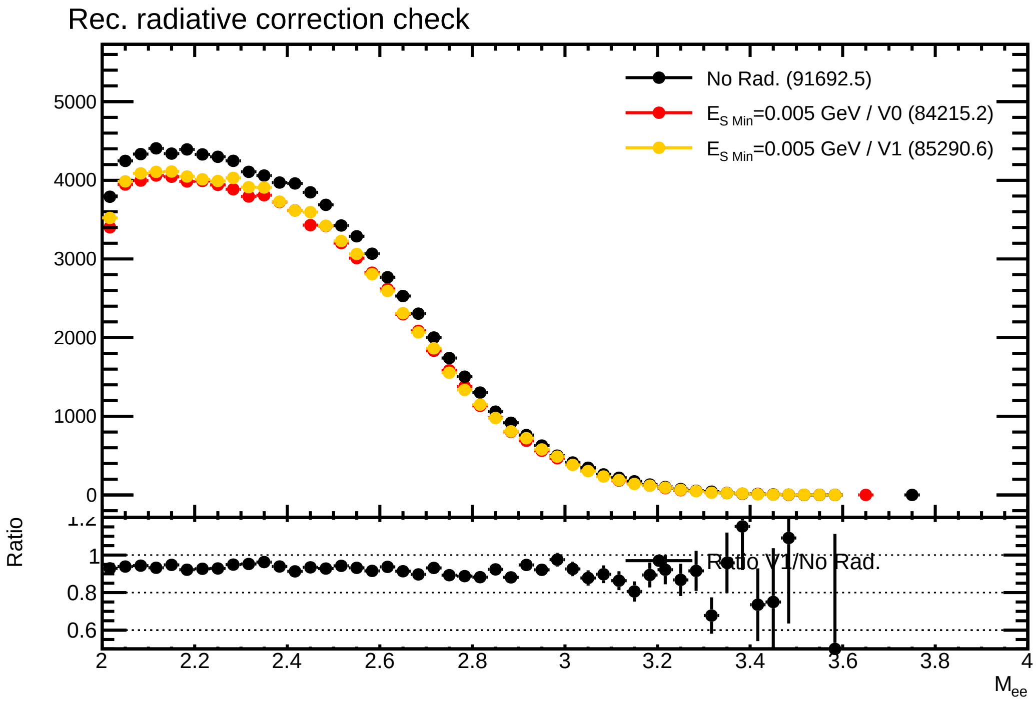

(b)

Figure 149: Reconstructed invariant mass of the lepton pair a) applying only a missing mass cut $|MM^2| < 0.4\ GeV^2$ and b) applying an additional virtuality cut $|Q^2| < 0.1 GeV^2$.

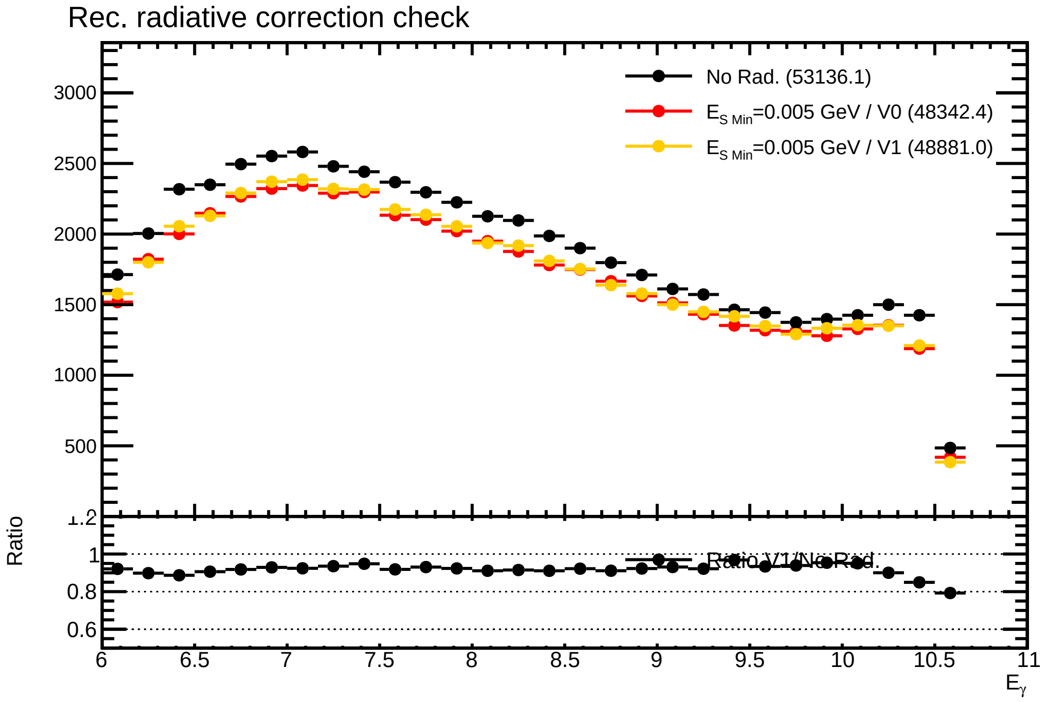

(a)

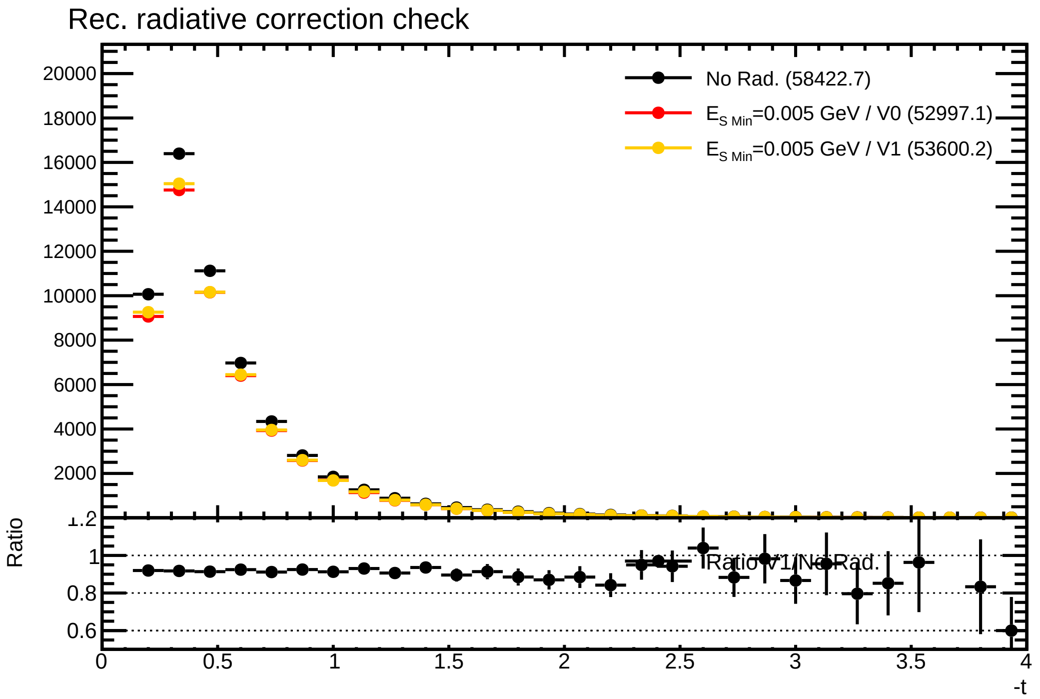

(b)

Figure 150: Reconstructed a) energy of the real photon and b) square of the transferred momentum to the proton. In both cases the usual selection cuts are applied: $|MM^2| < 0.4\,GeV^2$ and $|Q^2| < 0.1 GeV^2$.

Q Radiative effects for J/ψ events

Q.1 Formulae

In the case of vector meson production, the formulas used to compute δ are slightly different from the one given in [41]. To compute the radiative effect, the formulas derived in [42] have been implemented in the same way as for the Bethe-Heitler events shown in the previous section..

Q.2 Comparison with PHOTOS and non-radiated case

In this section, we compare various kinematical variables related to the radiative effect on J/ψ decay. The approach derived in Q.1 and the PHOTOS package [39] are compared with the non-radiated case. Apart from the missing mass spectrum, both radiative effect implementation yield very similar effects.

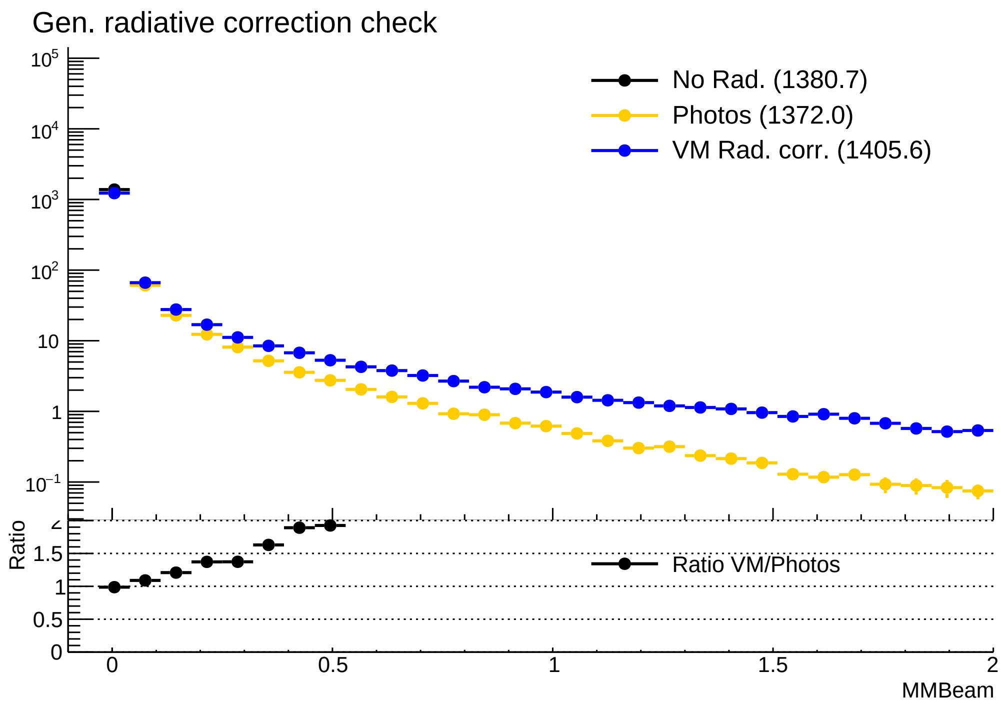

(a)

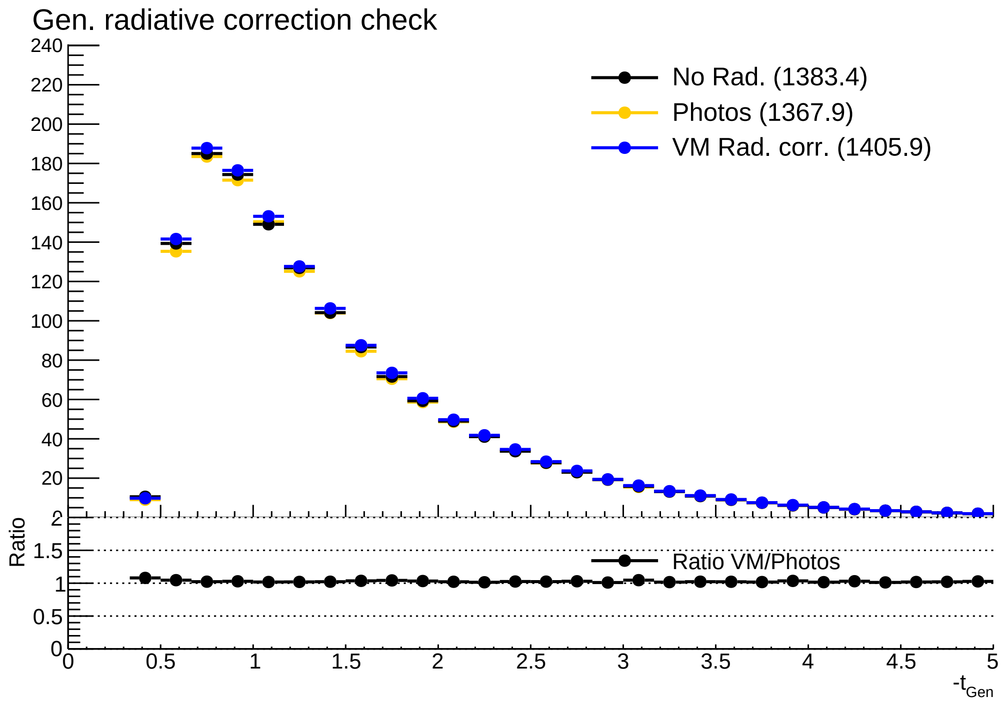

(b)

Figure 151: Generated a) missing mass of the system and b) transfered momentum squared to the proton t, for non-radiated J/ψ events, radiated using the approach developed for this analysis, or using the PHOTOS package.

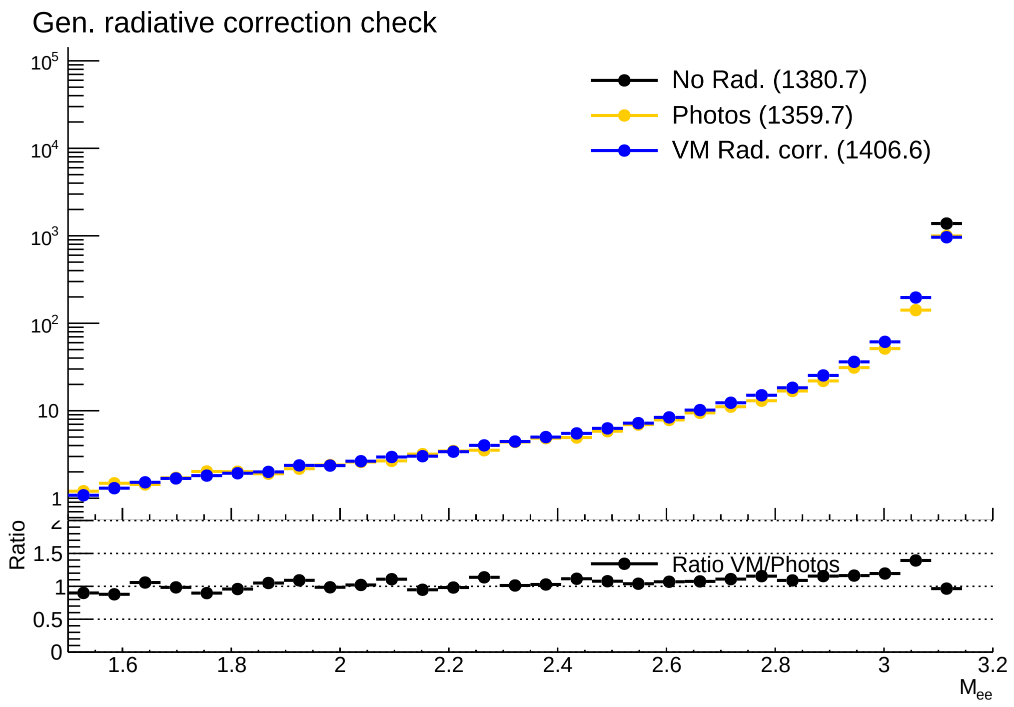

(a)

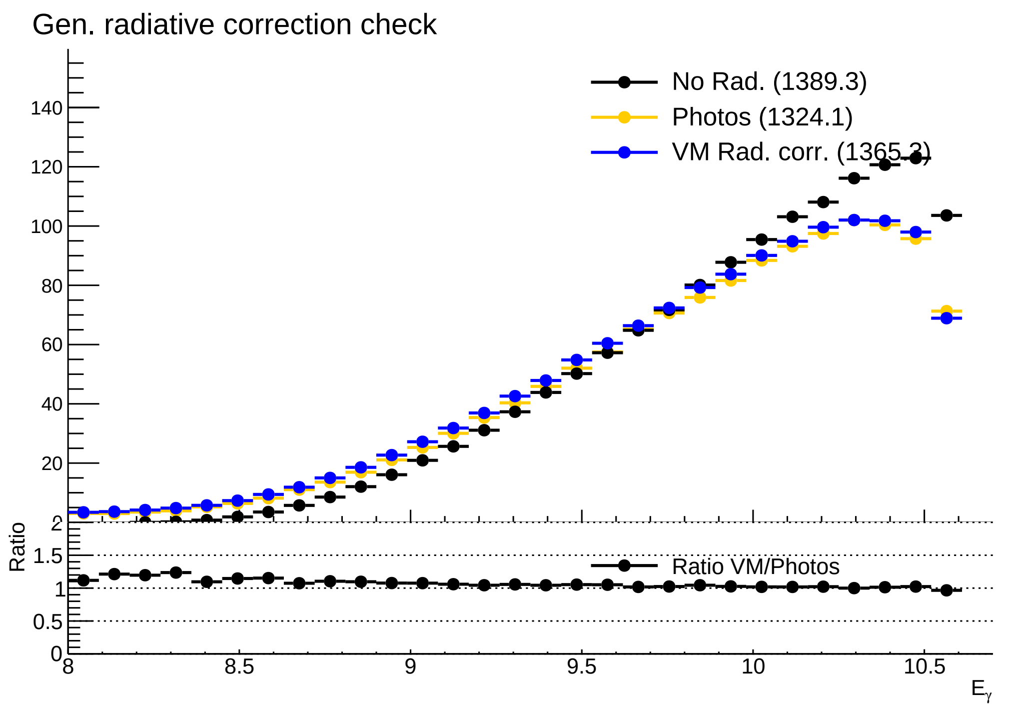

(b)

Figure 152: Generated a) invariant mass of the lepton pair and b) estimation of the photon energy from the three final state particle of interest, for non-radiated J/ψ events, radiated using the approach developed for this analysis, or using the PHOTOS package.

R Initial state radiation for the real photon flux.

Bremsstrahlung photon flux uses the formula (34.30) of Section 34 of PDG [43], "Passage of particles through matter". It is derived from Eq.(34.28) of bremmstrahlung cross-section with complete screening:

$$\frac{d\sigma}{dk} = \frac{4\alpha r_e^2}{k}\{(\frac{4}{3} - \frac{4}{3}y + y^2)[Z^2(L_{rad} - f(Z)) + ZL'_{rad}] + \frac{1}{9}(1-y)(Z^2+Z)\} \tag{69}$$

Here, $r_e = 2.818$ fm is the electron radius, $y = k/E$ is the fraction of electron energy E carried by the emitted photon with energy k, and Z is the atomic number. Ignoring the last piece, which is important for small y, the cross-section is approximated as:

$$\frac{d\sigma_b}{dk} = \frac{4\alpha r_e^2}{k}\{(\frac{4}{3} - \frac{4}{3}y + y^2)[Z^2(L_{rad} - f(Z)) + ZL'_{rad}]\}; \tag{70}$$

and using the definition of radiation length, X_0, PDG Eq.(34.25), the cross-section takes form (PDG Eq.(34.29)):

$$\frac{d\sigma_b}{dk} = \frac{A}{X_0 N_A k}(\frac{4}{3} - \frac{4}{3}y + y^2); \tag{71}$$

Number of bremsstrahlung photons in the energy range k_{min} to k_{max} emitted by electrons of energy E traveling a distance lr.l.($= d\rho N_A/A$, with d-linear distance) is an integral over k and given in PDG Eq(34.30):

$$\begin{aligned} N(k_{min}, k_{max}) &= \quad l\int_{k_{min}}^{k_{max}} \tfrac{A}{X_0 N_A}(\tfrac{4}{3}\tfrac{dk}{k} - \tfrac{4}{3}\tfrac{dk}{E} + \tfrac{kdk}{E^2}); & (72) \\ N(k_{min}, k_{max}) &= \tfrac{l}{X_0}\left(\tfrac{4}{3}\ln(\tfrac{k_{max}}{k_{min}}) - \tfrac{4(k_{max}-k_{min})}{3E} + \tfrac{(k_{max}^2 - k_{min}^2)}{2E^2}\right) & (73) \end{aligned}$$

Up to this point, all the derivations follow article Y-S Tsai [44] (PDG reference [42]). This article did not include radiative corrections to the bremsstrahlung; instead, it refers to Morak and Olsen's (MO) paper [45].

In the MO paper, all possible diagrams of radiative corrections have been studied and ended up in three correction types: virtual photon emission and absorption, real soft photon emission, and vacuum polarization. The latter one was found to be negligible for all ys. While very detailed, the paper is hard to use.

Fortunately, in another paper written by Schulz and Lutz [46] and where MO's formalism is used, the authors not only recalculated the radiative corrections to the bremsstrahlung spectrum for 5.1 GeV electrons but also compared their calculation results[1] with experimental data. Following notations of [46], the cross-section bremsstrahlung process is:

$$d\sigma^B = d\sigma_0^B(1 + \delta^B) \tag{74}$$

where $d\sigma_0^B$ is the lowest-order bremsstrahlung cross-section and $d\sigma^B$ is the cross section including radiative corrections. The δ^B is presented as (the same is in [45]):

$$\delta^B = F_1(y) + F_2(y)\ln(1-y) \tag{75}$$

Values of F_1 and F_2 are given in the paper in Table I. Formulas for F_1 and F_2 are not available in [46] and as mentioned above, while formulas are in [45] it was found hard to follow the definitions and to use them.

So, tabulated values of F_1 and F_2 were used to calculate δ^Bs from $y = 0.1$ to 0.995 using available points. Then, the y dependence is fitted. The results of calculations and the fit are shown in Fig.153.

[1]The new calculations by Schulz and Lutz is different from numbers presented in [45], but has been check by MO.

The calculated points (i.e. the curve) are slightly different from the one shown in [46], which is puzzling as the numbers used to make the graph are exactly what is in Table I of the paper.

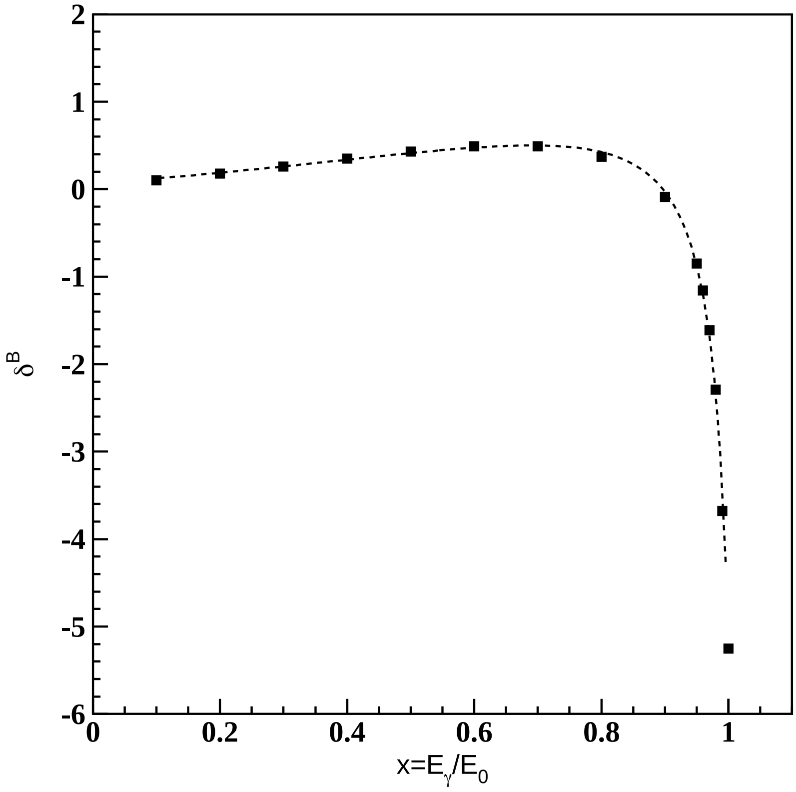

Figure 153: Solid points are recaculation of $\delta^B(\%)$ using vales of F_1 and F_2 from Table I of [46]. The dashed curve is the fit result.

In conclusion, radiative corrections matter for $y > 0.8$, the region of interest for this analysis, and reach about 6% at the end of the spectrum. The flux calculated using PDG Eq.(34.30) must be corrected as follows to correct for this ISR effect:

$$N^R(k_{min}, k_{max}) = N(k_{min}, k_{max})(1 + f) \tag{76}$$

where f is

$$f = 0.244039 + 0.69143 * x - 0.18276/(1.0264 - x) + 0.6784 * x * x \tag{77}$$

End of the document